UNIVERSITÀ DI PARMA

UNIVERSITA' DEGLI STUDI DI PARMA

RESEARCH DOCTORATE IN

Industrial Engineering

XXXVII CYCLE

Realization and investigation of the properties of biocomposites based on biopolymers for novel application in agri-food and biomedical fields

Coordinator:

Chiar.mo Prof. Gianni Royer Carfagni

Supervisors:

Chiar.mo Prof. Daniel Milanese

Chiar.mo Prof. Corrado Sciancalepore

Candidate: *Elena Togliatti*

Academic Years 2021/2022 – 2023/2024

Abstract

In recent decades, interest in bioplastics as a sustainable alternative to traditional plastics has increased considerably. The primary reasons for this are the biodegradability of these plastics and their lower environmental impact. This research project examines the development and characterization of biocomposites utilizing bio-based polymers, with a particular focus on poly(butylene adipate-co-terephthalate) (PBAT) and polyhydroxyalkanoates (PHA). The objective is to enhance the mechanical properties of these materials while ensuring their biodegradability and biocompatibility, with potential applications in packaging and biomedicine.

The study is centered on the examination of PBAT biocomposites reinforced with bioabsorbable calcium-phosphate glass (CPG) and a hybrid zein-titanium dioxide complex (ZTC). CPG provides the requisite bioactivity and mechanical strength for biomedical applications, while ZTC enhances the interfacial adhesion between the polymer matrix and the fillers. The biocomposites, prepared via solvent casting with up to 40 wt% filler concentrations, were characterized through microscopy and spectroscopy to assess their structural properties. The mechanical testing demonstrated that both fillers significantly reinforced the PBAT, enhancing its bioactivity and structural stability.

The study also examines the use of polyhydroxybutyrate (PHB) enhanced with glycerol trilevulinate (GT), a green plasticizer that improves flexibility and stability. The resulting PHB-GT composites were evaluated for processability through extrusion, injection molding, and fused deposition modeling (FDM) for potential applications in scaffolding. The mechanical tests demonstrated notable enhancements in flexibility. The present study investigates the incorporation of resorbable phosphate glass into plasticized PHB to create bioactive composites tailored for scaffold applications. These glass-filled PHB materials demonstrate enhanced mechanical properties, rendering them suitable for supporting tissue regeneration and bone growth.

Furthermore, the biodegradability of PBAT-CPG composites was examined under diverse environmental conditions, employing accelerated weathering tests and laboratory-scale composting simulations. Additionally, the biodegradation of plasticized PHB under anaerobic conditions indicated that optimal GT concentrations could accelerate biodegradation rates while maintaining favorable microbial activity, thereby underscoring the material's potential for sustainable applications in various fields.

Keywords: biocomposites, PHB, PBAT, mechanical characterization, FDM 3D printing, biomedical scaffolds, biodegradation

Table of contents

List of Figures

List of tables

List of acronyms

3D 3-dimensional

3-HB 3-hydroxybutyrate

AA adipic acid

ABS poly(acrylonitrile-butadiene-styrene)

AM Additive Manufacturing

ANOVA analysis of variance

ATBC acetyl tributyl citrate

ATP adenosine triphosphate

ATR attenuated total reflectance

BA butylene adipate

BDO butanediol

bio-PE bio-polyethylene

bio-PET bio-poly(ethylene terephthalate)

BT butylene terephthalate

BTE bone tissue engineering

C$_2$ acetate

CNCs cellulose nanocrystals

CNFs cellulose nano-fibers

CNT carbon nanotube

COD chemical oxigen demand

CPG calcium-phosphate glass

CR-3HB mixture of 3-hydroxybutyrate and crotonate

DIC digital image correlation

DINCH 1,2-cyclohexanedicarboxylic acid diisononyl ester

DMA dynamic mechanical analysis

DSC differential scanning calorimetry analysis

EDS energy-dispersive X-ray spectroscopy

Ex extrusion

FDM fused deposition modeling

FT-IR Fourier-transform infrared

GC gas chromatography

GT glycerol trilevulinate

HDFs human dermal fibroblasts

HDPE high-density polyethylene

HF hydrolyzed fermentation

HV hydroxyvalerate

IM injection molding

lcl-PHA long-chain-length PHA

LDPE low-density polyethylene

MA-PP maleated polypropylene

mcl-PHA medium-chain-length PHA

MFC microfibrillated cellulose

n-C$_4$ n-butyrate

n-C$_6$ n-caproate

OTR oxygen transmission rate

PE polyethylene

PBAT poly(butylene adipate-co-terephthalate)

PBS polybutylene succinate

PCL polycaprolactone

PG phosphate-based glass

PHA polyhydroxyalkanoates

PHB polyhydroxybutyrate poly(3-hydroxybutyrate)

PHBH poly(hydroxybutyrate-co-hexanoate)

PHBV poly(3-hydroxybutyrate-co-3-hydroxyvalerate)

PLA polylactic acid

PP polypropylene

PTSA *p*-toluenesulfonic acid monohydrate

SCG spent coffee ground

scl-PHA short-chain-length PHA

sCOD soluble chemical oxigen demand

SEM scanning electron microscopy

SF solids fermentation

TGA thermo-gravimetric analysis

TLM transmitted light microscope

TPA terephthalic acid

TPU thermoplastic polyurethane

TTS time-temperature superposition principle

UTT uniaxial tensile test

UV ultraviolet

VFA volatile fatty acids

WLF Williams-Landel-Ferry

WVTR water vapor transmission rate

ZTC zein-titanium dioxide complex

List of symbols

A filler spherical geometry parameter

A_f interfacial surface

B_y / B_B Pukánszky's empirical parameter that considers the strength of interactions

D degree of disintegration

D_{10} particle sizes below which 10% of the sample fall, in terms of volume density fraction

D_{50} particle sizes below which 50% of the sample fall, in terms of volume density fraction

D_{90} particle sizes below which 90% of the sample fall, in terms of volume density fraction

$D[4{:}3]$ / **D_{mean}** volumetric mean diameter

$D[1{:}0]$ numeric mean diameter

DM dry mass of the compost material

ΔD variation in degree of disintegration values

ΔE color variation

ΔH_c crystallization enthalpy

ΔH_m melting enthalpy

$\Delta H_{m,norm}$ normalized melting enthalpy

E tensile Young's modulus

E' dynamic storage modulus

E'_{red} reduced modulus

E'' loss modulus

E_K' Kerner's elastic modulus of the composite

$E_{K,0}'$ Kerner's elastic modulus of the matrix

E_m matrix modulus

E_p filler modulus

E_1 Maxwell's spring constant

E_2 Kelvin-Voigt's spring constant

ε_B tensile elongation at break

η_0 zero-shear viscosity

η_1 viscosity of Maxwell's dashpots

η_2 viscosity of Kelvin-Voigt's dashpots

$J(t)$ creep compliance

l thickness of the interphase

L actual length of the specimen

l_0 initial length of the specimen

λ relative elongation

λ^n correction factor characterizing the strain hardening tendency during polymer deformation

ν Poisson ratio of the matrix

MR mass reduction ratio

ξ particles aspect ratio parameter

R decrease in the total volatile solids content

ρ_f density of the filler

ρ_m density of the matrix

σ_B tensile stress at break

$\sigma_{B,T0,rel}$ relative true tensile stress at break of the matrix

σ_y yield stress of the composite

σ_{y0} yield stress of the matrix

σ_{yi} strength of the interphase

$\sigma_{B,T}$ true tensile stress at break of the composite

T toughness

T_c crystallization temperature

T_{deg} degradation temperature

$T_{g,DMA}$ / $T_{g,DSC}$ glass transition temperature

T_m melting temperature

T_{onset} onset temperature

$Tan\delta = E''/E'$ damping factor

$\tau = \eta_2 / E_2$ characteristic relaxation time

φ_f volumetric fraction of the filler

φ_m maximum packing factor of the filler

χ_c crystallinity degree

ψ packing factor of the filler particles

VS volatile solids content of the compost material

Introduction

1.1 Plastics: Benefits and Environmental Challenges

Plastic materials have long been utilized in a multitude of applications due to their advantageous characteristics. These include their lightweight nature, mechanical robustness, and effective barrier properties against moisture and gases, all at a relatively low cost. These qualities render plastics particularly suitable for packaging applications, where they have become the second most used material after cellulosic options[1].

As global demand for plastic continues to rise, production has correspondingly increased, although growth has slowed modestly in recent years. In 2022, global plastic production reached 400 million tons, with Europe accounting for approximately 14% of the global output. Furthermore, nearly 40% of the European market for plastic converters is allocated to the packaging sector. The demand is primarily met by polypropylene (PP), low-density polyethylene (LDPE), and high-density polyethylene (HDPE), with respective shares of 19.4%, 17.4%, and 12.4%[2,3].

While plastics offer numerous advantages, they also present significant environmental concerns, particularly due to their fossil-based origin and the complexities associated with their disposal. The recycling of end-of-life plastics, particularly multi-material packaging designed for the preservation of foodstuffs, presents a considerable challenge. This is due to the inherent difficulties and costs associated with recycling these materials. In instances where recycling is not a viable option, energy recovery or landfill disposal are frequently the only remaining alternatives. In 2015, approximately 63% of post-consumer plastic waste was packaging, contributing to a substantial environmental footprint[4].

The improper disposal of plastics has resulted in a multitude of ecological issues, most notably in marine environments. The accumulation of marine litter, which is predominantly composed of plastic, has been observed on European beaches, with the formation of extensive "plastic litter" in the oceans. This phenomenon is primarily driven by ocean currents. Disposable plastic items, including food containers, beverage lids, and cigarette filters, constitute approximately 50% of marine litter[5]. As plastic materials degrade, they break down into microplastics, which have the capacity to persist in ecosystems and pollute both aquatic and terrestrial environments. The contamination of the food chain by microplastics has resulted in the contamination of seafood, salt, honey, beer, and even drinking water. These findings have raised concerns about the potential long-term effects of microplastics on human health[5,6]. Despite the growing efforts to reduce plastic waste, the demand for plastic remains high in sectors like packaging, where its versatility, low cost, and performance are challenging to match alternative materials.

The concept of bioeconomy, established two decades ago, has driven innovative approaches to issues like plastic pollution, fossil fuel depletion, and greenhouse gas emissions[7]. Functioning as a bridge between biotechnology and the chemical industry, bioeconomy fosters the development of sustainable products produced through eco-friendly, "green" processes[8–10]. This shift is impacting the polymer industry by driving a transition from fossil-derived materials toward renewable resources, supporting broader sustainability efforts in manufacturing and resource use[11,12].

1.2 Bioplastics: Innovations, Classifications, and Sustainability

Bioplastics offer several environmental advantages and are gaining traction as a more sustainable alternative to traditional fossil-based plastics[13]. These materials align with the principles of the circular economy, as they are often recyclable or biodegradable, thereby reducing the likelihood of long-term environmental pollution[14]. By transitioning to bioplastics and developing enhanced recycling methods, industry has the potential to mitigate the impact of plastic waste and move toward a more sustainable future[15]. Although bioplastics currently constitute a minor share of global plastic production, the market is expanding, with biobased alternatives available across diverse sectors, including agri-food and biomedical applications[16].

The term "bioplastics" encompasses a range of materials and can be classified into three categories based on their origin and end-of-life behavior[16]. The first category comprises *bio-based* plastics, which are derived partially or entirely from renewable sources. Various biomass sources, including corn, starch, cellulose, lignin, oils, and organic waste, are used to produce monomers for these biopolymers[17,18]. It should be noted that, although these plastics are sourced from biomass, they are not necessarily biodegradable. Examples of bio-based, non-biodegradable plastics include bio-polyethylene (bio-PE) and bio-poly(ethylene terephthalate) (bio-PET).

The second category comprises *biodegradable* bioplastics, which undergo natural biochemical processes that break down the polymer into simpler molecules, including oligomers, carboxylates, methane (CH_4), and water (H_2O). Notable examples of this category include poly(butylene adipate-co-terephthalate) (PBAT) and polycaprolactone (PCL). Bioplastics derived from renewable biomass are particularly promising due to their environmental benefits, such as reduced energy needs in production, non-toxicity, and eco-friendly degradation with minimized greenhouse gas emissions[9,13].

The third category consists of bioplastics that are *both bio-based and biodegradable*, offering the advantages of renewable sourcing and complete biodegradability. The most used materials in this category include polylactic acid (PLA), polybutylene succinate (PBS), polyhydroxyalkanoates (PHA), and starch-based blends. These materials represent a promising avenue for sustainable applications.

It is also necessary to differentiate between the terms “(bio)polymers” and “(bio)plastics”. “(Bio)polymers” are macromolecules with high molecular weights that are formed by the repetition of structural units called monomers. In contrast, the term "(bio)plastics" refers to the final industrial materials, which consist not only of the (bio)polymer itself but also of various additives incorporated to achieve specific performance characteristics[19].

Nevertheless, the properties of bioplastics are not always competitive with those of conventional fossil-based polymers[20,21]. Therefore, it is essential to develop experimental methods aimed at enhancing their mechanical, thermal, and rheological properties, as well as their overall stability. Additives are essential in the manufacture of both traditional and bio-based plastics, including biopolymers. These additives improve the versatility and competitiveness of conventional plastics by enhancing critical properties: plasticizers increase flexibility and workability[22]; stabilizers provide thermal and UV resistance, improving durability[23]; and fillers improve stiffness, strength and cost efficiency[24]. By tailoring bioplastics to specific applications, these additives are expanding their use across sectors, from packaging[25] to medical devices[26]. To maintain the sustainability of bioplastics, biobased and biodegradable additives are increasingly employed[27]. A dedicated paragraph will be found later in the chapter.

This thesis explores this aspect by realizing composites to improve the mechanical properties of PBAT, and by blending PHA with plasticizer to mitigate its high stiffness.

1.3 Poly(butylene adipate-co-terephthalate) (PBAT)

PBAT (Figure 1.1) is a synthetic polymer of the aliphatic-aromatic co-polyesters family, fossil-based but completely biodegradable[28], and therefore belongs to the second category of bioplastics.

It is synthesized through polycondensation of butanediol (BDO), adipic acid (AA), and terephthalic acid (PTA)[29]. The two repetitive units composing the polymeric chain are butylene terephthalate (BT) and butylene adipate (BA), and their molar ratio influences the properties of the copolymer[28]. Despite it being primarily sourced from fossil materials, studies indicate that PBAT monomers can be potentially sourced renewably, enhancing its environmental appeal[30–32].

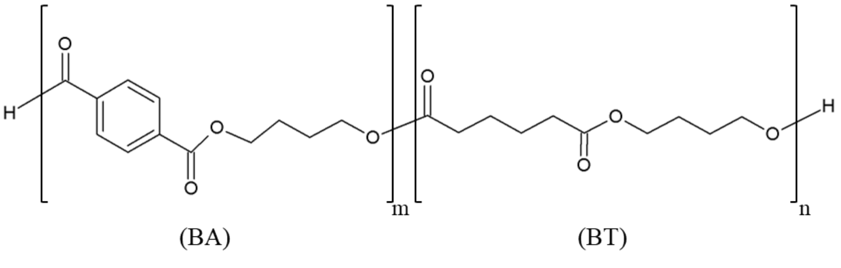

Figure 1.1 *PBAT molecular structure*

PBAT exhibits mechanical properties comparable to LDPE[33], including flexibility, toughness, and thermal resistance[29,33]. These characteristics render PBAT suitable for processing on standard polyolefin equipment, thereby further facilitating its adoption in a variety of applications, especially for packaging[34].

In contrast to conventional plastics, PBAT is fully biodegradable, with a decomposition time of approximately six weeks in soil under ambient conditions[33,35]. This biodegradability allows PBAT to serve as a sustainable alternative to non-biodegradable polymers in single-use and compostable products, such as mulch films[36,37], organic waste bags, shopping bags, and cling films. Nevertheless, the broader implementation of this material is limited by factors such as elevated production costs[29] and an increased permeability to water vapor[38].

1.4 Polyhydroxyalkanoates (PHA)

PHA represent a promising class of biodegradable polymers produced via bacterial fermentation, offering sustainable alternatives to conventional plastics across various sectors. PHA are produced from renewable resources, including sugars, vegetable oils, wastewater, and food waste. During the fermentation process, PHA are formed as an intracellular energy reserve under nutrient-limited conditions with an excess carbon source. This process yields a variety of PHA types, each with distinct properties that make them suitable for specific applications. The mechanical and thermal properties are influenced by structural differences, particularly chain length[39,40].

Short-chain-length PHA (scl-PHA), consisting of three to five carbon atoms, exhibit high crystallinity and rigidity, which often results in brittle material properties. In contrast, medium-chain-length PHA (mcl-PHA), with six to fourteen carbons, exhibit increased flexibility, lower crystallinity, and lower melting points, rendering them ideal for applications requiring flexibility. Long-chain-length PHA (lcl-PHA) are a relatively uncommon occurrence, yet they may offer distinctive properties that could be beneficial for specific applications[41,42].

One of the most extensively studied PHA is polyhydroxybutyrate (PHB) (Figure 1.2), a homopolymer that is known for its high crystallinity, which can reach up to 80%. This results in substantial rigidity and limited flexibility. Although PHB has a high melting temperature (170–190°C depending on molecular weight), its thermal stability is limited, as it starts degrading irreversibly at around 200°C. This presents a challenge for processing methods such as extrusion (Ex) and injection molding (IM), which require a higher degree of thermal stability. The brittle nature and narrow thermal processing range of PHB have historically constituted significant limitations to its potential applications. However, recent advancements suggest that these challenges may be overcome through blending or copolymerization, potentially making PHB a viable substitute for petroleum-based plastics in various sectors[43,44]. The use of suitable plasticizers represents a viable technique for overcoming the intrinsic brittleness of the polymer.

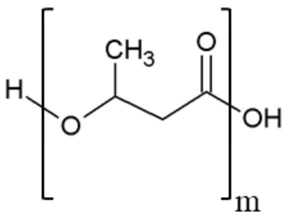

Figure 1.2 *PHB molecular structure*

Among the PHB derivatives, poly(3-hydroxybutyrate-co-3-hydroxyvalerate) (PHBV) (Figure 1.3) has received considerable attention. The incorporation of hydroxyvalerate (HV) units into this copolymer results in enhanced flexibility and a reduction in crystallinity relative to PHB. The HV component disrupts the polymer chain alignment, thereby enabling PHBV to be processed at lower temperatures. Furthermore, PHBV is biodegradable, with in vivo resorption times ranging from three to twelve months. This quality makes it particularly suitable for use in biodegradable medical implants and tissue engineering scaffolds. This degradation rate is consistent with the biological healing process, providing temporary support to developing tissues[45,46].

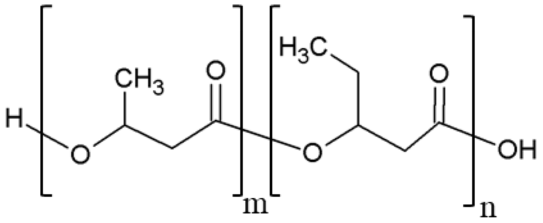

Figure 1.3 *PHBV molecular structure*

The biodegradability, biocompatibility, and tunable properties of PHA have led to a significant increase in the interest in their potential applications, which span a diverse range of fields including biomedical devices, packaging, electronics, agriculture, and environmental remediation. In the biomedical sector, the capacity of PHA to degrade without generating toxic or inflammatory responses is of considerable importance, as they maintain a stable pH during degradation, which is conducive to tissue compatibility. This property has resulted in the successful implementation of PHA in bone tissue engineering, where they can be processed into scaffolds that provide structural support and facilitate cell growth, ultimately undergoing resorption as new tissue regenerates[47,48].

In the field of packaging, PHA present a sustainable alternative to conventional plastics. They possess high resistance to moisture and mechanical stress, making them suitable for a range of packaging formats. Moreover, the thermal stability of PHBV and related copolymers has enabled their use in flexible electronic components and biodegradable sensors, aligning with the growing trend toward sustainable, single-use electronic devices. Additionally, PHA demonstrate considerable potential in agricultural applications, where they can serve as biodegradable mulch films or controlled-release carriers for fertilizers and pesticides, thereby reducing environmental impact[49,50].

In addition to their individual applications, PHA contribute to the broader field of sustainable development by offering a means of producing bio-based, fully biodegradable plastics. Market projections indicate that PHA production will experience a notable increase, from 104.64 ktons in 2023 to 1.003 million tons by 2028. This growth is attributed to the expansion of applications and the ongoing research aimed at enhancing the performance and reducing the production costs of PHA. The pursuit of enhanced processing characteristics for PHB and PHBV, including the blending with plasticizers or the combination with other biodegradable polymers, has demonstrated potential in the expansion of their usability across industrial sectors[34].

1.5 Biocomposites: A Pathway to Improved Bioplastic Properties and Sustainability

The potential of bioplastics is significantly expanded through the development of biocomposites, which results in a vast array of sustainable materials with enhanced, diverse properties that are well-suited to a broader spectrum of applications. Eco-friendly reinforced polymers offer a promising avenue for advancing sustainable materials with enhanced performance, effectively competing with traditional plastics in terms of functionality.

Biobased composite materials can be created by reinforcing biopolymers with fillers or nanofillers[51]. This approach enhances the structural and functional attributes of biopolymers while concurrently diminishing the carbon footprint of conventional plastics. The development of biocomposites from bioplastics has therefore become a primary strategy for enhancing functional and structural properties to meet the diverse demands of various applications. It is noteworthy that reinforced biocomposites exhibit increased stiffness, which is a commonly desired mechanical property[52,53].

Even in instances where certain properties may not undergo a notable enhancement, the incorporation of fillers in biocomposites remains an effective strategy for reducing the overall production costs associated with bioplastics[21].

The fabrication of biocomposites is typically achieved through in-situ polymerization, melt mixing, and solvent casting. Of these methods, solvent casting typically results in optimized material properties, as the liquid environment enables more homogeneous mixing and maximizes interfacial interactions between phases[54]. Solvent-mediated methods are commonly utilized in laboratory-scale polymeric formulations, frequently employing chloroform ($CHCl_3$)[55,56] or dichloromethane (CH_2Cl_2)[57,58] as solvents. However, both solvents are recognized as toxic substances. Although these methods are straightforward for research purposes[59], the use of toxic solvents presents scalability challenges in industrial applications. In contrast, melt-processing methods obviate the necessity for harmful chemicals and facilitate higher production rates using machinery that is analogous to industrial equipment. Among these techniques, twin-screw Ex is the most established for achieving uniform mixing in multi-component polymer composites[60–62].

It is important to consider that incorporating an additional phase into a matrix significantly alters its tensile properties. Consequently, the interphase interactions become critical in determining the overall performance of the composite. It is therefore essential to investigate the relationships between these phases. The interaction between reinforcing agents and the polymer matrix is often complicated by their different chemical compositions, highlighting the importance of understanding and predicting how fillers affect matrix properties. Optimum performance in composites is achieved when strong interphase bonds are formed between the matrix and the surfaces of the filler particles[63]. To this end, numerous theoretical models have been developed to describe the tensile properties of composites based on the combined properties of the matrix and filler[64–67]. These models establish relationships between the tensile properties of the composite and the volume fraction of the reinforcing phase, providing valuable insights that can guide the improvement of composite performance.

1.6 The Role of Fillers

The research into biopolymer-based composites is increasingly exploring the potential of a variety of natural and synthetic fillers[68] to enhance the mechanical, thermal, and functional properties of the materials in question while ensuring an appropriate biodegradability profile. These fillers can be classified into two principal categories: organic and inorganic, and include natural fibers, metals, and metal oxides. In applications where biodegradability is a requisite, bio-based fillers are frequently the preferred option.

The use of natural-derived organic fillers, including polysaccharides such as cellulose nanocrystals (CNCs)[69] or nano-fibers (CNFs)[70], lignin, chitosan, starch, and alginate[71,72], natural fibers[73,74], in conjunction with agricultural residues almonds shells and rice husk, vegetable peels, coffee grounds, egg-, and seafood shells[75–78] offers both reinforcement and environmental benefits by promoting a circular economy, thanks to their lightweight nature and natural abundance[79]. Additionally, they are highly compatible with biopolymers and can improve mechanical strength and flexibility while maintaining biodegradability[69,80].

Among the inorganic fillers, ceramic materials are often employed, such as glass beads[81], nanoclays[82,83], silica[84] or zinc[85] and magnesium oxide[86] nanoparticles. These fillers provide high mechanical strength and durability, rendering them optimal for applications requiring enhanced stability. In addition to their mechanical properties, select inorganic fillers, including silver nanoparticles, nanostructured alumina (Al_2O_3), silica (SiO_2), and titania (TiO_2), offer antimicrobial and UV-resistant properties, rendering them suitable for specialized applications such as medical packaging[87].

Besides the fact that some inorganic fillers may interfere with biodegradability, modifications to the surface of the inorganic filler can enhance the often poor compatibility with biopolymer matrices. Surface treatments with compatibilizing agents, such as maleic anhydride or epoxy or isocyanate molecules, have been demonstrated to enhance filler-matrix adhesion and stress transfer, thereby ensuring biocomposite integrity and durability, making them competitive with conventional synthetic counterparts[62,88]. Proteins are naturally amphiphilic molecules, comprising both hydrophilic (water-attracting) and lipophilic (oil-attracting) segments. These dual properties render proteins suitable as biocouplers, as their hydrophilic groups interact effectively with inorganic or polar systems, while their hydrophobic portions are compatible with polymer-like, non-polar environments. In polar conditions, the hydrophilic segments typically serve to shield the lipophilic regions. However, in the presence of apolar, oleophilic environments, the proteins undergo partial unfolding, thereby allowing the lipophilic segments to strongly adsorb at the organic/inorganic interface[89].

The strategic development of biopolymer composites through the selection and modification of both natural and synthetic fillers highlights the potential of these materials for a wide range of sustainable applications. By optimizing filler properties and their interaction with the polymer matrix, researchers and this thesis aim to create high-performance biodegradable composites as alternatives to conventional, petroleum-based materials. These advancements align with environmental objectives, promoting sustainability and reducing dependency on non-renewable resources, and signal progress toward achieving durable, eco-friendly materials across industries.

1.7 Zein-TiO_2 complex (ZTC)

Titanium dioxide (TiO_2) has recently gained attention as an effective reinforcing agent for developing hybrid inorganic-organic composites with enhanced physicochemical[90], mechanical, ultraviolet (UV)[91], gas barrier, water resistance, and antimicrobial properties[92,93]. TiO_2 is a particularly promising additive and is widely used as a white pigment additive (E171) in the food industry[92], and as a UV-blocking reinforcement in food packaging films[94]. Its use as a reinforcing agent for biopolymer is particularly interesting due to its nontoxic nature and compatibility with biological systems[95,96]. In studies by Kadam et al. [97], the incorporation of TiO_2 particles into zein films demonstrated notable improvements in film strength and durability.

Zein, a prolamin protein sourced from the byproducts of corn processing[98], is a renewable natural biopolymer with a long research history dating back to the early 20th century[99]. Despite its suitability for creating edible films and coatings, pure zein poses processing challenges. It lacks thermoplastic properties and has inherently poor mechanical strength, making it difficult to work with effectively[100–102].

Zein and TiO_2 can be coupled to create an organic-inorganic complex structure (zein-TiO_2 complex - ZTC), able to enhance the interfacial adhesion and interaction of TiO_2 and a biopolymer matrix such PBAT.

1.8 Bioglasses

Another promising biodegradable filler is bioactive glass particles[103,104]. Bioactive glasses, initially synthesized by Hench in 1969[105], are amorphous materials whose structure facilitates high bioactivity by eliminating chemical and structural barriers to solubility, thereby enabling efficient interaction with biological environments. This property renders bioactive glasses particularly well-suited for biomedical applications, particularly in bone tissue regeneration, where they facilitate the restoration of bone structure and function and enhance healing in cases of bone defects resulting from trauma, congenital conditions, or disease[105]. The composition of bioactive glasses can be precisely adjusted to optimize a range of properties, including solubility, biocompatibility, and mechanical strength.

A noteworthy example is phosphate-based glass (PG), wherein, in contrast to traditional silica-based glasses, phosphorus oxide constitutes the primary network[106], thereby facilitating compatibility with the bone matrix. Phosphates are naturally occurring in bone, and this glass type can be engineered for controlled solubility due to the hygroscopic nature of P_2O_5, thereby providing greater customization than traditional silica-based glasses. The composition of the material can be modified to regulate the rate of degradation. For example, the addition of calcium oxide can enhance the strength of the glass and reduce its degradation rate, whereas the incorporation of sodium oxide increases solubility by depolymerizing the glass network, thereby providing adaptability for a range of biomedical applications.

In addition to structural compatibility, bioactive glasses have been demonstrated to stimulate bone cell proliferation and differentiation, thereby inducing osteoinduction, which is the formation of new bone tissue. This dual property facilitates a regenerative approach that accelerates tissue healing and self-repair. Furthermore, bioactive glasses facilitate re-vascularization, augment enzyme activity, and promote the differentiation of mesenchymal stem cells, which are indispensable for efficacious tissue regeneration. Therapeutic efficacy may be further enhanced by the incorporation of specific elements into the glass matrix. Magnesium, for instance, which is naturally present in bone, promotes bone health, while strontium, known for its osteogenic, angiogenic, and antibacterial effects, can improve the regeneration of bone tissue, as well as the vascularization of surrounding tissue. In addition, the materials exhibit resistance to infection[107,108].

While initially developed for bone repair and tissue engineering applications, PG can be combined with antimicrobial agents such as silver oxide (Ag_2O) to reduce microbial contamination, thereby enhancing their suitability for hygienic, bioabsorbable applications[109–111].

Due to their customizable degradation rates and high mechanical strength, PG are optimal candidates for use as biodegradable fillers in sustainable composites. Their inherent rigidity, coupled with tunable solubility[106], enables the fabrication of bioabsorbable composites with customized mechanical and degradation characteristics, expanding the scope of their utilization across sustainable, biocompatible material innovations[103,104,106].

It is therefore possible to consider the use of calcium-phosphate glass (CPG) particles as a filler in a flexible biopolymer matrix, such as PBAT, with the objective of modifying its mechanical properties and adapting its biodegradability. Furthermore, the incorporation of PG particles in polymers such as PHA allows the fabrication of biocomposite materials that are characterized by high biocompatibility, and which have been designed for use in bone tissue repair.

1.9 Advances in Sustainable Plasticizers for Bioplastics

As already mentioned, the incorporation of additives is a standard method of obtaining plastics with the desired properties. In addition to the realization of composites to increase the strength of flexible polymers, the improvement of mechanical properties can also be considered by improving the flexibility of a rigid material.

Plasticizers increase flexibility by lowering the glass transition temperature (T_g) of a polymer, although this often reduces tensile strength. For effective plasticizing, the additive must be both compatible and miscible with the polymer, a relationship predicted by the Hansen Solubility Parameters (HSP)[112]. Plasticizers fall into two categories: internal and external. Internal plasticizers are incorporated directly into the polymer chain through copolymerization, resulting in specific but limited functional results. External plasticizers, on the other hand, are blended into the polymer without chemical bonding, making them more versatile and cost-effective. Their small molecular size allows them to fit between polymer chains, increasing molecular mobility and flexibility while reducing stiffness and production costs. This flexibility allows for a wider range of mechanical and thermal properties that can be adjusted by varying the concentration of the plasticizer[113].

Historically, the plasticizer market has been dominated by traditional petroleum-based plasticizers such as phthalates. While these plasticizers are cost effective and efficient, they also compromise biodegradability, biocompatibility and sustainability when used as additives for biopolymers[114]. In addition, these substances tend to leach out of materials, raising concerns about environmental and health risks[115]. As phthalates do not meet modern standards of renewability and non-toxicity, their use is increasingly restricted worldwide[116].

In the expanding field of bioplastics, there is a growing demand for sustainable additives, including bio- or green-based plasticizers, to support materials that match the performance of conventional plastics while maintaining environmentally friendly properties. By analyzing commercially available plasticizers, researchers are identifying functional groups that slow biodegradation or induce toxic effects and redesigning them to mitigate such issues[117]. By 2026, sustainable additives are expected to account for one-fifth of the plasticizer market, driven by the need for bioplastics that retain desired properties such as flexibility and durability[112]. Green plasticizers derived from natural sources such as vegetable oils, fatty acids and lignocellulosic biomass are gaining importance[113]. Despite their advantages, green plasticizers often face disadvantages such as higher production costs[118], lower plasticizing efficiency and leachability, which limit their versatility in different polymers[119]. For example, commonly used green plasticizers such as 1,2-cyclohexanedicarboxylic acid diisononyl ester (DINCH) and acetyl tributyl citrate (ATBC) have raised concerns. Research suggests that DINCH may affect biological systems[120], while ATBC has shown potential as an endocrine disruptor and neurotoxin[121]. Its high leachability exacerbates these safety concerns[122].

Among bio-based plasticizers, glycerol and levulinic acid stand out as sustainable “building blocks”. Glycerol, a non-toxic byproduct of biodiesel production, contains three hydroxyl groups that facilitate conversion transformations into various derivatives. Levulinic acid, derived from cellulosic waste biomass, is a renewable resource that supports sustainability and the circular economy without competing with food production[123]. Both offer promising routes to sustainable, biodegradable plasticizers compatible with eco-friendly manufacturing standards.

The design of bio-plasticizers follows the principles of green chemistry, with an emphasis on biodegradability, non-toxicity, and safety. By applying green chemistry principles, it is possible to develop environmentally friendly plasticizers that improve the mechanical properties and melt processability of polymers with minimal environmental impact. These advances support a sustainable future for bioplastics while minimizing health and environmental risks.

1.10 Design Principles of Scaffolds in Bone Regeneration

Human tissues are categorized as “rigid” or “soft” based on mechanical properties, with rigid tissues, like bone, providing structural support and soft tissues, like muscle, offering flexibility[124].

Bone tissue consists of roughly 65% inorganic matrix (mainly calcium phosphates and carbonates), 20% organic matrix (primarily collagen), and 15% water and lipids. The inorganic portion provides compressive strength, while the collagen-rich organic matrix enhances tensile resilience and shock absorption[125]. Bone undergoes continuous remodeling, responding to mechanical stress and physiological shifts through osteoblast and osteoclast activity, ensuring structural integrity and calcium balance[126].

Regenerative medicine, developed in the 20th century to address tissue and organ shortages, seeks to create biological alternatives to reduce immune rejection risks. Tissue engineering, a significant branch of regenerative medicine, merges life sciences with engineering to develop three-dimensional (3D) scaffolds supporting cellular growth[127,128]. Scaffolds serve as three-dimensional, temporary structures that guide cell adhesion, migration, proliferation, and differentiation, closely mimicking the extracellular matrix to aid new tissue formation[128].

Bone tissue engineering (BTE) aims to design biocompatible, bioactive scaffolds that stimulate new bone formation. Although promising for bone regeneration, BTE faces challenges, including scaffold vascularization and immune compatibility, which remain focal points of ongoing research[128]. In bone applications, scaffold design must balance porosity (supporting cell migration and nutrient flow) with mechanical strength to handle physiological loads and avoid stress shielding, which can cause bone resorption[129,130]. High porosity with interconnected pores between 100 and 800 microns facilitates nutrient flow, vascularization, and cell migration. Sufficient mechanical strength enables initial load support without excessive rigidity, fostering a gradual load transfer as regeneration progresses[131,132].

Materials used in scaffolds should degrade at rates aligned with tissue regeneration to ensure sustained support without premature breakdown. Thanks to biodegradation, removal is unnecessary after implantation[133]. In BTE, the use of biocompatible and bioresorbable polymers is common and the materials themselves have evolved significantly. The first generations focused on biocompatibility, while later generations introduced bioactivity and biodegradability. Today's biomimetic materials closely replicate natural tissue structures to enhance integration and minimize immune responses[134]. These materials exhibit osteoconductivity and osteoinductivity, encouraging bone cell growth and tissue regeneration[135]. This shift advances the potential for BTE to improve patient outcomes and reduce dependence on transplants, aiming to bridge the gap between research and clinical application.

Modern scaffold fabrication methods, particularly Additive Manufacturing (AM), allow for precise control over geometry, porosity, and biodegradability. This technique enables patient-specific scaffold designs, addressing the limitations of conventional fabrication techniques[129,133].

1.11 3D Printing with Bioplastics: Challenges and Innovations

AM is a revolutionary industrial process that creates objects and components by sequentially adding material layers, guided by CAD-based 3D models. In contrast to conventional manufacturing techniques, such as subtractive machining (milling, turning) and casting, which depend on the removal or shaping of material, AM allows the creation of complex designs without the need for specialized tooling. This has significant implications for sectors such as automotive, aerospace, and biomedicine. Fused deposition modeling (FDM), an extrusion-based AM technique, employs a layer-by-layer method to create solid objects from digital 3D models using thermoplastic filaments. The most used FDM materials are rigid, fossil- or bio-derived polymers, including PLA and poly(acrylonitrile-butadiene-styrene) (ABS)[69,136,137], with limited flexible options, including synthetic thermoplastic elastomers (thermoplastic polyurethane, TPU)[138].

The recent advancements in biodegradable materials, such as PBAT-based composites, have facilitated the production of flexible and sustainable filaments that are conducive to eco-friendly 3D printing applications[139]. These biocomposites facilitate the integration of design, manufacturing, and sustainability, enabling the creation of customized parts with a reduced environmental impact.

In the field of biomedicine, the use of unconventional polymers, such as PBAT, in FDM is constrained by compatibility issues with matrix fillers, which can compromise the mechanical integrity of the resulting material. Consequently, research is concentrated on the expansion of printable materials with biodegradable and flexible options[140].

As previously stated, PHA represent another category of bioplastic with considerable potential for use in the biomedical field, accounting for approximately 11% of the AM market[48]. PHA are suitable for applications such as drug delivery systems[141,142], or customizable scaffolds for bone and tissue regeneration[136,137]. Despite the current limited utilization of PHA-based FDM materials, which are affected by their complex melt properties, encouraging findings have been reported regarding the use of electrospinning[143,144] and selective laser sintering techniques[145].

One challenge in fabricating PHB for FDM lies in its crystallinity and stiffness. Up to this point, the processability of PHA has been enhanced through blending with PLA[146] or the addition of fossil-based plasticizers[147,148] for both Ex and 3D printing. In this regard, the existing green alternatives have not yet replaced the use of fossil-based plasticizers, which have instead been experiencing an increasing demand[149]. Indeed, only a few studies have investigated the use of green plasticizers to modify the properties and processability of PHA[150–152]. The advancement of PHA FDM filament fabrication through the blending of the biopolymer with an appropriate green plasticizer is beneficial for supporting advancements in tissue engineering and regenerative medicine.

1.12 Degradation and biodegradation

The study of degradation stability, or the resistance of biocomposites to physical and chemical changes resulting from environmental influences such as temperature, light, and moisture, is of critical importance for the evaluation of their durability. This is done to optimize the degradation outcome and mechanisms, as well as to avoid the occurrence of unwanted degradation throughout the lifespan of the material during use.

It is evident that biodegradability confers a substantial environmental benefit; however, it also renders bioplastics more vulnerable to environmental degradation, which in turn affects their longevity. The application of these materials, both in outdoor and indoor environments, exposes them to a range of factors, including sunlight, moisture, and fluctuating temperatures, which accelerate the degradation process. The natural weathering process necessitates extended exposure periods, rendering it impractical for industrial testing purposes. Accelerated degradation tests are conducted in controlled laboratory settings to simulate environmental stressors, with the objective of assessing the effects of UV radiation, heat, and humidity on the structural, chemical, and optical integrity of the polymers. The use of UV chambers allows for the standardization of exposure conditions and the acceleration of degradation. Nevertheless, translating the results of accelerated tests to real-world conditions remains a significant challenge due to the inherent variability in exposure[153,154]. The photodegradation of polymers is primarily attributed to chain scission and crosslinking through Norrish I and II reactions, which result in a reduction in molecular weight and the degradation of mechanical strength, particularly ductility[155,156]. The primary abiotic degradation pathways for both biodegradable and non-biodegradable materials are photodegradation, thermal degradation (via high-temperature applications), and chemical degradation (*e.g.*, extreme pH exposure)[157].

Polymer fragmentation under aerobic composting conditions represents an additional method for evaluating degradation. In accordance with the ISO Standard 20200, a material is regarded as degraded when it attains fragments smaller than 2 mm. The fragmentation of polymers increases the surface area available for microbial activity, thereby accelerating biodegradation. In aerobic conditions, this process transforms polymers into simpler molecules, including water (H_2O), carbon dioxide (CO_2), methane (CH_4), and intermediate compounds[157]. It should be noted that this laboratory-scale fragmentation test is not designed to determine complete biodegradability. Further testing is required to confirm compostability. The primary techniques used to assess bioplastic biodegradation in aerobic and anaerobic environments rely on four core methodologies: CO_2 emission tracking, spectroscopic analysis, visual assessment, and mass-loss measurements[158].

The biodegradation of biopolymers via aerobic and anaerobic fermentation employs microbial processes to facilitate the breakdown of materials into simpler compounds under controlled environmental conditions. In aerobic fermentation, microorganisms metabolize biopolymers in the presence of oxygen, converting them primarily into CO_2, H_2O, and biomass. This process is commonly employed in composting, wherein biopolymers such as PHA can undergo effective decomposition over the course of several months, contingent upon environmental variables including temperature, moisture, and pH[158–160].

The aerobic degradation process is aligned with sustainable waste management practices, as it results in the release of fewer greenhouse gases compared to conventional plastics. In contrast, anaerobic fermentation occurs in the absence of oxygen and results in the production of biogas, primarily CH_4, and CO_2, along with water and biomass. This process is particularly advantageous in the context of energy recovery, as CH_4 can be harnessed as a renewable energy source[161]. Anaerobic degradation is a slower process but is highly effective for biopolymers in low-oxygen environments, such as landfills or bioreactors[162].

By controlling conditions to restrict methane production, anaerobic fermentation of PHA represents an effective microbial recycling method for generating valuable volatile fatty acids (VFA). In this process, microorganisms degrade PHA in an anaerobic environment, resulting in the breakdown of these polymers into VFA, including acetate, propionate, and butyrate[163–165]. These VFA serve as essential biochemical intermediates and can be repurposed as substrates for synthesizing new PHA or other valuable bioproducts[165,166]. The anaerobic fermentation of PHA represents a recycling strategy that diverts bioplastic waste from conventional disposal and fosters the development of a circular bioeconomy[167]. This approach transforms bioplastics waste into a renewable resource, thereby promoting efficient waste management and supporting sustainable material reuse.

1.13 Structure of the thesis

This thesis brings together the findings of a three-year research project, which can be broadly divided into three main experimental sections.

The initial section, comprising **Chapter 2**, is dedicated to the reinforcement of a flexible biopolymer, PBAT, with two distinct rigid biofillers, namely ZTC and CPG particles. The filler production was in collaboration with the Department of Applied Science and Technology at Politecnico di Torino. The composites' properties are fully characterized. The objective of reinforcing PBAT is to enhance its mechanical properties while maintaining its biodegradability and biocompatibility. The final characterization in this chapter introduces the topic of three-dimensionally printed biomedical scaffolds, which is further developed in the subsequent chapter. The dissemination of this research resulted in the publication of four distinct research papers in international journals[36,168-170].

Chapter 3 constitutes the second section of the work and is dedicated to the use of PHB in biomedical applications. This work was conducted in collaboration with the Department of Civil, Chemical, Environmental and Materials Engineering at the University of Bologna, regarding the synthesis of the glycerol-levulinic acid-based bioplasticizer. The mechanical and thermal properties of PHB are initially optimized for FDM applications using conventional and novel bioplasticizers. The initial section of the chapter is disseminated as a publication in an international journal[171]. Subsequently, the fabrication and characterization of PHB composites with biocompatible bioglass are conducted. Additionally, the characterization and optimization of 3D-printed scaffolds are performed.

The third and final section comprises **Chapters 4** and **5**, which address the degradation of the materials produced in the preceding chapters. **Chapter 4** is focused on the physical degradation of PBAT-CPG composites through photo-degradation, induced by accelerated weathering, and disintegration under laboratory composting conditions[36]. In turn, **Chapter 5** investigates the biodegradation of plasticized PHB through anaerobic fermentation, aiming at the production of carboxylates. This analysis was conducted in collaboration with the Department of Environmental Engineering (ETE) at Wageningen University and Research (WUR).

The final **Chapter 6** is dedicated to drawing the conclusions of the work.

References

1. Piergiovanni, L. & Limbo, S. Food Packaging. Materiali, Tecnologie e Qualità Degli Alimenti. (Milan, 2010).

2. Plastics – the fast Facts 2023 • Plastics Europe. https://plasticseurope.org/knowledge-hub/plastics-the-fast-facts-2023/.

3. Briassoulis, D. & Giannoulis, A. Evaluation of the functionality of bio-based food packaging films. Polym Test 69, 39–51 (2018).

4. Ferreira, A. R. V., Alves, V. D. & Coelhoso, I. M. Polysaccharide-Based Membranes in Food Packaging Applications. Membranes 2016, Vol. 6, Page 22 6, 22 (2016).

5. He, D. et al. Microplastics in soils: Analytical methods, pollution characteristics and ecological risks. TrAC - Trends in Analytical Chemistry 109, 163–172 (2018).

6. Vitali, C., Peters, R. J. B., Janssen, H. G. & Nielen, M. W. F. Microplastics and nanoplastics in food, water, and beverages; part I. occurrence. TrAC Trends in Analytical Chemistry 159, 116670 (2023).

7. Stegmann, P., Londo, M. & Junginger, M. The circular bioeconomy: Its elements and role in European bioeconomy clusters. Resources, Conservation and Recycling: X 6, 100029 (2020).

8. Lettner, M., Schöggl, J. P. & Stern, T. Factors influencing the market diffusion of bio-based plastics: Results of four comparative scenario analyses. J Clean Prod 157, 289–298 (2017).

9. Harmsen, P. F. H., Hackmann, M. M. & Bos, H. L. Green building blocks for bio-based plastics. Biofuels, Bioproducts and Biorefining 8, 306–324 (2014).

10. Philp, J. C., Ritchie, R. J. & Allan, J. E. M. Biobased chemicals: The convergence of green chemistry with industrial biotechnology. Trends Biotechnol 31, 219–222 (2013).

11. Naser, A. Z., Deiab, I. & Darras, B. M. Poly(lactic acid) (PLA) and polyhydroxyalkanoates (PHAs), green alternatives to petroleum-based plastics: a review. RSC Adv 11, 17151–17196 (2021).

12. Costa, A., Encarnação, T., Tavares, R., Todo Bom, T. & Mateus, A. Bioplastics: Innovation for Green Transition. Polymers 2023, Vol. 15, Page 517 15, 517 (2023).

13. Rosenboom, J. G., Langer, R. & Traverso, G. Bioplastics for a circular economy. Nature Reviews Materials 2022 7:2 7, 117–137 (2022).

14. Spierling, S. et al. Bio-based plastics - A review of environmental, social and economic impact assessments. J Clean Prod 185, 476–491 (2018).

15. Serrano-Aguirre, L. & Prieto, M. A. Can bioplastics always offer a truly sustainable alternative to fossil-based plastics? Microb Biotechnol 17, e14458 (2024).

16. Reddy, M. M., Vivekanandhan, S., Misra, M., Bhatia, S. K. & Mohanty, A. K. Biobased plastics and bionanocomposites: Current status and future opportunities. Prog Polym Sci 38, 1653–1689 (2013).

17. Guleria, S. et al. Polyhydroxyalkanoates production from domestic waste feedstock: A sustainable approach towards bio-economy. J Clean Prod 340, 130661 (2022).

18. Tuck, C. O., Pérez, E., Horváth, I. T., Sheldon, R. A. & Poliakoff, M. Valorization of biomass: Deriving more value from waste. Science (1979) 337, 695–699 (2012).

19. Bewley, L., Morris, G. D. L. & Alperowicz, N. Plastics. Chem Week 172, (2010).

20. Peelman, N. et al. Application of bioplastics for food packaging. Trends Food Sci Technol 32, 128–141 (2013).

21. Siracusa, V., Rocculi, P., Romani, S. & Rosa, M. D. Biodegradable polymers for food packaging: a review. Trends in Food Science and Technology vol. 19 634–643 Preprint at https://doi.org/10.1016/j.tifs.2008.07.003 (2008).

22. Bocqué, M., Voirin, C., Lapinte, V., Caillol, S. & Robin, J. J. Petro-based and bio-based plasticizers: Chemical structures to plasticizing properties. J Polym Sci A Polym Chem 54, 11–33 (2016).

23. Samper, M. D., Fages, E., Fenollar, O., Boronat, T. & Balart, R. The potential of flavonoids as natural antioxidants and UV light stabilizers for polypropylene. J Appl Polym Sci 129, 1707–1716 (2013).

24. Giubilini, A., Sciancalepore, C., Messori, M. & Bondioli, F. Valorization of oat hull fiber from agri-food industrial waste as filler for poly(3-hydroxybutyrate-co-3-hydroxyhexanoate). J Mater Cycles Waste Manag 23, 402–408 (2021).

25. Genovesi, A., Aversa, C. & Barletta, M. Polyhydroxyalkanoates-based Cast Film as Bio-based Packaging for Fresh Fruit and Vegetables: Manufacturing and Characterization. J Polym Environ 31, 4522–4532 (2023).

26. Ren, Z. W. et al. Polyhydroxyalkanoates: the natural biopolyester for future medical innovations. Biomater Sci 11, 6013–6034 (2023).

27. Dintcheva, N. T., Infurna, G., Baiamonte, M. & D'Anna, F. Natural Compounds as Sustainable Additives for Biopolymers. Polymers 2020, Vol. 12, Page 732 12, 732 (2020).

28. Kijchavengkul, T. et al. Biodegradation and hydrolysis rate of aliphatic aromatic polyester. Polym Degrad Stab 95, 2641–2647 (2010).

29. Ferreira, F. V, Cividanes, L. S., Gouveia, R. F. & Lona, L. M. F. An overview on properties and applications of poly(butylene adipate-co-terephthalate)–PBAT based composites. Polymer Engineering and Science vol. 59 E7–E15 Preprint at https://doi.org/10.1002/pen.24770 (2019).

30. Volanti, M. et al. Terephthalic acid from renewable sources: early-stage sustainability analysis of a bio-PET precursor. Green Chemistry 21, 885–896 (2019).

31. Skoog, E., Shin, J. H., Saez-Jimenez, V., Mapelli, V. & Olsson, L. Biobased adipic acid – The challenge of developing the production host. Biotechnol Adv 36, 2248–2263 (2018).

32. Silva, R. G. C., Ferreira, T. F. & Borges, É. R. Identification of potential technologies for 1,4-Butanediol production using prospecting methodology. Journal of Chemical Technology and Biotechnology 95, 3057–3070 (2020).

33. Jian, J., Xiangbin, Z. & Xianbo, H. An overview on synthesis, properties and applications of poly(butylene-adipate-co-terephthalate)–PBAT. Advanced Industrial and Engineering Polymer Research vol. 3 19–26 Preprint at https://doi.org/10.1016/j.aiepr.2020.01.001 (2020).

34. Market – European Bioplastics e.V. https://www.european-bioplastics.org/market/.

35. Zumstein, M. T. et al. Biodegradation of synthetic polymers in soils: Tracking carbon into CO2 and microbial biomass. Sci Adv 4, (2018).

36. Togliatti, E., Milanese, D., Pugliese, D. & Sciancalepore, C. Viscoelastic Characterization and Degradation Stability Investigation of Poly(butylene-adipate-co-terephthalate) – Calcium-Phosphate Glass Composites. J Polym Environ 30, 3914–3933 (2022).

37. Kijchavengkul, T., Auras, R., Rubino, M., Ngouajio, M. & Fernandez, R. T. Assessment of aliphatic–aromatic copolyester biodegradable mulch films. Part I: Field study. Chemosphere 71, 942–953 (2008).

38. Murugan, G. et al. Enhancement of Barrier Properties of Fish Skin Gelatin based Film Layered with PLA and PBAT. J Polym Environ 31, 5416–5431 (2023).

39. Mannina, G., Presti, D., Montiel-Jarillo, G., Carrera, J. & Suárez-Ojeda, M. E. Recovery of polyhydroxyalkanoates (PHAs) from wastewater: A review. Bioresour Technol 297, 122478 (2020).

40. Saavedra del Oso, M., Mauricio-Iglesias, M., Hospido, A. & Steubing, B. Prospective LCA to provide environmental guidance for developing waste-to-PHA biorefineries. J Clean Prod 383, 135331 (2023).

41. Nigmatullin, R., Thomas, P., Lukasiewicz, B., Puthussery, H. & Roy, I. Polyhydroxyalkanoates, a family of natural polymers, and their applications in drug delivery. Journal of Chemical Technology & Biotechnology 90, 1209–1221 (2015).

42. Philip, S., Keshavarz, T. & Roy, I. Polyhydroxyalkanoates: biodegradable polymers with a range of applications. Journal of Chemical Technology & Biotechnology 82, 233–247 (2007).

43. Hong, S. G., Hsu, H. W. & Ye, M. T. Thermal properties and applications of low molecular weight polyhydroxybutyrate. J Therm Anal Calorim 111, 1243–1250 (2013).

44. Hablot, E., Bordes, P., Pollet, E. & Avérous, L. Thermal and thermo-mechanical degradation of poly(3-hydroxybutyrate)-based multiphase systems. Polym Degrad Stab 93, 413–421 (2008).

45. Rivera-Briso, A. L. & Serrano-Aroca, Á. Poly(3-Hydroxybutyrate-co-3-Hydroxyvalerate): Enhancement Strategies for Advanced Applications. Polymers10 10, (2018).

46. Tebaldi, M. L., Maia, A. L. C., Poletto, F., de Andrade, F. V. & Soares, D. C. F. Poly(-3-hydroxybutyrate-co-3-hydroxyvalerate) (PHBV): Current advances in synthesis methodologies, antitumor applications and biocompatibility. J Drug Deliv Sci Technol 51, 115–126 (2019).

47. Policastro, G., Panico, A. & Fabbricino, M. Improving biological production of poly(3-hydroxybutyrate-co-3-hydroxyvalerate) (PHBV) co-polymer: a critical review. Reviews in Environmental Science and Bio/Technology 2021 20:2 20, 479–513 (2021).

48. Giubilini, A., Bondioli, F., Messori, M., Nyström, G. & Siqueira, G. Advantages of additive manufacturing for biomedical applications of polyhydroxyalkanoates. Bioengineering vol. 8 1–31 Preprint at https://doi.org/10.3390/bioengineering8020029 (2021).

49. Ferri, M. et al. Fully Biobased Polyhydroxyalkanoate/Tannin Films as Multifunctional Materials for Smart Food Packaging Applications. ACS Appl Mater Interfaces 15, 28594–28605 (2023).

50. Raucci, A. et al. Characterization and application of porous PHBV-based bacterial polymers to realize novel bio-based electroanalytical (bio)sensors. Sens Actuators B Chem 379, 133178 (2023).

51. Aaliya, B., Sunooj, K. V. & Lackner, M. Biopolymer composites: a review. https://doi.org/10.1080/24759651.2021.1881214 3, 40–84 (2021).

52. Nanni, A. & Messori, M. Thermo-mechanical properties and creep modelling of wine lees filled Polyamide 11 (PA11) and Polybutylene succinate (PBS) bio-composites. Compos Sci Technol 188, 107974 (2020).

53. Sritham, E., Phunsombat, P. & Chaishome, J. Tensile properties of PLA/PBAT blends and PLA fibre-reinforced PBAT composite. MATEC Web of Conferences 192, 03014 (2018).

54. Oksman, K. et al. Review of the recent developments in cellulose nanocomposite processing. Compos Part A Appl Sci Manuf 83, 2–18 (2016).

55. Ashori, A., Jonoobi, M., Ayrilmis, N., Shahreki, A. & Fashapoyeh, M. A. Preparation and characterization of polyhydroxybutyrate-co-valerate (PHBV) as green composites using nano reinforcements. Int J Biol Macromol 136, 1119–1124 (2019).

56. Dasan, Y. K., Bhat, A. H. & Ahmad, F. Polymer blend of PLA/PHBV based bionanocomposites reinforced with nanocrystalline cellulose for potential application as packaging material. Carbohydr Polym 157, 1323– 1332 (2017).

57. Baiardo, M. et al. Thermal and mechanical properties of plasticized poly(L-lactic acid). J Appl Polym Sci 90, 1731–1738 (2003).

58. Farrag, Y., Montero, B., Rico, M., Barral, L. & Bouza, R. Preparation and characterization of nano and micro particles of poly(3-hydroxybutyrate-co-3-hydroxyvalerate) (PHBV) via emulsification/solvent evaporation and nanoprecipitation techniques. Journal of Nanoparticle Research 20, 1–17 (2018).

59. Kumar, V., Sehgal, R. & Gupta, R. Blends and composites of polyhydroxyalkanoates (PHAs) and their applications. Eur Polym J 161, (2021).

60. Hassaini, L. et al. Valorization of olive husk flour as a filler for biocomposites based on poly(3-hydroxybutyrate-co-3-hydroxyvalerate): Effects of silane treatment. Polym Test 59, 430–440 (2017).

61. Barbosa, J. L., Perin, G. B. & Felisberti, M. I. Plasticization of Poly(3-hydroxybutyrate- co-3-hydroxyvalerate) with an Oligomeric Polyester: Miscibility and Effect of the Microstructure and Plasticizer Distribution on Thermal and Mechanical Properties. ACS Omega 6, 3278–3290 (2021).

62. Yatigala, N. S., Bajwa, D. S. & Bajwa, S. G. Compatibilization improves physico-mechanical properties of biodegradable biobased polymer composites. Compos Part A Appl Sci Manuf 107, 315–325 (2018).

63. Móczó, J. & Pukánszky, B. Polymer micro and nanocomposites: Structure, interactions, properties. Journal of Industrial and Engineering Chemistry 14, 535–563 (2008).

64. Lewis, T. B. & Nielsen, L. E. Dynamic Mechanical Properties of Particulate-Filled Composites. J Appl Polym Sci 14, 1449–1471 (1970).

65. Pukanszky, B. Influence of interface interaction on the ultimate tensile properties of polymer composites. Composites 21, 255–262 (1990).

66. Halpin, J. C., Louis, S. T. & Kardos, J. L. The Halpin-Tsai Equations: A Review. Polym Eng Sci 16, 344–352 (1976).

67. Kerner, E. H. The Elastic and Thermo-elastic Properties of Composite Media. Proceedings of the Physical Society. Section B 69, 808–813 (1956).

68. Burford, T., Rieg, W. & Madbouly, S. Biodegradable poly(butylene adipate-co-terephthalate) (PBAT). Physical Sciences Reviews 1–30 (2021) doi:10.1515/PSR-2020-0078/MACHINEREADABLECITATION/RIS.

69. Giubilini, A. et al. 3D-Printing Nanocellulose-Poly(3-hydroxybutyrate- co-3-hydroxyhexanoate) Biodegradable Composites by Fused Deposition Modeling. ACS Sustain Chem Eng 8, 10292–10302 (2020).

70. Mukherjee, T. et al. Dispersion study of nanofibrillated cellulose based poly(butylene adipate-co-terephthalate) composites. Carbohydr Polym 102, 537–542 (2014).

71. Sabbatini, B. et al. An Overview of Natural Polymers as Reinforcing Agents for 3D Printing. ChemEngineering 2021, Vol. 5, Page 78 5, 78 (2021).

72. Udayakumar, G. P. et al. Biopolymers and composites: Properties, characterization and their applications in food, medical and pharmaceutical industries. J Environ Chem Eng 9, 105322 (2021).

73. Pereira da Silva, J. S., Farias da Silva, J. M., Soares, B. G. & Livi, S. Fully biodegradable composites based on poly(butylene adipate-co-terephthalate)/peach palm trees fiber. Compos B Eng 129, 117–123 (2017).

74. Ferreira, F. V. et al. Environmentally friendly polymer composites based on PBAT reinforced with natural fibers from the amazon forest. Polym Compos 40, 3351–3360 (2019).

75. Sánchez-Safont, E. L., Aldureid, A., Lagarón, J. M., Gámez-Pérez, J. & Cabedo, L. Biocomposites of different lignocellulosic wastes for sustainable food packaging applications. Compos B Eng 145, 215–225 (2018).

76. Zhang, H. & Sablani, S. Biodegradable packaging reinforced with plant-based food waste and by-products. Curr Opin Food Sci 42, 61–68 (2021).

77. Moustafa, H., Guizani, C. & Dufresne, A. Sustainable biodegradable coffee grounds filler and its effect on the hydrophobicity, mechanical and thermal properties of biodegradable PBAT composites. J Appl Polym Sci 134, 44498 (2017).

78. Bashir, A. S. M. & Manusamy, Y. Recent Developments in Biocomposites Reinforced with Natural Biofillers from Food Waste. Polymer - Plastics Technology and Engineering vol. 54 87–99 Preprint at https://doi.org/10.1080/03602559.2014.935419 (2015).

79. Yang, H. S., Wolcott, M. P., Kim, H. S., Kim, S. & Kim, H. J. Effect of different compatibilizing agents on the mechanical properties of lignocellulosic material filled polyethylene bio-composites. Compos Struct 79, 369–375 (2007).

80. Vatansever, E. et al. Development of CNC-reinforced PBAT nanocomposites with reduced percolation threshold: a comparative study on the preparation method. J Mater Sci 55, 15523–15537 (2020).

81. Hsieh, T. H., Shen, M. Y., Huang, Y. S., He, Q. Q. & Chen, H. C. Mechanical properties of glass bead-modified polymer composite. Polymers and Polymer Composites 26, 35–43 (2018).

82. Falcão, G. A. M., Almeida, T. G., Bardi, M. A. G., Carvalho, L. H. & Canedo, E. L. PBAT/organoclay composite films—part 2: effect of UV aging on permeability, mechanical properties and biodegradation. Polymer Bulletin 76, 291–301 (2019).

83. Pegoretti, A., Dorigato, A. & Penati, A. Tensile mechanical response of polyethylene-clay nanocomposites. Express Polym Lett 1, 123–131 (2007).

84. Venkatesan, R. & Rajeswari, N. Preparation, Mechanical and Antimicrobial Properties of SiO2/ Poly(butylene adipate-co-terephthalate) Films for Active Food Packaging. Silicon 2016 11:5 11, 2233–2239 (2016).

85. Venkatesan, R. & Rajeswari, N. ZnO/PBAT nanocomposite films: Investigation on the mechanical and biological activity for food packaging. Polym Adv Technol 28, 20–27 (2017).

86. Wang, X., Cui, L., Fan, S., Li, X. & Liu, Y. Biodegradable Poly(butylene adipate-co-terephthalate) Antibacterial Nanocomposites Reinforced with MgO Nanoparticles. Polymers 2021, Vol. 13, Page 507 13, 507 (2021).

87. George, A., Sanjay, M. R., Srisuk, R., Parameswaranpillai, J. & Siengchin, S. A comprehensive review on chemical properties and applications of biopolymers and their composites. Int J Biol Macromol 154, 329–338 (2020).

88. Dolza, C. et al. Development and Characterization of Environmentally Friendly Wood Plastic Composites from Biobased Polyethylene and Short Natural Fibers Processed by Injection Moulding. Polymers 2021, Vol. 13, Page 1692 13, 1692 (2021).

89. Krog, N. Additives in Dairy Foods: Emulsifiers. Encyclopedia of Dairy Sciences: Second Edition 61–71 (2011) doi:10.1016/B978-0-12-374407-4.00006-6.

90. Convertino, A. et al. TiO2 colloidal nanocrystals functionalization of PMMA: A tailoring of optical properties and chemical adsorption. Sens Actuators B Chem 126, 138–143 (2007).

91. Sciancalepore, C. et al. TiO2 nanorods/PMMA copolymer-based nanocomposites: highly homogeneous linear and non-linear optical material. Nanotechnology 19, 205705 (2008).

92. Anaya-Esparza, L. M. et al. Protein–tio2: A functional hybrid composite with diversified applications. Coatings vol. 10 1–29 Preprint at https://doi.org/10.3390/coatings10121194 (2020).

93. Sciancalepore, C. & Bondioli, F. Durability of SiO2–TiO2 Photocatalytic Coatings on Ceramic Tiles. Int J Appl Ceram Technol 12, 679–684 (2015).

94. Gomes de Menezes, F. L., de Lima Leite, R. H., Gomes dos Santos, F. K., Aria, A. I. & Aroucha, E. M. M. TiO2-enhanced chitosan/cassava starch biofilms for sustainable food packaging. Colloids Surf A Physicochem Eng Asp 630, (2021).

95. Irshad, M. A. et al. Synthesis, characterization and advanced sustainable applications of titanium dioxide nanoparticles: A review. Ecotoxicol Environ Saf 212, (2021).

96. Cao, Y., Chen, T. T., Wang, W., Chen, M. & Wang, H. J. Construction and functional assessment of zein thin film incorporating spindle-like ZnO crystals. RSC Adv 7, 2180–2185 (2017).

97. Kadam, D. M. et al. Effect of TiO2 nanoparticles on thermo-mechanical properties of cast zein protein films. Food Packag Shelf Life 13, 35–43 (2017).

98. Sandhu, K. S. & Singh, N. Some properties of corn starches II: Physicochemical, gelatinization, retrogradation, pasting and gel textural properties. Food Chem 101, 1499–1507 (2007).

99. Lawton, J. W. Zein: A history of processing and use. Cereal Chem 79, 1–18 (2002).

100. Tian, H., Liu, D. & Zhang, L. Structure and properties of soy protein films plasticized with hydroxyamine. J Appl Polym Sci 111, 1549–1556 (2009).

101. Kumar, R., Liu, D. & Zhang, L. Advances in Proteinous Biomaterials. J Biobased Mater Bioenergy 2, 1–24 (2008).

102. Oh, J. H., Wang, B., Field, P. D. & Aglan, H. A. Characteristics of edible films made from dairy proteins and zein hydrolysate cross-linked with transglutaminase. Int J Food Sci Technol 39, 287–294 (2004).

103. Sglavo, V. M. et al. Mechanical properties of resorbable calcium-phosphate glass optical fiber and capillaries. J Alloys Compd 778, 410–417 (2019).

104. Ceci-Ginistrelli, E. et al. Novel biocompatible and resorbable UV-transparent phosphate glass based optical fiber. Opt Mater Express 6, 2040 (2016).

105. Hench, L. L. & Polak, J. M. Third-Generation Biomedical Materials. Science (1979) 295, (2002).

106. Knowles, J. C. Phosphate based glasses for biomedical applications. Journal of Materials Chemistry vol. 13 2395–2401 Preprint at https://doi.org/10.1039/b307119g (2003).

107. Rabiee, S. M., Nazparvar, N., Azizian, M., Vashaee, D. & Tayebi, L. Effect of ion substitution on properties of bioactive glasses: A review. Ceram Int 41, 7241–7251 (2015).

108. Kaur, G. et al. A review of bioactive glasses: Their structure, properties, fabrication and apatite formation. J Biomed Mater Res A 102, 254–274 (2014).

109. Navarro, M. et al. New macroporous calcium phosphate glass ceramic for guided bone regeneration. Biomaterials 25, 4233–4241 (2004).

110. Baia, L., Baia, M., Kiefer, W., Popp, J. & Simon, S. Structural and morphological properties of silver nanoparticles-phosphate glass composites. Chem Phys 327, 63–69 (2006).

111. Baia, L., Muresan, D., Baia, M., Popp, J. & Simon, S. Structural properties of silver nanoclusters-phosphate glass composites. Vib Spectrosc 43, 313–318 (2007).

112. Halloran, M. W., Danielczak, L., Nicell, J. A., Leask, R. L. & Maric, M. Highly Flexible Polylactide Food Packaging Plasticized with Nontoxic, Biosourced Glycerol Plasticizers. ACS Appl Polym Mater 4, 3608–3617 (2022).

113. Vieira, M. G. A., Da Silva, M. A., Dos Santos, L. O. & Beppu, M. M. Natural-based plasticizers and biopolymer films: A review. Eur Polym J 47, 254–263 (2011).

114. Rahman, M. & Brazel, C. S. The plasticizer market: an assessment of traditional plasticizers and research trends to meet new challenges. Prog Polym Sci 29, 1223–1248 (2004).

115. Gao, D. W. & Wen, Z. D. Phthalate esters in the environment: A critical review of their occurrence, biodegradation, and removal during wastewater treatment processes. Science of The Total Environment 541, 986–1001 (2016).

116. Xuan, W., Hakkarainen, M. & Odelius, K. Levulinic Acid as a Versatile Building Block for Plasticizer Design. ACS Sustain Chem Eng 7, 12552–12562 (2019).

117. Jamarani, R., Erythropel, H. C., Nicell, J. A., Leask, R. L. & Marić, M. How Green is Your Plasticizer? Polymers 2018, Vol. 10, Page 834 10, 834 (2018).

118. Râpă, M., Darie-Nita, R. N., Matei, E. & Predescu, A. M. Bio-Based Plasticizers for Polyvinylchloride (PVC). 137–157 (2022) doi:10.1007/978-3-030-78455-3_7.

119. Jost, V. & Langowski, H. C. Effect of different plasticisers on the mechanical and barrier properties of extruded cast PHBV films. Eur Polym J 68, 302–312 (2015).

120. Campioli, E., Lee, S., Lau, M., Marques, L. & Papadopoulos, V. Effect of prenatal DINCH plasticizer exposure on rat offspring testicular function and metabolism. Scientific Reports 2017 7:1 7, 1–14 (2017).

121. Zhang, W. et al. Characterizing the obesogenic and fatty liver-inducing effects of Acetyl tributyl citrate (ATBC) plasticizer using both in vivo and in vitro models. J Hazard Mater 445, (2023).

122. Zygoura, P. D., Riganakos, K. A. & Kontominas, M. G. Study of the migration behavior of acetyl tributyl citrate from PVDC/PVC film into fish fillets as affected by intermediate doses of electron beam radiation. European Food Research and Technology 232, 1017–1025 (2011).

123. Halloran, M. W., Nicell, J. A., Leask, R. L. & Marić, M. Bio-based glycerol plasticizers for flexible poly(vinyl chloride) blends. J Appl Polym Sci 139, (2022).

124. Singh, G. & Chanda, A. Mechanical properties of whole-body soft human tissues: a review. Biomedical Materials 16, 062004 (2021).

125. Florencio-Silva, R., Sasso, G. R. D. S., Sasso-Cerri, E., Simões, M. J. & Cerri, P. S. Biology of Bone Tissue: Structure, Function, and Factors That Influence Bone Cells. Biomed Res Int 2015, 421746 (2015).

126. Hadjidakis, D. J. & Androulakis, I. I. Bone Remodeling. Ann N Y Acad Sci 1092, 385–396 (2006).

127. Almouemen, N., Kelly, H. M. & O'Leary, C. Tissue Engineering: Understanding the Role of Biomaterials and Biophysical Forces on Cell Functionality Through Computational and Structural Biotechnology Analytical Methods. Comput Struct Biotechnol J 17, 591–598 (2019).

128. Ikada, Y. Challenges in tissue engineering. J R Soc Interface 3, 589–601 (2006).

129. Roseti, L. et al. Scaffolds for Bone Tissue Engineering: State of the art and new perspectives. Mater Sci Eng C Mater Biol Appl 78, 1246–1262 (2017).

130. Chan, B. P. & Leong, K. W. Scaffolding in tissue engineering: general approaches and tissue-specific considerations. Eur Spine J 17 Suppl 4, (2008).

131. Turnbull, G. et al. 3D bioactive composite scaffolds for bone tissue engineering. Bioact Mater 3, 278–314 (2017).

132. Abbasi, N., Hamlet, S., Love, R. M. & Nguyen, N. T. Porous scaffolds for bone regeneration. Journal of Science: Advanced Materials and Devices 5, 1–9 (2020).

133. Roohani-Esfahani, S. I., Newman, P. & Zreiqat, H. Design and Fabrication of 3D printed Scaffolds with a Mechanical Strength Comparable to Cortical Bone to Repair Large Bone Defects. Scientific Reports 2016 6:1 6, 1–8 (2016).

134. Navarro, M., Michiardi, A., Castaño, O. & Planell, J. A. Biomaterials in orthopaedics. J R Soc Interface 5, 1137–1158 (2008).

135. Yu, X., Tang, X., Gohil, S. V. & Laurencin, C. T. Biomaterials for Bone Regenerative Engineering. Adv Healthc Mater 4, 1268–1285 (2015).

136. Vyavahare, S., Teraiya, S., Panghal, D. & Kumar, S. Fused deposition modelling: a review. Rapid Prototyp J 26, 176–201 (2020).

137. De Maria, C. et al. Biomimetic Tendrils by Four Dimensional Printing Bimorph Springs with Torsion and Contraction Properties Based on Bio-Compatible Graphene/Silk Fibroin and Poly(3-Hydroxybutyrate-co-3-Hydroxyvalerate). Adv Funct Mater 31, 2105665 (2021).

138. Chynybekova, K. & Choi, S. M. Flexible Patterns for Soft 3D Printed Fabrications. Symmetry 2019, Vol. 11, Page 1398 11, 1398 (2019).

139. Mayer-Laigle, C. et al. Flax shives-PBAT processing into 3D printed fluorescent materials with potential sensor functionalities. Ind Crops Prod 167, 113482 (2021).

140. Badouard, C. et al. Exploring mechanical properties of fully compostable flax reinforced composite filaments for 3D printing applications. Ind Crops Prod 135, 246–250 (2019).

141. Rebia, R. A., Sadon, N. S. B. & Tanaka, T. Natural antibacterial reagents (Centella, propolis, and hinokitiol) loaded into poly[(R)-3-hydroxybutyrate-co-(R)-3-hydroxyhexanoate] composite nanofibers for biomedical applications. Nanomaterials 9, (2019).

142. Barouti, G., Jaffredo, C. G. & Guillaume, S. M. Advances in drug delivery systems based on synthetic poly(hydroxybutyrate) (co)polymers. Prog Polym Sci 73, 1–31 (2017).

143. Lü, L. X., Wang, Y. Y., Mao, X., Xiao, Z. D. & Huang, N. P. The effects of PHBV electrospun fibers with different diameters and orientations on growth behavior of bone-marrow-derived mesenchymal stem cells. Biomedical Materials 7, 015002 (2012).

144. Paşcu, E. I., Stokes, J. & McGuinness, G. B. Electrospun composites of PHBV, silk fibroin and nano-hydroxyapatite for bone tissue engineering. Materials Science and Engineering C 33, 4905–4916 (2013).

145. Pereira, T. F. et al. 3D printing of poly(3-hydroxybutyrate) porous structures using selective laser sintering. in Macromolecular Symposia vol. 319 64–73 (2012).

146. Subramaniam, S. R. et al. 3D printing: Overview of PLA progress. AIP Conf Proc 2059, (2019).

147. Kanabenja, W. et al. 3D printing filaments from plasticized Polyhydroxybutyrate/Polylactic acid blends reinforced with hydroxyapatite. Addit Manuf 59, 103130 (2022).

148. Melčová, V. et al. FDM 3D Printed Composites for Bone Tissue Engineering Based on Plasticized Poly(3-hydroxybutyrate)/poly(d,l-lactide) Blends. Polymers 2020, Vol. 12, Page 2806 12, 2806 (2020).

149. Plasticizers Market Size, Share, Scope, Trends, Growth & Forecast. https://www.verifiedmarketresearch.com/product/plasticizers-market/.

150. Sinisi, A. et al. Levulinic acid-based bioplasticizers: a facile approach to enhance the thermal and mechanical properties of polyhydroxyalkanoates. Mater Adv 2, 7869–7880 (2021).

151. Pierucci, S. et al. Assessment of Different Plasticizer-Polyhydroxyalkanoate Mixtures to Obtain Biodegradable Polymeric Films. Chem Eng Trans 57, (2017).

152. Audic, J. L., Lemiègre, L. & Corre, Y. M. Thermal and mechanical properties of a polyhydroxyalkanoate plasticized with biobased epoxidized broccoli oil. J Appl Polym Sci 131, 39983 (2014).

153. González-López, M. E., Martín del Campo, A. S., Robledo-Ortíz, J. R., Arellano, M. & Pérez-Fonseca, A. A. Accelerated weathering of poly(lactic acid) and its biocomposites: A review. Polym Degrad Stab 179, 109290 (2020).

154. Tang, D., Zhang, C. & Weng, Y. Effect of multi-functional epoxy chain extender on the weathering resistance performance of Poly(butylene adipate-co-terephthalate) (PBAT). Polym Test 99, (2021).

155. Zhang, T., Han, W., Zhang, C. & Weng, Y. Effect of chain extender and light stabilizer on the weathering resistance of PBAT/PLA blend films prepared by extrusion blowing. Polym Degrad Stab 183, 109455 (2021).

156. Kijchavengkul, T. et al. Atmospheric and soil degradation of aliphatic-aromatic polyester films. Polym Degrad Stab 95, 99–107 (2010).

157. Lucas, N. et al. Polymer biodegradation: Mechanisms and estimation techniques - A review. Chemosphere vol. 73 429–442 Preprint at https://doi.org/10.1016/j.chemosphere.2008.06.064 (2008).

158. Ruggero, F., Gori, R. & Lubello, C. Methodologies to assess biodegradation of bioplastics during aerobic composting and anaerobic digestion: A review. Waste Management and Research 37, 959–975 (2019).

159. García-Depraect, O. et al. Biodegradation of bioplastics under aerobic and anaerobic aqueous conditions: Kinetics, carbon fate and particle size effect. Bioresour Technol 344, 126265 (2022).

160. Dilkes-Hoffman, L. S., Lant, P. A., Laycock, B. & Pratt, S. The rate of biodegradation of PHA bioplastics in the marine environment: A meta-study. Mar Pollut Bull 142, 15–24 (2019).

161. Hegde, S., Diaz, C. A., Dell, E. M., Trabold, T. A. & Lewis, C. L. Investigation of process parameters on the anaerobic digestion of a poly(hydroxyalkonate) film. Eur Polym J 148, 110349 (2021).

162. Bátori, V., Åkesson, D., Zamani, A., Taherzadeh, M. J. & Sárvári Horváth, I. Anaerobic degradation of bioplastics: A review. Waste Management 80, 406–413 (2018).

163. Jin, Y. et al. Volatile fatty acids production from saccharification residue from food waste ethanol fermentation: Effect of pH and microbial community. Bioresour Technol 292, 121957 (2019).

164. Reischwitz, A., Stoppok, E. & Buchholz, K. Anaerobic degradation of poly-3-hydroxybutyrate and poly-3-hydroxybutyrate-co-3-hydroxyvalerate. Biodegradation 8, 313–319 (1997).

165. Agler, M. T., Wrenn, B. A., Zinder, S. H. & Angenent, L. T. Waste to bioproduct conversion with undefined mixed cultures: The carboxylate platform. Trends Biotechnol 29, 70–78 (2011).

166. Myung, J. et al. Disassembly and reassembly of polyhydroxyalkanoates: Recycling through abiotic depolymerization and biotic repolymerization. Bioresour Technol 170, 167–174 (2014).

167. Samorì, C. et al. PHB into PHB: Recycling of polyhydroxybutyrate by a tandem “thermolytic distillation-microbial fermentation” process. Resour Conserv Recycl 178, 106082 (2022).

168. Sciancalepore, C. et al. Preparation and characterization of innovative poly(butylene adipate terephthalate)-based biocomposites for agri-food packaging application. J Appl Polym Sci 52370 (2022) doi:10.1002/app.52370.

169. Togliatti, E. et al. Design of Mechanical Properties of Poly(butylene-adipate-terephthalate) Reinforced with Zein-TiO2Complex. Material Design and Processing Communications 2022, (2022).

170. Sciancalepore, C. et al. Flexible PBAT-Based Composite Filaments for Tunable FDM 3D Printing. ACS Appl Bio Mater 5, 3219–3229 (2022).

171. Togliatti, E. et al. Enhancing melt-processing and 3D printing suitability of polyhydroxybutyrate through compounding with a bioplasticizer derived from the valorization of levulinic acid and glycerol. Addit Manuf 89, (2024).

Chapter 2

PBAT-based composites

2.1 Introduction

This chapter presents the production and characterization of biocomposites with a PBAT matrix and different concentrations of two different fillers. The objective of this research is to investigate the potential applications of reinforced PBAT in the packaging industry and biomedical sector, specifically in the development of flexible scaffolds designed for biomedical applications.

A bioabsorbable calcium-phosphate glass (CPG) previously produced at Polytechnic of Turin[1], was utilized in the form of micrometric particles as a reinforcing filler. Moreover, zein was used as a coupling agent and co-filler to prepare a complex structure with TiO_2 (Zein-TiO_2 Complex, ZTC) to act as a reinforcing phase in the second composition. The ZTC is a hybrid organic-inorganic filler[2] that enhances interfacial adhesion and interaction between the inorganic reinforcement, the TiO_2 and polymer matrix, the PBAT. Biocomposites were prepared via solvent casting with a filler concentration of up to 40 wt%.

The impact of the fillers on the morphological and structural characteristics of the composites was examined using microscopy and spectroscopy techniques. To evaluate the impact of filler particle addition on the mechanical and viscoelastic properties of the polymer, Uniaxial Tensile Test (UTT), Dynamic Mechanical Analysis (DMA), and creep analyses were conducted on dumbbell specimens. This enabled an evaluation of the efficacy of the reinforcement and a delineation of the variations in the conditions of use of the novel materials. Moreover, an analysis of the predictability of property modification and the interaction between the two phases was conducted through the application of Kerner's and Pukánszky's models.

The developed biocomposite materials, based on PBAT and ZTC, were furthermore used for producing extruded filaments with tailored properties and suitability for three-dimensional (3D) printing of complex solid systems. These materials exhibited remarkable biocompatibility properties, as demonstrated by the cytotoxicity tests. The advantages of these eco-friendly materials can thus be combined with the production of customizable design objects by additive manufacturing, with numerous potential applications in biomedical and healthcare research.

2.2 Composite modeling – literature review

As introduced in Chapter 1, composite modeling is a useful tool to analyze and predict mechanical properties of composite materials and consequently design the materials with the desired properties.

The most diffused theories for modeling composite properties are represented by Halpin-Tsai's[3] and Kerner-Nielsen's[4,5] models as far as elastic modulus is concerned, and by Pukánszky's[6] model regarding tensile strength and interfacial adhesion goodness.

For this chapter, the detailed and comprehensive publications of Lewis and Nielsen[7], Százdi et al.[8], Pukánszky[6,9] and Móczó et al.[10] have been taken as references for the description of the composite mechanical characteristics.

2.2.1 Tensile Modulus

Halpin developed a simplified model to predict the elastic modulus in composites filled with short fibers[11]. The model assumes that the fibers are aligned and oriented parallel or perpendicular to the direction of the stress applied, and the elastic moduli of the composites in the two cases are expressed by E_I in Equation 2.1 and E_L in Equation 2.2, respectively[12]:

$$E_I = E_m\left(1 - \varphi_f\right) + E_p\varphi_f \qquad \text{(Equation 2.1)}$$

$$E_L = E_m\left[\frac{1+\xi\beta\varphi_f}{1-\beta\varphi_f}\right] \qquad \text{(Equation 2.2)}$$

where E_p and E_m are, respectively, the filler and matrix moduli, φ_f is the volumetric fraction of the filler (Equation 2.3) (with g_f and g_m the masses of the filler and the matrix, and ρ_f and ρ_m the density of the filler and the matrix, respectively), and the parameter ξ represents the particles aspect ratio. β is a parameter defined in Equation 2.4.

$$\varphi_f = \frac{\frac{g_f}{\rho_f}}{\frac{g_f}{\rho_f}+\frac{g_m}{\rho_m}} \qquad \text{(Equation 2.3)}$$

$$\beta = \frac{\frac{E_p}{E_m}-1}{\frac{E_p}{E_m}+\xi} \qquad \text{(Equation 2.4)}$$

A similar model was developed by Kerner, who extensively studied the elastic properties of composite materials[5]. Kerner's equation can be expressed in the form of the following Equation 2.5[7]:

$$\frac{E_K'}{E_{K,0}'} = \frac{(1+AC\varphi_f)}{(1-C\varphi_f)} \qquad \text{(Equation 2.5)}$$

where E_K' and $E_{K,0}'$ are the elastic moduli of the composite and matrix, respectively; φ_f is the volumetric fraction of the filler phase; A (Equation 2.6) considers the spherical geometry of the filler and the Poisson ratio v of the matrix; C is defined, analogously to the former β parameter, as in Equation 2.7 and takes into account the relative elastic moduli of the phases.

$$A = \frac{7-5\upsilon}{8-10\upsilon} \qquad \text{(Equation 2.6)}$$

$$C = \frac{\frac{E_p}{E_m}-1}{\frac{E_p}{E_m}+A} \qquad \text{(Equation 2.7)}$$

Lewis and Nielsen[4,7] modified Kerner's model, pointing out that important factors, like the packing of the filler particles ψ, were neglected. ψ formulation (Equation 2.8) is given as a function of φ_f and the maximum packing factor of the filler φ_m:

$$\psi = 1 + \frac{1-\varphi_m}{\varphi_m^2} \cdot \varphi_f \qquad \text{(Equation 2.8)}$$

Generalized Kerner's equation was then proposed such as in the following (Equation 2.9):

$$\frac{E_K'}{E_{K,0}'} = \frac{(1+AC\varphi_f)}{(1-\psi C\varphi_f)} \qquad \text{(Equation 2.9)}$$

Generally, an increase in stiffness is expected when a matrix is filled with a reinforcing agent.

2.2.2 Yield Strength

A simple model to predict the yield strength as a function of the filler content was proposed by Nicolais and Narkis[13]. The model supposes that the presence of the filler reduces the cross-sectional area, and the load during deformation is carried by the only continuous phase, that is, the matrix. In the case of composites filled with uniformly dispersed spherical particles, the Nicolais and Narkis' equation is expressed as Equation 2.10

$$\sigma_{y,c} = \sigma_{y,m}\left(1 - 1.21\varphi_f^{2/3}\right) \qquad \text{(Equation 2.10)}$$

where $\sigma_{y,c}$ and $\sigma_{y,m}$ are the yield stresses of the composite and of the unfilled polymer, respectively. Equation 2.10, however, lacks in considering interaction between the particles and the matrix, assuming "no adhesion" therefore, the results often deviate from the predictions[10,13].

A modification from the previous model was presented by Pukánszky et al.[14], who made some adjusting considerations about the cross-section and came up with the following expression (Equation 2.11):

$$\sigma_y = \sigma_{y0} \frac{1-\varphi_f}{1+2.5\varphi_f} \exp\left(B_y \cdot \varphi_f\right) \quad \text{(Equation 2.11)}$$

which can be linearized as follows (Equation 2.12):

$$log\left(\sigma_{y,rel}\right) = log\left(\frac{\sigma_y\left(1+2{,}5\varphi_f\right)}{\sigma_{y0}\left(1-\varphi_f\right)}\right) = B_y \cdot \varphi_f \qquad \text{(Equation 2.12)}$$

where φ_f is the filler volumetric fraction, σ_y and σ_{y0} are the yield stresses of the composite and the matrix, respectively.

In Pukánszky's model, B_y is an empirical parameter that considers the strength of interactions defined as in Equation 2.13

$$B_y = \left(1 + A_f \rho_f l\right) \ln \frac{\sigma_{yi}}{\sigma_{y0}} \qquad \text{(Equation 2.13)}$$

featuring the extension of the interfacial surface (A_f), the thickness (l), and strength (σ_{yi}) of the interphase.

As it is clear from the formulation of B_y, the properties of heterogeneous materials are influenced by many factors, and the four main ones are: the properties of the single components, the composition, the structure, and the interfacial interactions[8]. In particular, the quality of the interaction is generally measured in terms of strength and thickness of the interphase[15], and in the case of Pukánszky's model, it is indeed given by the value assumed by B, which generally assumes values between 2 and 15 for polymer-based micro- and nanocomposites[10,16,17].

Particle size and size distribution are of critical importance in the reinforcement of composites, as interphase interaction occurs at the surface area, A_f. The utilization of smaller particles results in a higher specific surface area, which consequently leads to a more substantial reinforcement effect due to the intensification of interphase interactions. Typically, reinforcing agents are introduced into the matrix in the form of particles and fibers with micro- or nanometric dimensions. Nevertheless, an increase in particle size can have a detrimental effect on tensile strength, as larger particles are more prone to debonding from the matrix under load, which often results in premature failure. Conversely, particles that are too small may aggregate, thereby reducing the specific surface area and consequently weakening the composite's mechanical properties[10]. Incompatibility between polymers and fillers, arising from their different chemical natures, may also result in poor adhesion and significantly lower B values. In the most unfavorable scenario, where there is no adhesion between the filler and the matrix, no load transfer occurs to the filler, and the matrix alone bears the entire load, with the load-bearing section decreasing as the filler content increases[14].

To achieve higher values of filler-matrix adhesion and enhance interphase strength, it may be beneficial to consider surface treatment of the filler, functionalization of the polymer, and the use of compatibilizers. The modification of the surface treatment affects both the interactions between the particles and the interactions between the matrix and the filler. As a result, the properties of the composite are a combination of the two effects. In the case of cellulose and natural fibers, additional chemical modifications may be conducted through acetylation, cyanoethylation, peroxide treatment, and silane treatments[18,19]. The optimization of surface modification processes must consider both technical and economic factors, determining the most suitable type and quantity of reagents. In a study by Panaitescu et al.[19], the properties of maleated polypropylene (MA-PP) filled with microfibrillated cellulose (MFC) at different concentrations were examined. The results demonstrated a significant increase in tensile modulus and strength when compared to the simple PP-MFC composite system without a coupling agent. Similarly, Nanni et al.[20] observed that the use of maleic anhydride as a coupling agent in PP-spent coffee ground (SCG) systems resulted in enhanced mechanical properties without a concomitant decrease in tensile strength, even at high filler concentrations. Indeed, the B factor of the Pukánszky composite was found to be higher than that of the simple PP-SCG composite. Considering these findings, it can be reasonably assumed that the interfacial bonding has been enhanced, thereby facilitating improved stress transfer and more performing mechanical properties. Yang et al. produced polyethylene (PE) - lignocellulosic materials composites, obtaining analogous results but emphasizing that compatibilization with maleic anhydride has a more pronounced effect on the enhancement of PE properties compared to MA-PP, due to superior wetting[21]. The surface of bamboo fibers was modified using an aqueous solution of sodium hydroxide (NaOH) and salinization was performed to create epoxy composites. Both cases demonstrated increases in tensile strength and elongation at break, in comparison to the untreated filler-epoxy composite[22]. Metin et al. demonstrated that silane coupling agents enhanced interfacial adhesion between the filler and the matrix in a PP system containing treated zeolite, as compared to non-treated particles. Both tensile modulus and yield strength were improved[23]. The silanization of MFC in poly(hydroxybutyrate-co-hexanoate) (PHBH) composites was also observed to induce a more pronounced reinforcing effect compared to untreated cellulose, due to an enhanced interfacial compatibility.

2.2.3 Strength at Break

The composition-dependence of the tensile properties at break can also be discussed, through a modification of Equation 2.11, leading to Equation 2.14:

$$\sigma_{B,T} = \sigma_{B,T_0 rel} \lambda^n \frac{1-\varphi_f}{1+2{,}5\varphi_f} \exp\left(B_B \varphi_f\right) \quad \text{(Equation 2.14)}$$

where $\sigma_{B,T}$ and $\sigma_{B,T0,rel}$ are the true tensile stress at break of the composite and the corresponding true tensile stress at break of the matrix, respectively.

Tensile stress is an engineered quantity that refers to the initial cross-section and does not consider that the cross-section varies during deformation. In the calculation of stress at break, engineered tensile strength σ must be converted into true stress $\sigma_{B,T}$ (Equation 2.15) as a function of relative elongation λ (Equation 2.16), with L (Equation 2.17) the actual length and l_0 the initial length of the specimen, respectively.

$$\sigma_{B,T} = \sigma \cdot \lambda \qquad \text{(Equation 2.15)}$$

$$\lambda = {}^{L}/_{l_0} \qquad \text{(Equation 2.16)}$$

$$L = l_0 + \Delta l \qquad \text{(Equation 2.17)}$$

$\sigma_{B,T0,rel}$ (Equation 2.18) is the relative true tensile stress at break of the matrix ($\sigma_{B,T0}$, Equation 2.19), where λ^n is a correction factor characterizing the strain hardening tendency happening in the polymer structure during deformation by means of the parameter n[6].

$$\sigma_{B,T_0 rel} = \frac{\sigma_{B,T_0}}{\lambda^n} \qquad \text{(Equation 2.18)}$$

$$\sigma_{B,T_0} = \sigma_0 \cdot \lambda \qquad \text{(Equation 2.19)}$$

n value is derived from the slope of the last section of the true tensile curve, obtained by plotting $ln(\sigma_T)$ vs. $ln(\lambda)$.

Rearranging Equation 2.14, Equation 2.20 is obtained and linearized such as in Equation 2.21, representing the reduced stress at break, $\sigma_{B,Tred}$ as a function of filler φ_f:

$$\sigma_{B,T\,red} = \frac{\sigma_{B,T}\,(1+2{,}5\varphi_f)}{\lambda^n \sigma_{B,T_0 rel}(1-\varphi_f)} = \exp(B_B \varphi_f) \qquad \text{(Equation 2.20)}$$

$$\ln(\sigma_{B,T\,red}) = B_B \varphi_f \qquad \text{(Equation 2.21)}$$

B_B is defined analogously to Equation 2.13 but it can assume a different value from the one determined by the yield stress. Usually, both elongation and strength decrease with increasing filler content but sometimes reinforcing effects are observed[10].

Additional specialized models have been developed, building on the aforementioned models and incorporating system-specific factors for optimal fit. For example, new multi-component models have been proposed to estimate Young's modulus[24]. Another study investigated the effect of carbon nanotube (CNT) aspect ratio on the interaction strength parameter[25] by linking interfacial shear strength to interfacial stress transfer and integrating this with Pukánszky's model. Models for ternary composites have also been developed by modifying the Kerner-Nielsen and Pukánszky hypotheses to predict the tensile modulus of polypropylene

(PP)/nanoclay/calcium carbonate ($CaCO_3$) composites and the interphase properties of PP/montmorillonite/$CaCO_3$ composites, respectively[26,27].

2.3 Materials

PBAT, in the form of white granules with a diameter of about 3 mm, was purchased under the commercial name PBAT Ecoworld from MAgMa Spa (Chieti, Italy) and used without any preliminary operations. Its chemical-physical characteristics are reported in Table 2.1, as per data sheet.

Table 2.1 *PBAT characteristics from the technical data sheet*

Property	**Value**
Melt flow rate	≤5 g/10min
Density	1.26 g/cm^3
Tensile strength	≥17 MPa
Melting temperature	110-120 °C
Elongation at break	≥600 %
Vicat softening temperature	89 °C

The biodegradable CPG powder with a composition of 50 P_2O_5 – 10 CaO – 23 MgO – 11.5 Na O –2.5 B_2O_3 – 3 SiO_2 (in mol%) was prepared using the traditional melt-quenching method as described elsewhere[1]. Briefly, a mixture of oxides and carbonates was weighed and mixed in a dry box. The batched chemicals were melted in an alumina crucible at 1200 °C under a controlled atmosphere, and after 1 h the melt was quenched on a cold aluminum plate. The resulting glass fragments were then ground to powder using a ball mill (Pulverisette 0, Fritsch, Idar-Oberstein, Germany) overnight and sieved through a stainless-steel sieve (Giuliani Technology Srl, Turin, Italy) to achieve a final particle size of less than 45 µm.

Zein (CAS no. 9010-66-6) and TiO_2 (CAS no. 13463-67-7) were obtained from Sigma-Aldrich (Merck KGaA, Germany) and Carlo Erba (Johnson & Johnson, USA), respectively.

The ZTC complex, with a 1:1 ratio of zein to TiO_2, was prepared by dissolving zein (50 g) in ethanol (200 mL, Sigma-Aldrich) under constant magnetic stirring at 50°C, followed by the gradual addition of TiO_2 powder (50 g). The reagents were used as received without further modification. When the solution became white and homogeneous, it was poured onto a tray and dried in an oven at 60 °C for 16 hours to form a thin film. This film was then ground to a fine powder using a Pulverisette 0 ball mill (Fritsch, Germany) and then sieved (Giuliani Technology Srl, Turin, Italy) to obtain particle sizes below 25 µm.

The preparation of PBAT-CPG and PBAT-ZTC composites was carried out using a solvent casting approach with chloroform ($CHCl_3$—Sigma-Aldrich) as solvent[28].

For PBAT-CPG composites, the polymer was dissolved in chloroform, and the CPG filler particles were dispersed in the polymer solution. This mixture was cast onto a non-stick surface, spread with a spatula to reduce its thickness, and left under an extractor hood for 12 hours to allow solvent evaporation. The resulting films were reduced to pellets and heat-treated at 80 °C until a constant weight was achieved. The CPG filler content varied from 0 to 40 wt%, allowing evaluation of material properties at different concentrations. The obtained samples, containing 0 (pure PBAT), 2, 4, 10, 20, and 40 wt% of CPG, were named PBAT, PBAT+2% CPG, PBAT+4% CPG, PBAT+10% CPG, PBAT+20% CPG, PBAT+40% CPG, respectively.

Similarly, PBAT-ZTC composites were prepared by dissolving PBAT in chloroform and dispersing ZTC powder in the same solvent separately. The polymer solution and filler suspension were mixed to form a homogeneous phase, cast onto a non-stick surface, and left for solvent evaporation under an extractor hood for 12 hours. The films were then reduced to pellets and desiccated at 80 °C to constant mass. These composites were produced at varying ZTC concentrations of 0, 5, 10, 20, and 40 wt%, and labeled as PBAT, PBAT+5% ZTC, PBAT+10% ZTC, PBAT+20% ZTC, and PBAT+40% ZTC, respectively.

The solvent casting approach was selected for the preliminary exploratory phase due to its capacity to facilitate the efficient production of polymeric composites in a laboratory setting. This approach enables a comprehensive investigation of the properties of these materials while ensuring a manageable solvent consumption. If the characterization of the resulting materials yields promising results regarding their suitability for large-scale application, the production of the composites could be implemented on an industrial scale. Nevertheless, to reduce the environmental impact of the extensive use of solvents, alternative compounding techniques, such as twin-screw Ex, should be given due consideration.

The resulting pellets were used for the injection molding (IM) of dumbbell specimens, model 1BA, following the UNI EN ISO 527 standard for subsequent thermal, mechanical, and structural characterization. This process was carried out using a MegaTech H7/18-1 machine (Tecnica Duebi, Italy), with the specific process parameters, summarized in Table 2.2, which were maintained equal for both composites.

The PBAT-ZTC pellets were also used to produce composite filaments for 3D printing using a single screw extrusion system (Felfil Evo, Felfil, Italy). This system was equipped with a cooling fan array to cool the polymer melt and a spooler with a thickness sensor to maintain a constant filament diameter. The extruder temperature was set at 150 ± 10 °C with a screw speed of 3 rpm. The filament was produced with a diameter of 1.65 ± 0.10 mm and collected at a speed of approximately 0.8 ± 0.1 m/min.

Thickness control during Ex is fundamental to obtain a filament suitable for 3D printing, as the printers utilize filaments with diameter not exceeding 1.75 mm.

Table 2.2 *Injection molding parameters for PBAT-based composites*

Parameter	**Value**
Hopper temperature	80 °C
Plasticizing screw and barrel temperature	130 °C
Accumulation room temperature	135 °C
Nozzle temperature	130 °C
Mold temperature	15 °C
Injection rate	55 mm/s
Injection pressure	120 bar
Shot size	27 cm^3
Plasticizing screw rotation speed	50 rpm
Holding pressure	60 bar
Holding time	5 s
Cooling time	10 s

2.4 Methods

2.4.1 Uniaxial tensile test (UTT)

UTT were performed on both composites using a TesT dynamometer (Model 112, TesT GMBH Universal Testing Machine, Germany). Specimens were clamped at both ends and subjected to a constant tensile speed of 100 mm/min until failure. Tests were repeated on a minimum of seven specimens for each composite. Average values of Young's modulus (E [MPa]), yield stress (σ_y [MPa]), stress at break (σ_B [MPa]), elongation at break (ε_B [mm/m]), and toughness (T [MJ/m^3]) were calculated from the stress-strain curves.

Additional tensile tests were performed to determine the PBAT Poisson's ratio using a digital image correlation (DIC) technique. These tests were performed at a constant tensile rate of 5 mm/min, with images of the specimen taken approximately every 0.01 mm/mm of strain using a 5 MPx Dinolite digital camera (Almere, The Netherlands) (Figure 2.1). The images were processed using the open-source DICe software [Turner, D.Z. Digital Image Correlation Engine (DICe) Reference Manual, Sandia Report, SAND2015-10606 O, 2015], and the results were analyzed using theParaView visualization software[29].

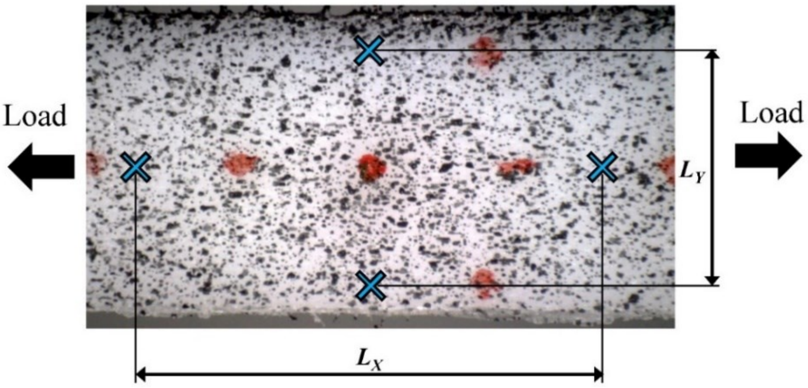

Figure 2. 1 *Representation of the procedure followed for PBAT Poisson's ratio evaluation*

During the tests, the distances between two points aligned with the loading direction (L_X [mm]) and two points orthogonal to the loading direction (L_Y [mm]) were monitored. The longitudinal strain (ε_X [mm/mm], Equation 2.22) and transverse strain (ε_Y [mm/mm], Equation 2.23) were calculated using the formulas:

$$\varepsilon_X = \frac{L_{Xi}}{L_{Xi} - L_{X0}} \quad \text{(Equation 2.22)}$$

$$\varepsilon_Y = \frac{L_{Yi}}{L_{Yi} - L_{Y0}} \quad \text{(Equation 2.23)}$$

where "0" is the initial distance and "i" is the distance at any point during the test. Poisson's ratio was then calculated as the slope of the best-fit linear regression of the plot of $-\varepsilon_Y$ versus ε_X, considering data up to a longitudinal strain of approximately 0.08 mm/mm (Figure 2.2). This procedure was repeated for three specimens, yielding an average Poisson's ratio of 0.46 ± 0.01.

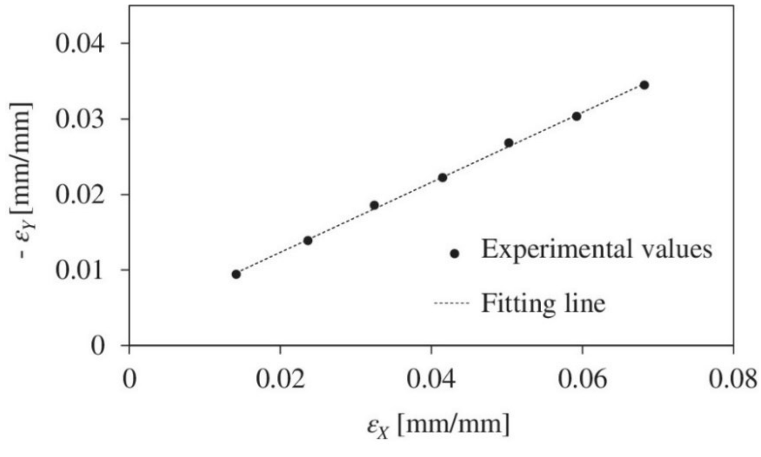

Figure 2.2 *Example of Poisson's ratio estimation from the longitudinal (ε_X) and transversal (ε_Y) strains*

Kerner's model

The modeling of Young's modulus was made applying generalized Kerner's model as proposed by Lewis and Nielsen[7] (Equation 2.9) to compare experimental values obtained from the mechanical analysis with predicted calculated values.

φ_f [adm] was calculated as in Equation 2.3, and ψ was calculated with Equation 2.8 considering φ_m equal to 0.632 (randomly close packed non-agglomerated spherical particles)[4].

Poisson's ratio υ had been experimentally calculated in the previous section to be 0.46 by means of DIC technique.

The moduli of the CPG and ZTC were experimentally calculated by Sglavo et al.[30] and by dynamic mechanical analysis (DMA), respectively.

Table 2.3 summarizes the values of the parameters used for the application of Kerner's model.

***Table 2.3** Values of material parameters used in Kerner's equation*

Parameter	Value	Method
E_m	92 MPa (PBAT+ZTC composites)	Experimental by UTT
	101.87 MPa (PBAT+CPG composites)	Experimental by UTT
$E_{p,ZTC}$	3900 MPa	Experimental by DMA
$E_{p,CPG}$	53.1 GPa	Experimental in literature[30]
ρ_m	1.26 g/cm^3	Tabulated in PBAT datasheet
$\rho_{f,ZTC}$	1.93 g/cm^3	Experimental by picnometric analysis
$\rho_{f,CPG}$	2.59 g/cm^3	Experimental in literature[30]
v	0.46	Experimental by DIC technique
φ_m	0.632	Tabulated in literature[4]

The values of $E_K'/E_{K,0}'$ calculated with Equation 2.9 were plotted against the volumetric fraction of the filler and overplotted with the experimental values of relative moduli, expressed as the ratio between the moduli of the composite and the matrix.

Pukánszky's model

Pukánszky's and modified Pukánszky's models were applied to analyze the trend of experimental tensile properties (σ_y and σ_B) in comparison with the calculated theoretical values[8] and to investigate the extension of the interphase interaction.

Pukanszky's model, Equation 2.11, was applied in its linearized form (Equation 2.12), so that in the semilogarithmic plot of $\log(\sigma_{y,rel})$ against φ_f, straight lines would be obtained. B value was therefore acquired as the slope of the fitting line.

Using the B value calculated for the yield stress, the modified Pukanszky's model was used for modeling the stress at break with Equation 2.21. Therefore, comparably to the yield stress, plotting $\log(\sigma_{B,T\,red})$ as a function of φ_f, a straight line was obtained, the slope of which gives the B_B value at break.

2.4.2 Particle size analysis

Particle size analysis for both CPG and ZTC particles was performed using a Mastersizer 3000 laser granulometer (Malvern Instruments Ltd., Malvern, UK). The analysis was performed in wet mode with water as the dispersion medium, using Mie theory for CPG particles and Fraunhofer theory for ZTC particles as the scattering models, respectively. The particles were dispersed in distilled water using the Hydro EV wet disperser at a stirring speed of 2700 rpm to ensure stable dispersion throughout the measurement period required to obtain approximately 30 replicates. The dimensional distribution of the particles was expressed using the standard percentiles D_{10} [µm], D_{50} [µm], and D_{90} [µm], which represent the particle sizes below which 10, 50, and 90% of the sample fall, in terms of volume density fraction. The mean particle size was expressed as the equivalent number of mean diameter, D_{mean} [µm].

2.4.3 Scanning Electron Microscopy (SEM) and Electron Dispersion Spectroscopy (EDS)

The microstructure of the composites at varying filler concentrations and the morphology of the CPG and ZTC powders were examined through Scanning Electron Microscopy (SEM). For SEM analysis, cross-sections of the injected samples were prepared by cutting the center portion with a sharp blade and fracturing it under cryogenic conditions for the CPG and ZTC composites, respectively. To confer conductivity upon the sample surfaces, an approximately 10 nm-thick gold layer was deposited onto the samples via sputtering. A field emission gun scanning electron microscope (FESEM, Nova NanoSEM 450, FEI Company, USA) was used for SEM characterization in backscattered electron mode to highlight compositional contrast. The imaging parameters included an accelerating voltage of 15 kV, a spot size of 4 (a.u.), and a working distance of approximately 6 mm.

Chemical elemental analysis was conducted with an Energy-Dispersive X-ray Spectroscopy (EDS) system, QUANTAX-200 (Bruker, Germany), which was equipped with a silicon drift detector (SDD) XFlash 6/10 that was integrated into the SEM setup.

2.4.4 Infrared spectroscopy

The Fourier-Transform Infrared (FT-IR) spectra were acquired to identify composite structural variations using the Perkin-Elmer Spectrum Two FT-IR spectrophotometer in attenuated total reflectance (ATR) mode with a diamond crystal plate. Each spectrum was taken on the cross-section of the injected samples, as the average of 16 scans, acquired in the range of 4000 – 400 cm^{-1} with a resolution of 4 cm^{-1}.

2.4.5 Differential Scanning Calorimetry (DSC)

The thermal parameters of the composites, including the glass transition temperature ($T_{g,DSC}$ [°C]), the melting temperature (T_m [°C]), and the crystallization temperature (T_c [°C]), were determined through Differential Scanning Calorimetry (DSC) analysis. Samples of composite materials with a mass of between 10 and 20 mg were subjected to analysis.

The PBAT-CPG composites were subjected to analysis using a Perkin Elmer DSC6000 (PerkinElmer, USA). A heating scan was conducted in the temperature range of -60 to 200 °C at a rate of 10 °C/min, followed by a cooling scan from 200 to 0 °C at the same rate.

The thermal parameters of PBAT-ZTC composites were determined using a DSC Q200 (TA Instruments, USA). The heating scan was conducted in the temperature range between -65 and 180 °C at a rate of 5 °C/min, followed by a cooling scan from 180 °C to 0 °C at the same rate.

2.4.6 Thermo-Gravimetric Analysis (TGA)

Thermo-Gravimetric Analyses (TGA) were conducted on PBAT-CPG using a Perkin Elmer TGA8000. The samples, with masses ranging from 10 to 20 mg, were heated from 30 to 600 °C at a heating rate of 10 °C/min in an N_2 atmosphere. The results are presented as the percentage change in sample weight as a function of temperature. The degradation temperature (T_{deg} [°C]) was calculated as the inflection point of the curve. The onset (T_{onset} [°C]) of the degradation curve was calculated as the intersection of the fitting lines of the initial plateau and the linear part of the degradation step.

2.4.7 Dynamic-Mechanical Analysis (DMA)

The viscoelastic properties of the materials were investigated using Dynamic-Mechanical Analysis (DMA - TA 800Q DMA, TA Instruments, USA) on rectangular specimens (dimensions 5 × 2 × 30 mm^3), obtained from injection-molded models. Dynamic storage (E' [MPa]) and loss (E'' [MPa]) moduli were measured from −55 to 60 °C with a temperature ramp of 3 °C/min allowing for a soaking time of 15 minutes once the starting temperature was reached. A sinusoidal strain of 10 µm and a frequency of 1 Hz were set, with a single cantilever clamp. The damping factor was obtained as the ratio between E'' and E', ($Tan\delta = E''/E'$) as a function of temperature[31,32]. The glass transition temperature ($T_{g,DMA}$ [°C]) for each composite was calculated as the temperature corresponding to the peak of the $Tan\delta$ curve[33]. Each composite material was tested in triplicate.

2.4.8 Creep Test

Additionally, the creep curves of pristine and filled PBAT-based composites were acquired in the creep experiments. The compliance, $J(t)$ [$\mu m^2/N$], was obtained from the ratio between the experimental strain ($\varepsilon(t)$) and the constant applied stress (σ_0=0.2 MPa)[34], according to Equation 2.24

$$J(t) = \frac{\varepsilon(t)}{\sigma_0} = \frac{\varepsilon(t)}{0.2 \cdot 10^6 Pa} \qquad \text{(Equation 2.24)}$$

The results were expressed as a function of the test time (10 min) at a fixed temperature (isothermal steps of 10 °C in the thermal range between −10 and 60 °C).

$J(t)$ of polymer materials can be modeled using the Burgers' model, which is a combination of Maxwell's and Kelvin-Voigt's elements[35,36]. As postulated by the Burgers model, creep compliance can be described by three discrete phases. The initial phase is the instantaneous elastic response ($J_1(t)$), the intermediate phase is the delayed elastic response ($J_2(t)$), and the final phase is the viscous flow ($J_3(t)$), as mathematically described in Equation 2.25

$$J(t) = J_1(t) + J_2(t) + J_3(t) = \frac{\sigma_0}{E_1} + \frac{\sigma_0}{E_2}\left(1 - e^{-\frac{t}{\tau}}\right) + \frac{\sigma_0}{\eta_1} t \qquad \text{(Equation 2.25)}$$

where E_1 = Maxwell's spring constant, E_2 = Kelvin-Voigt's spring constant, η_1 = viscosity of Maxwell's dashpots, and $\tau = \eta_2/E_2$ = characteristic relaxation time, i.e., the time required to generate 63.2% of deformation in the Kelvin-Voigt's units, with η_2 = viscosity of Kelvin-Voigt's dashpots.

To predict the behavior of the ZTC composite material under prolonged stress conditions, the time-temperature superposition (TTS) principle was also employed. This involved the generation of master curves at the reference temperature of 20 °C[37].

2.4.9 Fused deposition modeling (FDM) 3D printing

The extruded filaments of pure and ZTC-loaded PBAT were employed for Fused Deposition Modeling (FDM) 3D printing (BQ Hephestos 2) of two types of objects: a scaffold representing complex geometry and a ring, designed to macroscopically demonstrate the variations and customization in mechanical behavior that result from different composite material compositions. The temperature of the printing head was maintained at a range of 150 to 170 °C, with a printing speed of 20 mm/s. A nozzle with an extrusion diameter of 0.6 mm was utilized to print a layer height of 0.2 mm. The scaffolds were designed with a cylindrical geometry, measuring 20 mm in diameter and height. They were printed with a 45% fill density and a grid infill pattern, with adjacent layers offset by an angle of 90°. The scaffold walls were constructed with a width of three concentric shells, with an overlap of 50%. The rings had a diameter of 25 mm and a height of 3 mm, achieved by depositing three concentric shells overlapped by 50%. Additionally, a ring made of commercial polylactic acid (PLA) (Raised3D Premium filament) was printed alongside pure PBAT and various PBAT-ZTC composites for comparative purposes. All parameters were kept the same, except for the printing temperature, set at 215 °C. A six-loop brim was utilized as a platform to enhance the object adhesion to the printing plate.

2.4.10 Biocompatibility test

Human dermal fibroblasts (HDFs) were seeded in a 6-well plate at a density of 5×10^4 cells/mL in RPMI-1640 medium (Gibco, Life Technologies, Canada) supplemented with 10% fetal bovine serum (FBS), 2 mM L-glutamine, 100 U/mL penicillin, and 100 µg/mL streptomycin (Gibco, Life Technologies, Canada). The cells were maintained at 37 °C in a humidified atmosphere with 5% CO_2 to ensure optimal conditions for cell growth. Once the cells had attached, they were treated with sterile particles (2.5 mg/mL) of ZTC, PBAT, and the PBAT-based composites with varying ZTC content for 24, 48, and 96 hours. Images of the cells were obtained using the Axiovert 200 transmitted light microscope (TLM) (Carl Zeiss, Gottingen, Germany) at 10× magnification.

The viability of the cells was evaluated through the utilization of the CellTiter-Glo luminescent cell viability assay (Promega, USA), which quantifies adenosine triphosphate (ATP) to ascertain the presence of viable, metabolically active cells. In brief, HDFs were seeded in a 96-well plate at a density of 5×10^4 cells/mL and allowed to attach. On the subsequent day, the cells were treated with ZTC, PBAT, and PBAT-based composites in accordance with the previously specified conditions. The total ATP content of viable cells was determined following the CellTiter-Glo assay protocol at 24 and 48 hours. The luminescent signal was quantified using the EnSpire multimode plate reader (PerkinElmer, USA). The cell viability of treated cells was expressed as a percentage of the viability of the untreated control cells (CTRL). All data were subjected to statistical analysis using one-way analysis of variance (ANOVA) to ascertain any significant differences in variability among the multiple groups. Statistical significance was determined at a P-value < 0.01, with the significance level $\alpha = 0.01$ and a two-sided confidence interval.

2.5 Results and discussion

2.5.1 Tensile test and modeling

Figure 2.3 a-d illustrates the specimens of the various composites produced by IM, both prior to (a, c) and following (b, d) the tensile tests. In the case of PBAT-CPG, the specimens appearance remained largely unaltered as the percentage of filler increased. In contrast, the incorporation of ZTC had a discernible impact on the PBAT-ZTC composites, becoming evident even during the polymer-chloroform solution casting process. The introduction of ZTC resulted in a notable change in the visual appearance of the PBAT, which transitioned from a semi-transparent white to an opaque cream-white hue, even at the lowest concentration of filler.

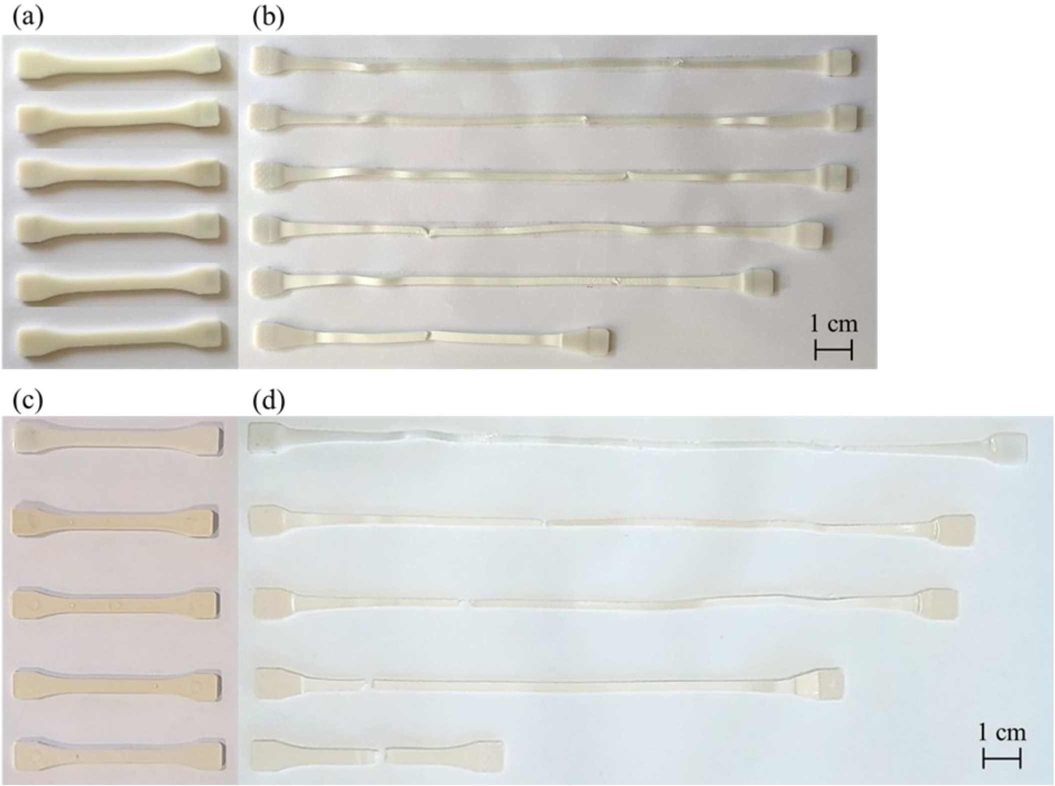

Figure 2.3 *Specimens 1BA obtained by injection molding, before (a and c), and after (b and d) tensile test. (a) and (b) from top to bottom: PBAT, PBAT+2% CPG, PBAT+4% CPG, PBAT+10% CPG, PBAT+20% CPG, PBAT+40% CPG. (c) and (d) from top to bottom: PBAT, PBAT+5% ZTC, PBAT+10% ZTC, PBAT+20% ZTC, and PBAT+40% ZTC*

The stress-strain curves PBAT and PBAT-based composites are typical of a flexible tough polymer material with a yield point and are shown in Figure 2.4. A color scale will be adopted in which a darker shade corresponds to a more loaded composite.

Three distinct phases can be defined in the tensile curves of the materials. The initial linear phase is attributable to elastic deformation and culminates in a peak corresponding to the formation of a central neck in the specimen, denoting the onset of plastic deformation. Following the yielding point, a second zone of plastic deformation occurs, in which the stress remains relatively constant. This corresponds to the propagation of necking along the entire central section of the specimen, due to the alignment of polymer chains along the tensile axis, up to the gripping areas. Ultimately, an escalation in stress levels is observed until the specimen reaches its failure point. The only composition that exhibited anomalous behavior was PBAT+40% ZTC, which displayed greater brittleness than the other materials. It failed after reaching the yield point and exhibited no plastic deformation.

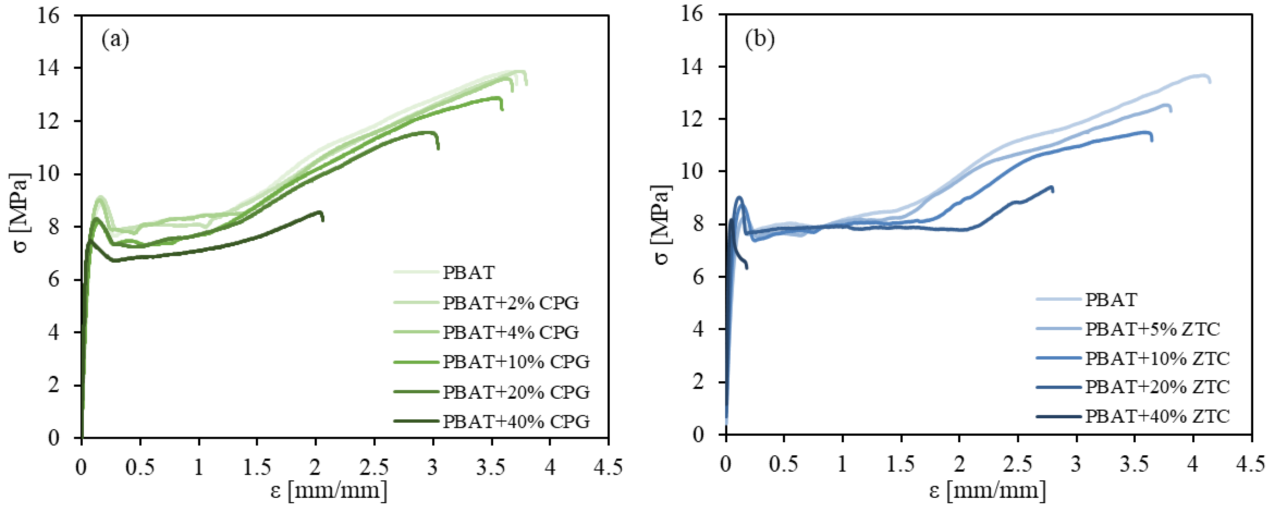

***Figure 2.4** Stress-strain curves of PBAT+CPG (a.) and PBAT+ZTC (b.) composites*

As the concentration of CPG increases, an increase in E is observed up to 82%, with a reduction of 20, 46, 54, and 72% in σ_y, σ_B, ε_B, and T, respectively. Similarly, the ZTC addition has been observed to exhibit a reinforcing effect with respect to both E and, most notably, σ_y. Specifically, an increase in filler content has been observed to result in increments of up to 44 and 10% for E and σy, respectively. Conversely, an overall reduction of 27, 33, and 42% was observed for σ_B, ε_B, and T, respectively.

The observed increase in E in both composites can be attributed to the addition of a stiffer component in relation to the matrix (reference to E_p and E_m can be found in Table 2.3). As is typical of polymer-based microcomposites, the incorporation of microfillers has been observed to increase the elastic modulus in comparison to the neat polymer. This improvement, observed in biocomposite samples[38,39], can be attributed to the formation of an interphase layer around the nanoparticles, which facilitates stress transfer at the interface. Moreover, the particles impede the mobility and deformation of the polymer matrix by introducing a mechanical restraint[40].

The numerical values of the aforementioned parameters are presented in Table 2.4.

***Table 2.4** Values of mechanical parameters collected from tensile test for PBAT-CPG and PBAT-ZTC composites*

	E [MPa]	**σ_y [MPa]**	**σ_B [MPa]**	**ε_B [mm/mm]**	**T [MJ/m^3]**
PBAT	102 ±25	8.9 ±0.5	14 ±1.0	3.8± 0.5	41.2± 6.5
PBAT+2% CPG	104 ± 19	9 ±0.2	13.9 ±0.2	3.8± 0.1	40.9 ±1.8
PBAT+4% CPG	109 ± 17	8.8± 0.4	13.7 ±0.6	3.8 ±0.2	39.8 ±3.1
PBAT+10% CPG	123 ±17	8.4 ±0.2	12.7 ±0.4	3.4 ±0.2	35.1 ±2.7
PBAT+20% CPG	138 ±21	8.3 ±0.3	11.3± 0.7	2.9 ±0.3	26.0 ±3.6
PBAT+40% CPG	186 ±36	7.2 ±0.2	7.6± 0.6	1.7 ±0.2	11.7± 1.9

	E [MPa]	**σ_y [MPa]**	**σ_B [MPa]**	**ε_B [mm/mm]**	**T [MJ/m^3]**
PBAT	126 ± 12	8.2 ± 0.2	13.1 ± 0.9	3.9 ± 0.5	36 ± 7
PBAT+5% ZTC	131 ± 10	8.4 ± 0.2	12.2 ± 0.6	3.6 ± 0.3	35 ± 4
PBAT+10% ZTC	149 ± 4	8.7 ± 0.2	11.4 ± 0.2	3.4 ± 0.2	32 ± 3
PBAT+20% ZTC	186 ± 11	9.0 ± 0.1	9.5 ± 0.5	2.6 ± 0.2	21 ± 2
PBAT+40% ZTC	350 ± 26	8.1 ± 0.3	5 ± 0.9	0.16 ± 0.03	1.2 ± 0.1

Due to the inferior toughness of PBAT+40% ZTC, leading to σ_B and ε_B that can be considered outside the trend, compared to the other composites, this composition was excluded from the theoretical modeling, discussed in the next paragraph, because too much deviation from linearity would have been observed in the theoretical tensile strength values.

Kerner's model

The stiffening effect provided by filler particles can be modeled by considering the theoretical approaches developed by the generalized Kerner's model for composites. E increase can be predicted for traditional micro-composites filled with homogeneously dispersed spherical particles by applying Nielsen-Lewis' formulation of Kerner's equation (Equation 2.9).

According to this model, composite modulus does not explicitly depend on the particle size and particle size distribution. Both these parameters and the effect of surface treatment affect the model previsions only indirectly through φ_m.

In Figure 2.5, the experimental moduli, expressed as the ratio between the composite (E_K') and the neat polymer ($E_{K,0}$') values, are compared to the theoretical predicted values.

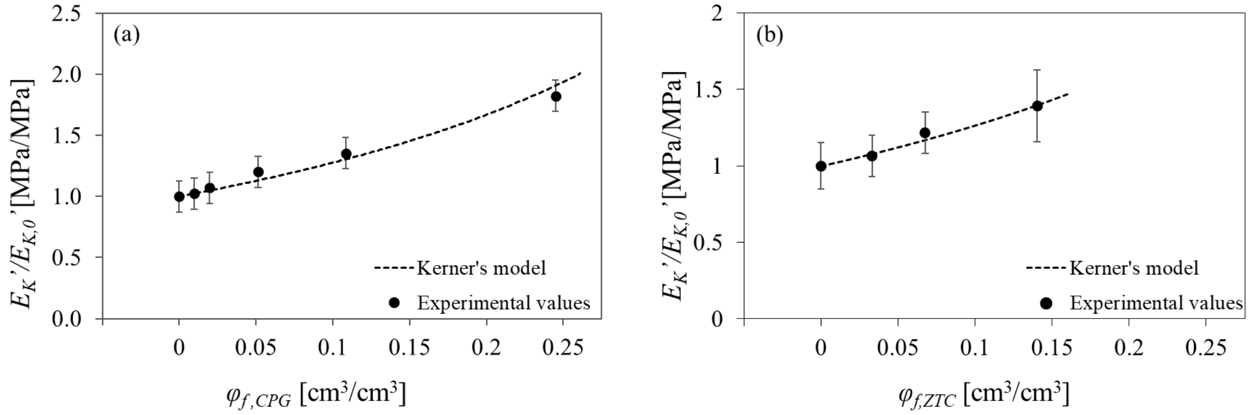

***Figure 2.5** Comparison between experimental Young's moduli and the corresponding theoretical values calculated with Kerner's model for (a) PBAT-CPG and (b) PBAT-ZTC composites*

The stiffening effect of CPG particles is in good agreement with the theoretical prediction based on the modified Kerner's equation, also at high CPG amounts. Very good correspondence is also found between theoretical and experimental values of ZTC composites, even at high ZTC concentrations, excluding, as explained in the previous paragraph, the concentration at 40% ZTC.

Usually, in composites filled with traditional micro fillers (chalk, calcium carbonate), the increase of the composite elastic modulus is generally associated with the decrease of the yield stress, because fillers decrease the effective cross-section of the matrix that carries the load during the deformation[41]. It is possible for deviations from Kerner's prediction to occur when the filler behaves as a network point, thereby increasing the composite cross-linking. This results in higher relative modulus values than those predicted by Kerner's model[42]. In such instances, more precise projections have been documented through the application of Halpin-Tsai's equation (Equation (2.2)). As the parameter ξ increases, the discrepancy between experimental and predicted data tends to diminish[43]. The reinforcing effect is largely determined by the intrinsic properties of both the filler and the matrix. The incorporation of a rigid filler into a flexible matrix, such as elastomers, results in enhanced stiffness and strength, thereby achieving greater reinforcement[10]. Conversely, when added to a stiffer matrix, the reinforcement effect is less pronounced[8]. A key objective in composite design is to obtain the best balance between reducing the cost of the original matrix and optimizing mechanical properties.

Pukánszky's model

To predict and analyze the yield stress, an attempt has been made to apply the Pukánszky model (Equation 2.11), considered the effective load-bearing cross section, as well as the influence of interfacial interaction and interphase formation through the *B* parameter. This parameter reflects the relative strength of the components, especially the interaction between the filler and the polymer matrix[10].

Figure 2.6 shows the relative tensile stress at yield ($\sigma_{y,rel}$) values for PBAT composites as a function of φ_f, according to equation 2.12, with a linear fit line that gives a B_y value of 2.30 ± 0.08 and 4.06 ± 0.12 for CPG and ZTC composites, respectively.

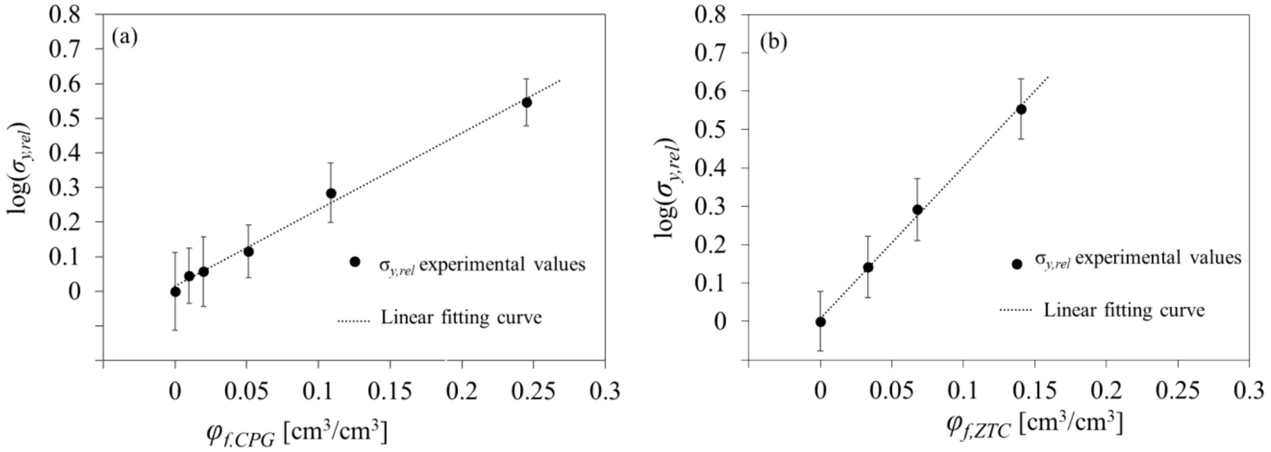

Figure 2.6 *Relative tensile stress at yield $\sigma_{y,rel}$, calculated according to Pukaszky's model, as a function of the filler volumetric fraction for (a) PBAT-CPG and (b) PBAT-ZTC composites*

B values for polymer-based micro- and nanocomposites typically range from 2 to 15[17,44,45]. The values obtained are therefore indicative of the formation of a positive interaction at the interphase between filler and matrix and are consistent with those observed for traditional rigid fillers[8]. To give some notable examples, recent studies have reported B values of 2.10 for PLA filled with hemp particle waste and 2.19 and 3.32 for PHBH and poly(3-hydroxybutyrate-co-3-hydroxyvalerate) (PHBV) filled with wine lees waste, respectively[46].

A low B value implies a weak interaction between matrix and filler, which affects the load-bearing capacity and mechanical performance of the composite as the filler content increases. In practice, the stresses would occur primarily in the matrix, which represents a progressively smaller percentage of the composite. Conversely, higher B values indicate stronger interphase adhesion, resulting in improved stress transfer from the matrix to the particles and improved mechanical performance[18].

In some cases, deviations from linearity occur due to structural effects such as filler aggregation, which reduces the interfacial area and negatively affects the phase interaction. This can even lead to negative B values[8,23,47].

The dependence of tensile strength at break, which typically decreases as filler content increases[48], closely mirrors that of yield characteristics.

Although fewer models are available for predicting ultimate properties compared to yield stress, Pukánszky's models for yield properties can also be applied to strength at break by incorporating true tensile strength to account for changes in specimen cross-section (Equation 2.14)[6].

The strain-hardening tendency of the polymer, represented by the parameter n, is derived experimentally from the true PBAT stress-strain curve, calculated as $\sigma_{B,T} = \sigma \cdot \lambda$, as illustrated in Figure 2.7. n was calculated considering the slope of a linear fit applied to the end section of the true curves, for $\log(\lambda) > 0.4$ and $\log(\lambda) > 0.5$ and obtaining $n_{CPG}= 1.703$ and $n_{ZTC}=1.588$, for PBAT-CPG and PBAT-ZTC composites, respectively.

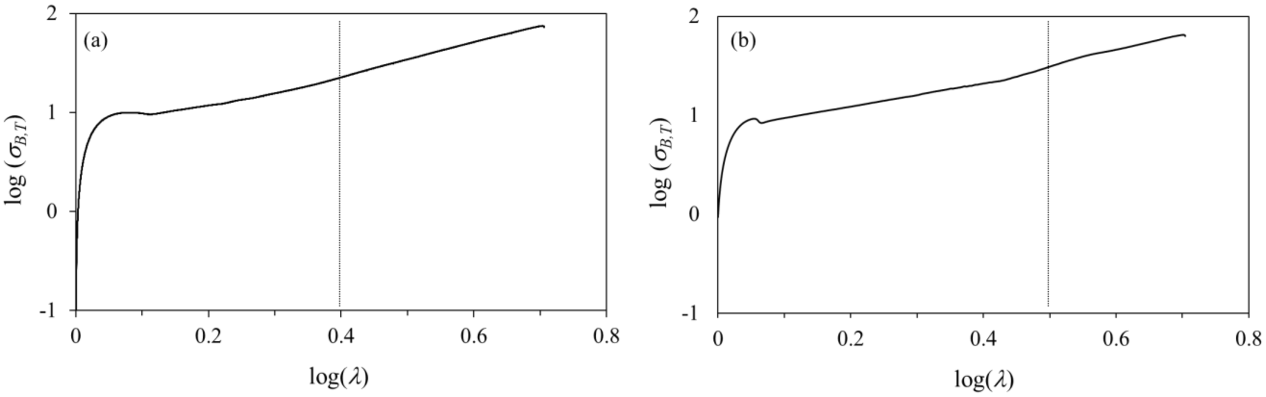

Figure 2.7 *True tensile curve of PBAT for (a) CPG composites and (b) ZTC composites*

A comprehensive examination of the overlapped true stress-elongation (σ-λ) curves of all PBAT-ZTC composites, comparable to the stress-strain curves illustrated in Figure 2.8, reveals a notable variation in the yielding region, accompanied by a reduction in tensile strength at failure. In particular, the materials display failure at lower σ_B and T values and corresponding elongation, with increasing filler.

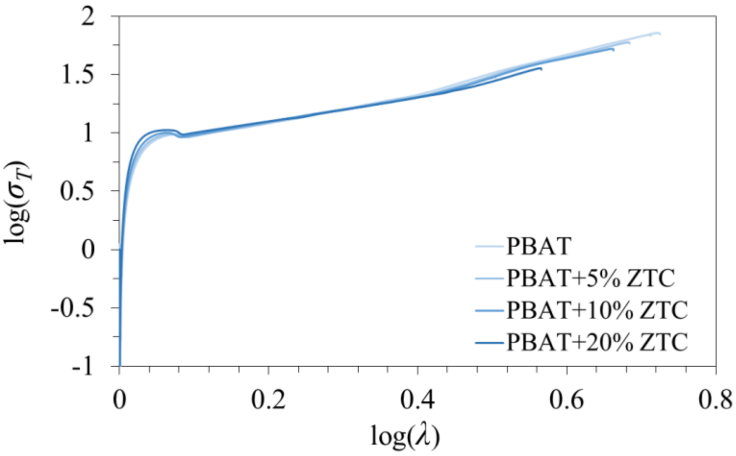

Figure 2.8 *True tensile curves of PBAT-ZTC composites*

The correlation utilized to define factor B_B for stress at break is analogous to the one employed for yield stress[10]. The value of factor B_B is obtained by calculating the slope of the linear fit of the theoretical data.

Regarding PBAT-CPG composites, a value of B_B = 2.25±0,04 was obtained (Figure 2.9a), that can be considered equivalent to B_y obtained for the modeling of yield stress, therefore its value was used in modified Pukanszky's model. Figure 2.9b depicts the experimental values of $\sigma_{B,T,red}$, as expressed in Equation (2.20), plotted on a semilogarithmic scale. A notable concordance is observed between the experimentally derived values and the theoretical model, with the latter exhibiting minimal discrepancy and falling within the experimental standard deviation.

The slope of the fitting line for $\sigma_{B,T}$ of PBAT-ZTC composites (Figure 2.10) gives a lower value of B_B compared to that obtained from the relative yield stress fitting, equal to 2.23 ± 0.12. Nevertheless, this value falls within the range indicating a good interfacial interaction[49]. However, the motivation for the different values of the adhesion parameter when applying Pukánszky's model to σ_y and $\sigma_{B,T}$ is not entirely clear.

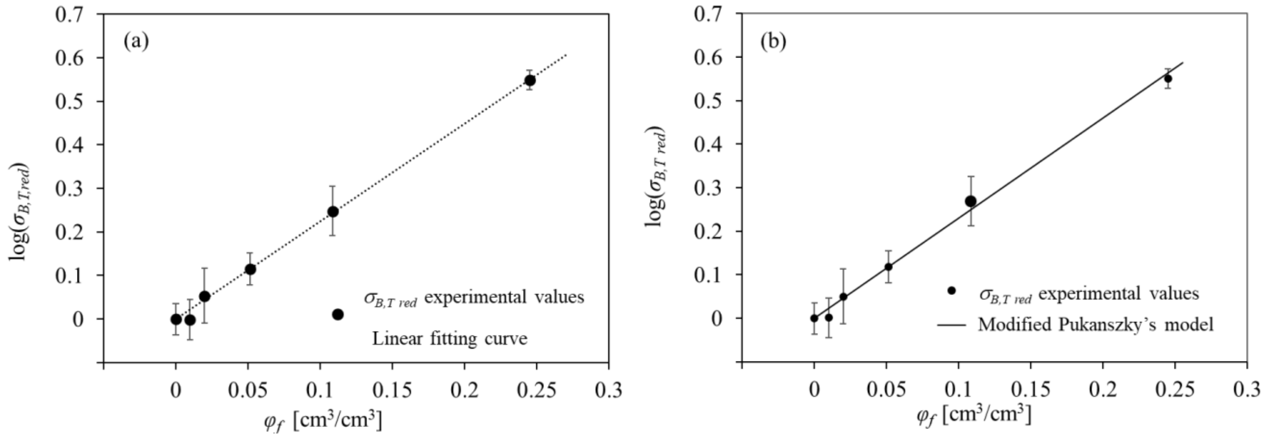

***Figure 2.9** (a) Relative tensile strength at break $\sigma_{B,T,red}$ calculated according to Pukanskzy's modified model as a function of volumetric CPG fraction with linear fit and (b) comparison between experimental reduced stress at beak and the corresponding theoretical values calculated with the modified Pukanszky's model*

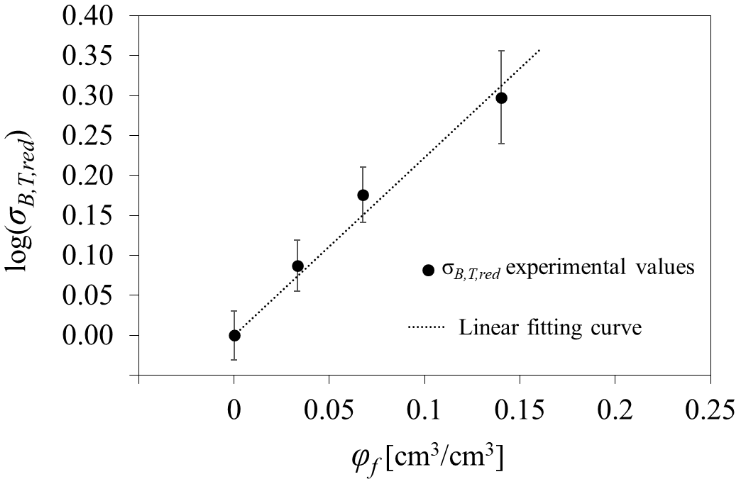

***Figure 2.10** Relative tensile strength at break $\sigma_{B,T,red}$ calculated according to Pukanskzy's modified model as a function of volumetric ZTC fraction with linear fit*

For comparison, the B_B value for PLA filled with natural fibers was found to be 2.29[17], while the B_B values for PP filled with carbon fibers, glass fibers, and wood flour were 4.45, 4.64, and 3.13, respectively[50]. These values are closer to the B-value obtained for yield stress in this study.

However, it's important to note that the true σ-ε curves (Figure 2.8) generally show a consistent trend with increasing filler content, where the deformation at failure decreases due to the increased stiffness of the composite. This behavior is not as evident in the engineered *σ-ε* curves (Figure 2.4b), where σ_B appears to vary significantly at a given *ε*. Increasing the *B* value can be achieved by addressing factors that influence the interfacial interaction, defined in Equation (2.13), such as lower particle dimensions or particle surface treatments, as discussed in Chapter 2.2.

2.5.2 SEM and EDS characterization

SEM and EDS characterization of the composites reveal key insights into their microstructural morphology, which is critical in supporting the observed mechanical properties.

The images reported refer to the specimen cross-section obtained by brittle fracture under cryogenic conditions. Since the images are taken using backscattered electrons, the dark gray background corresponds to the carbon-based polymer matrix, while the lighter particles that create high contrast correspond to the filler particles, that have heavier atomic weights.

Figure 2.11 depicts composites with varying CPG content. The images illustrate the homogeneous dispersion and distribution of filler particles in the matrix, exhibiting no aggregation or phase separation, even at elevated filler concentrations. Additionally, there are no voids at the interface, indicating favorable surface wettability and compatibility of the CPG particles with the polymer.

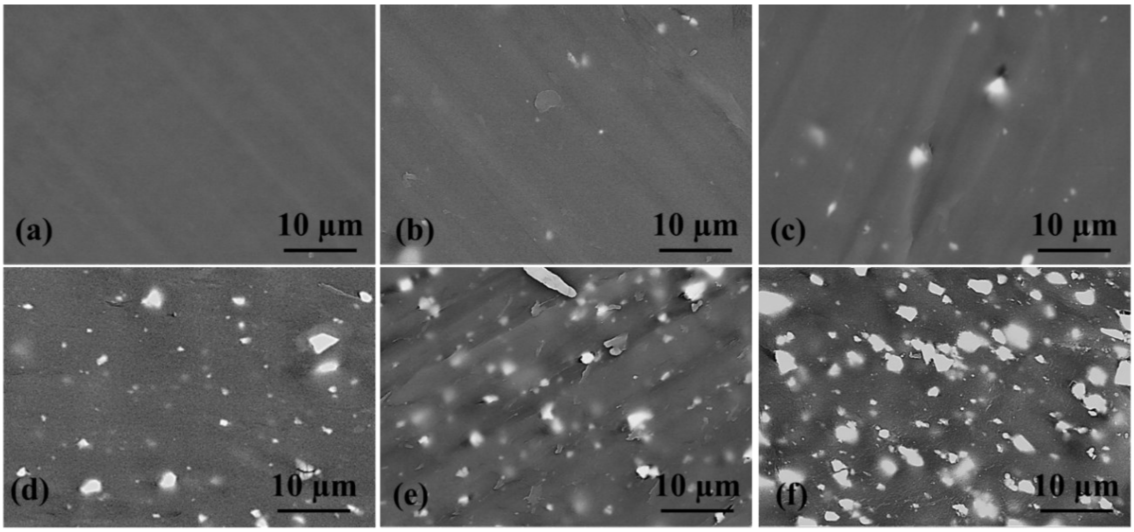

Figure 2.11 *SEM images of (a) PBAT, (b) PBAT+2% CPG, (c) PBAT+4% CPG, (d) PBAT+10% CPG, (e) PBAT+20% CPG, (f) PBAT+40% CPG*

The CPG particles exhibit irregular geometry, generally smaller than 35 µm, with particle size measurements confirming an average size D_{mean} of 13.2 ± 0.1 µm and D_{10}, D_{50}, and D_{90} values of 1.44 ± 0.03, 7.94 ± 0.14, and 35.6 ± 0.3 µm, respectively (Figure 2.12).

Similarly, Figure 2.13 shows the microstructure of PBAT and PBAT-ZTC composites, with homogeneous dispersion of the filler within the matrix.

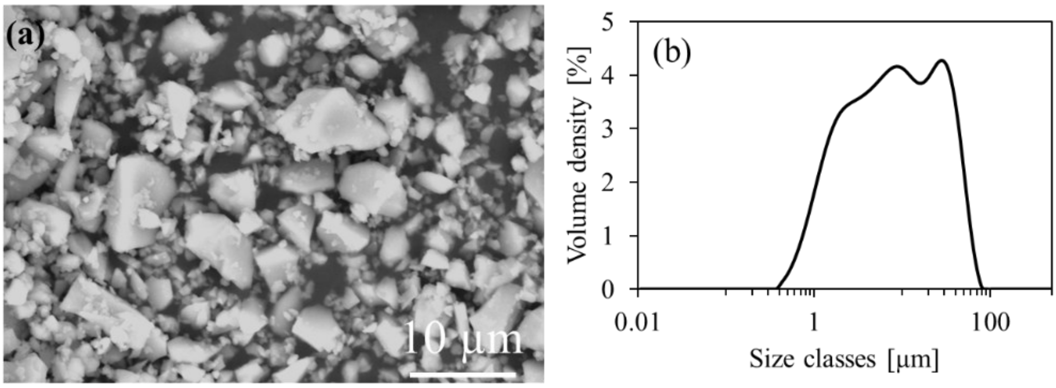

Figure 2.12 *SEM picture of (a) CPG particles and (b) their size distribution*

The absence of a clear boundary around the particles and the gradual transitions in shades of gray (Figure 2.13(e)) suggest the solid adhesion at the PBAT-ZTC interface, confirming the formation of an interface between the filler and matrix with an effective reinforcement provided by the filler. This observation is consistent with the notion of strong filler-matrix interactions, which are known to enhance the composite's viscoelastic properties.

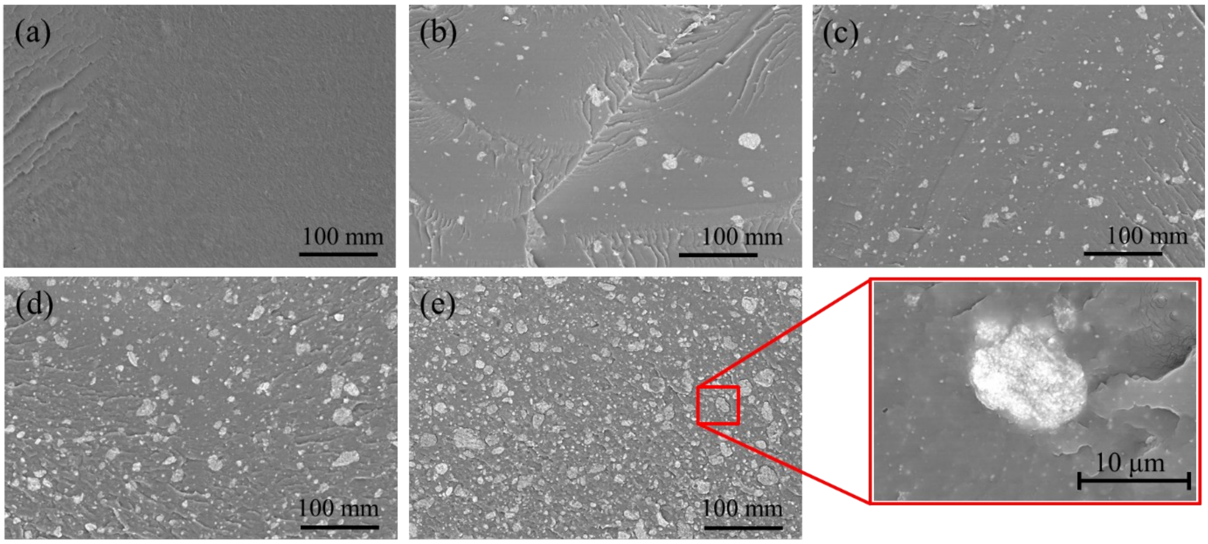

Figure 2.13 *SEM images of (a) PBAT, (b) PBAT+5% ZTC, (c) PBAT+10% ZTC, (d)PBAT+20% ZTC, (e) PBAT+40% ZTC. The inset reports the detail of the filler-matrix interface*

Following grinding and sieving, the ZTC particles exhibit an irregular geometry and are composed of smaller particle aggregates, presumed to be TiO_2 bound together by the zein protein matrix. This results in the particles exhibiting a rough, wrinkled surface (Figure 2.14(b)). The average size is less than 30 μm (Figure 2.14(a)), with a size distribution characterized by D_{10}, D_{50}, D_{90}, and D_{mean} equal to 0.7 ± 0.1, 10.7 ± 0.5, 29 ± 3, and 13 ± 1, respectively (Figure 2.14(c)).

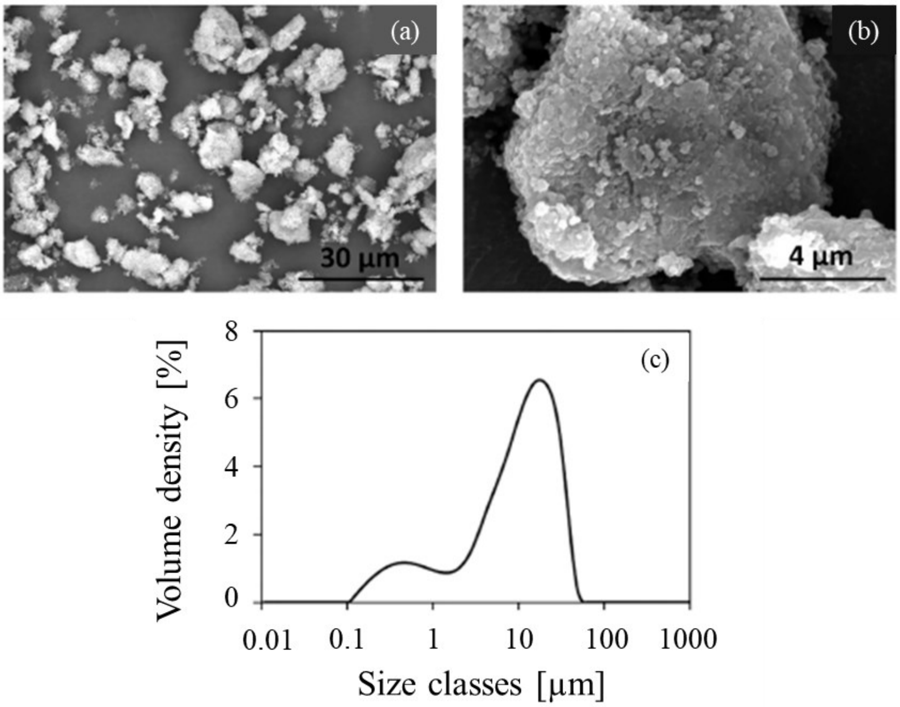

Figure 2.14 *(a,b) SEM picture of ZTC particles at different magnifications and (c) their size distribution*

The material composition is corroborated by the elemental analysis presented in Figure 2.15. The stacked spectra, which represent the pure matrix and increasing filler content, are reported for both PBAT-CPG (Figure 2.15a) and PBAT-ZTC (Figure 2.15b) composites. Spectra of pure fillers are reported as well in the respective graphs.

From the comparative analysis of the spectra, it can be observed that an increase in filler content has an impact on the intensity of the characteristic peaks associated with pure PBAT. Specifically, the intensity of the carbon (C) peak decreases, while the peaks associated with CPG elements (P, Ca, Na, K, Al, and Si), and titanium (Ti) increase as the CPG and ZTC percentages in the composite increase. Furthermore, a nitrogen (N) peak is discernible in the PBAT+40% ZTC sample, highlighted in the inset in Figure 2.15b. Whereas no notable alteration in the oxygen (O) peak is evident, likely due to the compensation between the polymer matrix and the combined glass and ZTC content.

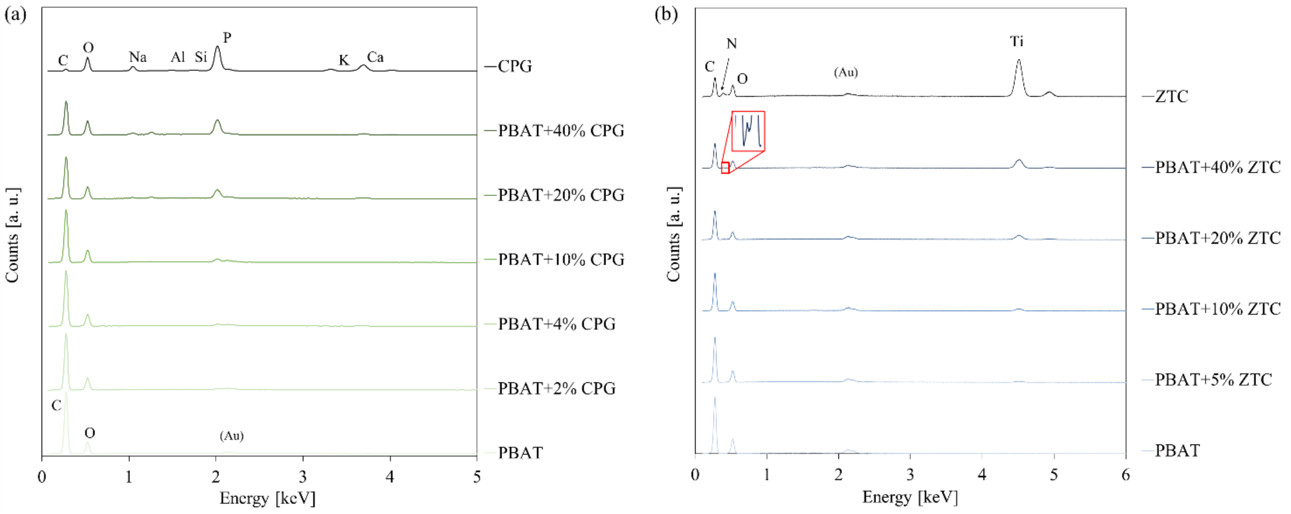

Figure 2.15 *EDS spectra of (a) CPG and PBAT-CPG composites and (b) ZTC and PBAT-ZTC composites. The inset highlights the peak relative to N*

2.5.3 FT-IR characterization

To gain insight into the structure of the polymer matrix and any potential modifications resulting from interactions between the polymer chains and filler particles, Figures 2.16a and 2.16b present the FT-IR spectra of PBAT-CPG and PBAT-ZTC composites, respectively, at varying filler concentrations and alongside pure filler powder. Table 2.5 summarizes the characteristic peaks for PBAT, CPG, and ZTC[51-53].

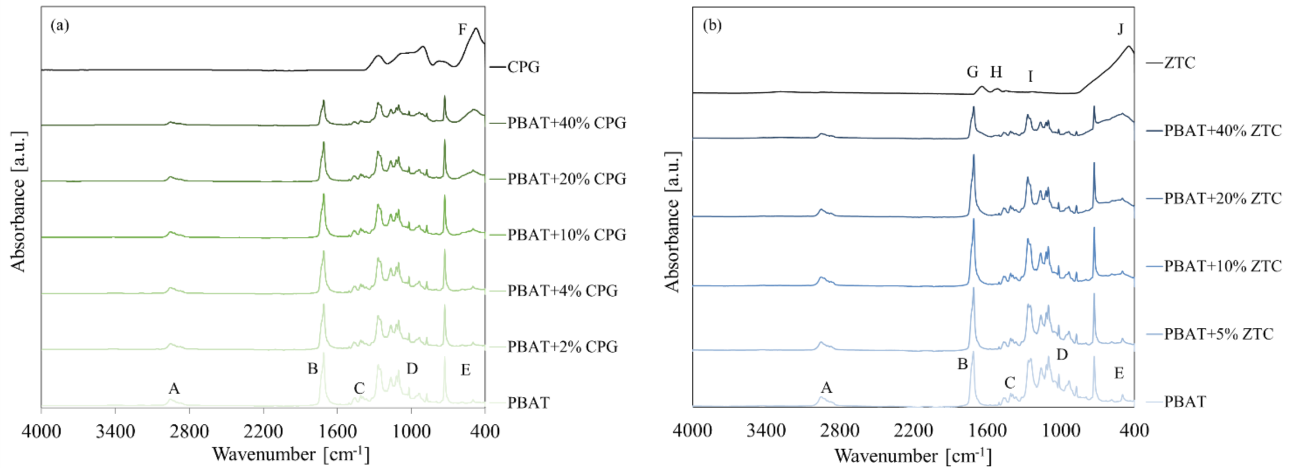

Figure 2.16 *FT-IR spectra of CPG and PBAT-CPG (a) and ZTC and PBAT-ZTC (b) composites*

***Table 2.5** Characteristic wavenumbers of FT-IR peaks for PBAT composites, CPG and ZTC fillers*

Peak	Wavenumber	Description
A	2800–2900 cm^{-1}	Symmetric and asymmetric stretching of methylene (–CH_2–) group in adipate and 1,4-butanedienol units
B	1714 cm^{-1}	Stretching of the carbonyl (C═O) group in the adipate and terephthalate units
C	1578–1453 cm^{-1}	Stretching of the double bonds (C═C) in the aromatic ring of terephthalate unit
D	1300–1000 cm^{-1}	(O=)C−O− symmetric and asymmetric stretching in the adipate and terephthalate units
E	725 cm^{-1}	Out-of-plane =C–H bending in the aromatic ring of terephthalate unit
F	520 cm^{-1}	Bending vibration of P–O bond (CPG)
G	1644 cm^{-1}	Amide I of zein protein
H	1516 cm^{-1}	Amide II of zein protein
I	1233 cm^{-1}	amide III of zein protein
J	446 cm^{-1}	Ti−O−Ti stretching in the TiO_2 network

In the case of PBAT-CPG (Figure 2.16a), the characteristic band at 1714 cm^{-1} of the carbonyl functional groups exhibits a shoulder to the main peak, present at higher wavenumbers. The observed blue shift can be attributed to the carbonyl portion of the adipate ester group, which does not exhibit a conjugative effect, differently the terephthalic unit between the phenylene and carbonyl groups, which does exhibit a conjugative effect[54].

Furthermore, the terephthalate unit exhibits a strong peak resulting from the out-of-plane deformation of the aromatic ring, which is not situated at its conventional position for para-substituted aromatics. Instead, it is observed at slightly lower wavenumbers, approximately 725 cm^{-1}. This shift is likely due to an interaction between the ester group and the aromatic ring.[55] Spectroscopic evidence shows that as the glass concentration increases, there is a general decrement in the intensity of the PBAT absorption peaks, accompanied by an increase in the CPG band at 520 cm^{-1}. No significant structural changes are observed as a result of possible interactions between the CPG and the polymer matrix.

A different behavior is observed regarding PBAT-ZTC composites. In the ZTC spectrum (top spectrum in Figure 2.16(b)), characteristic bands at wavenumbers of 1644, 1516, 1233, and 446 cm^{-1} can be identified. About the zein structure, the band observed at 1644 cm^{-1} (amide I) can be attributed to C=O stretching. In contrast, the bands at 1516 cm^{-1} (amide II) and 1233 cm^{-1} (amide III) cannot be ascribed to the motion of individual bonds, as they are representative of the combined effects of C–N stretching and N–H in-plane deformation[56,57]. The absorption bands observed in this spectrum are consistent with those typically observed in proteins and polypeptides[58], related to some normal modes of the peptide group, specifically the −C(O)−N(H)− moiety. The broad band exhibiting a peak at 446 cm^{-1} is attributed to Ti−O−Ti stretching within the TiO_2 network[59,60].

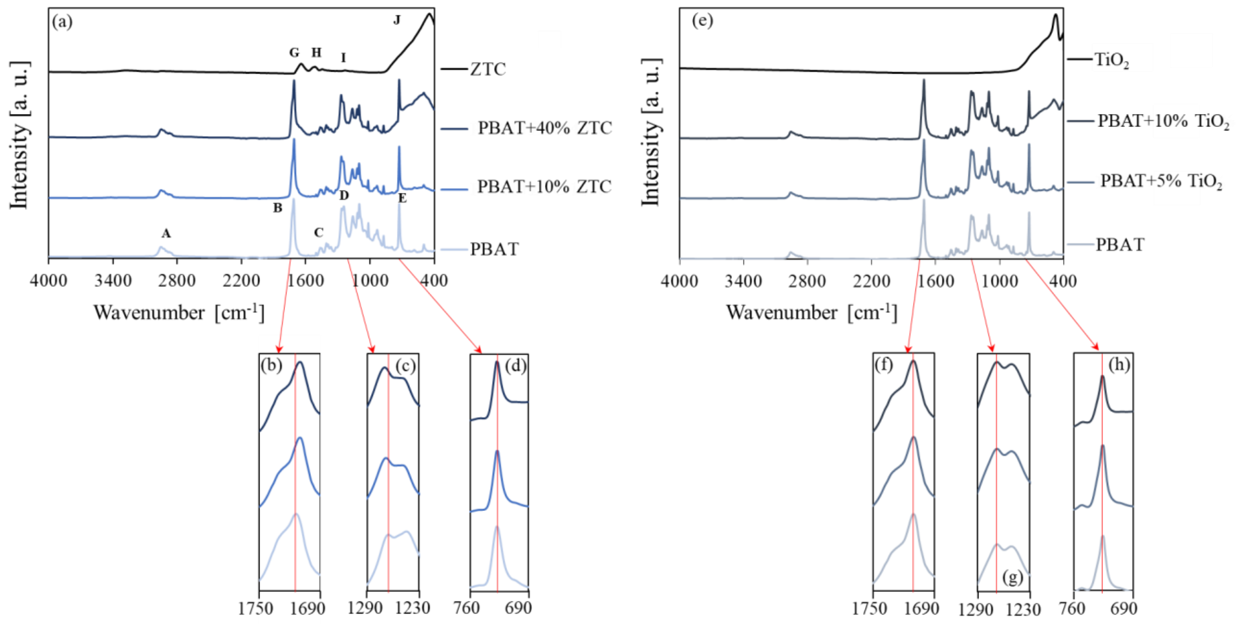

Figure 2.17 *IR spectra of pristine PBAT, PBAT+10% ZTC, and PBAT+40% ZTC composites as representative samples and ZTC powder (a). In the insets (b), (c), and (d), the exact position of some characteristic peaks for pristine PBAT and PBAT-ZTC composites is highlighted. IR spectra of pristine PBAT, PBAT+5%* TiO_2*, and PBAT+10%* TiO_2 *composites as representative samples and* TiO_2 *powder (e). In the insets (f), (g), and (h), the exact position of some characteristic peaks for pristine PBAT and PBAT-*TiO_2 *composites is highlighted*

The peaks characteristic of ZTC can be observed becoming more pronounced in the spectra of the composites as the concentration of the filler increases. Furthermore, the presence of ZTC can be supposed to produce different meaningful effects in the PBAT matrix, described by the insets of Figure 2.17, using PBAT+10% ZTC and PBAT+40% ZTC as representative examples, as follows.

First, the absorption of the PBAT carbonyl group (C=O) undergoes a red shift from 1714 to 1709 cm^{-1} (Figure 2.17(b)). This can be attributed to the formation of hydrogen bonds between the oxygen atom in the polymer C=O groups and the amine (−NH−/−NH_2) or hydroxyl (−OH) hydrogen in the structure of zein[61]. Macromolecular systems containing cellulose[57] and starch[62] have previously been observed to form hydrogen bonds between zein and polymer structures. Thus, good adhesion is formed at the interface between PBAT and the ZTC particle surface, as the formation of the intermolecular bonds provides the necessary driving force.

The formation of a hydrogen bond results in the depletion of electrons on the carbon atom in the (O=)C–O group, leading to a partial positive charge and an increase in electronegativity. As a result, the other oxygen in the ester group (C−O) would interact with covalent bonds of higher intensity, causing a blue shift in the C−O stretching from 1265 to 1270 cm^{-1} (Figure 2.17(c)). These shifts involving the ester groups are significant, especially when combined with the observation of the unshifted aromatic out-of-plane C–H bending of the terephthalic unit (728 cm^{-1}), which is not involved in hydrogen bonding (Figure 2.17(d)). The formation of hydrogen bonds proves that interactions take place at the PBAT-ZTC interface, reinforcing the findings that have already been revealed by the improved mechanical properties and the microstructural homogeneity of the composites.

To confirm the role of zein in the compatibilization between filler and matrix through hydrogen bonding, a comparison was made by preparing and characterizing equivalent systems containing only PBAT and TiO_2 (in the same concentration as the TiO_2 contained in the ZTC) using IR spectroscopy (Figure 2.17(e)). In this case, the C=O stretching peak characteristic of PBAT does not red shift in the presence of TiO_2. Similarly, the C–O ester bond stretching peak shows no blue shift (Figure 2.17(g)), and, finally, the C–H aromatic bending peak remains constant (Figure 2.17(h)). These observations confirm the hypothesis based on the previous result. Since no interfacial interactions were observed, the PBAT and TiO_2 systems were not further investigated in this study.

2.5.4 DSC characterization

The DSC heating and cooling scans of PBAT-CPG and PBAT-ZTC composites are illustrated in Figure 2.18a and 2.18b, and 2.18c and 2.19d, respectively.

During the heating scan, as the CPG and ZTC content varies, $T_{g,DSC}$ was observed to remain approximately constant at -30 ± 2 °C for both composites. T_m, corresponding to the peak of the transition, was also approximately constant at 120 ± 2 °C and 128 ± 2 °C for PBAT-CPG and PBAT-ZTC composites, respectively.

A more pronounced trend is observed in T_c during the cooling scan, with increasing values reported in the range of 78–85 °C and 94–99 °C in correlation with the CPG and ZTC percentages, respectively. With reference to the T_c, it can be postulated that the filler particles impede the movement of the polymer chains. However, they simultaneously act as a nucleating agent for PBAT macromolecules, thereby potentially influencing the crystallization process[63,64]. As a result, the attractive intermolecular forces become more significant at higher temperatures. As the concentration of CPG or ZTC in the system increases, a corresponding increase in the T_c value is observed.

Figure 2.19 illustrates that the normalized values of the melting (ΔH_m) and crystallization (ΔH_c) enthalpies. exhibit no discernible variation, indicating that the observed enthalpy alteration is negligible and independent of CPG concentration. Consequently, it may be postulated that the incorporation of CPG particles does not influence the thermal properties of PBAT.

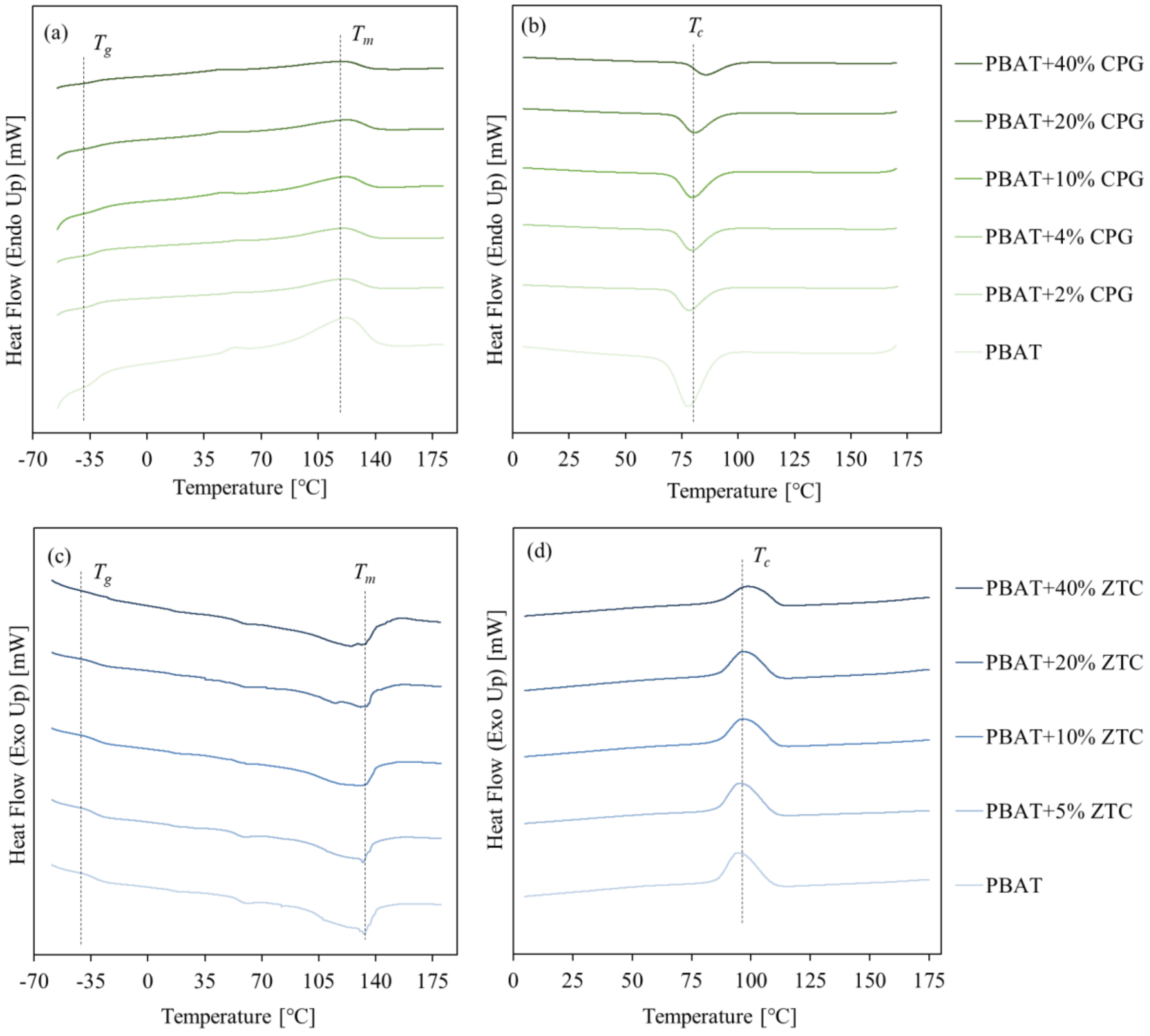

Figure 2.18 *DSC thermograms of PBAT-CPG composites heating (a) and cooling (b) scans, and of PBAT-ZTC composites heating (c) and cooling (d) scans*

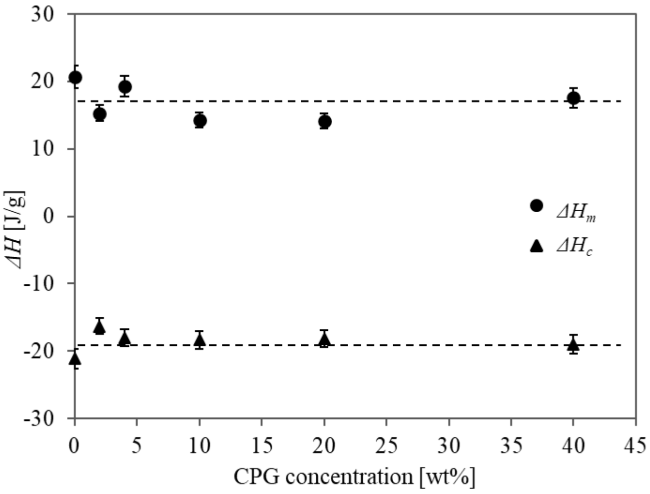

Figure 2.19 *Melting and crystallization enthalpies as a function of CPG concentration*

2.5.5 TGA characterization

The thermogravimetric analysis curves of all PBAT-CPG samples, representing the mass loss as a function of temperature are presented in Figure 2.20. The trend of the curves remains approximately constant as the temperature increases, then decreases sharply, and then assumes an approximately constant trend. Subsequently, all samples undergo single-step thermal degradation within a narrow temperature range.

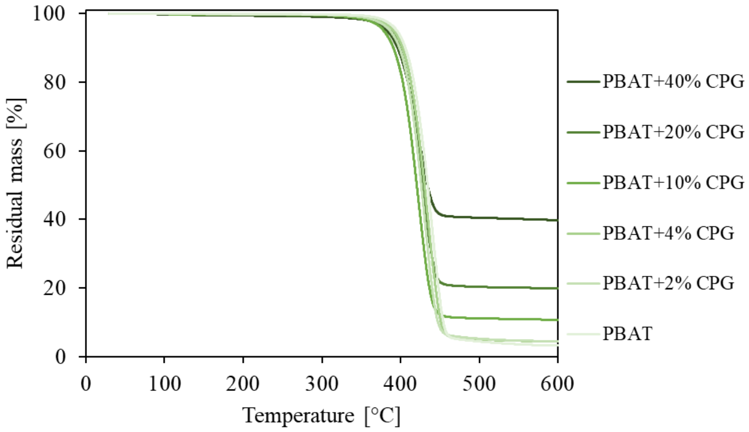

Figure 2.20 *Thermograms of PBAT-CPG composites*

T_{onset} was found to be located at approximately 440 to 420 °C, with a slight decreasing trend evident at increasing filler concentration. The degradation temperature, calculated by considering the inflection point of the experimental curves, also presents a slight decreasing trend with increasing glass loading. However, the variation in values is relatively minor, approximately 5%. Therefore, it can be concluded that even at high loading concentrations, the thermal stability of PBAT composites is not significantly compromised in comparison to pure polymer.

The residual mass observed at the plateau reached by the curve following the heating ramp is equivalent to the CPG content. As an inorganic component, with T_g at around 435-450 °C[30] and T_m over 700°C[65], the CPG does not undergo degradation at the temperatures involved in the pyrolysis of the polymer.

The derived values are reported in Table 2.6.

Table 2.6 *Temperatures of thermal degradation*

	Degradation temperature (T_d) [°C]	**Onset temperature (T_{onset}) [°C]**	**Residual mass (%)**
PBAT	441 ± 3	409 ± 2	3.2 ± 0.2
PBAT+2% CPG	431 ± 3	402 ± 2	4.4 ± 0.2
PBAT +4% CPG	436 ± 3	406 ± 2	4.4 ± 0.2
PBAT +10% CPG	423 ± 3	394 ± 2	10.7 ± 0.5
PBAT +20% CPG	427 ± 3	400 ± 2	19.9 ± 0.9
PBAT +40% CPG	424 ± 3	393 ± 2	39.7 ± 2

2.5.6 DMA characterization

Figure 2.21 a-f represent *E*’, *E”* and *Tanδ* as a function of temperature of all PBAT-based composites with increasing fillers content.

As illustrated in Figures 2.21a and 2.21d, the storage modulus (*E′*) of both PBAT-CPG and PBAT-ZTC-based composites exhibits an increase in response to an increase in filler content at low temperatures. At -60°C the values range from 3.0 ± 0.2 GPa for the pristine PBAT to 5.7 ± 0.2 GPa and 4.3 ± 0.2 GPa for the PBAT with 40% CPG and ZTC, respectively. As the temperature increases, the *E′* values decrease by approximately one order of magnitude across all samples within the analyzed thermal range. An inflection point is evident at approximately −20 °C, which corresponds to the glass transition temperature, where the polymer chains begin to exhibit initial movement, marking the transition from a rigid to a more flexible state[66].

In the rubbery state, all samples show a decrease in *E′* with increasing temperature. Nevertheless, the reinforcing effect given by the addition of the filler persists across the whole analyzed temperature range. Indeed, an examination of the data regarding the values of *E′* as a function of filler concentration at varying temperatures, both below and above T_{gDMA}, reveals that *E′* increases with filler concentration, irrespective of the temperature under consideration.

Once the temperature surpasses 50 °C, the further reduction in *E′* is presumed to result from the initial melting of the crystalline regions within the polymer matrix, which consequently induces a further decline in viscosity. Beyond this temperature, the material transitions from a solid to a non-solid state.

The qualitative assessment of the reinforcement efficiency of fillers in the polymer matrix can be achieved by determining the slope of the fitting line which is obtained by plotting the reduced modulus (E'_{red}) against filler concentration at various temperatures. E'_{red} is defined as the ratio of the composite's storage modulus (*E′*) to that of pristine PBAT (E'_0) at a specific temperature.

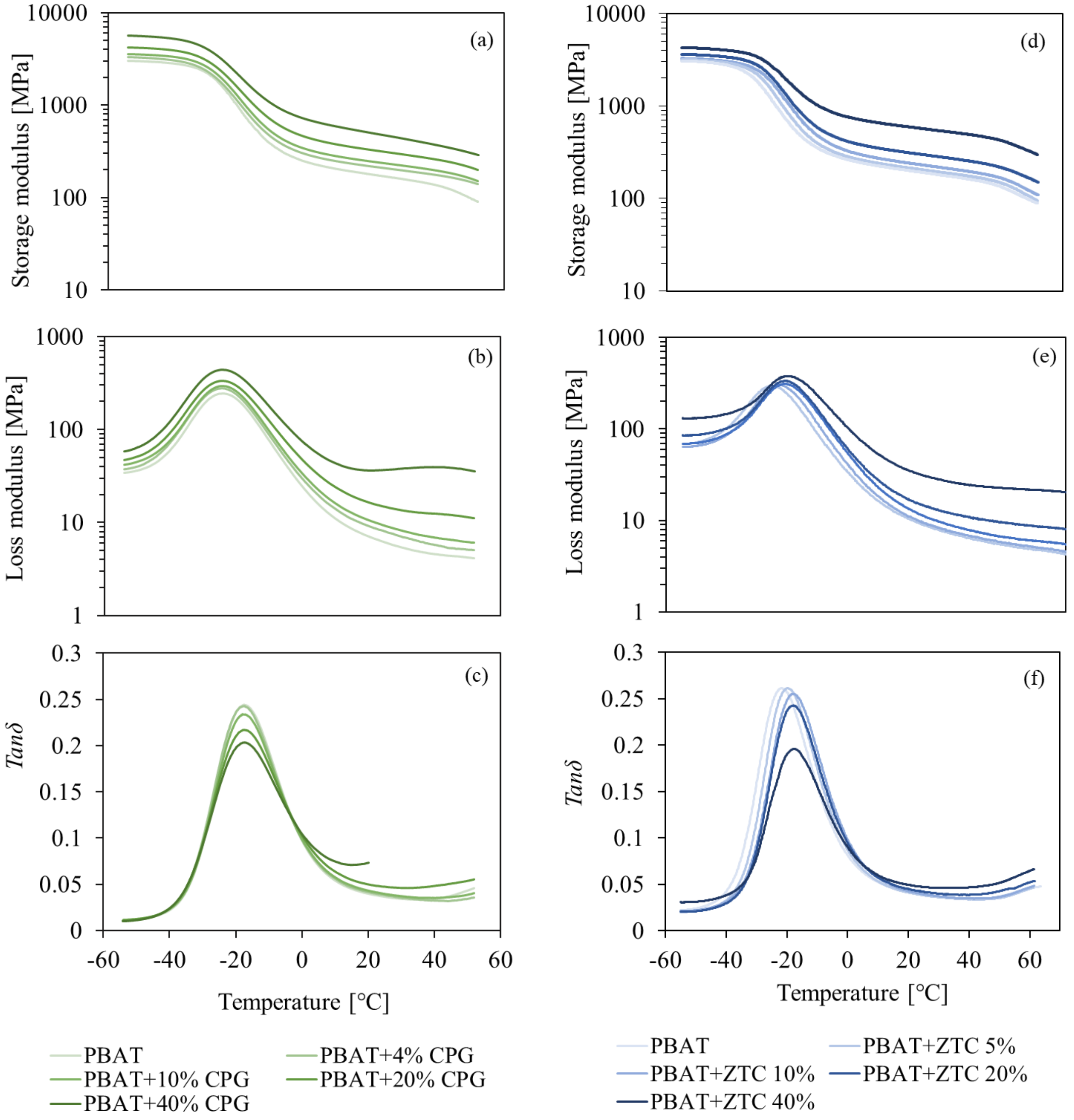

Figure 2.21 *(a) Storage modulus, (b) Loss modulus and (c) damping factor of PBAT-CPG composites and (d) Storage modulus, (e) Loss modulus and (f) damping factor of PBAT-ZTC composites*

The enhancement in E' for the composites in comparison to pristine PBAT becomes more evident at temperatures exceeding T_{gDMA}, as illustrated by the steeper slope in Figure 2.22, which depicts E'_{red} as a function of CPG (a) and ZTC (b) content at varying temperatures.

Below T_{gDMA}, the mobility of polymer chains is restricted within the glassy state, where only atomic bonds undergo bending and stretching vibrations. Consequently, any further stiffening is advantageous but limited.

In contrast, in the rubbery state, the viscosity of the polymer typically decreases[67], which leads to the activation of viscous flow in the polymer chains and, consequently, a deterioration in the material's mechanical properties. The role of filler particles in restricting intermolecular movement is of considerable importance in preventing a decline in mechanical performance as temperature rises. In the specific case of PBAT-ZTC composites, the enhanced structural stiffness can be attributed not only to the physical obstruction of rigid particles but also to the higher density of chemical interactions between the polymer matrix and protein structures.

The creation of composites with high filler content can, therefore, extend the temperature range over which they can be effectively utilized in comparison to unfilled PBAT. Furthermore, the reinforcing effect is more pronounced within the rubbery plateau (approximately 0 to 40 °C, above T_{gDMA}), than in the glassy state (below T_{gDMA}), and remains consistent, enabling composite materials to retain their mechanical properties for applications across a more extensive thermal range than unfilled PBAT.

The observed trend in E' is consistent with findings from other studies on biocomposite systems reinforced with natural fibers, which have reported increased stiffness, particularly above T_{gDMA}. These findings reinforce the hypothesis that filler materials enhance the stiffness of the composites to a greater extent than the neat polymer matrix[68].

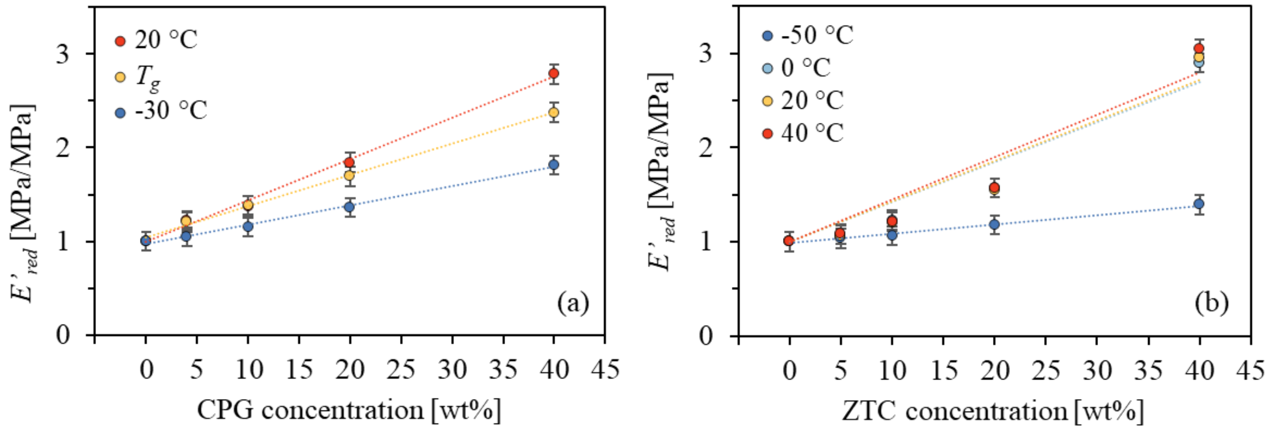

Figure 2.22 *Normalized increment in storage modulus for (a) PBAT-CPG and (b) PBAT-ZTC composites*

The E'' values (Figures 2.21b and 2.21e) were employed to calculate *Tanδ*. The *Tanδ* curves for PBAT-CPG composites (Figures 2.21c) exhibit a peak that diminishes in intensity as the concentration of CPG in the composites increases, without any discernible change in temperature. Similarly, Figure 2.21f depicts the trend of *Tanδ* for composites with varying ZTC concentrations as a function of temperature. As the concentration of fillers increases, a progressive reduction in peak height is observed, accompanied by a slight shift towards higher temperatures. This can be attributed to the increased interaction between the filler particles and the matrix, facilitated by a larger interfacial area[69-71], which reduces the fraction of free polymer chains[72]. In contrast, the lack of variation in both intensity and temperature of the *Tanδ* peak has been interpreted in other polymer systems as an indication of weak filler-matrix interactions, particularly in nanostructured fillers where aggregation and phase separation are more likely to occur[73].

Figure 2.23 presents the values of T_{gDMA}, defined as the temperature corresponding to the peak in the *Tanδ* curves, as a function of filler concentration. No discernible trend in T_{gDMA} was observed as the CPG content increased (Figure 2.23a). In particular, the T_{gDMA} values for the various composites remain relatively consistent, falling within the range of the experimental standard deviation. This stable T_{gDMA} trend indicates that the interaction between the matrix and filler is characterized by good adhesion without the formation of a strong chemically bonded interphase layer[74]. This allows for the preservation of the thermal stability of the composite while maintaining the desired level of adhesion between the two components. In instances where a more robust interphase is established, an elevation in T_{gDMA} is frequently observed[70]. This is a noteworthy observation about PBAT-ZTC composites (Figure 2.23b). As the concentration of fillers is increased, an indicative increase in T_{gDMA} is observed, due to an enhanced intensity of interactions between the particles and the polymer. These interactions are presumed to be more intense than those occurring between individual polymer chains in the matrix. Nevertheless, the resulting experimental data demonstrate only modest statistical differences.

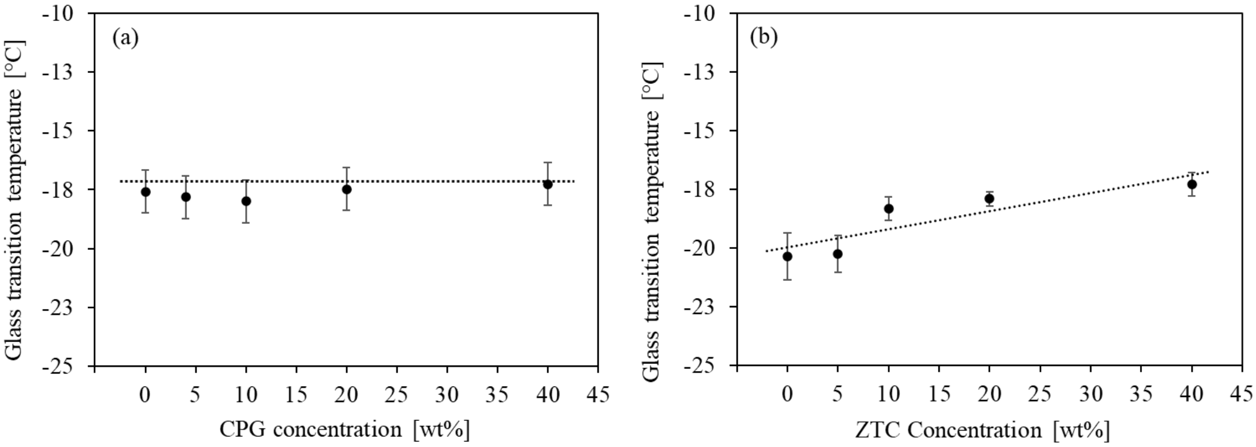

***Figure 2.23** Glass transition temperature as a function of filler content of (a) PBAT-CPG composites and (b) PBAT-ZTC composites*

2.5.7 Creep characterization

Figure 2.24 displays the creep behavior, quantified by the creep compliance, $J(t)$, of PBAT-based composites at various temperatures (ranging from -10 to 60 °C, in 10 °C increments) as a function of test time. The results demonstrate a clear trend of reduced creep compliance with increasing concentrations of CPG and ZTC at all tested temperatures, which is indicative of enhanced creep resistance. Moreover, the divergence in creep resistance between neat PBAT and the composites is more evident at higher filler concentrations and temperatures.

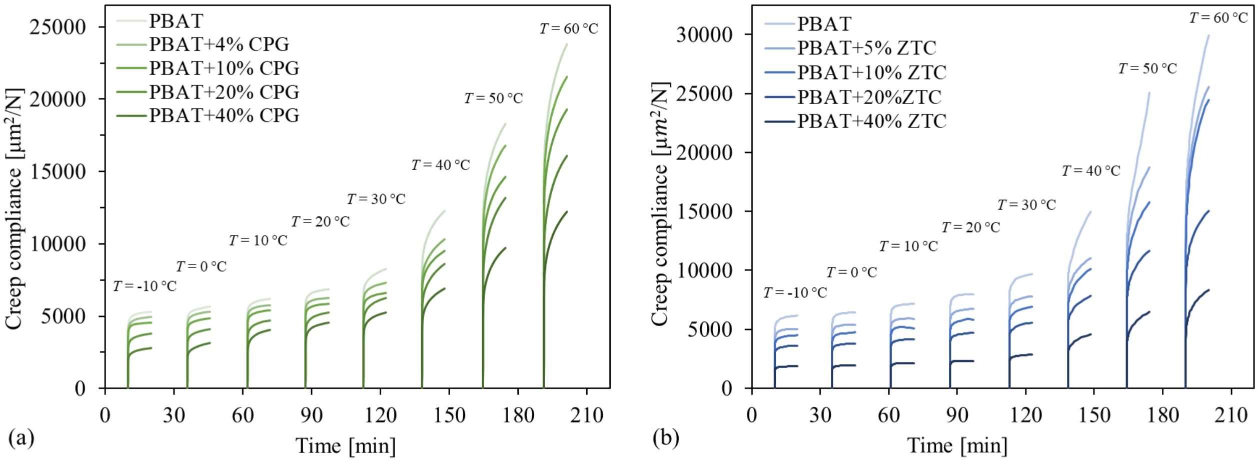

Figure 2.24 *Creep compliance of (a) PBAT-CPG composites and (b) PBAT-ZTC composites*

In accordance with the Burgers' model (Equation 2.25), the alterations in the creep curves and the overall decline in $J(t)$ with rising filler concentration can be ascribed to a diminution in the instantaneous elastic response. This is likely caused by an increase in Maxwell's parameters (E_1 and η_1), which results in a reduction in both elastic strain and viscous flow. Moreover, the increase in the exponential parameter of Kelvin's dashpot (E_2/η_2) results in a reduction in the delayed elastic strain.

Concurrently, as the temperature rises above 20 °C, the viscosity of the polymeric matrix decreases, resulting in a reduction of the viscosity of the Maxwell element (η_1) and an associated decrease in the relaxation time in the Kelvin-Voigt element, which is dependent on η_2. In graphical representation, this results in a marked increase in the slope of the viscous section of $J(t)$, particularly evident in the creep curves for composites with a low filler concentration. Indeed, the absence of interchain bonds, resulting from the presence of the filler, is such that it does not impede the flow of polymer chains. From a practical viewpoint, this mechanical enhancement is particularly advantageous for composites exposed to prolonged operational conditions[75].

It is often observed that composite systems, such as bioplastics, are filled with natural fibers[75,76], and polyamide 66 with nanoclay[77] exhibit a reinforcing effect in terms of creep behavior.

Master curves

The enhanced creep resistance mechanism (lower strain and slower deformation) in PBAT-ZTC composites was further validated through the generation of the master curves at 20 °C by applying the Williams-Landel-Ferry (WLF) model[37], as illustrated in Figure 2.27. The application of the TTS principle allowed to project the *J(t)* behavior of all PBAT-based composites at 20 °C and predict it over extended periods, up to 10 years, which is a duration that far exceeds that of laboratory tests. It was observed that the filled polymers exhibited significantly lower final *J(t)* values over the entire period, thereby allowing these materials to be more suited for extended use and in a wider range of applications.

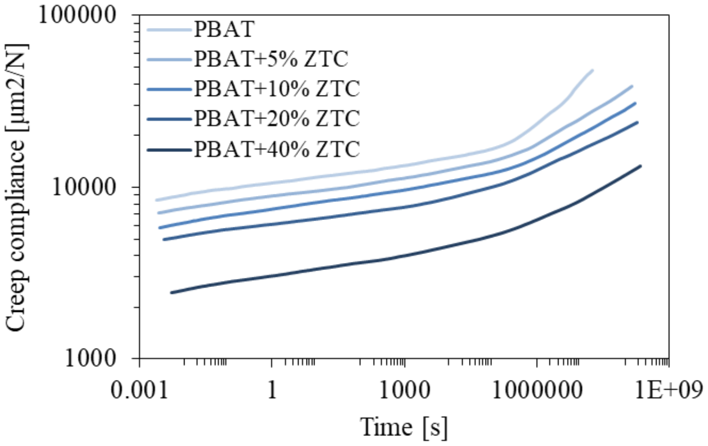

Figure 2.25 *Master curves of PBAT-ZTC composites generated by the TTS principle at 20 °C*

2.5.8 FDM processing

To demonstrate the possibility of printing three-dimensional objects from PBAT-based composites, biocomposite filaments with varying ZTC content were first extruded (Figure 2.26) and then used as input material for FDM printing of solid structures. Under optimized Ex conditions, the flow remained constant, producing about 30 meters of uniform filaments with a constant diameter for each composition. Due to the high ZTC content in the PBAT+40% ZTC formulation, the resulting filament had a rougher surface structure.

Cylindrical scaffolds were produced for each composite formulation using a filament deposition pattern that alternated between 0° and 90° (Figure 2.27(b-f)), based on the 3D model shown in Figure 2.27(a). The printed scaffolds were found to be consistent with the designed model in terms of size and geometry, with comparable filament consistency between pure PBAT and composites with varying ZTC content.

Optical microscope images (Optika B-380 series microscope, Optika Srl, Italy) provided greater detail of the scaffold's internal structure, demonstrating regular strand deposition, consistent pore dimensions, and strand continuity throughout the Ex process. The strands exhibited a circular cross-section of approximately 400 μm, with no collapse observed in unsupported sections (upper insets of Figure 2.27). An examination of the side walls of the scaffold provided insight into the layering, indicating the presence of good interlayer adhesion, mutual contact between adjacent strands, and the absence of delamination (lower insets of Figure 2.27)[78].

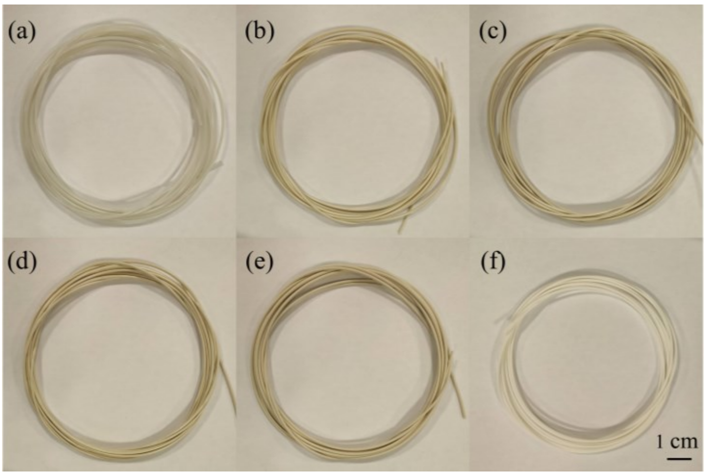

Figure 2.26 *FDM filaments of (a) PBAT, (b) PBAT+5% ZTC, (c) PBAT+10% ZTC, (d) PBAT+20% ZTC, (e) PBAT+40% ZTC, and (f) commercial PLA as a comparison*

The printing of ring structures (Figure 2.28(b)), which were then subjected to elastic deformation by applying a mass of 200 g, corresponding to a weight of 1.962 N (Figure 2.28(c)), allowed the ability to adjust the flexibility as a function of the filler content to be studied. The 3D model of the ring is shown in Figure 2.28(a). The deformation of the rings decreased as the ZTC increased, allowing the mechanical properties of the printed objects to be tailored for specific applications. The PLA ring fabricated as a control reference showed no deformation, as expected, and the PBAT-based rings recovered their original shape when the load was removed (Figure 2.28(d)).

To determine the necessary load to achieve an elliptical deformation of the rings, tensile tests were conducted on the 3D-printed structures using a dynamometer. Custom steel bars connected to the load cell were used as support for the rings, that were subjected to tensile deformation test at a constant speed of 50 mm/min. The rings went from a stress-free circular configuration (Figure 2.29) to an elliptical geometry due to deformation along the tensile axis. The requisite force to geometrically deform the specimens as described is indicated by the stiffness (*S*) *[N/mm]*, which is calculated from the slope of the linear segment of the load-displacement curve[79]. As illustrated in Figure 2.29, the *S* value demonstrated an increase with increasing ZTC content, from 0.44 ± 0.18 N/mm for pure PBAT to 1.09 ± 0.15 N/mm for PBAT+ZTC 40%. This finding is in accordance with the qualitative results described above.

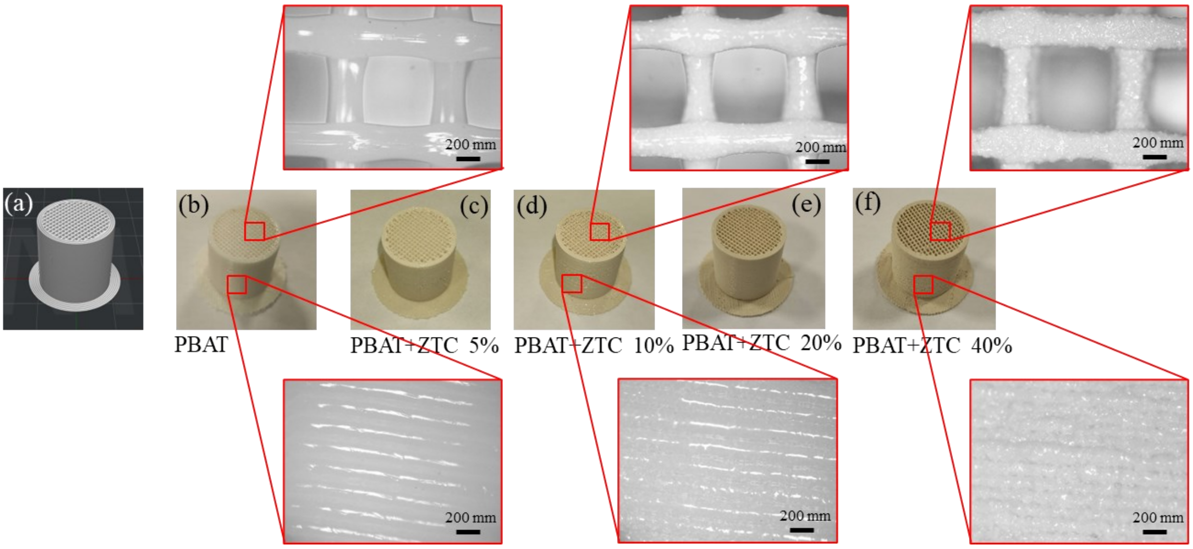

Figure 2.27 *FDM 3D printed scaffolds: (a) 3D model, (b) PBAT, (c) PBAT+5% ZTC, (d) PBAT+10% ZTC, (e) PBAT+20% ZTC, (f) PBAT+40% ZTC. In the insets, the details of the infill pattern and the lateral layering for some representative samples*

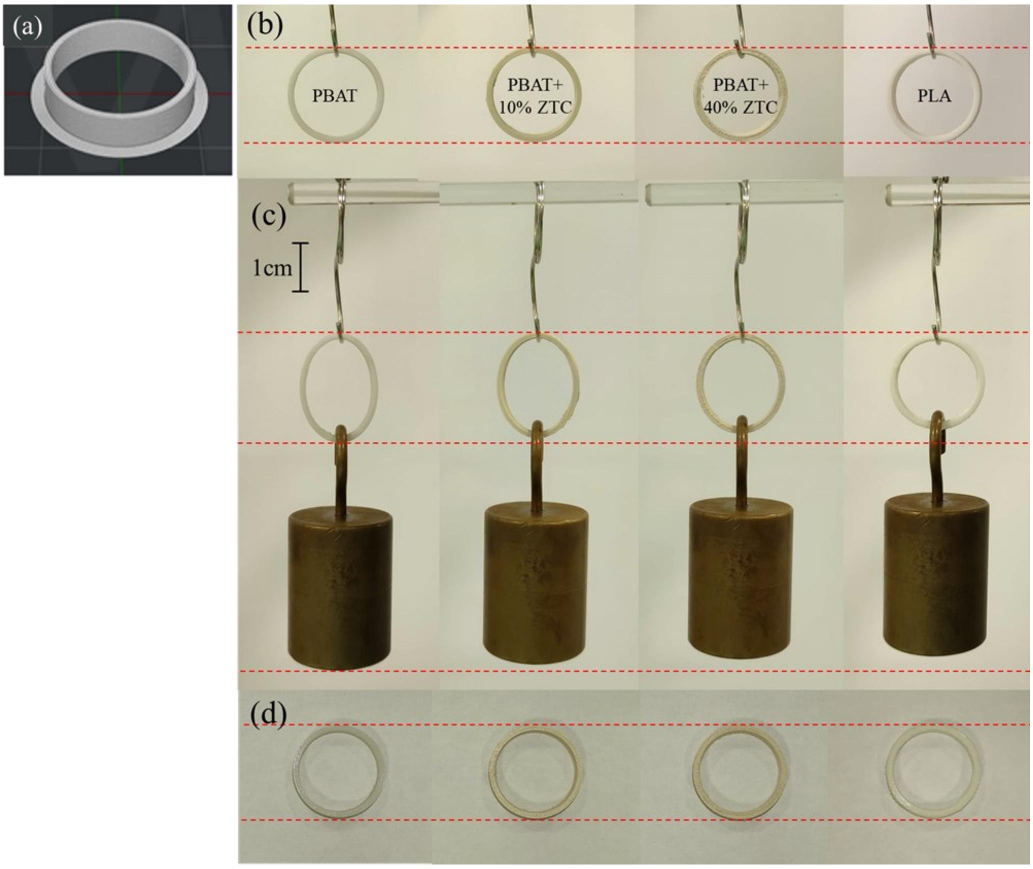

Figure 2.28 *FDM 3D printed rings: (a) 3D model; (b) PBAT, PBAT+10% ZTC, and PBAT+40% ZTC as representative samples and PLA as reference; (c) ring elastic deformation due to the force application and (d) deformation recovery after force removal*

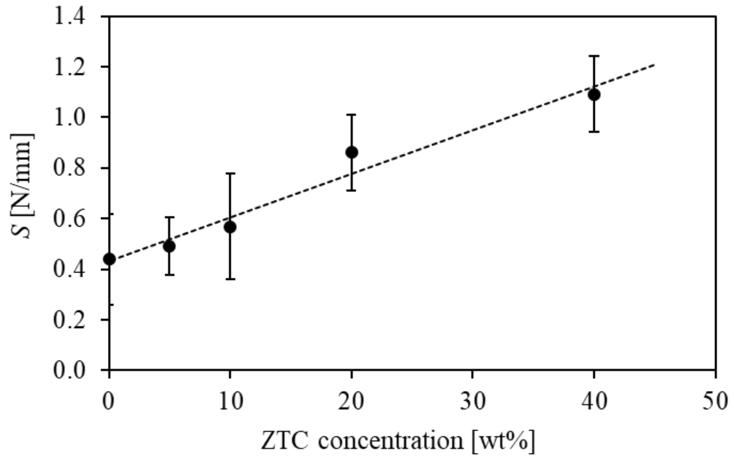

Figure 2.29 *S values as a function of the ZTC content. In the inset, the schematization of the analyzed ring deformation*

2.5.9 Biocompatibility test

As previously outlined, PBAT-based composites have exhibited considerable potential and versatility when reinforced with biofillers. This focus on PBAT adaptability extends beyond packaging and into biomedical applications, where its flexibility and biocompatibility [80] are leveraged to create flexible scaffolds for tissue engineering. The incorporation of additives or bioactive compounds into PBAT scaffolds makes it possible to obtain tunable properties, allowing to meet the requirements of varying environments. This can lead to the design of structures that promote cellular attachment and proliferation, essential for tissue regeneration. By examining the behavior of PBAT-based scaffolds in a biological environment, we can deepen the understanding of how their properties can be tailored for medical purposes, thereby expanding their potential applications beyond packaging into advanced fields such as regenerative medicine.

To evaluate the biocompatibility of the produced PBAT-ZTC composites, 2.5 g/mL biocomposite small grains with different ZTC content were added to cultured HDFs, and the effects on cell morphology, growth, and viability were evaluated.

Transmitted light microscopy images (Figure 2.30(a−z)) of HDFs depict the growth of cells in the absence (CTRL) or presence of ZTC powder, PBAT, and PBAT-composites at different ZTC content. The dark regions in the images correspond to the material grains in contact with the cells.

After up to 96 hours of growth in direct contact with the tested materials, the HDFs present a morphology consistent with the one from the cells grown in the CTRL reference, and show no signs of cellular stress, with a morphology identical to that of CTRL cells. The images in Figure 2.30 illustrate that there are no substantial variations in the proliferation of HDFs cultured in direct contact with PBAT composites in comparison to the CTRL, irrespective of the duration of the cell culture or the ZTC content. Indeed, HDFs exhibit normal proliferation, especially when observing the enhanced confluence of cells cultured for 48 and 96 hours compared to 24 hours, which is comparable to the control.

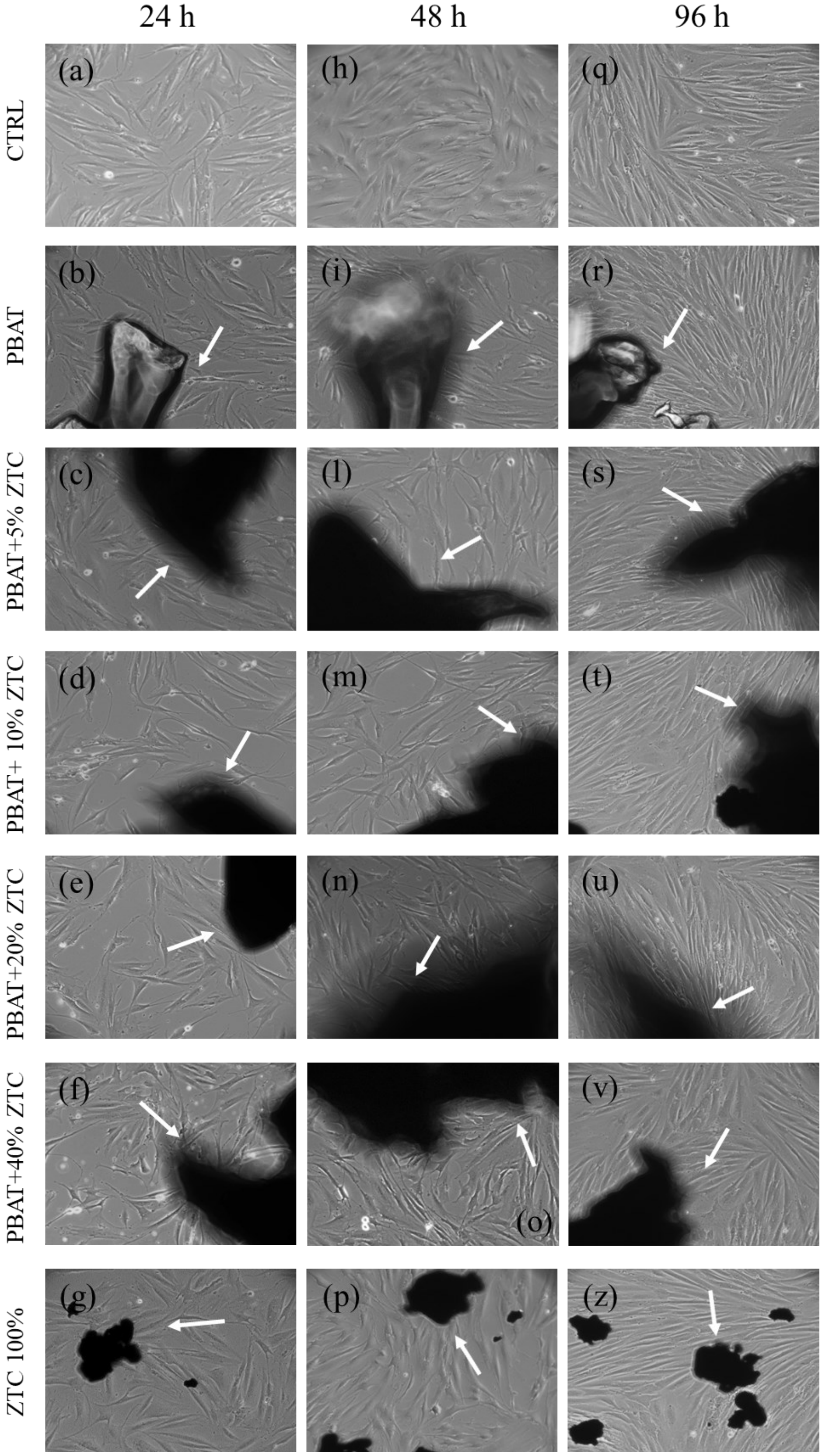

Figure 2.30 *TLM images of HDFs grown for 24 (a–g), 48 (h–p), and 96 h (q–z). Untreated HDFs (CTRL), pure PBAT, PBAT+ZTC from 5 to 40%, and ZTC powder 100% are shown. Optical magnification is 10×. White arrows indicate normal shaped, healthy HDFs that grow in proximity of PBAT, PBAT-based composites, and ZTC*

To gain further insight into the potential cytotoxicity of PBAT composites, a highly sensitive luminescence-based cell viability assay was employed to quantify the intracellular ATP levels as an effect of cell viability. The luminescent response obtained from the in vitro test is a direct measurement of the number of viable cells in the culture, as ATP is a biomolecule directly related to the metabolic activity. 0The experimental results (Figure 2.31) demonstrate that the viability of HDFs among the different samples analyzed is not statistically different, regarding viability at 24 and 48 hours. P values obtained from ANOVA test, were indeed 0.034 and 0.028, respectively, and are both higher than the chosen level of significance ($\alpha = 0.01$). Consequently, the composites can be considered non-cytotoxic, as they do not alter the viability of HDFs in comparison to the control[81].

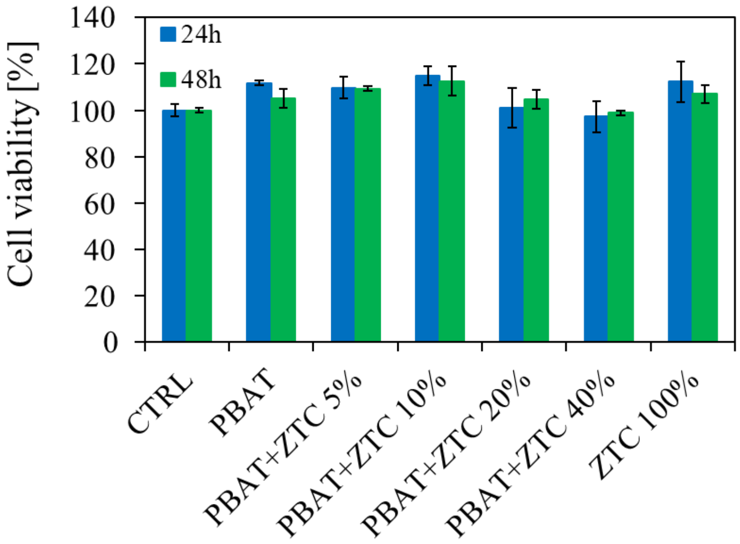

Figure 2.31 *Cell viability of HDFs grown for 24 h (blue bars) or 48 h (green bars) in the presence of pure PBAT, PBAT-based composites (from 5 to 40%), and ZTC 100%. Values are expressed as % of the viability measured in the HDFs control sample (CTRL) that has a 100% cell viability reference value*

Since these newly formulated biobased materials present a flexible and biocompatible nature, new applications in fields such as biomedicine[82], pharmaceutics[82], sensing[83], and robotics[84] can be explored. Currently, FDM 3D printing technology especially faces challenges due to the limited availability of sustainable, eco-friendly materials for producing soft systems[85].

The selection of the most appropriate material for FDM 3D printing can allow for the creation of sophisticated solutions, including anatomical models and medical training devices[85], drug delivery systems[86], customized laboratory equipment[87], and tissue engineering scaffolds[88,89] designed for biologically active environments.

It is noteworthy that 3D printing has been employed to create organ models with enhanced realism for surgical practice. In order to accurately replicate the mechanical properties of diverse tissues, it is essential to utilize materials with tailored characteristics, including varying degrees of elasticity and flexibility[89].

2.6 Conclusions

This experimental activity was focused on the development and characterization of biocomposite materials based on a PBAT matrix, proposed as a sustainable alternative to the conventional materials that are currently used in agrifood packaging. Composite materials with varying CPG and ZTC content, up to 40 wt%, were prepared using solvent casting for the purpose of investigating their mechanical, thermal, dynamic-mechanical, and viscoelastic properties.

The results demonstrate that the incorporation of both CPG and ZTC particles markedly enhances the stiffness of the PBAT matrix. Nonetheless, certain drawbacks were observed in terms of yield strength, elongation at break, and toughness. The findings were corroborated by theoretical models such as Kerner's and Pukánszky's, which exhibited a significant correlation between the experimental data and the predicted values of E_K' and $\sigma_{y,rel}$ and $\sigma_{B,T}$, respectively. The objective of polymer composite design is to enhance the intrinsic properties of the polymer. In this context, the theoretical models employed represent a promising approach for investigating the impact of incorporating a reinforcing phase on the tensile characteristics of the polymer matrix. Furthermore, the positive correlation serves to validate the efficacy of the solvent casting approach as a means of preparing composite materials at the laboratory scale, validating the possibility of upscaling the fabrication to less environmentally impacting methodologies, such as melt compounding.

SEM images of specimen cross-sections demonstrated the uniform dispersion of filler particles throughout the matrix, even at the highest concentrations, with no evidence of agglomeration or phase segregation. In particular, the adhesion between the phases in PBAT-ZTC composites was notable, indicating the formation of a strong interface between the filler surface and the PBAT. This resulted in an efficient and adjustable reinforcement of the pristine polymer, confirming the findings from mechanical characterization.

FT-IR spectra demonstrated that the chemical structure of PBAT-CPG composites remained unaltered, except for a reduction in the absorption intensity of the peaks corresponding to the polymer as the concentration of the filler increased. The same behavior was observed in the EDS analysis, which revealed the elemental composition peaks. It is noteworthy that in the case of PBAT-ZTC composites, the shift of the carbonyl band indicated the formation of hydrogen bonds resulting from the interaction of the protein with the matrix.

Thermal analyses indicated that the addition of the fillers did not negatively affect the thermal stability of PBAT.

The incorporation of fillers into the PBAT matrix resulted in the enhancement of the viscoelastic and thermo-mechanical properties of the pristine polymer. An increase in storage modulus (E') was observed, with no notable changes in the T_g regarding PBAT-CPG composites. In contrast, an increase in T_g was obtained for PBAT-ZTC composites, confirming what was observed with FT-IR and strengthening the hypothesis of the formation of a strong interface between ZTC and PBA. This reinforcing effect was further confirmed by a reduction in creep compliance, which can be attributed to the reduction in polymer chain mobility and consequent enhancement of material resistance to deformation under constant stress resulting from the addition of fillers. As a result, the material can be used in a broader range of applications, offering enhanced thermal performance and long-term durability. Furthermore, a successful methodology for the fabrication of PBAT-based biocomposite filaments for FDM 3D printing was developed, resulting in the successful creation of diverse solid structures.

According to preliminary cytocompatibility test, the direct contact of PBAT-ZTC composites with HDFs grown in vitro did not produce harmful effect, as evidenced by observations made under transmitted light microscopy and cell viability assays.

The findings suggest that CPG-filled PBAT composites may offer a promising biodegradable alternative to conventional thermoplastic materials, such as polyethylene (PE). Consequently, they represent an appealing solution for reducing the environmental impact of agri-food packaging materials while maintaining the functional requirements of such materials (the degradability of PBAT-CPG composites will be discussed in Chapter 4). The incorporation of rigid CPG fillers enables the modification and customization of the mechanical and functional properties by altering the filler content, rendering these composites particularly well-suited for utilization in the agri-food packaging domain. Furthermore, the data demonstrate that PBAT composites with varying ZTC concentrations exhibit adaptable mechanical properties, an environmentally friendly design, and compatibility with additive manufacturing techniques, in addition to short-term biocompatibility, suggesting the potential for advanced biomedical applications.

References

1. Ceci-Ginistrelli, E. et al. Novel biocompatible and resorbable UV-transparent phosphate glass based optical fiber. Opt Mater Express 6, 2040 (2016).

2. Anaya-Esparza, L. M. et al. Protein–tio2: A functional hybrid composite with diversified applications. Coatings vol. 10 1–29 Preprint at https://doi.org/10.3390/coatings10121194 (2020).

3. Halpin, J. C., Louis, S. T. & Kardos, J. L. The Halpin-Tsai Equations: A Review. Polym Eng Sci 16, 344–352 (1976).

4. Landel, R. F. & Nielsen, L. E. Mechanical Properties of Polymers and Composites. Mechanical Properties of Polymers and Composites (CRC Press, Boca Raton, Florida, United States, 1993). doi:10.1201/B16929.

5. Kerner, E. H. The Elastic and Thermo-elastic Properties of Composite Media. Proceedings of the Physical Society. Section B 69, 808–813 (1956).

6. Pukanszky, B. Influence of interface interaction on the ultimate tensile properties of polymer composites. Composites 21, 255–262 (1990).

7. Lewis, T. B. & Nielsen, L. E. Dynamic Mechanical Properties of Particulate-Filled Composites. J Appl Polym Sci 14, 1449–1471 (1970).

8. Százdi, L., Pukánszky, B., Vancso, G. J. & Pukánszky, B. Quantitative estimation of the reinforcing effect of layered silicates in PP nanocomposites. Polymer (Guildf) 47, 4638–4648 (2006).

9. Pukánszky, B. Interfaces and interphases in multicomponent materials: Past, present, future. European Polymer Journal vol. 41 645–662 Preprint at https://doi.org/10.1016/j.eurpolymj.2004.10.035 (2005).

10. Móczó, J. & Pukánszky, B. Polymer micro and nanocomposites: Structure, interactions, properties. Journal of Industrial and Engineering Chemistry 14, 535–563 (2008).

11. Halpin, J. C. Stiffness and Expansion Estimates for Oriented Short Fiber Composites: http://dx.doi.org/10.1177/002199836900300419 3, 732–734 (2016).

12. Gil, A. L. et al. Strategies to Improve the Mechanical Properties of Starch-based Materials: Plasticization and Natural Fibers Reinforcement. doi:10.4322/polimeros.2014.054.

13. Nicolais, L. & Narkis, M. Stress-strain behavior of styrene-acrylonitrile/glass bead composites in the glassy region. Polym Eng Sci 11, 194–199 (1971).

14. Turcsanyi, B., Pukanszky, B. & Tudos, F. Composition dependence of tensile yield stress in filled polymers. J Mater Sci Lett 7, 162 (1988).

15. Zare, Y. New models for yield strength of polymer/clay nanocomposites. Compos B Eng 73, 111–117 (2015).

16. Lazzeri, A. & Phuong, V. T. Dependence of the Pukánszky's interaction parameter B on the interface shear strength (IFSS) of nanofiller- and short fiber-reinforced polymer composites. Compos Sci Technol 93, 106–113 (2014).

17. Faludi, G., Dora, G., Renner, K., Móczó, J. & Pukánszky, B. Biocomposite from polylactic acid and lignocellulosic fibers: Structure–property correlations. Carbohydr Polym 92, 1767–1775 (2013).

18. George, J., Sreekala, M. S. & Thomas, S. A review on interface modification and characterization of natural fiber reinforced plastic composites. Polym Eng Sci 41, 1471–1485 (2001).

19. Panaitescu, D. M. et al. Polymer composites with cellulose microfibrils. Polym Eng Sci 47, 1228–1234 (2007).

20. Nanni, A., Colonna, M. & Messori, M. Fabrication and characterization of new eco-friendly composites obtained by the complete recycling of exhausted coffee capsules. Compos Sci Technol 222, (2022).

21. Yang, H. S., Wolcott, M. P., Kim, H. S., Kim, S. & Kim, H. J. Effect of different compatibilizing agents on the mechanical properties of lignocellulosic material filled polyethylene bio-composites. Compos Struct 79, 369–375 (2007).

22. Lu, T. et al. Effect of surface modification of bamboo cellulose fibers on mechanical properties of cellulose/epoxy composites. Compos B Eng 51, 28–34 (2013).

23. Metin, D., Tihminlioğlu, F., Balköse, D. & Ülkü, S. The effect of interfacial interactions on the mechanical properties of polypropylene/natural zeolite composites. Compos Part A Appl Sci Manuf 35, 23–32 (2004).

24. Younis, C., Bourkas, G., Prassianakis, I., Kytopoulos, V. & Sideridis, E. Estimation of elastic moduli of particulate composites by new models and comparison with moduli measured by tension, dynamic, and ultrasonic tests. Advances in Materials Science and Engineering 2010, (2010).

25. Zare, Y. & Rhee, K. Y. Effects of critical interfacial shear strength between a polymer matrix and carbon nanotubes on the interphase strength and Pukanszky's 'B' interphase parameter. (2020) doi:10.1039/d0ra00978d.

26. Zare, Y., Rhee, K. Y. & Park, S. J. Simple Models for Interphase Characteristics in Polypropylene/Montmorillonite/CaCO3 Nanocomposites. Physical Mesomechanics 23, 182–188 (2020).

27. Zare, Y. & Garmabi, H. Analysis of tensile modulus of PP/nanoclay/CaCO3 ternary nanocomposite using composite theories. J Appl Polym Sci 123, 2309–2319 (2012).

28. Li, G., Shankar, S., Rhim, J. W. & Oh, B. Y. Effects of preparation method on properties of poly(butylene adipate-co-terephthalate) films. Food Science and Biotechnology 2015 24:5 24, 1679–1685 (2015).

29. Ahrens, J., Geveci, B. & Law, C. ParaView: An End-User Tool for Large-Data Visualization. Visualization Handbook 717–731 (2005) doi:10.1016/B978-012387582-2/50038-1.

30. Sglavo, V. M. et al. Mechanical properties of resorbable calcium-phosphate glass optical fiber and capillaries. J Alloys Compd 778, 410–417 (2019).

31. Sciancalepore, C., Moroni, F., Messori, M. & Bondioli, F. Acrylate-based silver nanocomposite by simultaneous polymerization–reduction approach via 3D stereolithography. Composites Communications 6, 11–16 (2017).

32. Adegoloye, G., Beaucour, A. L., Ortola, S. & Noumowé, A. Concretes made of EAF slag and AOD slag aggregates from stainless steel process: Mechanical properties and durability. Constr Build Mater 76, 313–321 (2015).

33. Pothan, L. A., Oommen, Z. & Thomas, S. Dynamic mechanical analysis of banana fiber reinforced polyester composites. Compos Sci Technol 63, 283–293 (2003).

34. Vlasveld, D. P. N., Bersee, H. E. N. & Picken, S. J. Creep and physical aging behaviour of PA6 nanocomposites. Polymer (Guildf) 46, 12539–12545 (2005).

35. Militký, J. & Jabbar, A. Comparative evaluation of fiber treatments on the creep behavior of jute/green epoxy composites. Compos B Eng 80, 361–368 (2015).

36. Durante, M., Formisano, A., Boccarusso, L., Langella, A. & Carrino, L. Creep behaviour of polylactic acid reinforced by woven hemp fabric. Compos B Eng 124, 16–22 (2017).

37. Williams, M. L., Landel, R. F. & Ferry, J. D. The Temperature Dependence of Relaxation Mechanisms in Amorphous Polymers and Other Glass-forming Liquids. J Am Chem Soc 77, 3701–3707 (1955).

38. Giubilini, A., Sciancalepore, C., Messori, M. & Bondioli, F. New biocomposite obtained using poly(3-hydroxybutyrate-co-3-hydroxyhexanoate) (PHBH) and microfibrillated cellulose. J Appl Polym Sci 137, 48953 (2020).

39. Giubilini, A., Sciancalepore, C., Messori, M. & Bondioli, F. Valorization of oat hull fiber from agri-food industrial waste as filler for poly(3-hydroxybutyrate-co-3-hydroxyhexanoate). J Mater Cycles Waste Manag 23, 402–408 (2021).

40. Taurino, R., Sciancalepore, C., Collini, L., Bondi, M. & Bondioli, F. Functionalization of PVC by chitosan addition: Compound stability and tensile properties. Compos B Eng 149, 240–247 (2018).

41. Galeski, A., Bartczak, Z., Argon, A. S. & Cohen, R. E. Morphological Alterations during Texture-Producing Plastic Plane Strain Compression of High-Density Polyethylene. Macromolecules 25, 5705–5718 (1992).

42. Barrera, G. et al. Magnetite-epoxy nanocomposites obtained by the reactive suspension method: Microstructural, thermo-mechanical and magnetic properties. Eur Polym J 94, 354–365 (2017).

43. Degli Esposti, M. et al. Epoxy resin/TiO2 nanocomposites prepared by the Reactive Suspension Method: Dynamic-mechanical properties and their prediction by theoretical models. Mater Today Commun 31, 103347 (2022).

44. Venkatesan, R. & Rajeswari, N. Preparation, Mechanical and Antimicrobial Properties of SiO2/ Poly(butylene adipate-co-terephthalate) Films for Active Food Packaging. Silicon 2016 11:5 11, 2233–2239 (2016).

45. Renner, K., Kenyó, C., Móczó, J. & Pukánszky, B. Micromechanical deformation processes in PP/wood composites: Particle characteristics, adhesion, mechanisms. Compos Part A Appl Sci Manuf 41, 1653–1661 (2010).

46. Battegazzore, D., Noori, A. & Frache, A. Natural wastes as particle filler for poly(lactic acid)-based composites: https://doi.org/10.1177/0021998318791316 53, 783–797 (2018).

47. Kiss, A., Fekete, E. & Pukánszky, B. Aggregation of CaCO3 particles in PP composites: Effect of surface coating. Compos Sci Technol 67, 1574–1583 (2007).

48. Maiti, S. N. & Sharma, K. K. Studies on polypropylene composites filled with talc particles. Journal of Materials Science 1992 27:17 27, 4605–4613 (1992).

49. Kun, D. & Pukánszky, B. Polymer/lignin blends: Interactions, properties, applications. Eur Polym J 93, 618–641 (2017).

50. Várdai, R. et al. Comparative study of fiber reinforced PP composites: Effect of fiber type, coupling and failure mechanisms. Compos Part A Appl Sci Manuf 133, 105895 (2020).

51. Paszkiewicz, S. et al. Synthesis and characterization of poly(ethylene terephthalate- co -1,4-cyclohexanedimethylene terephtlatate)- block -poly(tetramethylene oxide) copolymers. RSC Adv 7, 41745–41754 (2017).

52. Baia, L., Baia, M., Kiefer, W., Popp, J. & Simon, S. Structural and morphological properties of silver nanoparticles-phosphate glass composites. Chem Phys 327, 63–69 (2006).

53. Beigoli, S., Hekmat, A., Farzanegan, F. & Darroudi, M. Green synthesis of amorphous calcium phosphate nanopowders using Aloe Vera plant extract and assessment of their cytotoxicity and antimicrobial activities. J Solgel Sci Technol 98, 508–516 (2021).

54. Cai, Y., Lv, J. & Feng, J. Spectral Characterization of Four Kinds of Biodegradable Plastics: Poly (Lactic Acid), Poly (Butylenes Adipate-Co-Terephthalate), Poly (Hydroxybutyrate-Co-Hydroxyvalerate) and Poly (Butylenes Succinate) with FTIR and Raman Spectroscopy. J Polym Environ 21, 108–114 (2013).

55. Socrates, G. Infrared and Raman Characteristic Group Frequencies:Tables and Charts. (John Wiley & sons, Chichester, 2001).

56. Cao, Y., Chen, T. T., Wang, W., Chen, M. & Wang, H. J. Construction and functional assessment of zein thin film incorporating spindle-like ZnO crystals. RSC Adv 7, 2180–2185 (2017).

57. Ali, S., Khatri, Z., Oh, K. W., Kim, I. S. & Kim, S. H. Zein/cellulose acetate hybrid nanofibers: Electrospinning and characterization. Macromol Res 22, 971–977 (2014).

58. Forato, L. A., Bernardes-Filho, R. & Colnago, L. A. Protein structure in KBr pellets by infrared spectroscopy. Anal Biochem 259, 136–141 (1998).

59. Rajkumar, S. et al. Synthesis of Ag-incorporated TiO2 nanoparticles by simple green approach as working electrode for dye-sensitized solar cells. Journal of Materials Science: Materials in Electronics 33, 4965–4973 (2022).

60. Man, Y. et al. Synthesis and characterization of rutile titanium dioxide/polyacrylate nanocomposites for applications in ultraviolet light-shielding materials. Polym Compos 36, 8–16 (2015).

61. Gianazza, E., Viglienghi, V., Righetti, P. G., Salamini, F. & Soave, C. Amino acid composition of zein molecular components. Phytochemistry 16, 315–317 (1977).

62. Chen, X. et al. Development and characterization of a hydroxypropyl starch/zein bilayer edible film. Int J Biol Macromol 141, 1175–1182 (2019).

63. Lai, L. et al. Stiffening, strengthening, and toughening of biodegradable poly(butylene adipate-co-terephthalate) with a low nanoinclusion usage. Carbohydr Polym 247, 116687 (2020).

64. Lule, Z. C., Shiferaw, E. W. & Kim, J. Thermomechanical Properties of SiC-Filled Polybutylene Succinate Composite Fabricated via Melt Extrusion. Polymers 2020, Vol. 12, Page 418 12, 418 (2020).

65. Mandlule, A., Döhler, F., Van Wüllen, L., Kasuga, T. & Brauer, D. S. Changes in structure and thermal properties with phosphate content of ternary calcium sodium phosphate glasses. J Non Cryst Solids 392–393, 31–38 (2014).

66. Jawaid, M., Abdul Khalil, H. P. S., Hassan, A., Dungani, R. & Hadiyane, A. Effect of jute fibre loading on tensile and dynamic mechanical properties of oil palm epoxy composites. Compos B Eng 45, 619–624 (2013).

67. Wang, J. shyong & Porter, R. S. On the viscosity-temperature behavior of polymer melts. Rheologica Acta 1995 34:5 34, 496–503 (1995).

68. Nanni, A., Parisi, M., Colonna, M. & Messori, M. Thermo-Mechanical and Morphological Properties of Polymer Composites Reinforced by Natural Fibers Derived from Wet Blue Leather Wastes: A Comparative Study. Polymers 2021, Vol. 13, Page 1837 13, 1837 (2021).

69. Sciancalepore, C., Bondioli, F. & Messori, M. Non-hydrolytic sol–gel synthesis and reactive suspension method: an innovative approach to obtain magnetite–epoxy nanocomposite materials. J Solgel Sci Technol 81, 69–83 (2017).

70. Kang, S. et al. Preparation and characterization of epoxy composites filled with functionalized nanosilica particles obtained via sol-gel process. Polymer (Guildf) 42, 879–887 (2001).

71. Romanzini, D., Lavoratti, A., Ornaghi, H. L., Amico, S. C. & Zattera, A. J. Influence of fiber content on the mechanical and dynamic mechanical properties of glass/ramie polymer composites. Mater Des 47, 9–15 (2013).

72. Baia, L., Muresan, D., Baia, M., Popp, J. & Simon, S. Structural properties of silver nanoclusters-phosphate glass composites. Vib Spectrosc 43, 313–318 (2007).

73. Phothisarattana, D., Wongphan, P., Promhuad, K., Promsorn, J. & Harnkarnsujarit, N. Blown film extrusion of PBAT/TPS/ZnO nanocomposites for shelf-life extension of meat packaging. Colloids Surf B Biointerfaces 214, 112472 (2022).

74. Dorigato, A., D'Amato, M. & Pegoretti, A. Thermo-mechanical properties of high density polyethylene - Fumed silica nanocomposites: Effect of filler surface area and treatment. Journal of Polymer Research 19, (2012).

75. Nanni, A. & Messori, M. Thermo-mechanical properties and creep modelling of wine lees filled Polyamide 11 (PA11) and Polybutylene succinate (PBS) bio-composites. Compos Sci Technol 188, 107974 (2020).

76. Georgiopoulos, P., Kontou, E. & Niaounakis, M. Thermomechanical properties and rheological behavior of biodegradable composites. Polym Compos 35, 1140–1149 (2014).

77. Yang, J.-L., Zhang, Z., Schlarb, A. K. & Friedrich, K. On the characterization of tensile creep resistance of polyamide 66 nanocomposites. Part I. Experimental results and general discussions. (2006) doi:10.1016/j.polymer.2006.02.065.

78. Singamneni, S., Smith, D., LeGuen, M. J. & Truong, D. Extrusion 3D printing of polybutyrate-adipate-terephthalate-polymer composites in the pellet form. Polymers (Basel) 10, (2018).

79. Haddad, R., Peltz, T., Bertollo, N., Walsh, W. R. & Nicklin, S. Looped suture properties: implications for multistranded flexor tendon repair. J Hand Surg Eur Vol 40, 234–238 (2015).

80. Wang, S. & Xing, Q. Preparation and in vitro biocompatibility of PBAT and chitosan composites for novel biodegradable cardiac occluders. E-Polymers 22, 705–718 (2022).

81. Fukushima, K., Rasyida, A. & Yang, M. C. Characterization, degradation and biocompatibility of PBAT based nanocomposites. Appl Clay Sci 80–81, 291–298 (2013).

82. Tan, D. K., Maniruzzaman, M. & Nokhodchi, A. Advanced Pharmaceutical Applications of Hot-Melt Extrusion Coupled with Fused Deposition Modelling (FDM) 3D Printing for Personalised Drug Delivery. Pharmaceutics 2018, Vol. 10, Page 203 10, 203 (2018).

83. Georgopoulou, A., Sebastian, T. & Clemens, F. Thermoplastic elastomer composite filaments for strain sensing applications extruded with a fused deposition modelling 3D printer. Flexible and Printed Electronics 5, 035002 (2020).

84. Chynybekova, K. & Choi, S. M. Flexible Patterns for Soft 3D Printed Fabrications. Symmetry 2019, Vol. 11, Page 1398 11, 1398 (2019).

85. Luque, M. C., Calleja-Hortelano, A. & Romero, P. E. Use of 3D Printing in Model Manufacturing for Minor Surgery Training of General Practitioners in Primary Care. Applied Sciences 2019, Vol. 9, Page 5212 9, 5212 (2019).

86. Okwuosa, T. C. et al. On demand manufacturing of patient-specific liquid capsules via co-ordinated 3D printing and liquid dispensing. Eur J Pharm Sci 118, 134–143 (2018).

87. Salentijn, G. I. J., Oomen, P. E., Grajewski, M. & Verpoorte, E. Fused Deposition Modeling 3D Printing for (Bio)analytical Device Fabrication: Procedures, Materials, and Applications. Anal Chem 89, 7053–7061 (2017).

88. Haryńska, A., Gubanska, I., Kucinska-Lipka, J. & Janik, H. Fabrication and Characterization of Flexible Medical-Grade TPU Filament for Fused Deposition Modeling 3DP Technology. Polymers 2018, Vol. 10, Page 1304 10, 1304 (2018).

89. Ferretti, P. et al. Application of TPU-sourced 3d printed FDM organs for improving the realism in surgical planning and training. Proceedings of the International Conference on Industrial Engineering and Operations Management 6658-6669 (2021) doi:10.46254/AN11.20211136

Chapter 3

PHA for Biomedical Applications

3.1 Introduction

This chapter introduces a different theme from the previous chapter and focuses on polyhydroxyalkanoates (PHA), a class of biopolymers that are gaining attention for several reasons, not least because of their biocompatibility[1], which makes them suitable for use in the biomedical sector[2]. In addition, PHA are also attracting interest as potential packaging material[3]. Despite the expansion of the market for PHA[4], their elevated cost and deficient mechanical properties[5] present obstacles, rendering them optimal candidates for enhancement using suitable plasticizers.

This study, which was conducted in collaboration with the Department of Civil, Chemical, Environmental and Materials Engineering of Bologna University, examines the preparation of poly(3-hydroxybutyrate) (PHB) compounds using glycerol trilevulinate (GT) as a bioplasticizer, with the objective of enhancing the performance of PHB. The carboxylic acid-rich structure and steric hindrance of GT render it particularly effective for plasticizing polyesters such as PHB, thereby enhancing the mechanical properties and long-term stability of the resulting compounds[6]. GT was synthesized via a green, solvent-free esterification process using bio-based levulinic acid and glycerol, with synthesis optimization achieved through kinetics studies.

The plasticized PHB compounds were evaluated for processability via extrusion (Ex), injection molding (IM), and Fused Deposition Modeling (FDM) to produce scaffolds with controlled porosity for potential bone tissue regeneration applications. Thermal, rheological, and thermo-mechanical properties of the compounds were examined through differential scanning calorimetry (DSC), viscosity test, dynamic mechanical analysis (DMA), and tensile test, respectively.

A comparative analysis was conducted to evaluate the potential use of GT as a sustainable alternative to commercial green plasticizers, such as 1,2-cyclohexanedicarboxylic acid diisononyl ester (DINCH) and acetyl tributyl citrate (ATBC), for the plasticizing of PHB compounds.

Following this analysis, the most promising formulation of GT-plasticized PHB was then selected for a second phase, consisting in the further development of FDM 3D-printed bone tissue scaffolds. Porous scaffolds are of critical importance for providing structural and biological support for new bone growth and are designed to biodegrade at a rate that matches the tissue regeneration process.

The polymer matrix was selected as plasticized PHB, and different concentrations of resorbable phosphate glass, prepared by melt quenching, were incorporated to form PHA-bioactive glass composites.

The thermal properties of the resulting materials were analyzed using DSC and thermo-gravimetric analysis (TGA). The optimization of printing parameters ensured the attainment of high standards of internal morphology and filament deposition quality. The distribution of the filler within the polymer matrix and the effect of the GT and bioglass on the thermo-mechanical properties of the formulations were investigated through microscopy. Moreover, dumbbell-shaped specimens were produced through IM and subjected to tensile testing to investigate the material's mechanical properties at varying filler concentrations. To further characterize the PHB-bioglass composites, compression tests were conducted to evaluate the structural integrity of the printed scaffolds. Lastly, wettability tests with commercial cow blood were performed using contact angle measurements to evaluate the potential scaffold behavior in a biological setting.

The objective of this exploratory work is to design and manufacture customized scaffolds that can be used to replace bone defects in a way that is anatomically accurate and offers tailored solutions to the limitations of conventional prosthetics.

3.2 Materials

Poly(3-hydroxybutyrate-co-3-hydroxyvalerate) (PHBV), Mw = 240,000 g mol^{-1}, was obtained from Gruppo MAIP (IamNATURE B6 T P001Y), and used without any pretreatment except oven drying (ISCO NSV 9090) at 45 °C for a minimum of 4 hours. The polymer was analyzed by nuclear magnetic resonance (1H NMR) to obtain detailed information on its composition. The related experimental procedure is not reported in this thesis[7]. The 1H NMR investigation showed the presence of 0.3 % mol of 3-hydroxyvaleric acid units (3HV) with respect to 3-hydroxybutyric acid (3HB). This negligible amount of 3HV units cannot produce significant modification of the polymer properties. Therefore, the material will be referred to as just PHB.

Reagents for the synthesis of the GT plasticizer were purchased from Sigma-Aldrich. Additionally, sodium bicarbonate ($NaHCO_3$, ≥ 99.5 %, obtained from Carlo Erba), *p*-toluenesulfonic acid monohydrate (PTSA, 98.5 %, obtained from Alfa Aesar) were also used.

The commercial plasticizers 1,2-cyclohexane dicarboxylic acid diisononyl ester (Hexamoll® DINCH) and acetyl tributyl citrate (ATBC, ≥ 98%) were purchased from BASF and Sigma-Aldrich, respectively.

For the glass synthesis, magnesium sulphate ($MgSO_4$, 99.5%) and anhydrous sodium carbonate (Na_2CO_3, 99.5%) were purchased from Carlo Erba; sodium dihydrogen phosphate monohydrate (NaH_2PO_4 - H_2O, ACS, 98.0-102.0%) and strontium hydrogen phosphate ($SrHPO_4$, 51-53%) were obtained from Thermo Scientific, and calcium hydrogen phosphate ($HCaPO_4$) was obtained from SAFC®.

3.2.1 Notes on plasticizer synthesis

GT was used after synthesis, carried out by colleague researchers from the University of Bologna, through a solvent-free methodology, with procedures optimized based on previously reported methods[6]. Briefly, a mixture of glycerol, levulinic acid, and PTSA catalyst was heated to 110°C for 24 hours, neutralized with sodium bicarbonate, extracted with ethyl acetate, and washed with sodium bicarbonate and sodium chloride solutions. After drying with sodium sulfate, the solvent was removed by rotary evaporation, yielding a yellow viscous product. Yield and selectivity were optimized through reaction kinetics studies. Fourier Transform Infrared was used to monitor the reaction and conduct structural analysis. NMR spectroscopy was used to confirm the chemical structure of GT and evaluate the composition of PHB. For more detailed procedure description and discussion, please refer to the work published in the literature[7].

3.2.2 Bioglass synthesis

The bioglass was obtained by the melt-quenching technique, which involves heating to a high temperature followed by rapid cooling. The composition used for the preparation was as follows: diphosphorus pentoxide (P_2O_5, 51.32 mol%), magnesium oxide (MgO, 23.61 mol%), sodium oxide (Na_2O, 11.80 mol%), calcium oxide (CaO, 10.27 mol%), strontium oxide (SrO, 3.00 mol%). The precursors were mixed and placed in a silica crucible, which in turn was placed in a furnace at room temperature, where they were progressively heated up to 1000°C, the temperature at which the formation of a glass in the form of a thick liquid is complete and then poured onto a cold plate.

The total obtained glass quantity ($m_{g,TOT}$) obtained was calculated with Equation 3.1, as the difference between the total mass obtained after casting, equals the sum of the cast glass ($m_{g,cast}$) and the mass of the crucible after the fusion ($m_{cr,f}$), and the mass of the empty crucible before synthesis ($m_{cr,i}$).

$$m_{g,TOT} = \left(m_{g,cast} + m_{cr,f}\right) - m_{cr,i} \quad \text{(Equation 3.1)}$$

For the purposes of subsequent processing steps, it is only the mass of the cast glass that can be considered useful, as the remaining mass remains attached to the walls of the crucible and cannot be recovered.

The obtained mass was then used to calculate the yield of the synthesis, expressed as a relative mass loss between theoretical mass (calculated by stoichiometry) and obtained mass, through Equation 3.2.

$$Theoretical\ loss\ (\%) = \frac{m_{g,TOT,th} - m_{g,TOT}}{m_{g,TOT,th}} \cdot 100 \qquad \text{(Equation 3.2)}$$

Once cooled to room temperature, the phosphate glass was ground using the Planetary Micro Mill PULVERISETTE 7 (FRITSCH GmbH) until a powder was obtained and subsequently sieved (stainless-steel sieve, Retsch, Germany) to obtain particles with a homogeneous size of less than 50 µm.

Additional mass loss during milling was calculated as the ratio between the difference in glass mass before ($m_{g,i}$) and after milling ($m_{g,f}$) and the initial amount of glass cast, as follows (Equation 3.3)

$$Milling\ loss\ (\%) = \frac{m_{g,i}-g_{g,f}}{m_{g,i}} \cdot 100 \qquad \text{(Equation 3.3)}$$

3.3 Methods

3.3.1 Compounds preparation

PHB granules, initially 2-4 mm in diameter, were ground under cryogenic conditions using an IKA A11 analytical mill. The use of liquid nitrogen resulted in a reduction in temperature to below the glass transition temperature (T_g [°C]), thereby increasing the brittleness of the material and facilitating its reduction to granules smaller than 2 mm. This step was essential for subsequent processing on a twin-screw extruder. The ground polymer and plasticizer, and subsequently the bioglass powder, according to the compositions given in Table 3.1, were pre-mixed at room temperature. To compare the results, the compounds will be subdivided into three distinct sets of data: pure PHB and PHB compounded with different concentrations of GT (named *GT-set*), pure PHB and PHB compounded with 5wt% of the three different plasticizers used (named *5%-set*), and finally, the PHB5GT reinforced with different concentrations of bioglass powder (*Glass-set*).

It is noteworthy that for the glass-filled composites, the plasticized PHB5GT formulation was selected as the matrix (named “Neat”), and the glass weight percent refers to the plasticized PHB, not just to the polymer.

Prior to Ex, the premixes underwent four hours of oven drying at 40°C with the aim of removing residual moisture and ensuring homogeneity during Ex. A co-rotating twin-screw extruder (RES-2 P/12A Explorer Extruder, Zamac Mercator, Poland) with a screw diameter of 11 mm and a screw ratio L/D of 40 was used to process the premixed materials, in the configuration of internal mixer. The screw profile varied along its length, facilitating melt homogenization through compaction and transport of the polymer from the hopper to the head. The appropriate temperatures and screw rate suitable for Ex have been determined experimentally, based on the melting temperature reported in the polymer datasheet. The temperature profile of the six extruder heating zones, as illustrated in Table 3.2, was maintained at a constant level for all compositions. The highest temperature was maintained in zones 3 and 4, where mixing occurs, in order to reduce the viscosity of the polymer and ensure proper mixing with the plasticizer. Subsequently, Zones 5 and 6 present a lower temperature in order to prevent thermal degradation of the polymer and to achieve a consistency suitable for Ex.

***Table 3.1** Compositions of the PHB compounds produced with twin-screw extruder*

Sample denomination	**Matrix content**	**Plasticizer content**	**Bioglass content**	**Experiment group**
PHB	100%wt PHB	-	-	*GT-set*
PHB2.5GT	97.5%wt PHB	2.5%wt GT	-	*GT-set*
PHB5GT	95%wt PHB	5%wt GT	-	*GT-set / 5%-set*
PHB10GT	90%wt PHB	10%wt GT	-	*GT-set*
PHB5ATBC	95%wt PHB	5%wt ATBC	-	*5%-set*
PHB5DINCH	95%wt PHB	5%wt DINCH	-	*5%-set*
PHB5GT Neat	95%wt PHB	5%wt GT	-	*Glass-set*
PHB5GT5V	95%wt PHB	5%wt GT	5%wt	*Glass-set*
PHB5GT10V	95%wt PHB	5%wt GT	10%wt	*Glass-set*
PHB5GT20V	95%wt PHB	5%wt GT	20%wt	*Glass-set*

After Ex, the blends were air-cooled and shredded into pellets (Figure 3.1) using a Felfil Desktop Plastic Shredder (Felfil) (Italy).

The pellets derived from the twin-screw processing were partially utilized in the creation of injection-molded samples using a Babyplast 10/12, equipped with a model 5A dumbbell sample mold in accordance with ISO 527 standards. The IM parameters are presented in Table 3.3. The variation in the parameters was set experimentally.

***Table 3.2** Temperature profile of the twin screw extruder*

	Head [± 1 °C]	**Zone 6** [± 1 °C]	**Zone 5** [± 1 °C]	**Zone 4** [± 1 °C]	**Zone 3** [± 1 °C]	**Zone 2** [± 1 °C]	**Zone 1** [± 1 °C]	**Hopper** [± 1 °C]	**Screw speed** [rpm]
GT-set and *5%-set*	150	158	160	162	162	155	150	40	30
Glass-set	150	155	156	158	158	151	146	40	80-100

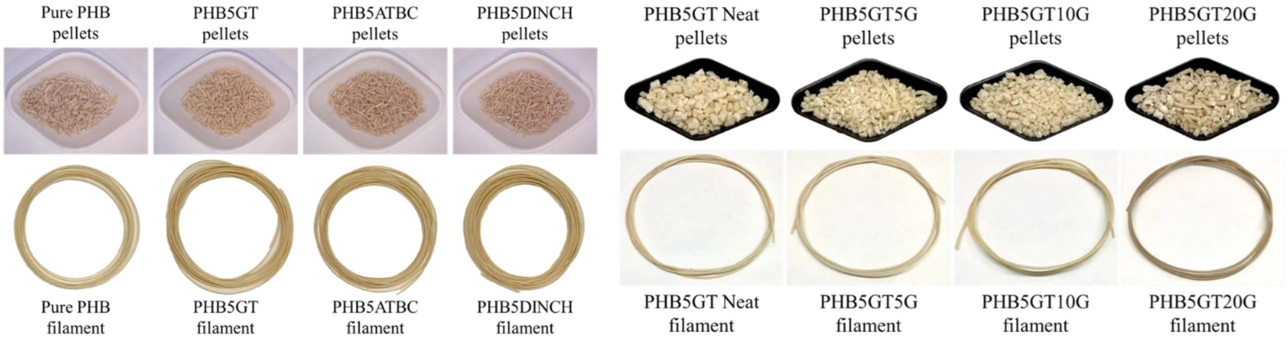

Figure 3.1 *Representative images of the extruded filaments obtained from different PHB formulations and pellets produced by filament cutting*

Table 3.3 *Injection-molding process parameters optimized for each formulation*

		PHB	PHB 2.5G	PHB 5GT	PHB 10G	PHB 5ATB	PHB 5DINCH	PHB5GT Neat	PHB5GT 5G	PHB5GT 10G	PHB5GT 20G
Temperatures [°C]	Plasticization cylinder	180	180	180	180	180	180	177	175	175	175
	Injection cylinder	170	165	165	160	165	170	170	165	165	165
	Nozzle	150	145	145	140	145	150	155	145	145	145
Shot size		15	19	20	21	17	17	15	15	15	15
Cooling time [s]		10	10	15	15	10	10	90	90	50	30
Extraction time [s]		0.1	0.07	0.07	0.07	0.05	0.05	0.1	0.1	0.1	manual

The plasticizing pressure, the injection pressure, the injection time, and the mold closing pressure were maintained at constant values equal to 80 bar, 40 bar, 3.5 s, and 70 bar, respectively. The extraction pressure was maintained at a value of 70 bar for all formulations except for PHB5GT20G, for which was set at 40 bar.

The remaining portion of the pellet resulting from twin-screw processing and shredding was employed to produce filaments suitable for FDM 3-dimensional (3D) printing. To this end, a benchtop extrusion system (Felfil Srl., Italy) comprising a single-screw extruder with an integrated cooling fan was employed. The filament diameter was set to 1.55 ± 0.1 mm by a thickness controller equipped with a spooler, in order to meet the maximum diameter requirement of 1.75 mm needed for 3D printing. To enhance the efficiency of filament Ex in the production of *Glass-set*, the manual pull mode of the extruder was set to a speed between 0.25 and 0.8 m/min, allowing for optimal processing parameters. The Ex parameters are presented in Table 3.4.

Table 3.4 *Single screw extrusion parameters for the calibrated filament production*

	Extrusion temperature [°C]	**RPM**	**Pull speed [m/min]**
PHB	186 ± 2	4	-
PHB2.5GT	184 ± 2	3	-
PHB5GT	183 ± 2	3	-
PHB10GT	180 ± 2	3	-
PHB5ATBC	185 ± 2	3	-
PHB5DINCH	185 ± 2	3	-
PHB5GT Neat	184 ± 2	2	0.25 – 0.30
PHB5GT5G	183 ± 2	3	0.62 – 0.74
PHB5GT10G	184 ± 2	3	0.71 – 0.76
PHB5GT20G	183 ± 2	3	0.72 – 0.80

3.3.2 3D printing

The filaments obtained after single screw Ex were used to 3D print complex porous scaffolds using the FDM technique. SolidWorks software was used to design cylindrical scaffolds with a 15 mm diameter and 5 mm height.

The scaffolds of *GT-set* and *5%-set* were then processed with PrusaSlicer software to set the appropriate printing parameters and 3D printed with a Prusa i3MKS+ printer equipped with a 0.4 mm nozzle. The layer height was set to 0.2 mm, and the strand width was set to 0.4 mm. The infill density and geometry were adjusted to 30% and set to a linear pattern, with the infill direction alternating by 90° between adjacent layers. A printing speed of 25mm/s was employed, and the Ex flow was set to 1.1 to compensate for any variability in the filament diameter. The cylinders were printed with 2 wall loops and no top or bottom layers. A 4-mm brim and an appropriate amount of glue were adopted to ensure proper adhesion to the building plate, which was heated to 60 °C. The printing temperature ranged between 200 and 180 °C, to investigate optimal conditions.

Slightly different parameters were used to optimize the fabricated scaffolds from the *Glass-set*. The printer used was a Hephestos2 (BQ) and the printing parameters were set using Ultimaker Cura software. The printing temperature was maintained at 186 °C for all formulations, the printing speed was reduced to 10 mm/min, the strand width was set at 0.38 mm, the brim plate adhesion was changed into a 3-layer, 4-mm expansion raft with a 0.2 mm air gap from the object, the two wall loops were removed, and finally, the infill density was set to 62%.

The infill design was chosen to obtain pores between 300 µm and 400 µm in size, which, based on the literature[8,9], is considered optimal to ensure the growth and subsequent differentiation of cells into osteoblasts and to promote angiogenesis.

The decision to remove the 2 wall loops was made to provide even better porosity at the sides of the scaffolds, as the lack of a complete and therefore non-porous outer contour ensures that cells can proliferate at the edge and not just in the central part of the scaffolds. In addition, during compression tests, we do not obtain zones of different resistance, but rather a structurally homogeneous whole.

3.4 Material characterizations

3.4.1 Fourier Transform Infra-Red Spectroscopy (FT-IR)

Fourier Transform Infra-Red (FT-IR) spectral data were obtained using a PerkinElmer Spectrum Two spectrometer with a diamond attenuated total reflection (ATR) crystal. Each spectrum was obtained by performing 16 scans with a spectral range of 4000 to 400 cm^{-1}. The resulting data were subsequently analyzed using Spectrum 10 software from PerkinElmer. The FT-IR setup enabled the structural analysis of the polymer, the pure plasticizer, and the various compounds.

3.4.2 Differential Scanning Calorimetry (DSC)

The thermal properties of plasticized PHB compounds and glass-containing composites were evaluated by Differential Scanning Calorimetry (DSC). The melting temperature (T_m [°C]), glass transition temperature (T_{gDSC} [°C]), melting enthalpy (ΔH_m [J/g]), and crystallinity degree (χ_c [%]) were derived from the scans.

A Q10 instrument from TA Instruments was used for analysis of *GT-se*t and *5%-set*, in a nitrogen atmosphere with a purge flow rate of 20 mL/min. Samples of approximately 10 mg were analyzed in triplicates. A DSC Q200 (TA Instruments, USA) was used for *Glass-set*. Similarly, analyses were performed in a nitrogen atmosphere at a flow rate of 50 ml/min and samples of 10 to 15 mg were analyzed in duplicates. In both cases, the thermal cycle was composed of a heating ramp from -60 °C to 200 °C, followed by a cooling ramp to return to -60 °C and a second heating ramp to 200 °C. All ramps were conducted at 10 °C/min.

The curves obtained from the DSC were then processed using TA Universal Analysis 2000 software (TA Instruments) to extrapolate T_m and ΔH_m from the first heating scan, T_c from the cooling scan, and $T_{g,DSC}$ from the second. χ_c was then calculated using Equation 3.4a, where ΔH_m is the melting enthalpy obtained from the DSC measurement while $\Delta H^0_{m,}$ is the melting enthalpy of the PHB if it were 100% crystalline, assumed to be 146 J/g[10,11].

$$\chi_c\,(\%) = \frac{\Delta H_m}{\Delta H_m^0} \cdot 100 \qquad \text{(Equation 3.4a)}$$

For the *Glass-set*, a modification of Equation 3.4a into Equation 3.4b allowed to take account of the melting enthalpy of the sample, normalized on the effective mass of polymer contained in the sample ($\Delta H_{m,norm}$), calculated as in Equation 3.5.

$$\chi_c\,(\%) = \frac{\Delta H_{m,norm}}{\Delta H_m^0} \cdot 100 \qquad \text{(Equation 3.4b)}$$

$$\Delta H_{m,norm} = \frac{\Delta H_m}{(1-\%glass)} \qquad \text{(Equation 3.5)}$$

3.4.3 Thermo-Gravimetric Analysis (TGA)

Thermo-Gravimetric Analysis (TGA) was conducted on samples of Glass-set using a Perkin Elmer TGA8000. The samples, with masses of 8-10 mg, were heated from 30 to 600°C at a heating rate of 10 °C/min in an N_2 atmosphere with purge flow of 20 ml/min. The results are presented as the percentage change in sample weight as a function of temperature. The degradation temperature (T_d [°C]) was calculated as the inflection point of the curve and the onset temperature (T_{onset} [°C]) as the point at which the tangent to the initial baseline intersects with the tangent from the steepest part of the degradation curve. T_{onset} marks the beginning of significant weight loss.

3.4.4 Viscosity

Under steady-state conditions, viscosity measurements were conducted using a rotational rheometer (Physica MCR 301 from Anton Paar, GmbH Austria) equipped with a Peltier heating system and a solvent trap kit. The relationship between shear rate and viscosity was analyzed at 190 °C, with shear rates ranging from 0.01 to 100 s^{-1}. A cone-plate geometry (CP50–1) was utilized for these experiments, featuring a diameter of 50 mm, an angle of 0.989°, and a gap of 99 µm. The steady-state viscosity data obtained were fitted using the Carreau-Yasuda model[12] to calculate the zero-shear viscosity, η_0. To ensure reproducibility, all experiments were performed three times.

3.4.5 Optical microscopy

The structure of the printed scaffolds was examined macroscopically using a USB digital microscope with MicroCapture Plus software and an OPTIKA B-380 series optical microscope (Optika Srl, Italy) with OPTIKA PROVIEW software for higher magnification. This allowed for a detailed assessment of individual strand deposition quality and evaluation of the overall porosity.

3.4.6 Scanning Electron Microscopy (SEM)

To gain a more detailed visual representation of the internal morphology and dispersion of the bioglass within the polymer matrix, as well as the compatibility between the PHB and the bioplasticizer, a series of analyses were conducted on samples of glass-set using the Nova NanoSEM 450 field emission scanning electron microscope (FE-SEM) (FEI Company, Bruker Corporation), with an acceleration voltage of 15 kV. These evaluations were conducted by analyzing the cross-section of the filaments. For illustrative purposes, a printed scaffold containing 20 wt% glass was selected as a representative example. All samples were obtained by cryo-fracturing the material in liquid nitrogen to achieve a brittle fracture surface. The analyzed sections were then electroplated with 10 nm of gold to ensure electric conductivity.

3.4.7 Tensile test

Uniaxial tensile tests (UTT) were performed on all sets of injection-molded samples (*GT-set*, *5%-set*, and *Glass-set*) using a 112, TesT GMBH Universal Testing Machine (Germany), equipped with a 2 kN load cell. Ten specimens of each material composition were tested, after clamping both ends, at a constant tensile speed of 0.5 mm/min, at room temperature until failure. The tensile properties of Young's modulus (E [MPa]), tensile strength (σ_B [MPa]), elongation at break (ε_B [mm/mm]), and toughness (T [MJ/m^3]) were recorded from the stress-strain curves and compared, to evaluate the effect of the plasticizer on mechanical properties.

3.4.8 Dynamic-Mechanical Analysis (DMA)

Thermal-mechanical properties of *GT-set* and *5%-set* were also investigated, according to *ASTM D7028,* through Dynamic Mechanical Analysis (DMA) using a TA Q800 instrument, on duplicate rectangular samples of dimensions 2×4×35 mm^3 obtained from the central part of the injection-molded specimens which were stored in vacuum at room temperature before testing. The test took place in single cantilever mode applying an amplitude strain deformation of 10 µm at a frequency of 1 Hz. The temperature ramp included an initial soak time of 10 min at -60 °C followed by a 3 °C/min ramp to 175 °C.

Dynamic storage (E' [MPa]) and loss (E'' [MPa]) moduli were collected, and damping factor (*Tanδ*) was calculated as the ratio between E'' and E' (*Tanδ* = E''/E'). The glass transition temperature ($T_{g,DMA}$ [°C]) for each composite was calculated as the temperature corresponding to the peak of the *Tanδ* curve.

Based on E' values obtained from the DMA analysis, the reduced modulus (E'_{red} [MPa/MPa]) was calculated according to Equation 3.6, similarly to Chapter 2:

$$E'_{red} = \frac{E'_{i-th}}{E'_{PHB}} \quad \text{(Equation 3.6)}$$

3.4.9 Compression test

To determine the mechanical properties of the biocomposite printed scaffolds of *Glass-set*, a compression test was performed on ten replicates for each batch of material produced. The tests were conducted at room temperature at a rate of 1 mm/min, with displacement monitoring, using an MTS 810 (USA) servohydraulic press, equipped with a 25 kN load cell. The test was considered concluded not at the complete failure of the specimen, but when the recorded force dropped below a value of 0.5 kN after surpassing the peak. The resulting data were used to generate stress-deformation graphs and extrapolate the stiffness, the maximum stress, maximum deformation at failure, and the energy absorbed as a function of the percentage of bioglass present in the scaffolds. These values were calculated by adapting the calculations employed for the tensile properties, considering the cross-section of the scaffold as it was 100% solid to normalize the values of strength.

3.4.10 Contact angle

To produce films suitable for contact angle measurements on composites of the *Glass-set*, sections of the filaments were subjected to a hot-pressing process using a laboratory press (Gibitre Instruments S.R.L., Italy). This was conducted following a cycle that comprised two minutes of temperature hold at 165 °C, followed by 10 seconds of nominal pressure of 180-190 kg at the same temperature.

The films were subjected to a contact angle test using commercial cow blood (PAEX, GmbH, Germany), with the objective of simulating the wettability of the glass-filled PHB scaffolds in accordance with their intended application in the body environment. The cow blood was utilized without further preparation and inserted into a 1ml plastic syringe equipped with an 18-gauge steel needle. To this aim, an optical contact angle measurement and contour analysis system (OCA 15EC, DataPhysics Instruments, Germany) was employed. A volume of 5 µl was dispensed onto the film with the sessile drop method, and the contact angle was calculated using the dpiMAX OCA software with an elliptical fit. The results are expressed as the mean value of the left and right angles, with a mean of 10 replicates for each composition.

Contact angle measurement can be achieved through the detection of the contour of the deposited drop and the subsequent measurement of the contact angle. The latter is defined as the angle "between the tangent to the solid surface and the tangent to the liquid-fluid interface at the contact line among the three phases"[13]. The extent of the contact angle determines the wettability of the surface. For values greater than 90°, the surface is considered poorly wettable and defined as hydrophobic in the case of water or hygrophobic in the case of other liquids. Conversely, for values of the contact angle smaller than 90°, the surface is considered wettable and defined as hydrophilic or hygrophilic, respectively, in the case of water or other liquids[13].

3.5 Results and discussion: Study of plasticized PHB

3.5.1 Processability

The processability of PHB through conventional methods, such as Ex and IM, presents significant challenges due to its narrow thermal processing window and susceptibility to thermal degradation. In this context, an investigation into the compounding of PHB with additives such as GT and other commercial plasticizers may offer potential solutions to improve its melt stability and processing performance during Ex and IM.

The experimental identification of the optimal temperature profile for the twin-screw extruder represented a significant challenge. In preliminary attempts, the application of a temperature profile between 175 °C and 180 °C, based on the T_m reported in the data sheet, resulted in the degradation of PHB. The polymer displayed a darker coloration and high fluidity, which is likely the result of alterations in its molecular structure, including the fragmentation of polymer chains and/or the formation of undesirable functional groups. This alteration was also observed during the subsequent processability of the material during filament production using the single-screw extruder, which exhibited even greater adverse effects.

Accordingly, the temperature profile selected for the twin-screw Ex of plasticized PHB formulations (Table 3.2) is the one that yielded the most favorable results in terms of processing and ensures the consistency of the material flowing from the Ex head exit. The extruded materials have exhibited homogeneity and continuous flow, although the observed melt strength has not been sufficient to produce a windable filament[14]. Subsequently, IM was employed to fabricate dog bone specimens for the evaluation of the mechanical properties of the plasticized PHB formulations (Figure 3.2). During the process, the key parameters, including temperature, shot size, cooling time, and extraction time, were optimized as outlined in Table 3.3. To ensure adequate material fluidity for injection, the temperature of the plasticization cylinder was maintained at 180 °C, which is slightly above the T_m of the neat PHB. It is noteworthy that the injection cylinder and nozzle temperatures were reduced by 5 °C (to 170 °C) for PHB2.5GT, PHB5GT, and PHB5ATBC, and by 10 °C for PHB10GT, in comparison to the temperature used for neat PHB. The temperatures for PHB5DINCH remained unchanged at 180 °C, consistent with those used for pristine PHB (Table 3.3). The reduction in injection temperature is indicative of the enhanced fluidity imparted by the plasticizers. The molded specimens exhibited no significant differences in appearance, apart from minor chromatic variations due to the color of the plasticizers used (Figure 3.2). Notably, the decrease in injection temperature did not impact on the final surface quality of the samples, while it effectively minimized the potential for thermal degradation.

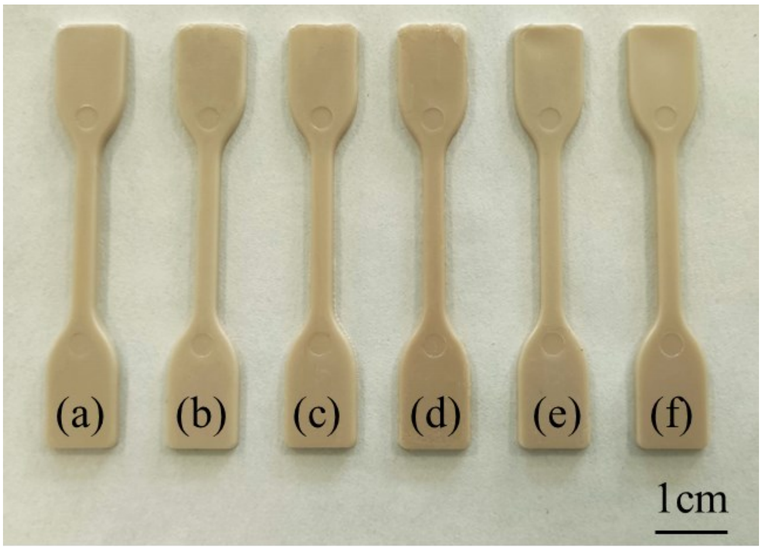

Figure 3.2. *Injection-molded specimens: (a) PHB, (b) PHB2.5GT, (c) PHB5GT, (d) PHB10GT, (e) PHB5ATBC and (f) PHB5DINCH*

3.5.2 DSC characterization

DSC was used to investigate the thermal properties of the extruded compound. The introduction of the plasticizer between the polymer chains induces a weakening of the interactions between the macromolecules functional groups. This, in turn, increases the mobility of the macromolecules and reduces the energy required to initiate their movement[15].

Extrapolation of the values from the thermograms presented in Figure 3.3a, allowed to observe a reduction in $T_{g,DSC}$ (Figure 3.4a), indicative of the phenomenon described. In particular, a decrease in $T_{g,DSC}$ was observable from 4 °C for pure PHB to 0 °C and -5 °C with the addition of only 2.5 and 5 wt% of GT, respectively. This decline suggests a notable and substantial plasticization effect. No additional reduction in $T_{g,DSC}$ was observed with the incorporation of 10 wt% GT, with the resulting temperature approximately -4 °C, comparable to that of PHB5GT.

The DSC curves (Figure 3.3) were subjected to further processing in order to evaluate the impact of GT on the T_m and χ_c, calculated in accordance with Equation 3.4a, of PHB. The melting processability of semicrystalline polymers, such as PHB, can be significantly evaluated by considering the parameter T_m.

As illustrated in Figure 3.4c, the addition of plasticizers has resulted in a reduction of the T_m, which decreased from 177 °C for the pure polymer to 175, 173, and 169 °C for 2.5, 5, and 10 wt% of GT, respectively. Additionally, the reduction in the T_m has been accompanied by a decline in χ_c (Figure 3.4b). Notably, the PHB exhibited an χ_c of 59%, which decreased to 58% for PHB2.5GT and to 52% for PHB5GT. However, 10 wt%

of GT did not result in any further reduction. Similarly, the plasticizing effect of GT became evident during the cooling scan of DSC analysis. As illustrated in Figure 3.3c, an incremental increase in GT content led to a discernible decline in the crystallization temperature of the formulations. In particular, the T_c of PHB exhibited a decline from 119 °C to 115 °C and 112 °C, respectively, with the incorporation of 2.5% and 5% GT. Nevertheless, a 10 wt% GT addition did not result in a further decrease in T_c (Figure 3.3d).

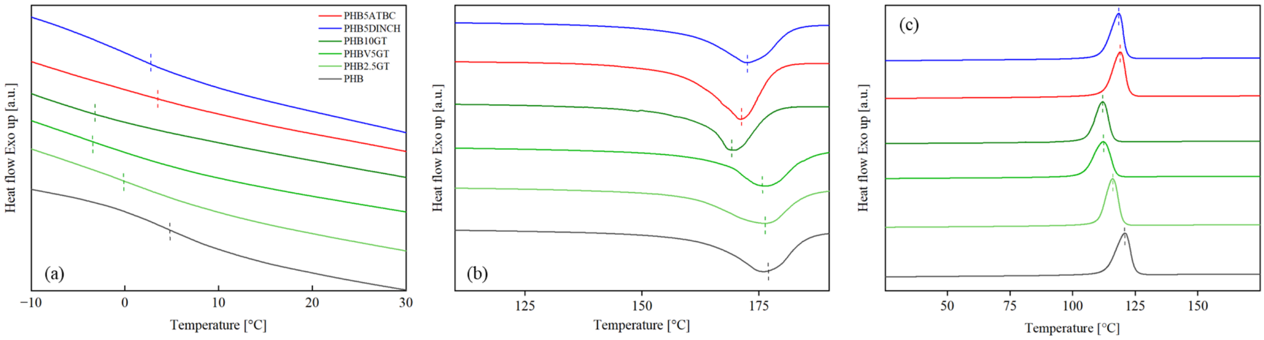

Figure 3.3 *DSC thermograms of neat PHB and PHB-GT compounds after twin-screw extrusion processing. Highlight of the curves (a) second heating scan from -10 to 30 °C (T_g), (b) first heating scan from 110 to 190 °C (T_m), and (c) cooling scan from 175 to 25 °C (T_c)*

Based on the analysis of the experimental results, PHB5GT was identified as the most promising formulation and was selected for comparison with the formulations containing 5 wt% of the commercial plasticizers ATBC and DINCH (*5%-set*). Figure 3.4a illustrates that a 5wt% GT addition was more effective than a 5wt% ATBC and 5wt% DINCH addition in lowering the $T_{g,DSC}$ to a significantly greater extent. This finding indicates that the incorporation of the two commercial plasticizers had a negligible impact on $T_{g,DSC}$ in comparison to neat PHB. In contrast, the effects of the GT, ATBC, and DINCH plasticizers on the T_m were found to be comparable, as illustrated in Figure 3.4b. Additionally, it is noteworthy that GT demonstrated greater efficacy than the two commercial additives in reducing the χ_c (Figure 3.4c) and the T_c, as illustrated in Figure 3.4d. The latter additives had only a minor effect on these parameters. A summary of the DSC results is provided in Table 3.5 for reference.

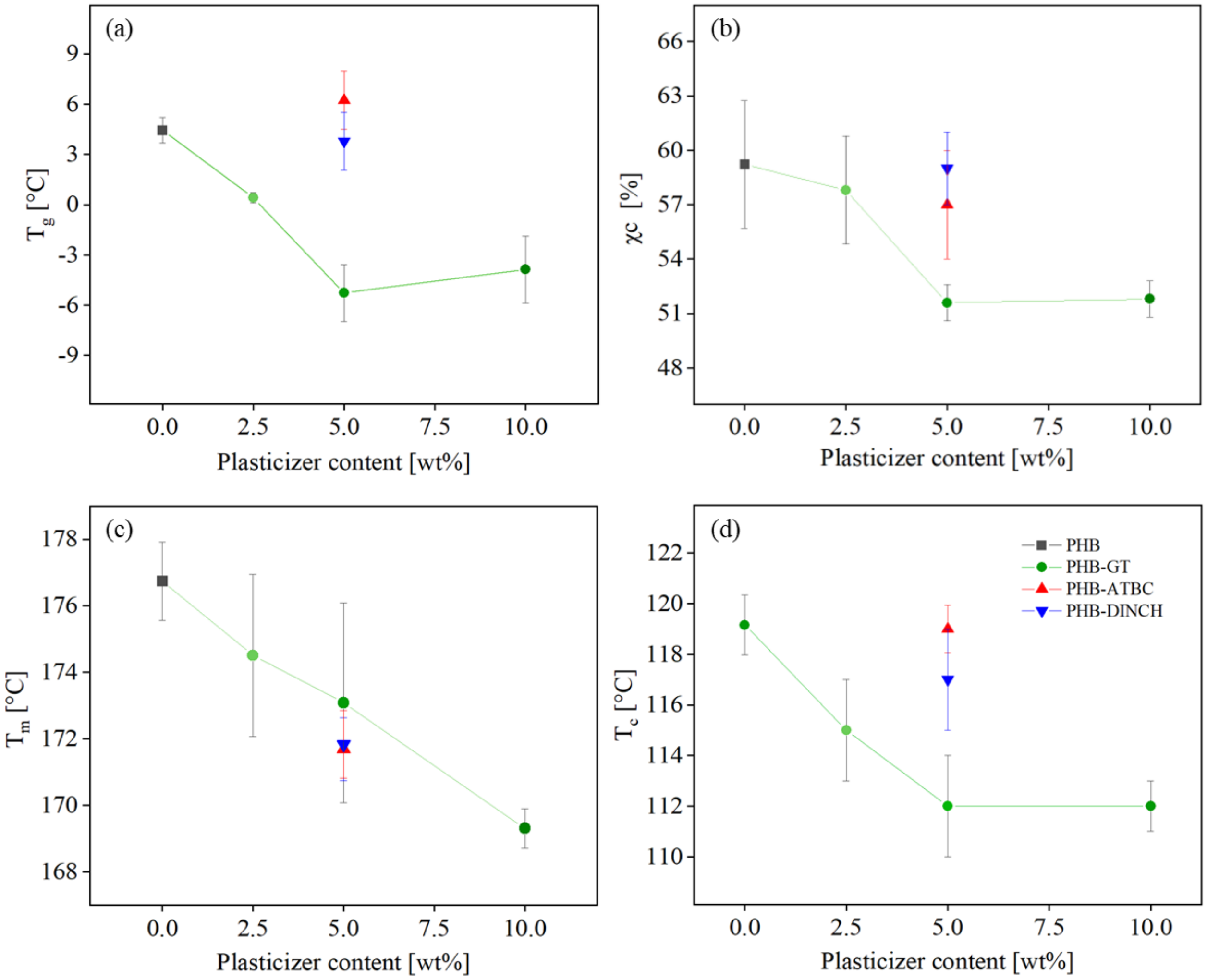

Figure 3.4 *(a) Glass transition temperature (T_g), (b) crystallinity degree (χ_c), (c) melting temperature (T_m), calculated by Eq. 2), and (d) crystallization temperature (T_c) of neat PHB, PHB-GT compounds and PHB compounded with 5% wt. of ATBC and DINCH*

Table 3.5 *Thermal properties extrapolated from DSC thermograms. Glass transition temperature ($T_{g,DSC}$), melting temperature (T_m) and crystallinity degree (χ_c) of GT-set and 5%-set*

	T_g (°C)	**T_m (°C)**	**χ_c (%)**
PHB	4 ± 1	177 ± 1	59 ± 4
PHB2.5GT	0 ± 1	175 ± 2	58 ± 3
PHB5GT	-5 ± 2	173 ± 3	52 ± 1
PHB10GT	-4 ± 2	169 ± 1	52 ± 1
PHB5ATBC	6 ± 2	172 ± 1	57 ± 3
PHB5DINCH	4 ± 2	172 ± 1	59 ± 2

3.5.3 TGA characterization

The thermal stability of the material was not significantly affected by the plasticizers, as evidenced by TGA results.

In consideration of the processing temperatures employed with twin-screw Ex, IM, and single-screw Ex, the mass loss was determined to be less than 0.5% was obtained. This minimal loss is considered acceptable, likely attributable to the evaporation of residual moisture rather than any significant polymer degradation. As illustrated in Figure 3.5, the TGA curves for all the materials exhibited a single degradation event, indicating that the degradation process occurs in a single step. This suggests that the plasticizer is distributed homogeneously within the polymer matrix[16]. The onset of the degradation curve T_{onset} was calculated by identifying the point of intersection between the plateau of the initial phase and the linear degradation phase. For the *GT-set,* the T_{onset} was approximately 305±2 °C, while slightly higher values were observed for the commercial bioplasticizers, with ATBC and DINCH showing T_{onset} values around 308 °C and 310 °C, respectively. The temperature at which the maximum rate of degradation occurs, designated as the degradation temperature T_d, was derived from the inflection point on the TGA curve, which corresponds to the peak of the derivative[17].

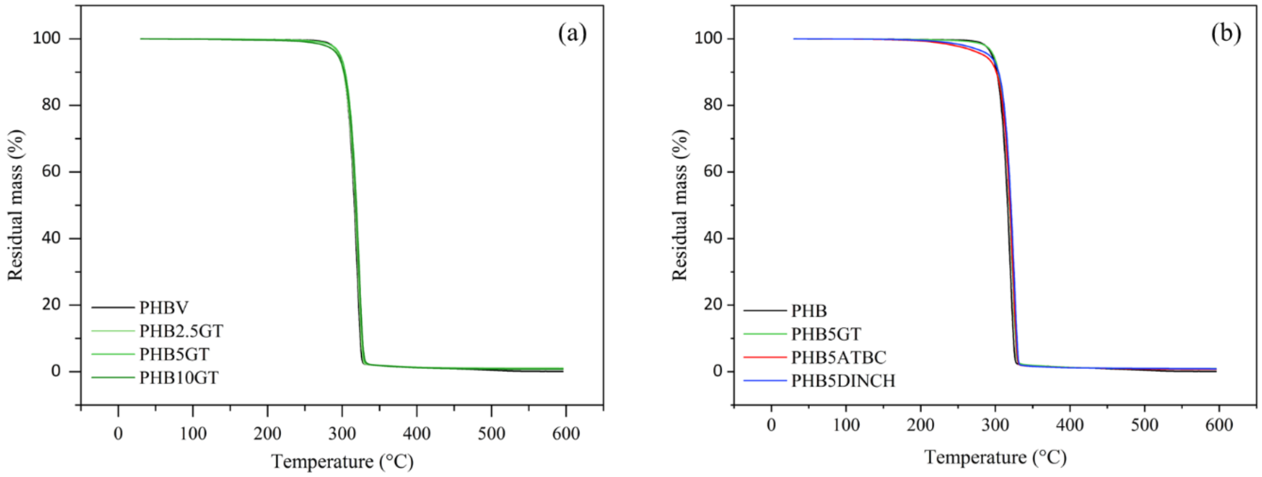

Figure 3.5 *Thermograms of (a) GT-set, and (b) 5%-set compounds*

The mean T_d values for the GT-set were approximately 321 ± 1 °C across all compositions, indicating that varying plasticizer concentrations did not significantly affect the thermal degradation properties. This is particularly noteworthy, as the use of bioplasticizers often results in decreased thermal stability[16,18]. In contrast, ATBC and DINCH exhibited a slight increase in the degradation temperature of PHB, though the observed variation did not exceed the standard deviation range and thus was not found to be significant. At the end of the heating ramp, more than 99% weight loss was achieved for all compounds, corresponding to approximately total degradation of the organic matter.

These TGA results, summarized in Table 3.6, corroborate the assertion that the plasticizers exerted a negligible influence on the material's overall thermal stability, thereby ensuring consistency across the various formulations and guaranteeing that the materials can withstand the requisite processing conditions.

Table 3.6 *Thermal degradation parameters obtained by TGA for GT-set and 5%-set*

	Degradation temperature (T_d) [°C]	**Onset temperature (T_{onset}) [°C]**	**Residual mass (%)**
PHB	321.6 ± 0.4	306.4 ± 0.4	0.56 ± 0.62
PHB2.5GT	320.4 ± 2.4	304.4 ± 2.1	1.03 ± 0.05
PHB5GT	321.3 ± 2.2	305.1 ± 2.0	0.89± 0.05
PHB10GT	322 ± 0.5	306.4 ± 0.1	0.9± 0.1
PHB5ATBC	323.3 ± 1.3	308.3 ± 0.7	0.9 ± 0.1
PHB5DINCH	326.5 ± 0.9	310.4 ± 1.6	0.8 ± 0.2

3.5.4 Viscosity measurements

The rheology of a polymer is typically affected by the incorporation of plasticizers in the reduction of the strength of the intermolecular forces[19]. As a result, a decrease in viscosity is obtained, directly impacting the melt processing parameters including the temperature and shear rate necessary for material processing. The examination of the rheological behavior of plasticized polymer compounds allows the optimization of the processing conditions, reducing time and energy consumption.

The rheological characteristics of PHB/GT blends were examined at 190 °C over a shear rate range of 0.001 to 1000 s^{-1}, representing the typical values required for techniques such as Ex, IM, and FDM[20,21]. A shear-thinning behavior, where the viscosity declined in correlation with an increase in the shear rate, was displayed by all samples. This phenomenon can be attributed to the gradual alignment of the polymer chains[22]. As Figure 3.6 illustrates, an increase in the plasticizer content resulted in a further reduction in viscosity. The initial viscosity (η_0) of pure PHB was 65 Pa•s, and the addition of 2.5, 5, and 10 wt% GT resulted in a reduction of this value to 53, 47, and 35 Pa•s, respectively. As anticipated, the highest GT content (10 wt%) produced the most substantial viscosity drop across the entire shear rate range. The behavior of PHB2.5GT and PHB5GT was found to be quite similar between 0.001 and 1 s⁻¹. However, at higher shear rates, they began to diverge. PHB5GT exhibited a more pronounced decrease in viscosity, particularly between 10 and 100 s⁻¹, a range typically associated with Ex[21]. The viscosity decline became even more pronounced in the 100 to 1000 s⁻¹ range, which is characteristic of IM[21] and FDM[20]. Furthermore, an investigation was conducted to assess the rheological behavior of PHB5ATBC and PHB5DINCH in identical conditions, to evaluate the effects of plasticization. As reported in Figure 3.6, the performance of was comparable to PHB5GT, with a η_0 of 46 Pa•s. In contrast, PHB5DINCH demonstrated an η_0 of 54 Pa•s, exhibiting behavior that was analogous to that observed in PHB2.5GT. Across the shear rate range relevant to processes through Ex, IM, and FDM, the viscosity levels observed with both commercial plasticizers (ATBC and DINCH) were found to be highly comparable to those observed with 5 wt% GT.

These findings suggest that GT is a promising bio-based plasticizer for PHB. Furthermore, the incorporation of plasticizers can significantly influence the mechanical properties of polymers[23].

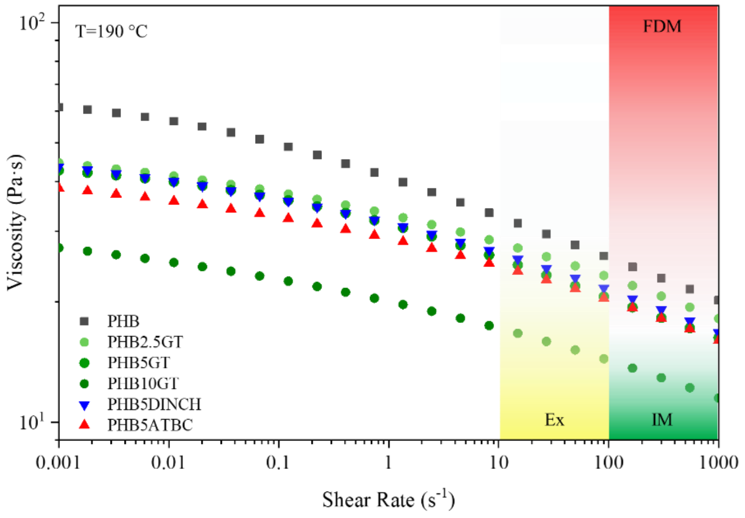

Figure 3.6 *Rheological behavior at 190°C of neat PHB and its compounds with GT, ATBC and DINCH. The shaded areas represent the typical range of shear rate for extrusion (Ex, yellow), injection-molding (IM, green) and fused deposition modelling (FDM, red)*

3.5.5 FT-IR characterization

The spectra reported in Figure 3.7 represent the plasticizers and the plasticized formulations. The FT-IR analysis indicated that there were no notable alterations in the chemical structure of PHB or the various compounds under examination (the peak assignments are detailed in Table 3.7). The unaltered structure revealed that thermal processing did not produce any observable deterioration in material quality. Furthermore, the incorporation of plasticizers did not result in any discernible alterations to the polymeric structure, even when subjected to thermal processing[24,25].

Table 3.7 *FT-IR peak assignments for PHB and all used plasticizers (DINCH, ATBC and GT) and their corresponding descriptions*

	Peak wavenumber (cm^{-1})				**Description**
Letter ref.	**DINCH**	**ATBC**	**GT**	**PHB**	
A, D, G, J	2955-2850	2960-2874	2960-2920	2980-2850	C-H in CH_3 and CH_2 asymmetric and symmetric stretching
B, E, H, K	1729	1736	1735 (ester) 1713 (ketone)	1720	C=O stretching
L	-	-	-	Doublet 1274-1260	C(=O)-O stretching
C, F, I, M	1170	1178	1149	1179	C-C(=O)-O stretching
N	-	-	-	Doublet 1053-1043	C-C(=O) stretching
O	-	-	-	977	CH_3 rocking
P	-	-	-	514	C-C (skeletal) deformations

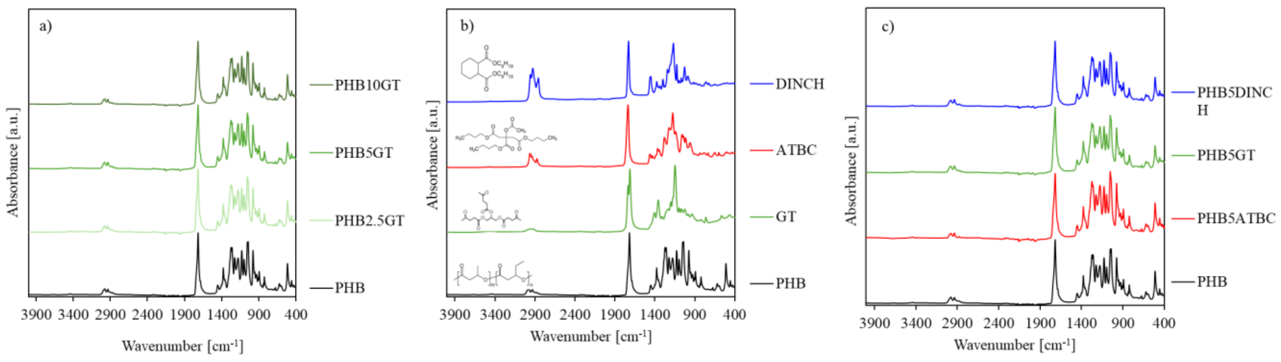

Figure 3.7. *a) FT-IR spectra of the polymer matrix, PHB, and the plasticizers DINCH, ATBC, and GT; b) FT-IR spectra of PHB plasticized with GT; c) FT-IR spectra of PHB and PHB plasticized with 5% wt. GT, ATBC and DINCH*

3.5.6 DMA characterization

To gain a deeper insight into the viscoelastic behavior of the polymeric compounds, the specimens were subjected to DMA. As may be expected, in the *GT-set*, an increase in plasticizer content resulted in a reduction in E' across the entire temperature range. This trend aligns with previous findings by Scandola et al., who attributed the reduction to a decrease in the polymer's crystalline content as plasticizer concentration increased[26] (Figure 3.8a).

As the GT content increased, the E'' which correlates with the rheological behavior and energy dissipation resulting from irreversible polymer chain movement, also exhibited a downward shift towards lower temperatures. Concurrent with this phenomenon was a rise in the subtended area (Figure 3.8b). These observations indicate that an increasing proportion of energy is consumed in the relaxation of the polymer chains at lower temperatures, which demonstrates an effective plasticization effect.

A broadening and a shift of the initial peak, corresponding to $T_{g,DMA}$, observable in the $Tan\delta$ curves (Figure 3.8c) can be attributed to β relaxation[26]. The addition of different amounts of GT resulted therefore in an earlier onset of transition and a reduction in $T_{g,DMA}$, which is the primary effect of incorporating a plasticizer into a rigid polymer, thereby enhancing flexibility[27]. Furthermore, a second peak, associated with α relaxation, related to the mobility of more extended segments of the polymeric chains, was observed to shift towards lower temperatures in proportion to the plasticizer content[28]. The observed reduction in E' and broadening of $Tan\delta$ can be attributed to the presence of the plasticizer molecules, which, when distributed uniformly in the polymer matrix, can be postulated to weaken intermolecular interactions and increase free volume in the polymer[23,29].

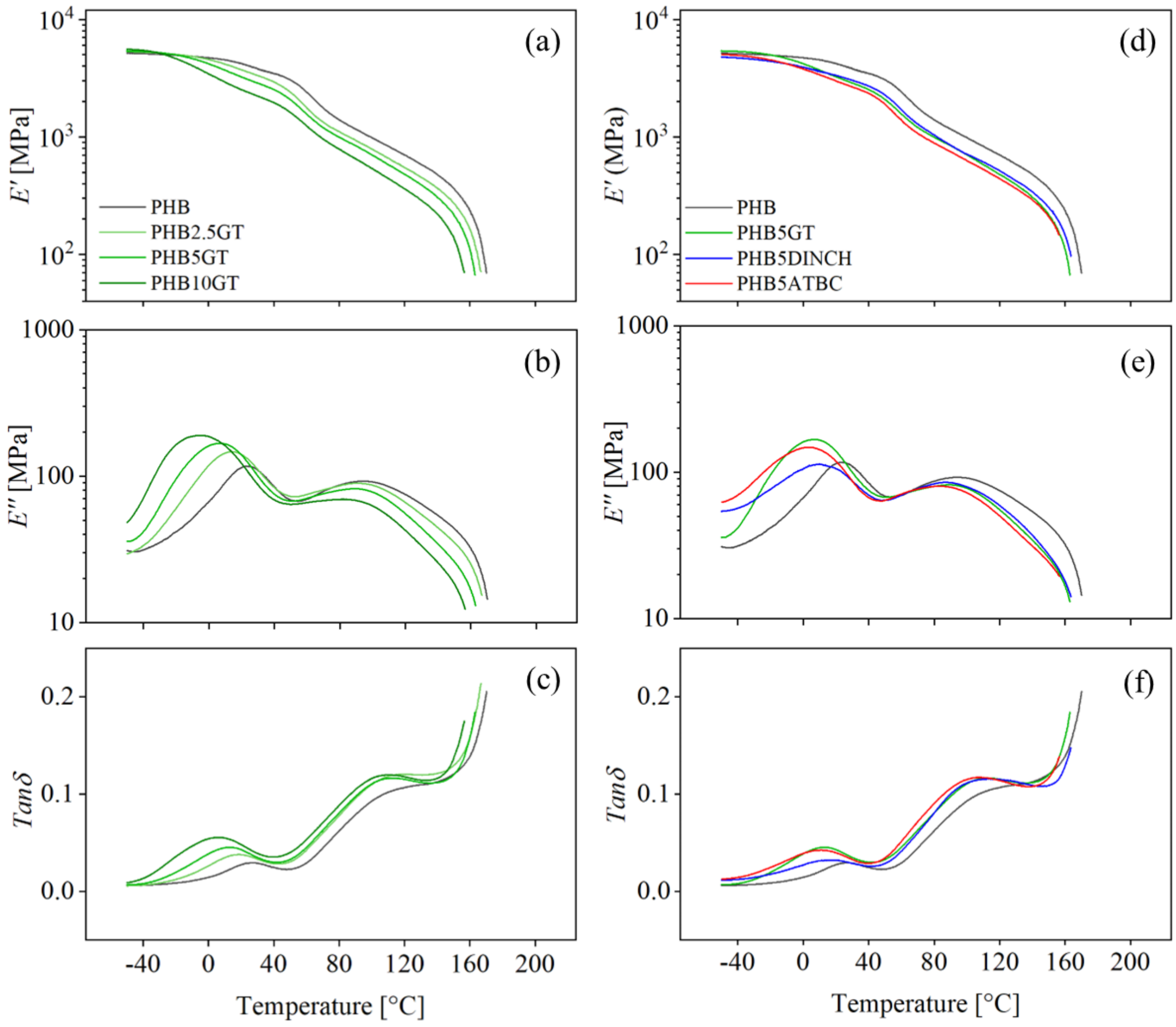

Figure 3.8 *(a) Storage modulus (E'), (b) loss modulus (E"), and (c) damping factor (Tanδ) of GT-set, and (d) E', (e) E", and (f) Tanδ of and 5%-set, obtained from DMA tests*

The DMA curves for the *5%-set* are shown in Figure 3.8d-f. The compounding with 5 wt% of GT, DINCH, and ATBC gives *E'* values (Figure 3.8d) lower than those of pure PHB. Notably, the reduction in *E'* obtained with PHB5GT is similar to the one observed with the addition of ATBC, which has been demonstrated as one of the most effective citrate-based plasticizers for PHA[30].

All plasticized formulations exhibited a reduction in $T_{g,DMA}$ compared to the unmodified PHB as shown in Figure 3.9a and summarized in Table 3.8.

Figure 3.9 also reports the reduced modulus (E_{red}) (Equation 3.6). To further clarify the influence the plasticizers have on the thermo-mechanical behavior of PHB, E_{red} was calculated at various temperatures. The temperatures of 0 °C (below T_g, Figure 3.9b), 25 °C (room temperature, Figure 3.9c), and 36 °C (average body temperature, Figure 3.9d) were considered in light of PHB's potential biomedical applications[31]. A general reduction in E_{red} is observed with increasing GT content at all temperatures (Figure 3.9b-d). Moreover, the decline in E_{red} is more pronounced at temperatures above the glass transition region ($T_{g,DMA}$, and E_{red} values are provided in Table 3.8), emphasizing greater plasticization efficiency in conditions relevant to practical applications and processing. For example, in the case of PHB5GT, the E_{red} is observed to decrease by approximately 12% below T_g, and by more than 24% above T_g, in comparison to pure PHB. Similarly, varying concentrations of plasticizer yield analogous outcomes. A comparison between E_{red} values for GT and commercial plasticizers at 25 and 36 °C (Figure 3.9b-d) reveals comparable behavior. The intercalation of plasticizer molecules among macromolecular chains weakens intermolecular forces, which lowers T_g and enhances flexibility and strain at break.

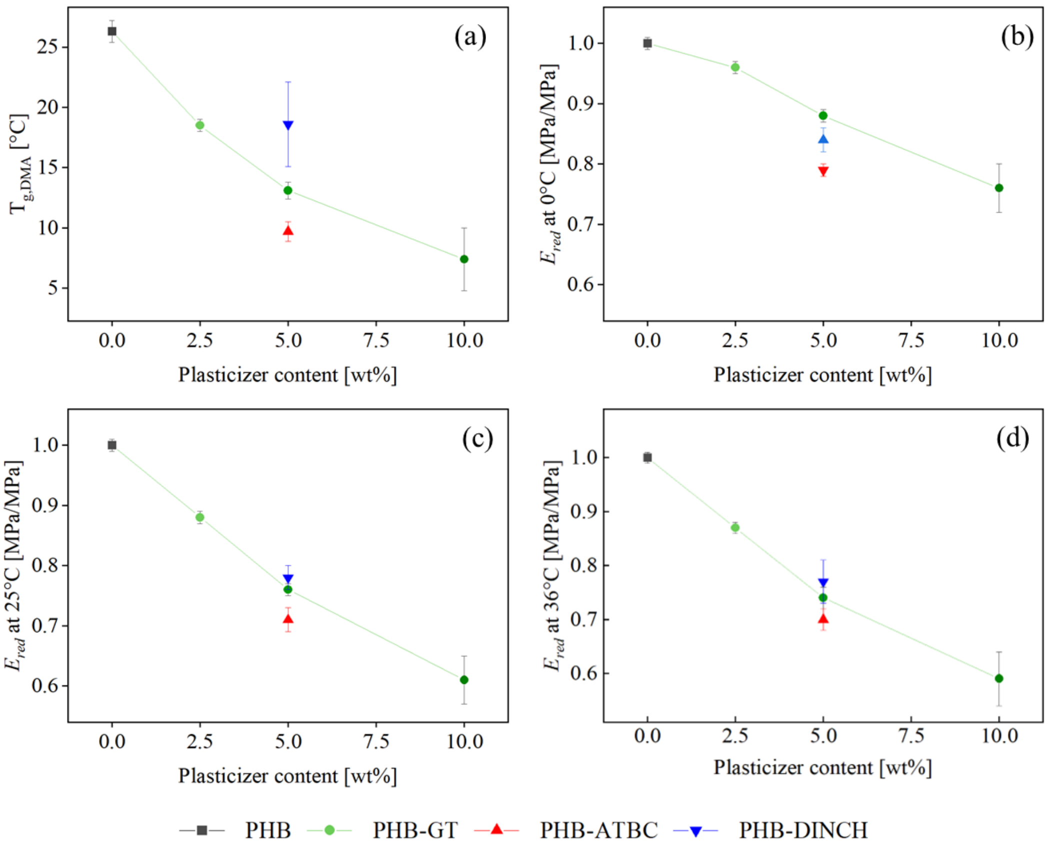

Figure 3.9 *(a) Glass transition temperature from DMA data ($T_{g,DMA}$); E_{red} (calculated by Equation 3.6) extrapolated at (b) 0°C, (c) 25°C, and (d) 36°C, as a function of the plasticizer GT content*

Table 3.8 *Glass transition temperatures ($T_{g,DMA}$) and reduced moduli (E_{red}) for each composition determined at different temperatures (0, 25 and 36°C) for GT-set and 5%-set*

	$T_{g,DMA}$ [C°]	**E_{red}@0°C [MPa/MPa]**	**E_{red}@25°C [MPa/MPa]**	**E_{red}@36°C [MPa/MPa]**
PHB	26.3 ± 0.9	1.00 ± 0.01	1.00 ± 0.01	1.00 ± 0.01
PHB2.5GT	18.5 ± 0.5	0.96 ± 0.01	0.88 ± 0.01	0.87 ± 0.01
PHB5GT	13.1 ± 0.7	0.88 ± 0.01	0.76 ± 0.01	0.74 ± 0.02
PHB10GT	7.4 ± 2.6	0.76 ± 0.04	0.61 ± 0.04	0.59 ± 0.05
PHB5ATBC	9.7 ± 0.8	0.79 ± 0.01	0.71 ± 0.02	0.70 ± 0.02
PHB5DINCH	18.6 ± 3.5	0.84 ± 0.02	0.78 ± 0.02	0.77 ± 0.04

3.5.7 Tensile test characterization

To further investigate the mechanical behavior of PHB and plasticized formulations, the use of UTT was employed. The data for E, σ_B, ε_B, and T are presented in Table 3.9.

Table 3.9 *Average value and standard deviation of the mechanical properties determined by tensile test for GT-set and 5%-set*

	Young's modulus (E) [MPa]	**Tensile strength (σ_B) [MPa]**	**Elongation at break (ε_B) [%]**	**Toughness (T) [MJ·m^{-3}]**
PHB	2454 ± 84	27.8 ± 1.7	1.16 ± 0.1	0.17 ± 0.02
PHB2.5GT	1808 ± 71	23.9 ± 1.8	1.40 ± 0.1	0.19 ± 0.04
PHB5GT	1753 ± 126	23.5 ± 1.9	1.53 ± 0.1	0.20 ± 0.05
PHB10GT	1311 ± 98	14.1 ± 1.7	1.09 ± 0.2	0.08 ± 0.03
PHB5ATBC	1479 ± 65	20.4 ± 2.1	1.54 ± 0.2	0.18 ± 0.04
PHB5DINCH	1638 ± 50	21.0 ± 1.3	1.34 ± 0.1	0.14 ± 0.03

PHB is recognized as a polymer with high stiffness and limited elongation at break[5]._Despite the persistence of typical brittle fracture across all formulations (Figure 3.10), the incorporation of GT resulted in a notable reduction in E and a comparatively smaller decline in σ_B relative to unmodified PHB.

The incorporation of 2.5 and 5 wt% GT resulted in a 26% and 28% reduction in stiffness, respectively, as observed in Figure 3.11a, as well as a 14% and 16% decrease in σ_B, as shown in Figure 3.11b. In light of the typical brittleness of PHB and the relatively low concentrations of GT employed, the observed increases in ε_B of 21% and 32% (Figure 3.11c) were noteworthy, resulting in a substantial narrowing of the mechanical gap between PHB and conventional plastic materials. For PHB10GT, E followed a similar decreasing trend, while σ_B showed a sharp decrease of 49% (Figure 3.11a and b). In contrast, ε_B did not consistently increase with increasing GT content but decreased by 6% compared to neat PHB when 10 wt% GT was added (Figure 3.11c).

The results of the mechanical testing indicated that a GT concentration of 5 wt% provided the optimal balance between a reduction in stiffness and an enhancement in elongation at break. Furthermore, it was observed that the mechanical performance of said formulation was comparable to that of commercial plasticizers, such as ATBC and DINCH, at the same concentration (Figure 3.11a-c). Furthermore, the incorporation of GT enhanced the *T* of the material in question, when compared to pure PHB. PHB5GT showed superior performance overall. However, an increase in the additive content beyond 5 wt% led to a decline in toughness (Figure 3.11d).

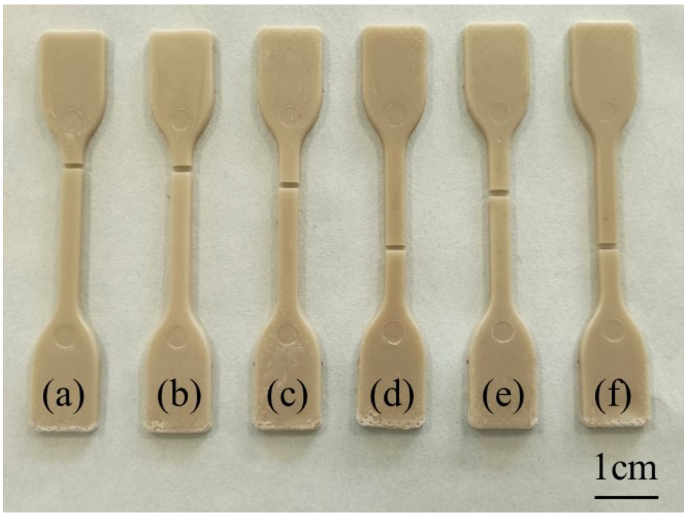

Figure 3.10. *Injection-molded specimens after fracture achieved by tensile test: (a) PHB, (b) PHB2.5GT, (c) PHB5GT, (d) PHB10GT, (e) PHB5ATBC and (f) PHB5DINCH*

PHB5GT and PHB5ATBC demonstrated comparable toughness improvements (0.20 and 0.18 MJ/m³, respectively) relative to neat PHB (0.17 MJ/m³), whereas PHB5DINCH exhibited a decline to 0.14 MJ/m³, aligning with the observed trend in other mechanical parameters.

The findings of the UTT substantiate the hypothesis that GT molecules effectively facilitate an increase in the free space between macromolecular chains, thereby reducing intermolecular forces and enhancing chain mobility.

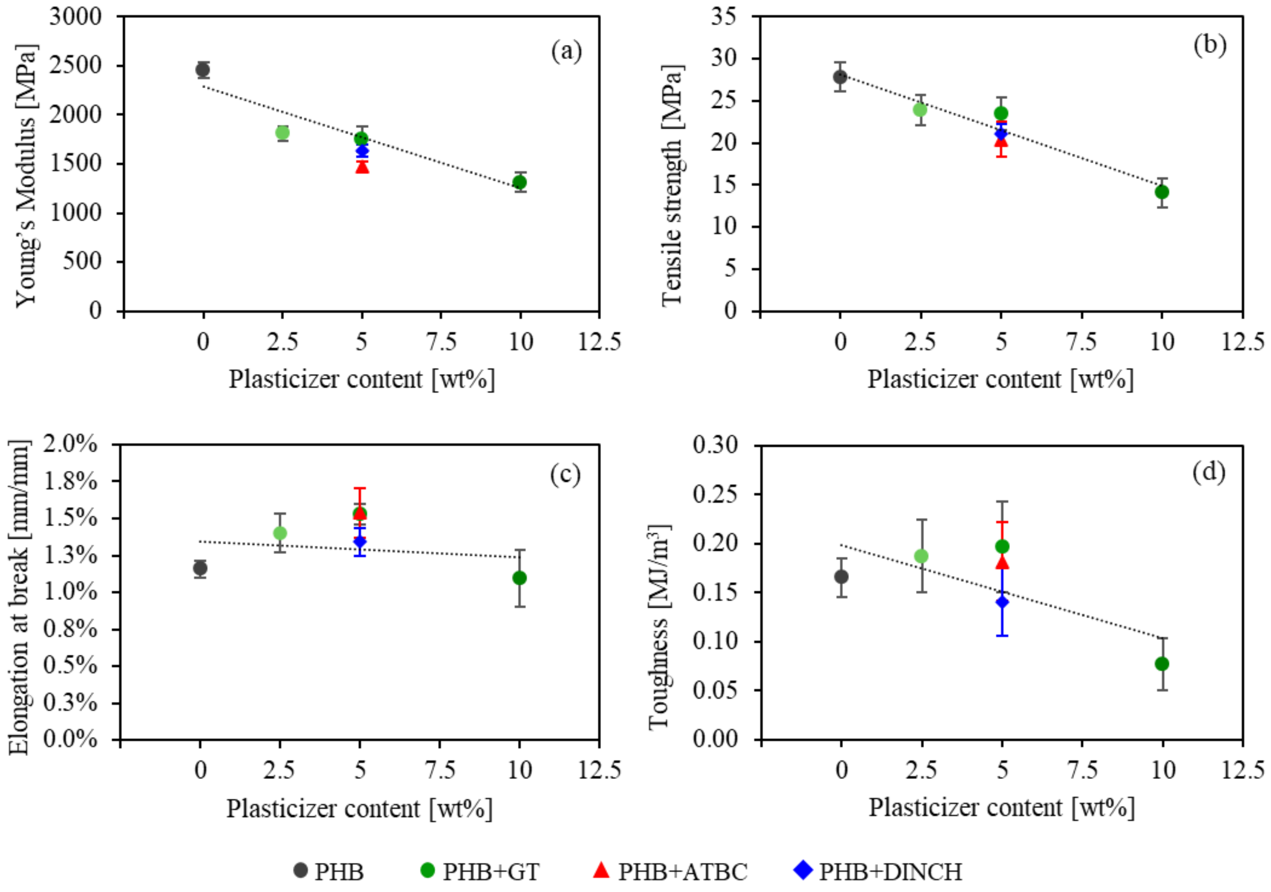

Figure 3.11 *(a) Young's modulus (E), (b) tensile strength (σ_B), (c) elongation at break (ε_B) and (d) toughness (T) as a function of the plasticizer content, obtained by UTT*

3.5.8 Analysis of FDM printed scaffolds through optical microscopy

The filaments obtained with single screw Ex were used to fabricate porous scaffolds through FDM.

The potential of this kind of scaffold in biomedical applications like the regeneration of bone tissues[32,33] can be supported by the previously demonstrated non-toxicity of GT[6]. The scaffolds are customizable and designed with the specific intention of replicating the intricate structure of bone, thereby providing an optimal environment for cellular proliferation and angiogenesis. Bone regeneration scaffolds are typically constructed with an interconnected porous design that facilitates the transport of nutrients and the elimination of cellular metabolic waste[34].

The cylindrical scaffolds, illustrated in Figure 3.12a, were 3D-printed at varying temperatures and plasticizer concentrations to enhance print quality. The initial printing temperature was set at 200 °C for all formulations, and this value was then reduced in 5 °C increments down to 180 °C. When the temperature was reduced below 180 °C, the polymer failed to attain the requisite molten state viscosity or even a complete melting, in accordance with the DSC results on T_m (Figure 3.4). Optical microscopy was employed to assess the quality of the printed scaffolds in relation to the printing temperature and the formulation composition.

The printed porous scaffolds have been analyzed through optical microscopy to investigate the quality of the printed object, as a function of both the printing temperature and compound composition. A temperature of 190 °C yielded satisfactory print quality with a 2.5 wt% GT concentration, and a further reduction to 180 °C was achievable for the PHB5GT and PHB10GT samples (Figure 3.12a). It is noteworthy that the PHB5GT scaffold (Figure 3.12A) exhibited comparable print resolution to that of pure PHB printed at the temperature of 200 °C. Conversely, the PHB10GT exhibited filament thinning and irregularity in unsupported regions, resulting in a droplet-like shape at filament intersection points. This effect may be attributed to a considerable drop in the viscosity of the molten material, which is indicated in Figure 3.7.

Overall, the incorporation of GT resulted in a reduction in printing temperature by up to 20 °C without affecting the resolution of pure PHB filament printed at 200 °C (Figure 3.12a). This finding is significant because it is widely acknowledged that 200 °C marks the onset of thermal degradation in PHB, resulting in a rapid and uncontrollable decline in molecular weight[35,36].

As already highlighted by the previous characterizations, PHB5GT was chosen as the most promising formulation and therefore further investigations were made. As the printing temperature increased from 180 to 200 °C, the material viscosity decreased, resulting in filament thinning, particularly in unsupported areas of the print. Considering 195 and 200 °C, the two highest tested printing temperatures, the thinning phenomenon intensified, resulting in the filament failing and compromising the integrity of the print geometry, as illustrated in Figure 3.12b. Filament deposition was found to be most consistent and uninterrupted at 180 °C (Figure 3.12b). At this temperature, the scaffold's internal pores exhibited the greatest stability in maintaining a square shape across the entire surface, including the perimeter, with a resolution comparable to that of pristine PHB printed at 200 °C. Furthermore, the printability of PHB5GT at 180 °C was evaluated in comparison to formulations containing 5 wt% of commercial plasticizers, namely ATBC and DINCH. As illustrated in Figure 3.12c, the incorporation of commercial plasticizers resulted in the formation of minor irregularities at the junctions of overlapping layers, leading to a reduction in printing resolution in comparison to PHB5GT.

Analyses conducted using the UTT, DSC, and DMA methodologies revealed that the PHB compounds exhibited an adequate degree of stiffness across a wide range of temperatures, accompanied by high crystallinity and a melting temperature that is promising for use in bone and cartilage repair[37]. The potential to produce scaffolds via FDM 3D printing with precise control over shape and porosity, enabled by enhanced processability through bioplasticizer incorporation, represents a significant advantage for the use of these materials in a variety of biomedical applications[38].

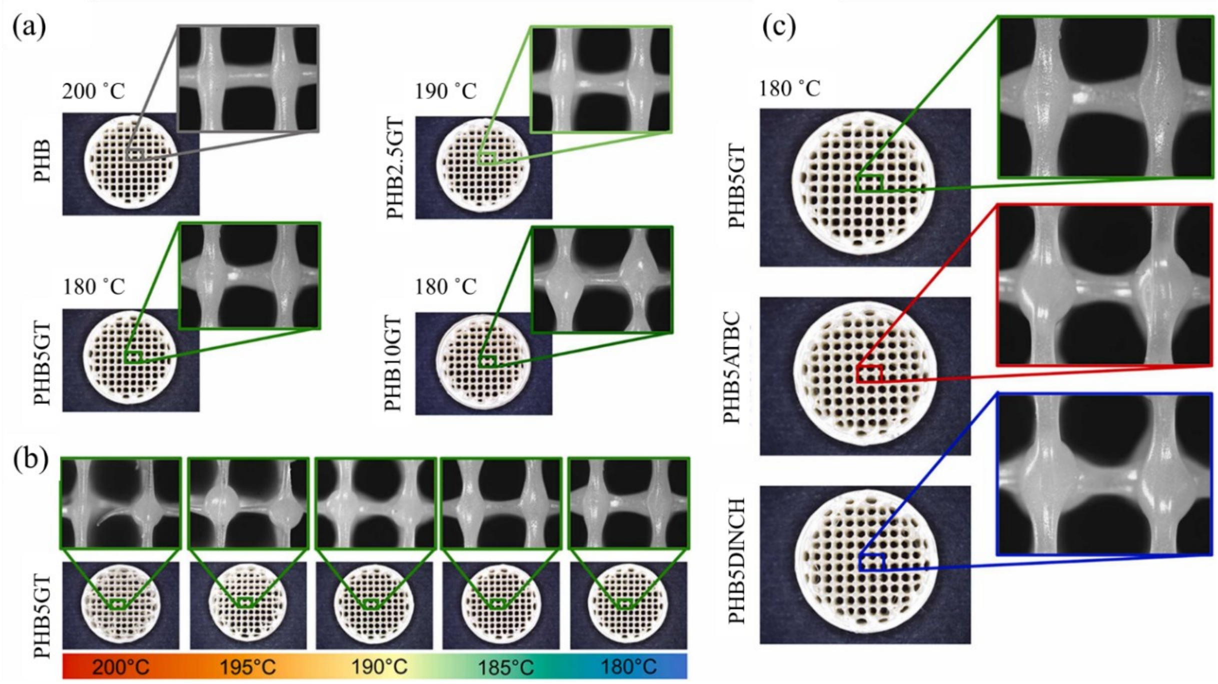

Figure 3.12 *Optical images of the scaffolds printed at different temperatures as the concentration of GT varies: (a) scaffolds printed at decreasing temperature with increasing GT concentration; (b) scaffolds, obtained with PHB5GT formulation, printed at increasing temperatures from 180 to 200 °C; (c) scaffolds printed at 180 °C with three different plasticizers (5% wt. formulations), respectively GT, ATBC and DINCH. In the insets, the internal strands of the scaffolds are shown in detail*

3.6 Results and discussion: Study of PHB-bioglass composites designed for biomedical scaffolds

3.6.1 Glass preparation

The total glass yield was about 9% lower than the theoretical value predicted by stoichiometric calculations, as expressed by Equation 3.2. The causes of these losses during melting may be due to the presence of volatile precursor fractions that evaporate during the high-temperature process. Alternatively, they may result from undesirable partial chemical reactions that prevent the complete conversion of the reactants. Another potential cause of mass loss is the adhesion of some of the molten glass to the crucible walls during the process, which reduces the amount of material that can actually be used for composite preparation.

In addition to the theoretical loss during melting, the mass loss during handling and grinding was calculated to be approximately 2%, in accordance with Equation 3.3. It is essential to consider processing losses when calculating the total amount of glass powder required to prepare the compound.

3.6.2 DSC characterization

Analogously to the plasticized PHB formulations, DSC analysis was employed to analyze the thermal properties at varying composite compositions.

In contrast with the anticipated result, no notable elevation in the $T_{g,DSC}$ was discerned. The progressive addition of bio-glass filler, which is inherently stiffer than the polymer, may restrict the mobility of polymer chains, thereby causing the $T_{g,DSC}$ to assume higher values[39,40]. Specifically, the incorporation of bio-glass resulted in a nearly constant $T_{g,\,DSC}$ (Figure 3.13a), or even slightly decreasing for the composition at higher wt% of glass, with values ranging from -3.3 to -6.7 °C.

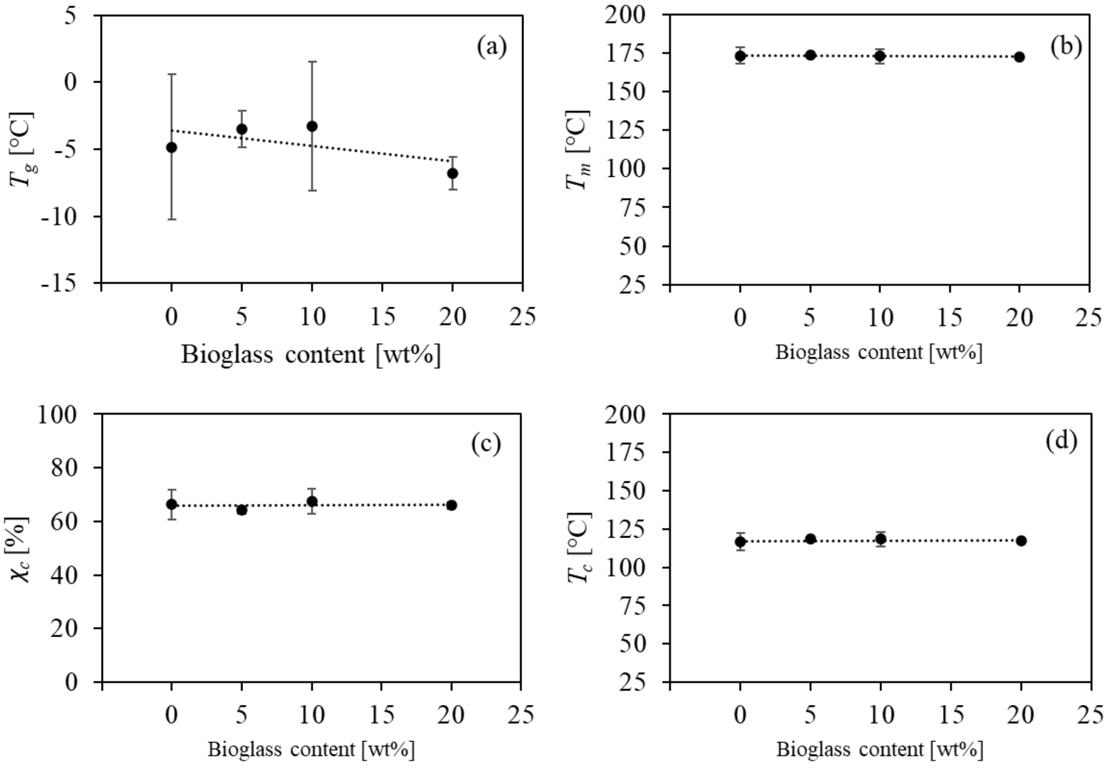

Figure 3.13 *(a) Glass transition temperature ($T_{g,DSC}$), (b) melting temperature (T_m), (c) degree of crystallinity (χ_c), and (d) crystallization temperature (T_c) of the PHB-glass composites as a function of wt% of bioglass*

Furthermore, the incorporation of bio-glass had a negligible effect on the T_m (Figure 3.13b), which remained in the range of 172-174 °C. This suggests that the material's thermal characteristics were maintained and that there was no risk of approaching the degradation temperature (Figure B). It is noteworthy that in the thermogram corresponding to the melting process during the first heating (Figure 3.14), the materials do not exhibit a single, distinct peak. Instead, a shoulder is observed a lower temperatures alongside the main peak. Multiple melting behavior is likely indicating the coexistence of two crystalline phases[41], and it is a phenomenon commonly observed in polyesters such as PHA[42,43].

Furthermore, the $\Delta H_{m,norm}$ (values found in Table 3.10) and therefore χ_c (Figure 3.13c), calculated with (Equation 3.4b) exhibited minimal alterations with increasing filler content, oscillating between 64 and 68 %.

It is interesting to note that, in contrast to previous observations for PBAT composites (Chapter 2), where an increase in the T_c (Figure 3.13d) was observed with the addition of fillers, PHB-bioglass composites exhibited a constant T_c regardless of the concentration of fillers. This suggests that the bio-glass particles do not act as nucleating agents and do not influence the crystallinity of the polymer matrix.

The thermal stability of these composites can be attributed to the homogeneous distribution and appropriate particle size of the bio-glass, as well as strong adhesion between the bio-glass and polymer matrix. Since the bio-glass does not undergo structural changes at the temperatures used for DSC analysis, it does not chemically interact with or alter the thermal behavior of the polymer phase. Consequently, the processability of the composites remains unaffected.

Table 3.10 summarizes the values of the thermal properties extrapolated from the DSC thermograms (Figure 3.14) of the four materials.

***Table 3.10** Thermal properties extrapolated from DSC thermograms of Glass-set*

	$T_{g, DSC}$ °C]	**T_m [°C]**	**ΔH_m [J/g]**	**$\Delta H_{m,norm}$ [J/g]**	**χ_c [%]**	**T_c [°C]**
PHB5GT Neat	-4.5 ± 0.7	173.8 ± 0.5	93 ± 6	93 ± 6	64±4	116.7 ± 0.5
PHB5GT5V	-3.5 ± 0.7	173.5 ± 0.1	89± 2	98 ± 2	64±1	118.7 ± 0.1
PHB5GT10V	-3.3. ± 0.7	173.0 ± 0.1	89 ± 6	94 ± 7	68±5	118.5 ± 0.1
PHB5GT20V	-6.7 ± 0.7	172.6 ± 0.5	77± 1	97 ± 2	66±1	117.4 ± 0.1

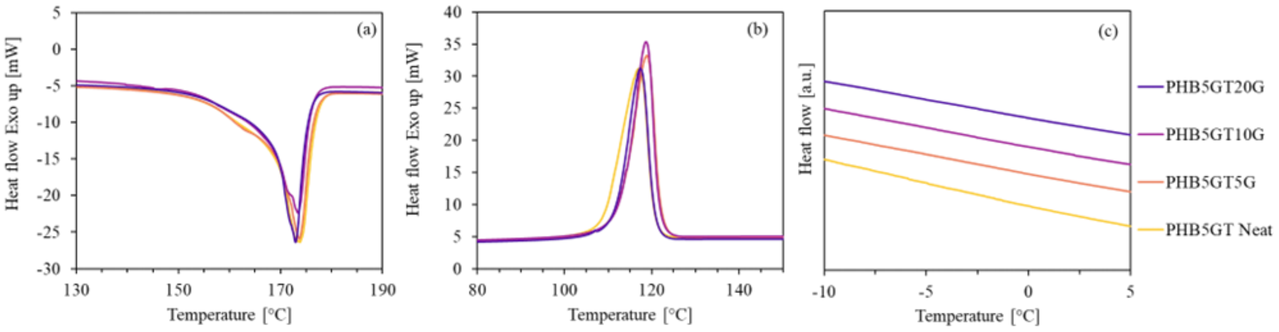

Figure 3.14 *Thermograms of Glass-set. (a) melting peak from the first heating scan, (b) crystallization peak from the cooling scan, and (c) glass transition from the second heating scan.*

3.6.3 TGA characterization

Figure 3.15 illustrates the thermograms of the thermal degradation of glass composites. Similarly, as with the findings regarding the *GT-set* in the preceding analysis (Chapter 3.5.3), a single degradation step was evident, and the incorporation of glass powder did not affect the degradation step.

As evidenced in Table 3.11, both the onset temperature (T_{onset}) and the degradation temperature (T_d) exhibited constant values at varying filler content, with a mean of 308 ± 1 °C and 326 ± 1 °C, respectively. It can be reasonably inferred that the thermal stability of PHB5GT Neat is not influenced by the concentration of glass, even outside the temperature range investigated by the DSC.

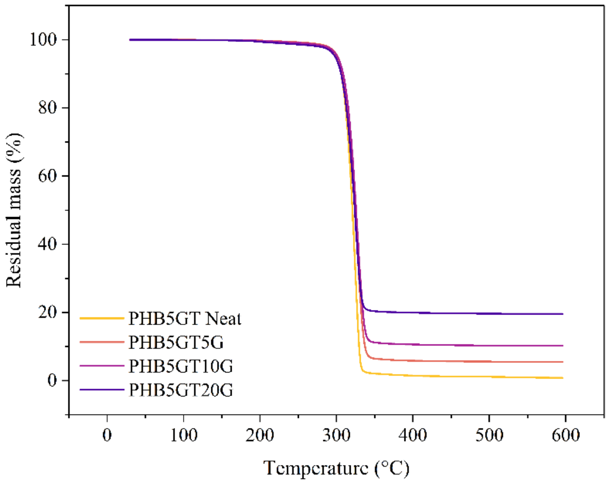

Figure 3.15 *TGA thermograms of Glass-set composites*

Table 3.11 *Thermal degradation parameters obtained by TGA for Glass-set*

	T_d [°C]	T_{onset} [°C]	Residual mass (%)
PHB5GT Neat	325 ± 1	308± 1	0.9± 0.1
PHB5GT5G	326 ± 1	310± 1	5.6± 0.2
PHB5GT10G	327 ± 1	308± 2	10.3± 0.1
PHB5GT20G	326 ± 2	308± 1	19.6± 0.1

As observed in the TGA analysis of PBAT-based composite materials (Chapter 2.5.5), the residual mass at the plateau following the degradation of the polymer (Table 3.11) is precisely equivalent to the amount of glass. Due to its inorganic composition and T_g of approximately 435-450 °C[44], as well as its T_m exceeding 700 °C[45], the phosphate glass remains stable and does not degrade at the temperatures typically reached during polymer pyrolysis.

Additionally, the mass loss recorded at the temperatures involved in the processing of the materials is less than 0.4%, which is reasonable to attribute to the evaporation of any residual moisture.

3.6.4 Tensile test characterization

The mechanical properties of the *Glass-set* were evaluated on the injection-molded specimens (Figure 3.16a) through UTT under identical conditions as those employed for the *GT-set* and the *5%-set* (Chapter 3.5.7).

As illustrated in Figure 3.16, a notable change in color is evident with an increase in bioglass content, which is discernible to the naked eye, as shifting towards darker and more brown-grey hues compared to the Neat.

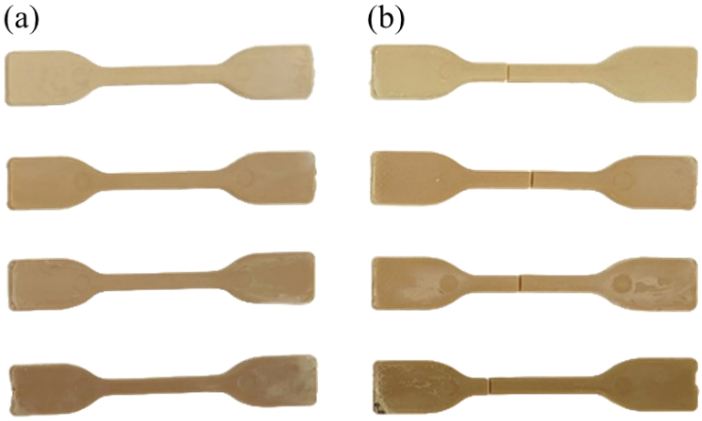

Figure 3.16 *Injection molded 5A specimens of Glass-set before (a) and after (b) the tensile test. From top to bottom: PHB5GT Neat, PHB5GT5G, PHB5GT10G, PHB5GT20G*

The data for E, σ_B, ε_B, and T are summarized in Table 3.12 and the relative trends are reported in Figure 3.16.

All compositions exhibited brittle behavior (Figure 3.16b), which was further enhanced by the high content of filler. In general, the composition PHB5GT5G demonstrated slightly inferior performance compared to the unmodified PHB5GT Neat, while PHB5GT10G exhibited highly comparable properties. The sole PHB5GT20G exhibited a marked decline in mechanical performance. The overall trend is however declining, as highlighted by the fitting dotted lines overlapped to the experimental values in Figure 3.17.

To analyze the properties more specifically, it can be considered that E remained constant, except for PHB5GT10G, which demonstrated an increase of 9%. Regarding tensile strength, PHB5GT10G exhibited a mean value comparable to that of PHB5GT Neat, while a decrement in σ_B of 21% and 35% was observed with the addition of 5 wt% and 20 wt% bioglass, respectively. A decline in the ε_B was also observed in all formulations, with the greatest reduction occurring in PHB5GT20G, which exhibited a 39% decrease. The toughness was similarly affected by the composition of the composites, with a general moderate reduction between PHB5GT Neat and PHB5GT10G, with the values falling within the standard deviation range, and a more pronounced reduction of 64% for the PHB5GT20G.

Table 3.12 *Average value and standard deviation of the mechanical properties of Glass-set determined by tensile test*

	Young's modulus (E, MPa)	**Tensile strength (σ_B, MPa)**	**Elongation at break (ε_B, %)**	**Toughness (T, MJ·m^{-3})**
PHB5GT Neat	1763 ± 47	11.7 ± 0.8	0.8 ± 0.1	0.05 ± 0.01
PHB5GT5G	1791 ± 66	9.2 ± 1.7	0.5 ± 0.1	0.03 ± 0.01
PHB5GT10G	1920 ± 68	11.7 ± 1.7	0.7 ± 0.1	0.04 ± 0.01
PHB5GT20G	1767 ± 41	7.6 ± 0.7	0.5 ± 0.1	0.02 ± 0.005

In comparison to the unfilled matrix, PHB5GT10G seems to represent the most promising composition, exhibiting a moderate increase in E without compromising tensile strength. It can be postulated that the combination of 5 wt% GT with 10 wt% bioglass results in the most favorable balance of stiffness, strength and toughness. This optimizes the mechanical reinforcement while maintaining sufficient structural integrity in the composite. This result is valuable, in consideration of the applications in the bone tissue regeneration the scaffolds have been designed for.

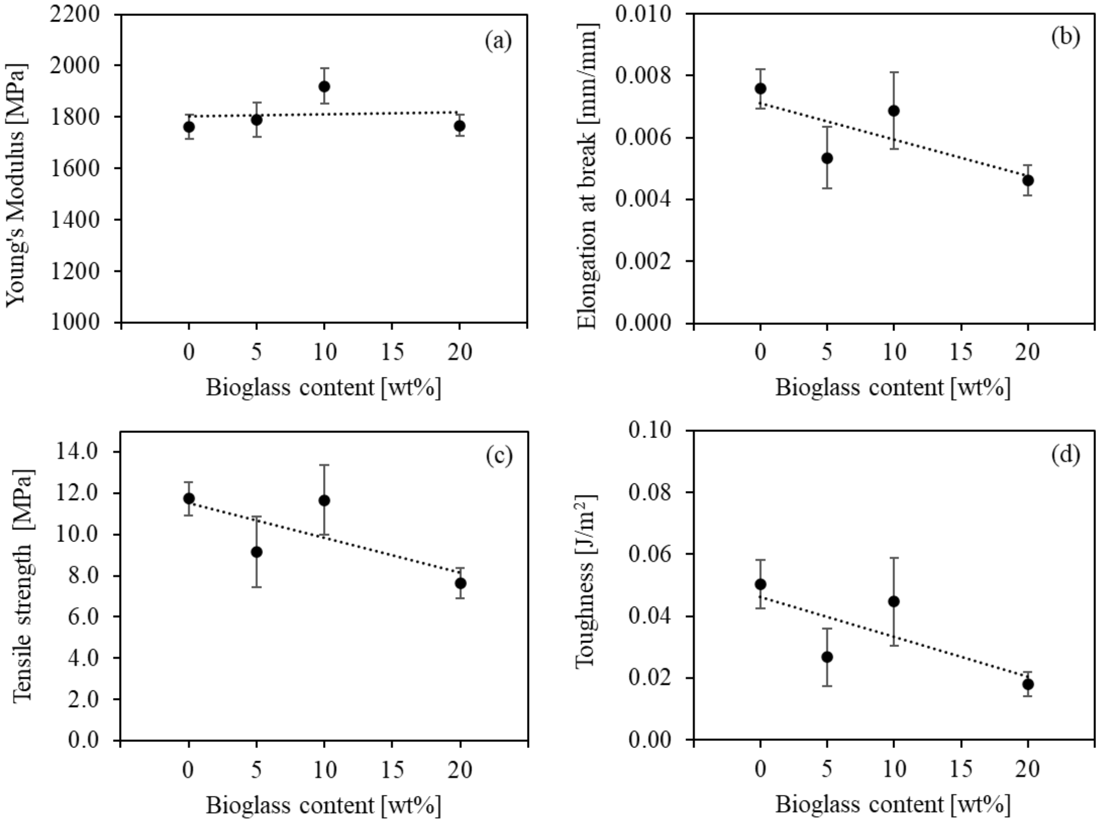

Figure 3.17 *Values of (a) E, (b) ε_B, (c) σ_B, and (d) T of the Glass-set collected from the tensile test*

3.6.5 Compression test characterization

The 3D printed scaffolds were subjected to compression test to gather information about the mechanical performance of the printed structure and the influence of varying amounts of bio-glass on these parameters. The low value of compression speed applied (1mm/min) was chosen to avoid impact fracture and better represent a possible scenario of bone tissue under stress.

The compressive mechanical properties were calculated adapting the calculation used for the tensile properties. The numerical values of stiffness, maximum stress, deformation at failure and toughness are collected in Table 3.13, while Figure 3.18 reports the trends as a function of the filler content.

The mechanical properties of the scaffolds, including modulus, maximum strength, deformation at failure, and toughness, demonstrated a general decline as the bio-glass content increases. Specifically, scaffolds containing 5% and 10% bioglass exhibited enhanced compressive properties when compared to the PHB5GT Neat scaffold. This indicates that at lower bioglass concentrations, the reinforcement provided by the bio-glass enhances the mechanical strength of the structure, potentially due to improved load distribution and interaction between the polymer matrix and bioglass particles. However, at a bioglass concentration of 20%, a notable decline in compressive properties is evident. This decline can be attributed to an excess of filler material that compromises the polymer matrix, resulting in reduced cohesion and structural integrity.

Table 3.13 *Values of compressive mechanical parameters*

	Stiffness [MPa]	**Maximum strength [MPa]**	**Deformation at failure [mm/mm]**	**Toughness [MJ·m^{-3}]**
PHB5GT Neat	281±61	16.1±2.6	0.20±0.03	2.1±0.6
PHB5GT5G	318±32	22.4±1.2	0.24±0.03	3.3±0.4
PHB5GT10G	294±63	18.7±1.2	0.23±0.07	2.7±0.7
PHB5GT20G	243±17	15.5±2.5	0.15±0.01	1.4±0.2

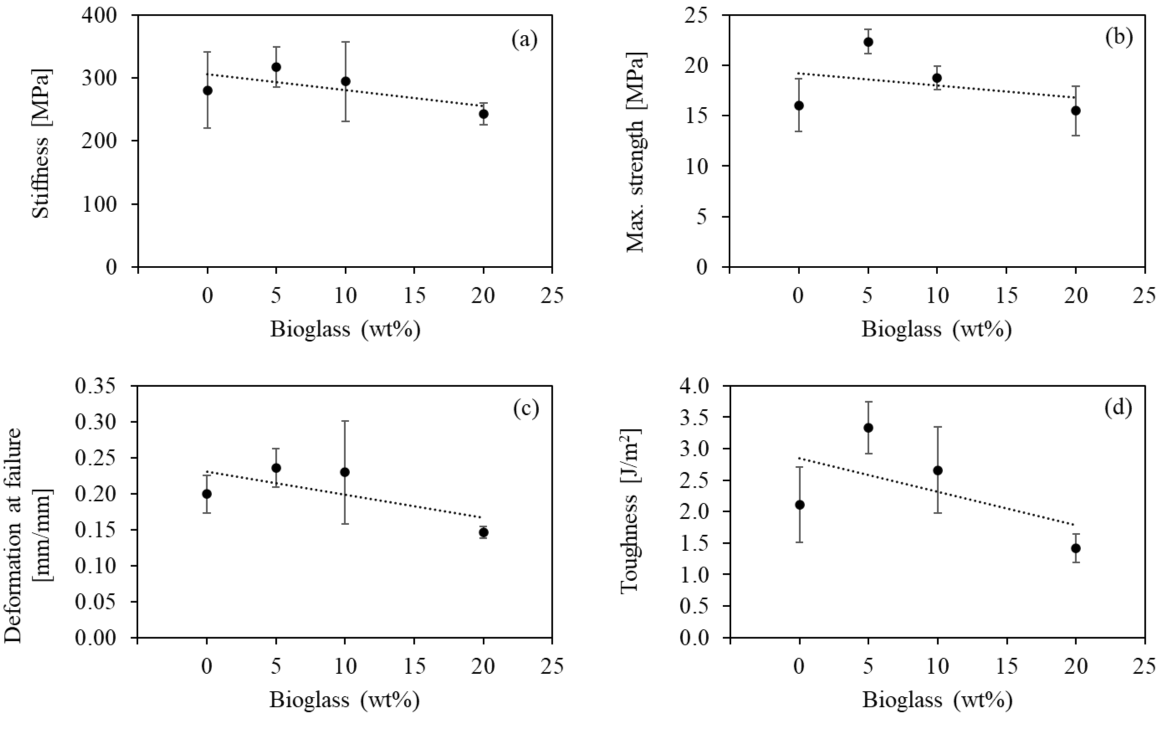

Figure 3.18 *Trends of compressive mechanical properties of Glass-set composites. (a) Stiffness, (b) maximum strength, (c) maximum deformation at failure, and (d) toughness*

In contrast to the outcomes observed at UTT, where PHB5GT10G demonstrated the most favorable mechanical properties, PHB5GT5G seemed to exhibit the optimal combination of mechanical properties upon compression, as evidenced by Figure 3.19, which depicts the overlap of the stress-deformation curves for all compositions. Consequently, it can be proposed that an intermediate concentration of bioglass filler may offer the most optimal balance between tensile and compressive mechanical properties.

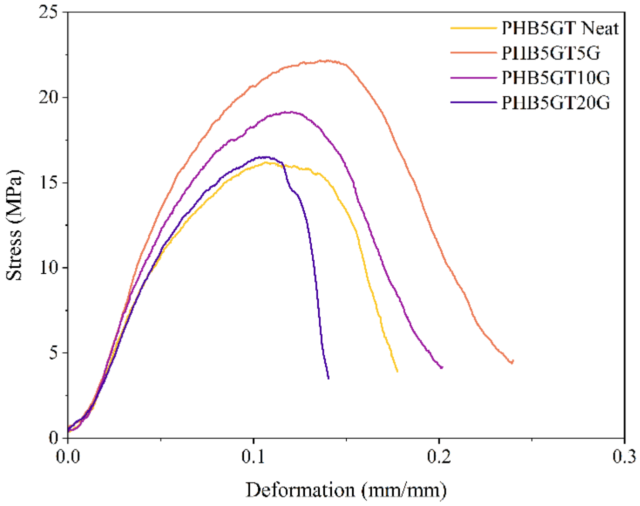

Figure 3.19 *Compression test stress-deformation curves of the Glass-set composites*

This illustrates the necessity for finding an optimal balance between filler content and mechanical performance, as excessive reinforcement can have a detrimental impact on the overall structure. While moderate amounts of bio-glass can enhance scaffold strength and toughness, an excess of bio-glass results in a decline in mechanical performance. This underscores the importance of optimizing filler concentration for specific applications in tissue engineering.

3.6.6 Optical microscopy characterization

Optical microscopy analysis allowed for the evaluation of the macroscopic structure and overall morphology of the scaffolds, as shown in Figure 3.20.

As illustrated in the insets of the upper line, the scaffold's design excludes the presence of solid outer perimeters. This has been done to ensure porosity on the surface of the scaffold, thus promoting uniform osteoblast proliferation and potential vascularization throughout the structure. In the absence of this feature, three-dimensional bone growth would be constrained to the central region, thereby impeding the scaffold's integration with the surrounding tissue. A noteworthy aspect is the quality of filament deposition across the scaffold layers. At the intersection points between the strands form two adjacent layers, successful adhesion of the filaments is observed, indicating optimal printing conditions compatible with the material's thermal properties. This strong adhesion contributes to the scaffold's cohesion, integrity, and stability during both the printing process and subsequent mechanical stress, ensuring the required resistance and structural robustness for biomedical applications.

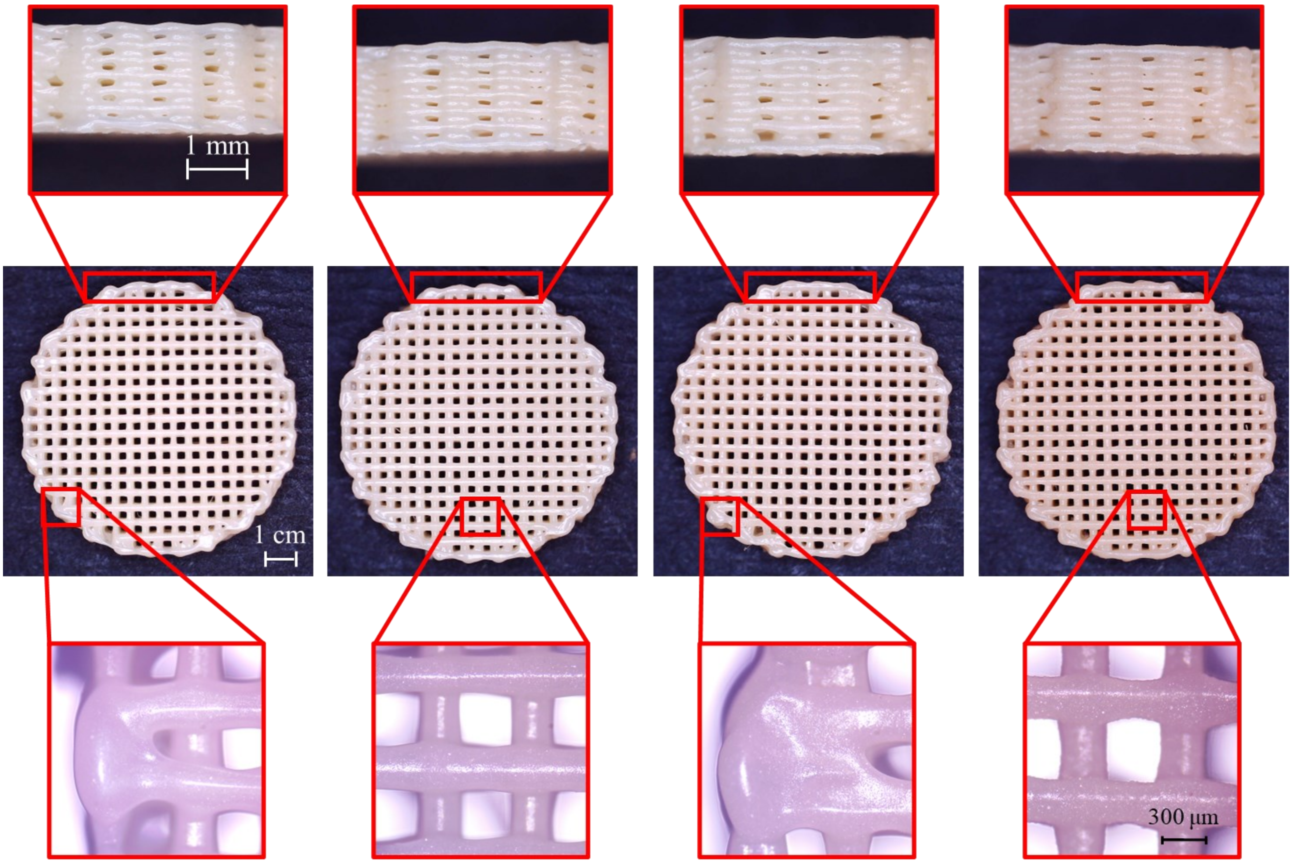

Figure 3.20 *From left to right: PHB5GT Neat, PHB5GT5G, PHB5GT10G, and PHB5GT20G. In the insets, in the bottom line the details of the infill pattern, and in the top line the lateral layering showing the porosity*

Figure 3.21 depicts a representative sample of the scaffold containing 5% by weight of phosphate glass. However, the same observations can be applied to the other three compositions. The image corroborates the accuracy of the pore size specifications, which were established during the design phase and range between 300 and 400 μm. The pores are distributed in a uniform manner, and this interconnected macro-porosity is supposed to be facilitating cell colonization and growth[8,9].

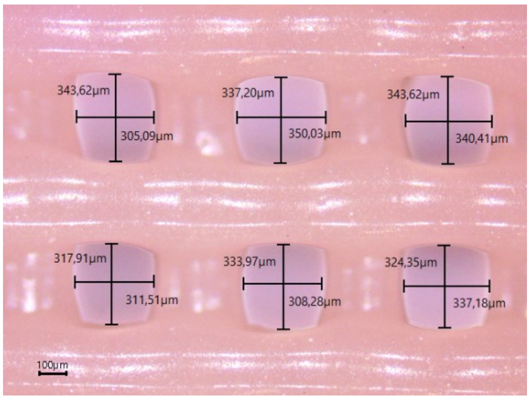

Figure 3.21 *Structure of the PHB5GT5G scaffold, as a representative sample, analysis pore shape and size*

3.6.7 SEM characterization

A more in-depth structural characterization was performed using SEM to investigate the cross-section of the filaments.

As illustrated in Figure 3.22, the miscibility between the polymer and the bio-plasticizer, present in equal amounts across all four compositions, appears satisfactory, with no visible morphological signs of phase separation. This is a crucial element in ensuring plasticization efficiency is maintained.

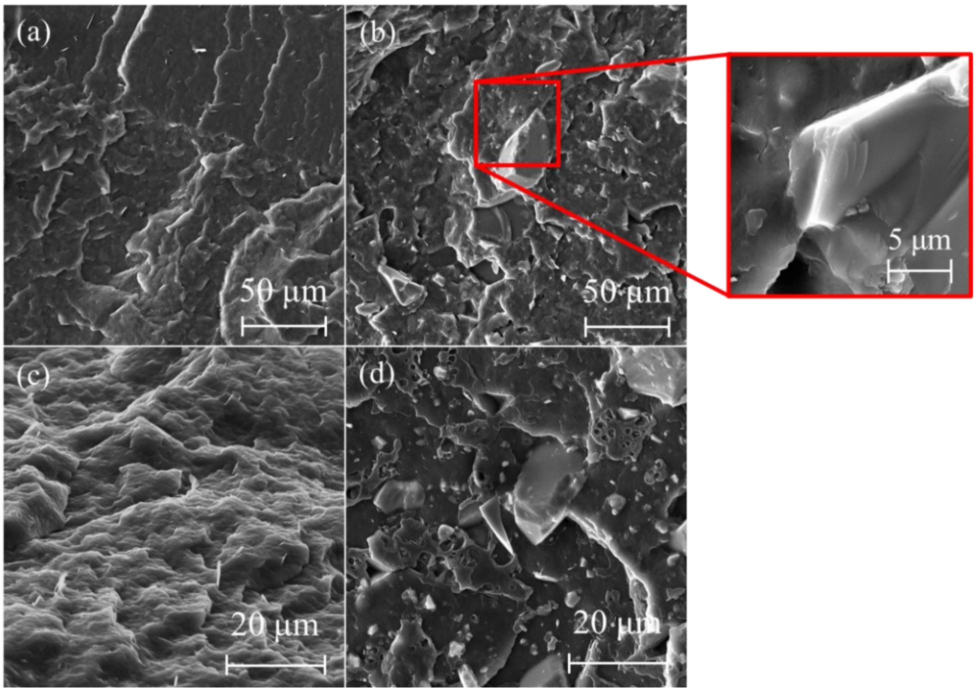

Figure 3.22 *SEM images at different magnifications, top and bottom lines. (a) and (c) PHB5GT Neat, (b) and (d) PHB5GT20G*

Prior research has demonstrated that exceeding the miscibility limit results in phase separation, predominantly due to the coalescence of the excess insolubilized additive into discrete "droplets" dominions [6]. Such phase separation has the effect of compromising the material's integrity, resulting in the migration of the plasticizer to the surface of the polymer and a marked decline in the mechanical and thermal properties of the material.

The spatial distribution of the phosphate glass particles is observed to be uniformly homogeneous, with no areas exhibiting concentration differences or aggregation. This uniformity has a beneficial impact on the composite's mechanical and thermal properties, as it prevents the formation of filler agglomerates that could cause a reduction in performance.

As evidenced by the inset magnification, the interface between the polymer matrix and the rigid filler is clearly delineated, continuous, and with no discernible separation grooves. This guarantees strong adhesion, facilitating effective stress transfer between the two phases. This, in turn, enhances the mechanical properties and mitigates the risk of excessive embrittlement. Additionally, the dispersed phase particles exhibit an average diameter of less than 50 µm and an irregular shape. This morphology maximizes the contact area and ensures a more uniform distribution within the polymer matrix. These factors further improve the interaction between the glass and PHB, enhancing the anchoring of the filler within the matrix. This observation aligns with mechanical property trends.

Figure 3.23 depicts SEM images captured at different magnifications on the 3D printed scaffold after cryogenic fracture. Only PHB5GT20G is illustrated, as a representative sample. The porous structure of the scaffold is clearly visible. The precision of the deposition process results in a regular and well-defined structure. Furthermore, the consecutive layers deposited are observed to adhere effectively to one another. Finally, the regularity of the dispersion of bioglass particles within and on the surface of the composite filament is evident, thus facilitating the promotion of bone tissue regeneration.

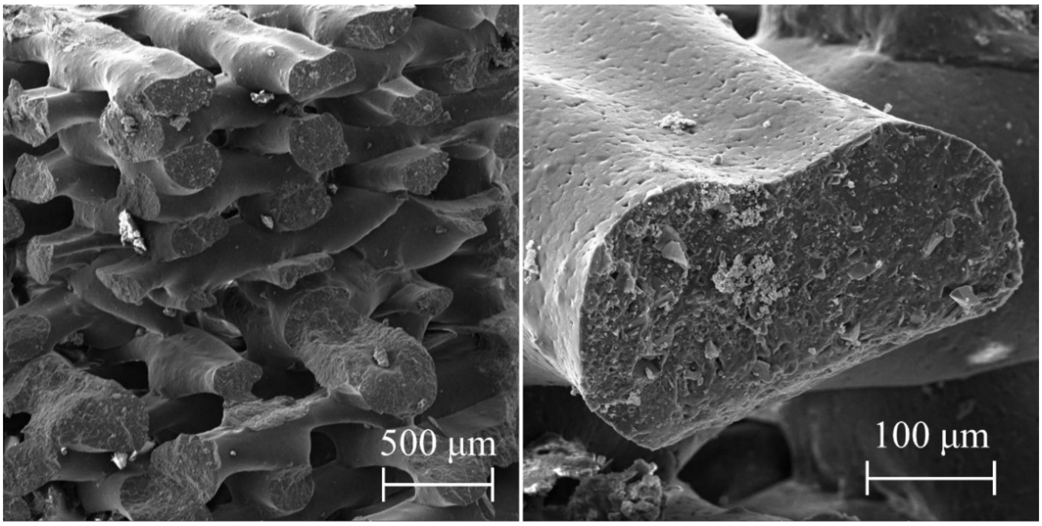

Figure 3.23 *SEM images at different magnifications of a section of PHB5GT20G 3D printed scaffold*

3.6.8 Contact angle measurements

Contact angle measurements were conducted to ascertain the wettability of PHB-glass composites, particularly with commercial cow's blood, with the aim of replicating the intended application of the scaffolds within the human body. The values of the contact angle are reported in Table 3.14.

The drop deposited on the films (Figure 3.24 a-d), which were obtained by hot pressing, exhibited a geometry that enabled the material to be defined as hydrophilic, with a contact angle of less than 90°. Specifically, the contact angle was approximately 75°. No notable discrepancy was observed in the contact angle values at varying bioglass concentrations. The observed variation was indeed within the range of the standard deviation (Figure 3.24e).

These findings, as a preliminary measurement, are considered satisfactory for evaluating the wettability of PHB-glass composites and their potential applicability in the intended biological environment.

Table 3.14 *Contact angle values extrapolated with elliptical fit*

	Mean contact angle (°)
PHB5GT Neat	75.8 ± 2.5
PHB5GT5G	75.7 ± 1.9
PHB5GT10G	74.5 ± 2.2
PHB5GT20G	74.6 ± 1.6

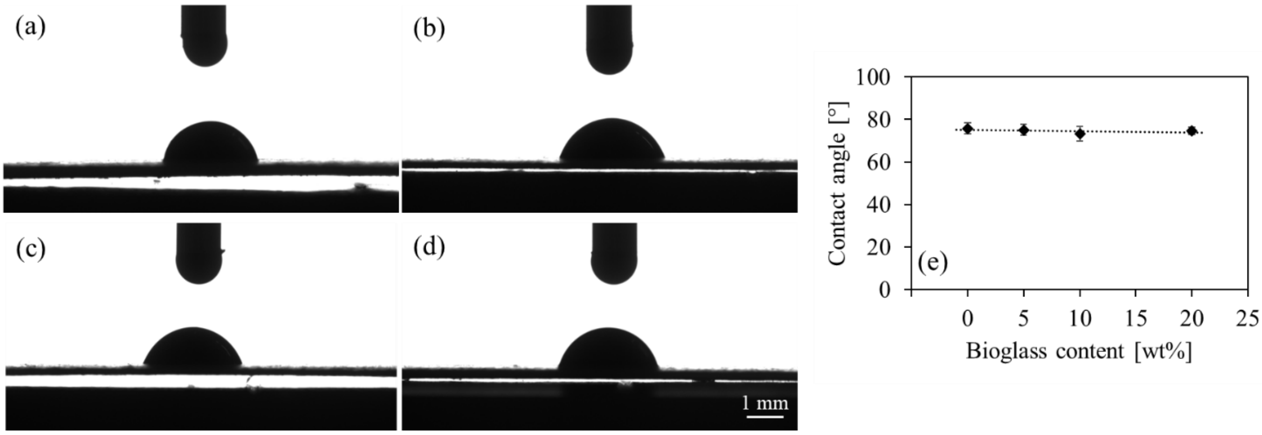

Figure 3.24 *Cow blood drop for contact angle measurements on films of (a) PHB5GT Neat, (b) PHB5GT5G, (c) PHB5GT10G, and (d) PHB5GT20G. (e) trend of contact angle as a function of glass concentration*

3.7 Conclusions

The rising interest in polyhydroxybutyrate (PHB) for a variety of applications has driven research toward the development of additives that enhance its properties, thereby rendering it a viable alternative to conventional fossil-based plastics. To achieve this, it is necessary to improve the limited melt processability and mechanical properties of PHB while maintaining its biodegradability and biocompatibility.

This study examined the compounding of PHB with glycerol trilevulinate (GT), a bio-plasticizer synthesized from levulinic acid and glycerol, and compared its performance with two commercial plasticizers, ATBC and DINCH, which have been the subject of health concerns. Furthermore, bioactive phosphate glass containing strontium and magnesium, elements that promote bone cell proliferation and differentiation, was synthesized and incorporated into plasticized PHB (5% GT) at various concentrations (0%, 5%, 10%, 20%) to create composite materials for 3D-printed porous scaffolds.

The results demonstrated that GT was an effective plasticizer, lowering the glass transition and melting temperatures of PHB, as evaluated by DSC and DMA, while increasing its flexibility and toughness, particularly at the concentration of 2.5 and 5wt%, as demonstrated by UTT. Thermal analysis also demonstrated that the incorporation of bioglass did not affect the glass transition temperature, melting temperature, or crystallinity, which is advantageous for maintaining the composite's processability. Rheological analysis demonstrated that GT reduced melt viscosity, with 5 wt% providing an optimal balance between plasticization and minimal leaching. Furthermore, GT facilitated enhanced processability by reducing the 3D printing temperature by 20°C, resulting in the production of scaffolds with smoother and more uniform strands in comparison to those manufactured with ATBC or DINCH.

The results of mechanical tests on PHB-bioglass composites indicate that the addition of 5 and 10% filler results in a slight yet discernible change in strength and flexibility. This suggests that an intermediate composition between 5 and 10% may provide optimal values of tensile and compressive mechanical properties. Conversely, the addition of a higher percentage of glass leads to an embrittlement of the material and a relative decline in mechanical properties.

The results of the morphological analysis indicated that the pore sizes (300-400 µm) were uniform and well-distributed, thereby optimal to induce cell proliferation. The favorable miscibility between PHB and GT, in conjunction with the positive adhesion between bioglass particles and PHB, effectively prevented excessive embrittlement.

In conclusion, it can be stated that GT represents a safer and more effective alternative to commercial plasticizers for biopolyesters. The characterization and processing tests resulted in the identification of optimal parameters, which were then employed to fabricate plasticized and composite PHB samples with complex geometry by 3D printing.

Nevertheless, comprehensive and detailed analyses of the produced materials are essential to accurately evaluate their true biocompatibility and ensure that they meet the necessary standards for safe application.

References

1. Zhang, L. et al. Improved mechanical property and biocompatibility of poly(3-hydroxybutyrate-co-3-hydroxyhexanoate) for blood vessel tissue engineering by blending with poly(propylene carbonate). Eur Polym J 43, 2975–2986 (2007).

2. Giubilini, A., Bondioli, F., Messori, M., Nyström, G. & Siqueira, G. Advantages of additive manufacturing for biomedical applications of polyhydroxyalkanoates. Bioengineering vol. 8 1–31 Preprint at https://doi.org/10.3390/bioengineering8020029 (2021).

3. Masood, F. Polyhydroxyalkanoates in the Food Packaging Industry. Nanotechnology Applications in Food: Flavor, Stability, Nutrition and Safety 153–177 (2017) doi:10.1016/B978-0-12-811942-6.00008-X.

4. Koller, M. & Mukherjee, A. A New Wave of Industrialization of PHA Biopolyesters. Bioengineering 2022, Vol. 9, Page 74 9, 74 (2022).

5. Rivera-Briso, A. L. & Serrano-Aroca, Á. Poly(3-Hydroxybutyrate-co-3-Hydroxyvalerate): Enhancement Strategies for Advanced Applications. Polymers10 10, (2018).

6. Lenzi, L. et al. Further Step in the Transition from Conventional Plasticizers to Versatile Bioplasticizers Obtained by the Valorization of Levulinic Acid and Glycerol. ACS Sustain Chem Eng 11, 9455–9469 (2023).

7. Togliatti, E. et al. Enhancing melt-processing and 3D printing suitability of polyhydroxybutyrate through compounding with a bioplasticizer derived from the valorization of levulinic acid and glycerol. Addit Manuf 89, (2024).

8. Roohani-Esfahani, S. I., Newman, P. & Zreiqat, H. Design and Fabrication of 3D printed Scaffolds with a Mechanical Strength Comparable to Cortical Bone to Repair Large Bone Defects. Scientific Reports 2016 6:1 6, 1–8 (2016).

9. Turnbull, G. et al. 3D bioactive composite scaffolds for bone tissue engineering. Bioact Mater 3, 278–314 (2017).

10. Gunaratne, L. M. W. K. & Shanks, R. A. Multiple melting behaviour of poly(3-hydroxybutyrate-co-hydroxyvalerate) using step-scan DSC. Eur Polym J 41, 2980–2988 (2005).

11. Giubilini, A., Sciancalepore, C., Messori, M. & Bondioli, F. New biocomposite obtained using poly(3-hydroxybutyrate-co-3-hydroxyhexanoate) (PHBH) and microfibrillated cellulose. J Appl Polym Sci 137, 48953 (2020).

12. Yasuda, K., Armstrong, R. C. & Cohen, R. E. Shear flow properties of concentrated solutions of linear and star branched polystyrenes. Rheol Acta 20, 163–178 (1981).

13. Marmur, A., Volpe, C. Della, Siboni, S., Amirfazli, A. & Drelich, J. W. Contact angles and wettability: Towards common and accurate terminology. Surf Innov 5, 3–8 (2017).

14. Martino, L., Berthet, M. A., Angellier-Coussy, H. & Gontard, N. Understanding external plasticization of melt extruded PHBV–wheat straw fibers biodegradable composites for food packaging. J Appl Polym Sci 132, 41611 (2015).

15. Kirkpatrick, A. Some Relations Between Molecular Structure and Plasticizing Effect. J Appl Phys 11, 255–261 (1940).

16. Brdlík, P., Borůvka, M., Běhálek, L. & Lenfeld, P. The Influence of Additives and Environment on Biodegradation of PHBV Biocomposites. Polymers (Basel) 14, 838 (2022).

17. Rivas, L. F. et al. Reprocessability of PHB in extrusion: ATR-FTIR, tensile tests and thermal studies. Polimeros 27, 122–128 (2017).

18. Žiganova, M. et al. Visco-Elastic and Thermal Properties of Microbiologically Synthesized Polyhydroxyalkanoate Plasticized with Triethyl Citrate. Polymers (Basel) 15, 2896 (2023).

19. Vita, S. et al. Univariate and multivariate strategies for the rheological tests evaluation: Influence of additives in composite materials. J Appl Polym Sci 137, (2020).

20. Feng, K. C. et al. The influence of roughness on stem cell differentiation using 3D printed polylactic acid scaffolds. Soft Matter 14, 9838–9846 (2018).

21. Khor, C. Y. et al. Three-dimensional numerical and experimental investigations on polymer rheology in meso-scale injection molding. International Communications in Heat and Mass Transfer 37, 131–139 (2010).

22. Torres, M. D., Hallmark, B. & Wilson, D. I. Effect of concentration on shear and extensional rheology of guar gum solutions. Food Hydrocoll 40, 85–95 (2014).

23. Bocqué, M., Voirin, C., Lapinte, V., Caillol, S. & Robin, J. J. Petro-based and bio-based plasticizers: Chemical structures to plasticizing properties. J Polym Sci A Polym Chem 54, 11–33 (2016).

24. Socrates, G. Infrared and Raman Characteristic Group Frequencies:Tables and Charts. (John Wiley & sons, Chichester, 2001).

25. Silverstein, R. M., Webster, F. X. & Kiemle, D. J. Infrared spectrometry. in Spectrometric identification of organic compounds (eds. Brennan, D., Yee, J., Wolfman-Robichaud, S. & Rigby, S.) 83–138 (John Wiley and Sons, Inc., 2005).

26. Scandola, M. et al. Viscoelastic and thermal properties of bacterial poly(D-(-)-fl-hydroxybutyrate). Int J Biol Macromol 10, 373–377 (1988).

27. Vieira, M. G. A., Da Silva, M. A., Dos Santos, L. O. & Beppu, M. M. Natural-based plasticizers and biopolymer films: A review. Eur Polym J 47, 254–263 (2011).

28. Gallot-Lavallée, O. & Heux, L. Dielectric spectroscopy on a PHBV bio-polymer. Annual Report - Conference on Electrical Insulation and Dielectric Phenomena, CEIDP 559–562 (2013) doi:10.1109/CEIDP.2013.6748275.

29. Kumar, V., Sehgal, R. & Gupta, R. Blends and composites of polyhydroxyalkanoates (PHAs) and their applications. Eur Polym J 161, (2021).

30. Alhanish, A. & Ghalia, M. A. Developments of biobased plasticizers for compostable polymers in the green packaging applications: A review. Biotechnol Prog 37, e3210 (2021).

31. Braunegg, G., Lefebvre, G. & Genser, K. F. Polyhydroxyalkanoates, biopolyesters from renewable resources: Physiological and engineering aspects. J Biotechnol 65, 127–161 (1998).

32. Sciancalepore, C. et al. Flexible PBAT-Based Composite Filaments for Tunable FDM 3D Printing. ACS Appl Bio Mater 5, 3219–3229 (2022).

33. Esposti, M. D. et al. Comparative Study on Bioactive Filler/Biopolymer Scaffolds for Potential Application in Supporting Bone Tissue Regeneration. ACS Appl Polym Mater 4, 4306–4318 (2022).

34. Abbasi, N., Hamlet, S., Love, R. M. & Nguyen, N. T. Porous scaffolds for bone regeneration. Journal of Science: Advanced Materials and Devices 5, 1–9 (2020).

35. Kunioka, M. & Doi, Y. Thermal Degradation of Microbial Copolyesters: Poly(3-hydroxybutyrate-co-3-hydroxyvalerate) and Poly(3-hydroxybutyrate-co-4-hydroxybutyrate). Macromolecules 23, 1933–1936 (1990).

36. Nguyen, S., Yu, G. E. & Marchessault, R. H. Thermal degradation of poly(3-hydroxyalkanoates): Preparation of well-defined oligomers. Biomacromolecules 3, 219–224 (2002).

37. Ferri, M. et al. Fine Tuning of the Mechanical Properties of Bio-Based PHB/Nanofibrillated Cellulose Biocomposites to Prevent Implant Failure Due to the Bone/Implant Stress Shielding Effect. Polymers (Basel) 15, 1438 (2023).

38. Lim, J., You, M., Li, J. & Li, Z. Emerging bone tissue engineering via Polyhydroxyalkanoate (PHA)-based scaffolds. Materials Science and Engineering: C 79, 917–929 (2017).

39. Nagarajan, V., Mohanty, A. K. & Misra, M. Biocomposites with Size-Fractionated Biocarbon: Influence of the Microstructure on Macroscopic Properties. ACS Omega 1, 636–647 (2016).

40. Howard, G. J. & Shanks, R. A. The Influence of Filler Particles on the Mobility of Polymer Molecules. Journal of Macromolecular Science: Part A - Chemistry 17, 287–295 (1982).

41. Mathot, V. B. F. . & Benoist, L. . Calorimetry and Thermal Analysis of Polymers. (Hanser Publishers ; Distributed in the USA and in Canada by Hanser/Gardner Publications, 1994).

42. Pearce, R. & Marchessault, R. H. Multiple melting in blends of isotactic and atactic poly(β-hydroxybutyrate). Polymer (Guildf) 35, 3990–3997 (1994).

43. Hu, Y., Zhang, J., Sato, H., Noda, I. & Ozaki, Y. Multiple melting behavior of poly(3-hydroxybutyrate-co-3-hydroxyhexanoate) investigated by differential scanning calorimetry and infrared spectroscopy. Polymer (Guildf) 48, 4777–4785 (2007).

44. Sglavo, V. M. et al. Mechanical properties of resorbable calcium-phosphate glass optical fiber and capillaries. J Alloys Compd 778, 410–417 (2019).

45. Mandlule, A., Döhler, F., Van Wüllen, L., Kasuga, T. & Brauer, D. S. Changes in structure and thermal properties with phosphate content of ternary calcium sodium phosphate glasses. J Non Cryst Solids 392–393, 31–38 (2014).

Chapter 4

Degradation of PBAT-CPG composites

4.1 Introduction

In this chapter, the degradation behavior of PBAT-CPG composites, previously formulated and characterized in Chapter 2, is systematically explored. Understanding the degradation mechanisms of biopolymers is critical for optimizing their performance across diverse applications, as it enables improvements in both durability and biodegradability.

PBAT's degradation is highly sensitive to environmental factors such as temperature, moisture, and microbial activity. Under industrial composting conditions, where these variables are tightly controlled, PBAT is degraded within a few months[1]. However, in natural environments like soil or marine ecosystems, the degradation process can be significantly slower due to less favorable conditions[2,3]. This variability makes PBAT suitable for compostable packaging but also underscores the need for effective waste management to ensure proper biodegradation.

In this study, composite pellets with varying CPG concentrations (PBAT, PBAT+4% CPG, PBAT+10% CPG, PBAT+20% CPG, PBAT+40% CPG), produced by solvent casting, were hot-pressed into films to ensure consistent testing under different degradation mechanisms. An artificially accelerated weathering test was first conducted, simulating environmental factors like high humidity, elevated temperature, and UV radiation. This test helps predict the material's performance in real-world conditions by assessing changes in properties such as strength, flexibility, and color. The results provide critical insights into how external factors affect the long-term stability of biopolymer films in exposed environments. Additionally, the films were evaluated for oxygen and water vapor permeability, key factors influencing their barrier properties.

In the second phase, the films underwent disintegration testing under laboratory-scale composting conditions, simulating the end-of-life scenario where these materials are disposed of in organic waste streams. Disintegration was monitored through optical and spectroscopic analyses to capture physical and chemical changes over time, offering a detailed understanding of the biodegradation pathways of the composites.

This chapter aims to provide a comprehensive evaluation of the end-of-life properties of PBAT-CPG composites, contributing to the development of biopolymer products that balance functionality with environmental sustainability.

4.2 Materials

The PBAT-CPG composites produced in Chapter 2 were employed in a study investigating the physical degradation of these materials in film form. Given the similarity in the properties obtained with 2% and 4% of filler, the composition of PBAT+2%CPG was not included in this study. For purposes of comparison, a reference film was produced using a commercial low-density polyethylene (LDPE, Riblene FC 39 D), provided by Versalis (Eni SpA, Italy).

Prior to processing, the composite pellets were subjected to drying at 80 °C for a minimum of four hours or until a constant mass was attained, with the objective of eliminating any residual moisture.

Films with dimensions of 10 x 10 cm^2 and a thickness of 0.3 to 0.4 mm were fabricated from the pelletized PBAT-CPG composites using a Collin P 200 T press machine, set at a molding temperature of 130 °C and maintained at 100 bar for three minutes. The LDPE film was molded at a temperature of 190 °C. The parameters used for making the films are summarized in Table 4.1.

Table 4.1 *Film molding parameters*

Parameter	**Value**
Molding temperature	130 °C (190 °C for LDPE)
Lamination time	3 min
Degassing cycles	10
Maintaining	100 bar for 3 min
Water cooling	100 bar until 50 °C
Air cooling	10 s

4.3 Methods

4.3.1 Permeability test

To analyze the permeability to oxygen and water vapor, a thin-film permeability tester (MultiPerm, Extrasolution Srl, Italy) was utilized, equipped with temperature and relative humidity controls. The tests were conducted in accordance with the standards set forth by the American Society for Testing and Materials (ASTM), specifically ASTM D3985 for oxygen transmission rate (OTR) and ASTM F1249 for water vapor transmission rate (WVTR). The operating conditions utilized for all the samples analyzed are presented in Table 4.2.

Table 4.2 *Settings used for permeability tests*

Parameter	Value
Set point temperature	23 °C
Relative moisture	1.0 ± 0.1 %
Carrier flow	12.3 ml/min

4.3.2 Accelerated Weathering Test

The accelerated aging behavior of the samples was evaluated using a QUV Accelerated Weathering Tester (Q-LAB), in accordance with the ASTM D 4329 standard and the G154 cycle.

Two film samples of each concentration, each measuring 5 × 5 cm^2, were prepared for the aging test, along with two LDPE samples used as references. All samples were secured on a holder and subjected to a combined cycle of ultraviolet (UV) radiation, elevated temperature, and humidity.

In particular, the cycle consisted of two primary phases. The samples were first subjected to a 320-minute UV exposure at a radiant intensity of 0.68 W/m^2 and a wavelength of 340 nm, with the temperature maintained at 60 °C. This was followed by a 160-minute exposure to water vapor at 50 °C, with the UV lamps turned off. The initial UV exposure was designed to closely mimic the midday summer sunlight, particularly in the critical wavelength range from 365 nm down to the solar cutoff at 295 nm, with peak emission at 340 nm.

After each daily cycle, the sample holders were removed and stored in a closed container at room temperature to prevent residual heat and moisture from affecting the results. The test cycle was repeated five days a week, with a two-day interval between each cycle. To ensure uniform exposure, the position of each sample was rotated weekly. In accordance with the established standard, the test duration was deemed sufficient when a "defined change in a material property" was observed, which in this case took four weeks.

Each week, the samples were removed and analyzed using Fourier-transform infrared spectroscopy (FT-IR), optical microscopy, and CIE L*a*b* colorimetry to detect any changes in molecular structure and visual appearance. At the conclusion of the test period, Scanning Electron Microscopy (SEM) images were obtained of both the original and weathered samples, and energy-dispersive X-ray spectrometry (EDS) was conducted on the same samples.

4.3.3 Disintegration Test

The disintegration test was conducted in accordance with the technical standard EN ISO 20200, which specifies conditions for composting. To conduct the test, four film samples, each measuring 2.5×2.5 cm², were cut from the films of each PBAT-based material. LDPE was employed as a non-degradable reference material.

The composting reactors were polypropylene (PP) containers, each provided with a 5 mm diameter hole to facilitate air circulation and gas exchange. The dry synthetic solid waste was prepared in accordance with the standard, comprising 40 wt% sawdust (sourced from OBI Italy), 30 wt% rabbit feed (Vitakraft, Germany), 10 wt% mature compost (Punta allo Zero S.r.l. for Coop, Italy) as inoculum, 10 wt% corn starch (Unilever, Italy), and 5 wt% sugar (MAXI S.r.l., Italy). The remaining 4 wt% was composed of corn seed oil (Oleificio Salvadori S.r.l., Italy), while the final 1 wt% was urea (supplied by Merck-Sigma, Germany). The components were thoroughly mixed, and after deionized water was added to achieve a moisture content of 55%.

The polymeric samples were subjected to a drying process at 40°C until a constant mass was attained. Afterward, the samples were weighed, and the masses were recorded. The samples of each material were placed together in a single reactor, supported by an iron mesh. The quantity of wet synthetic solid waste in each reactor was adjusted to maintain a test material to wet synthetic waste mass ratio of 0.5%. Subsequently, the reactors were weighed, and the total mass was recorded. The reactors were therefore placed in an ISCO NSV 9090 oven at a temperature of 58 ± 2 °C. In accordance with the established protocol, the reactors were weighed at regular intervals, the water content was replenished, and the compost was thoroughly mixed throughout the 88-day testing period.

To monitor the fragmentation process, samples were recovered weekly, rinsed with deionized water, dried overnight at 40 °C, and weighed. Images of the films' external morphology were captured using a USB digital microscope with MicroCapture Plus software.

The degree of disintegration (D [adm]) was calculated as the mean value using Equation 4.1, excluding any outlier measurement:

$$D = \frac{m_i - m_r}{m_i} \cdot 100 \qquad \text{(Equation 4.1)}$$

where m_i is the initial dry mass of the test material and m_r is the residual mass at the time of the measurement. The D values were presented in a graph as a function of time.

To validate the test, the variation in D values (ΔD [adm]), calculated with Equation 4.2 based on three replicates for each material, should not exceed the standard requirement of 10%.

$$\Delta D = \frac{D_{max} - D_{min}}{\bar{D}_i} \qquad \text{(Equation 4.2)}$$

where D_{max} and D_{min} are the maximum and minimum values of D, respectively, and D_i is the mean value of the three.

To minimize excessive deterioration of the samples due to handling, the measurements were conducted at two-week intervals following the sixth week. The dry mass (*DM* [adm]) of the compost material was determined both before and after the test by drying two samples of known volume at 105 °C (ISCO NSV 9090) until a constant mass was reached. The result was expressed as a percentage of the total mass of the sample divided by 100. Subsequently, the dried compost samples were subjected to calcination at 550 °C for eight hours (LKN 75, Nannetti), cooled overnight, and weighed. The drying process was repeated until a constant mass was obtained. The volatile solids (*VS* [adm]) content, corresponding to mass loss, was calculated for each sample by subtracting the residual mass obtained by calcination from the total dry solids content and expressed as a percentage of the *DM* divided by 100. The *VS* content is a significant parameter, as it provides an indication of the organic matter content in the compost (ISO 20200).

The decrease in the total *VS* content (R [adm]) was calculated with Equation 4.3:

$$R = \frac{[m_i \cdot (DM)_i \cdot (VS)_i] - [m_f \cdot (DM)_f \cdot (VS)_f]}{[m_i \cdot (DM)_i \cdot (VS)_i]} \cdot 100 \qquad \text{(Equation 4.3)}$$

where m_i is the initial mass of the wet synthetic waste introduced into the reactor, m_f is the final mass of the compost, $(DM)_i$, $(VS)_i$, $(DM)_f$ and $(VS)_f$ are the initial dry mass, the initial volatile-solids content, the final dry mass, and the final volatile-solids content of the synthetic waste, respectively.

The test is deemed valid when the R value reaches or exceeds 30%. At the conclusion of the testing period, a sample from the residual material of each tested specimen was subjected to analysis via FT-IR.

4.3.4 Colorimetric Analysis

Colorimetric analysis was conducted on weathered samples using a Spectro Connect 2.5 (Techkon, Germany). Measurements were taken at five points on each film sample, with one measurement taken at the center and four measurements taken at diagonal positions from the center. Throughout the aging test, CIE $L^*a^*b^*$coordinates were recorded. In this system, L represents the brightness, a indicates red or green coloration (positive or negative, respectively), and b indicates yellow or blue coloration.

The color variation (*ΔE* [adm]) of the different composites over time was calculated using the following equation (Equation 4.4):

$$\Delta E = \sqrt{(L_t - L_0)^2 + (a_t - a_0)^2 + (b_t - b_0)^2} \qquad \text{(Equation 4.4)}$$

where L_t, a_t and b_t represent the values at the time of the measurement, while L_0, a_0 and b_0 are the initial values collected before the weathering process.

4.3.5 Scanning Electron Microscopy (SEM) and Electron Dispersion Spectroscopy (EDS)

The objective of elemental analysis was to investigate potential alterations in the surface characteristics and chemical composition of the samples that had undergone aging degradation.

SEM images were captured using a field emission gun scanning electron microscope (FEG-SEM, Nova NanoSEM 450, FEI company, USA) with a backscatter detector. All images were obtained with an accelerating voltage of 15 kV, an arbitrary spot size of 4, and a working distance of approximately 6 mm, at different magnifications.

EDS was conducted using the system QUANTAX-200 (Bruker, Germany), equipped with the silicon drift detector (SDD) XFlash 6/10.

4.3.6 Fourier Transform Infrared Analysis (FT-IR)

To investigate the chemical structure changes occurring during the degradation period, FT-IR spectroscopy was conducted using a Spectrum Two instrument (Perkin Elmer, USA) in attenuated total reflectance (ATR) mode. The analysis parameters included a resolution of 4 cm^{-1}, 16 scans per measurement, and a wavenumber range from 400 to 4000 cm^{-1}. The measurements were conducted in duplicate. In the accelerated weathering test, duplicate measurements were taken at two points in the center of each specimen. In the fragmentation test, each specimen was subjected to analysis individually.

4.4 Results and Discussion - Permeability characterization

Table 4.3 and Figure 4.1 illustrate the oxygen (a) and water vapor (b) permeability of the material under investigation. Although the trends are only indicative due to overlapping standard deviations, it is important to note that while water vapor permeability appears to increase in proportion to CPG content, oxygen permeability shows a slightly decreasing trend.

With reference to oxygen permeability, significantly lower values are observed in pure PBAT and its composites in comparison to LDPE[4]. Furthermore, the incorporation of CPG fillers enhances the barrier properties of the composites, as evidenced by a reduction in oxygen permeability with an increase in CPG content. Concerning water vapor permeability, PBAT-based materials exhibit values that are more than ten times higher than those of LDPE, with a discernible increasing trend as the quantity of filler is increased.

This discrepancy in permeability is attributed to the polar nature of the bonds within the PBAT polymer chain, in contrast to the predominantly nonpolar macromolecular structure of LDPE. Polar molecules, such as water, which are characterized by the O-H bond, interact more favorably with the ester groups in PBAT, thereby facilitating permeation through the polymer. In contrast, nonpolar molecules, such as oxygen (O=O) or carbon dioxide (O=C=O), exhibit reduced permeation through the polymer. Consequently, PBAT-based materials permit the passage of greater water vapor permeability while exhibiting reduced oxygen permeability compared to LDPE. This effect is further amplified in the presence of polar inorganic fillers, such as CPG.

Given that CPG is soluble in aqueous environments[5], it is to be expected that the water vapor permeability would increase in proportion to the quantity of filler present. This selective permeability indicates that the material may be particularly suited for applications where oxygen sensitivity is a greater concern than moisture control.

However, as discussed in Chapter 2, the primary objective of incorporating CPG into the PBAT matrix was to enhance the material's rigidity, rather than to improve its barrier properties. Nevertheless, the diminished oxygen permeability evidenced in the tests offers an additional advantage to the utilization of PBAT-based biodegradable composites, which are designed to replace LDPE in packaging applications. It is noteworthy that the high water vapor permeability may not necessarily be a disadvantage for packaging applications. Studies have demonstrated that the enhanced humidity permeability observed in PBAT films can facilitate the distribution of moisture generated by the metabolic activity of vegetables, thereby preventing condensation within the packaging and reducing the likelihood of mold formation[6]. However, this factor must be considered when assessing the comprehensive stability of the material.

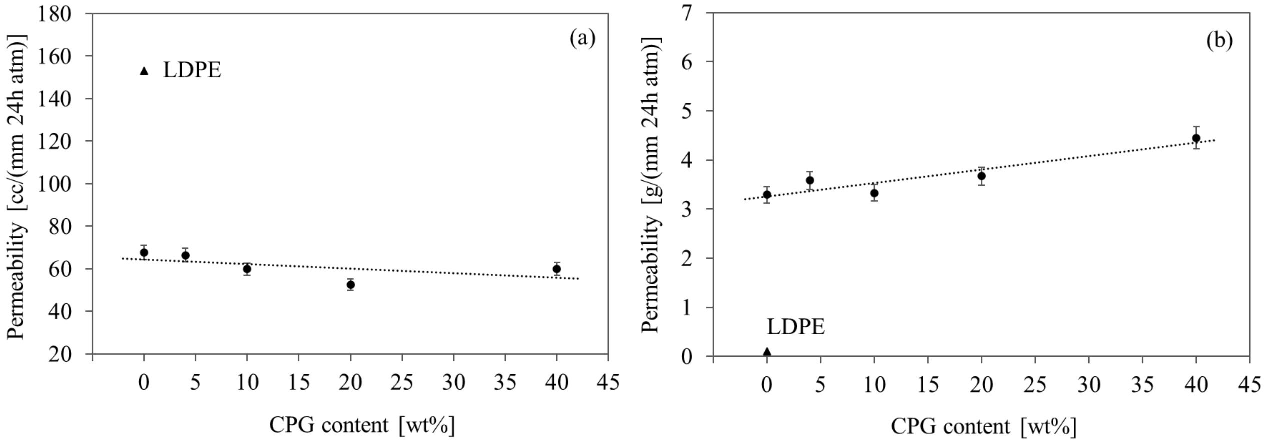

Figure 4.1 *(a) Oxygen and (b) water vapor permeability as a function of the CPG concentration. The LDPE permeability values have been added for the sake of comparison*

Table 4.3 *Oxygen and water vapor permeability values for LDPE and PBAT-based composites*

	Film thickness [mm]	**Oxygen permeability [cc mm/(m^2 24h atm)]**	**Water vapor permeability [g mm/(m^2 24h atm)]**
PE	0.57	153 ± 5	0.10 ± 0.05
PBAT	0.34	68 ± 5	3.3 ± 0.2
PBAT+2%CPG	0.35	66 ± 5	3.3 ± 0.2
PBAT+4%CPG	0.41	67 ± 5	3.6 ± 0.2
PBAT+10%CPG	0.37	60 ± 5	3.3 ± 0.2
PBAT+20%CPG	0.36	53 ± 5	3.7 ± 0.3
PBAT+40%CPG	0.40	60 ± 5	4.5 ± 0.3

4.5 Results and Discussion - Accelerated Weathering Test

The stability of PBAT-based composites under weathering agents was evaluated by subjecting film samples to accelerated aging tests. The objective of this process was to replicate the effects of environmental exposure, such as sunlight, in a more condensed timeframe by irradiating the samples with ultraviolet light at elevated temperatures and high humidity levels. Aging can result in irreversible alterations to the characteristics of polymers, with typical consequences including discoloration, brittleness, adhesiveness, and loss of mechanical integrity[7,8].

4.5.1 Colorimetric Analysis

Colorimetric analysis was conducted to monitor color alterations in the composites on a weekly basis, employing the calculation method outlined in Equation 4.4. The ΔE values were plotted against time in weeks and fitted with linear equations (Figure 4.2a), where the slope of each line, representing the rate of color change, was observed to increase with higher CPG concentrations. This trend is illustrated in Figure 4.2b, which depicts a correlation between increasing filler content and more pronounced color variation, particularly a shift towards yellowing, indicative of accelerated material degradation[8].

As illustrated in Figure 4.3, digital microscope images demonstrate progressive alterations in the visual characteristics of the composite samples over the course of the test. Composites with higher concentrations of glass microparticles exhibited a greater tendency to fracture over time, becoming increasingly brittle and more challenging to handle than the untested specimens. This deterioration suggests that the material is undergoing degradation, which will be further investigated through microscopic and spectroscopic analyses. The formation of cracks in the PBAT+20% CPG samples was first observed during the second week of the test. Initially, these cracks were only visible under backlighting conditions, but by the third week, larger cracks had formed (Fig. 4.3i). Cracking also began in the PBAT+40% CPG samples in the third week (Fig. 4.3ii), while PBAT+10% CPG showed cracks during the final week of testing. By the conclusion of the fourth week, the degradation of the 40 wt% filler-loaded specimens had reached a point where their handling for analysis became challenging, thereby marking the conclusion of the test. In contrast, the non-degradable reference material, LDPE, exhibited no discernible signs of deterioration.

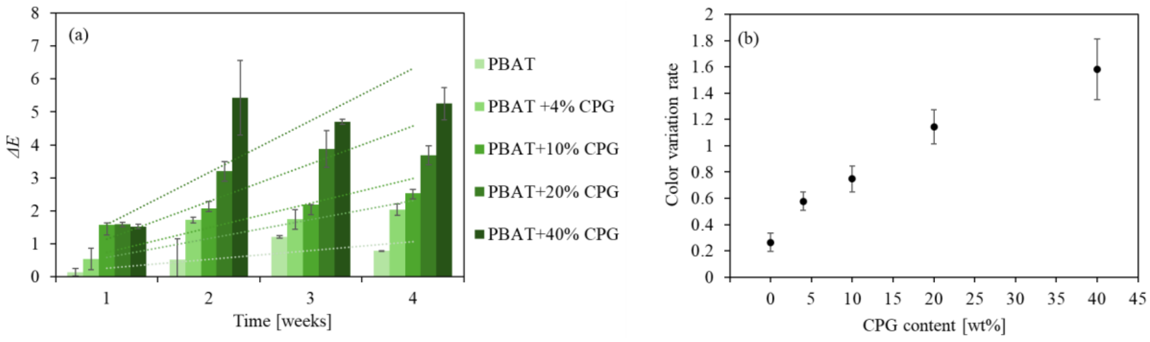

Figure 4.2 *(a) Color variation of the composition over time, with linear fitting line. (b) Color variation rate as a function of the filler content*

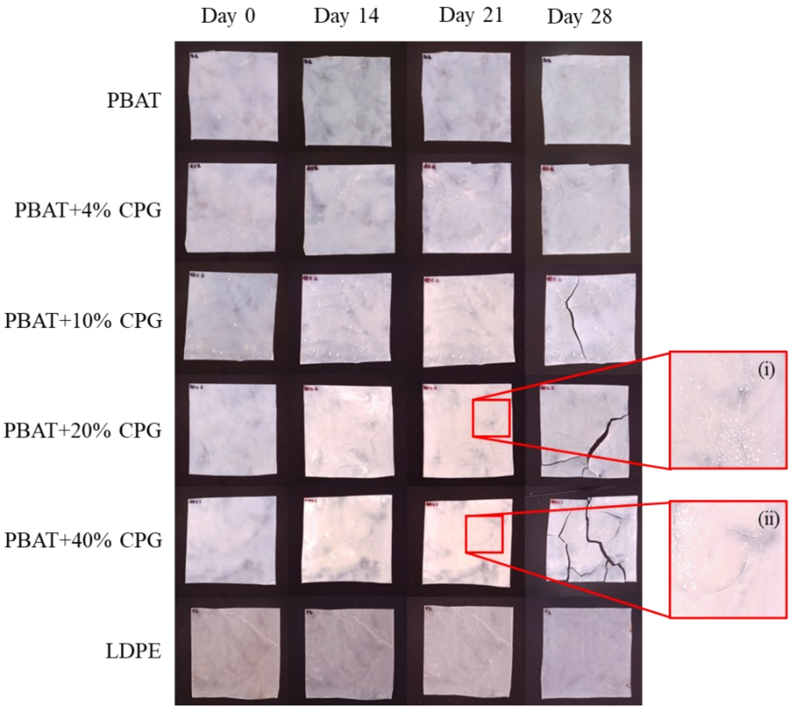

Figure 4.3 *Digital microscope pictures of PBAT+CPG composites and LDPE over time during the weathering test. Details (i) and (ii) represent cracking on PBAT+20%CPG and PBAT+40%CPG samples, respectively, at the third week of test*

4.5.2 SEM characterization

A detailed examination of the surface microstructure via SEM provides insight into the underlying cause of the observed brittle behavior in the composite materials. Figure 4.4 depicts the surface morphology of the composites both prior to (left side of Figure 4.4) and after (right side of Figure 4.4) the weathering test. In the SEM images of the unaged samples, the grey regions are indicative of the polymer matrix, whereas the white particles dispersed throughout this matrix correspond to the filler material. The SEM images were obtained using backscattered electrons, which provide compositional information based on the atomic number of the interacting atoms. Therefore, the higher-contrast particles in the images are the inorganic, phosphorus-based compounds, which are heavier than the carbon-based polymer matrix, resulting in greater electron scattering.

A comparison of the microstructures before and after the weathering test indicates that, due to its hydrophilic nature, the CPG filler absorbed water vapor during the second phase of the test cycle. This resulted in the dissolution of the filler and the formation of a thin layer over the PBAT matrix. During the interval between test days, the dissolved glass layer desiccated, covering the entire sample surface and forming a phase with greater brittleness and rigidity on top of the polymer film. Furthermore, it is possible that the polymer itself absorbed water, which would occur naturally in weathering conditions as a result of contact with rain or environmental moisture. This process of water absorption followed by drying resulted in repeated cycles of swelling and shrinking. The accumulation of stress over time, particularly in the glass-covered areas, ultimately resulted in the formation of cracks. These surface stresses had an impact on the overall composite structure[8], resulting in a stiffer and more brittle macroscopic behavior, as previously observed in the digital images in Figure 4.3.

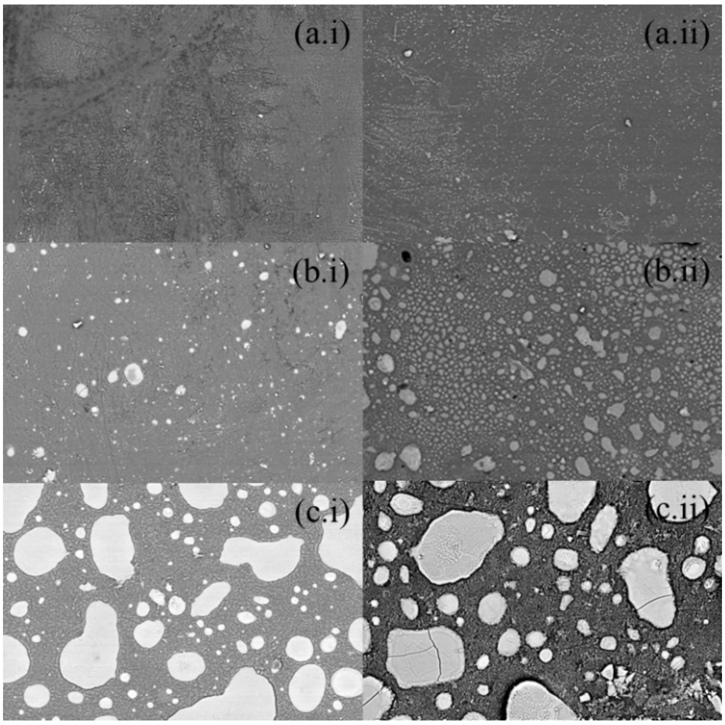

Figure 4.4 *Surface microstructure of PBAT (a), PBAT+10%CPG (b), PBAT+40%CPG (c), as representative samples, before (i) and after (ii) four weeks of weathering test*

Following the aging process, the contrast between the polymer matrix and the filler remains visible in the SEM images, but the entire structure appears in varying shades of gray. This differs from the brighter areas observed in the unaged samples, where the CPG particles stood out against the gray polymer background. This visual change supports the hypothesis that the CPG dissolved and spread across the specimen surface during the test. Further confirmation of this observation will be provided by the EDS results discussed in the next section.

4.5.3 EDS characterization

EDS analysis was performed on unaged samples at two distinct locations: one on a glass particle and the other within the PBAT matrix.

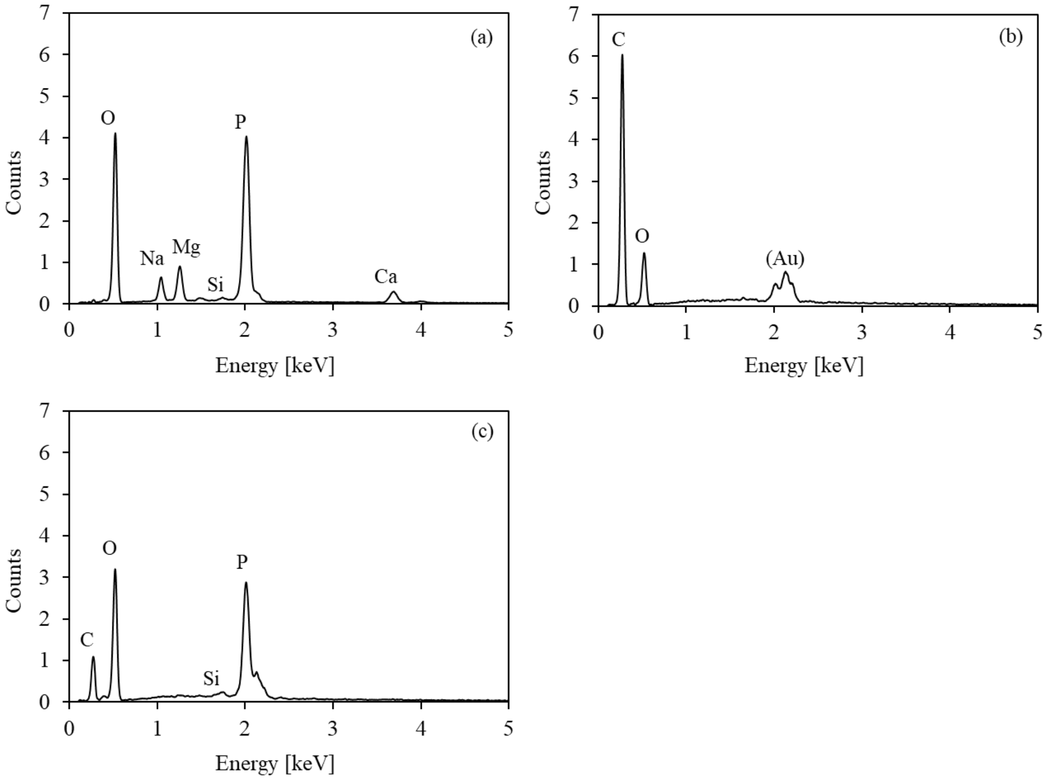

***Figure 4.5** EDS analysis on a glass particle in unaged specimen (a), on PBAT surface of unaged specimen (b), and on a generic point of aged specimen surface (c)*

The resulting spectra from these points are presented in Figure 4.5a and 4.5b, respectively. As illustrated in Figure 4.5a, the peaks corresponding to the elements that compose the CPG, including oxygen, phosphorus, calcium, magnesium, sodium, and silicon, are readily detectable. In contrast, Figure 4.5b demonstrates that only carbon and oxygen peaks are observable within the PBAT matrix. The presence of a spurious peak associated with gold can be attributed to the application of a nanometer-thick metal layer to the specimen, which serves to enhance conductivity and prevent charge accumulation during analysis. In the context of a specimen that was subjected to the weathering process (Figure 4.5c), the concurrent identification of peaks associated with both the glass filler and the polymer matrix at a specific point on the specimen's surface lends support to the earlier hypothesis regarding the behavior of the CPG particles.

4.5.4 FT-IR characterization

The structural modifications to the materials that occurred as a result of the weathering test were examined using FT-IR spectroscopy. The variations observed in the spectrum are indicative of alterations in the chemical structure of macromolecules resulting from the weathering process, which is primarily characterized by exposure to humidity and UV radiation. In the case of bioplastics, particularly those derived from polycondensation processes like PBAT, water can facilitate chemical degradation through hydrolysis reactions that lead to the breakdown of polymer chains. Moreover, UV radiation (wavelengths shorter than 400 nm) represents a substantial source of polymer degradation through photochemical reactions[8]. UV radiation in sunlight contains photons with sufficient energy to cleave both inter- and intramolecular bonds[7].

To facilitate comparison of FT-IR spectra from each composite at various measurement intervals, the data were normalized to the highest peak at 725 cm^{-1}, which is associated with aromatic ring out-of-plane bending and is assumed to be resistant to oxidation. This peak typically appears around 830 cm^{-1}, but its wavenumber is shifted to a lower value due to conjugative interactions between the aromatic ring and the ester groups in the terephthalate unit[9].

Table 4.4 outlines the characteristic peaks of PBAT-CPG composites, while Figure 4.6 illustrates the spectra of PBAT and PBAT+CPG composites at various filler concentrations at various measuring times. As found previously in Chapter 2, the incorporation of CPG does not result in any alteration to the structure of the polymer matrix; the peaks associated with PBAT remain unaltered. The presence of CPG is primarily indicated by a band at 520 cm^{-1}, which is characteristic of phosphorus-oxygen bonds. The intensity of this band increases in relation to the filler content in the composite[10-13].

Table 4.4 *Characteristic FT-IR absorption peaks of PBAT-CPG composites*

Wavenumber [cm^{-1}]	**Description**
2800–2900	Adipate and 1,4-butandienol (−CH_2−) groups symmetric and asymmetric stretching
1710	Adipate and terephthalate carbonylic (C=O) stretching in ester group
1577–1504	Aromatic benzene ring (C=C) bond stretching
1267–1250	((O=)C–O) bond asymmetric stretching in ester group
1110	((C−)C–O) bond stretching in 1,4-butanediol group
1014	Aromatic benzene ring (C–H) bond in-plane bending in terephthalate unit
725	Aromatic benzene ring (C–H) bond out-of-plane bending in terephthalate unit
520	P–O bond bending

In the case of pristine PBAT (Figure 4.6a), the FT-IR spectra over the aging period do not reveal significant changes; the only noteworthy observation is the formation of a very weak band between 3000 and 3700 cm^{-1}, which indicates the presence of hydroxyl groups. Given the absence of other significant modifications, the formation of (OH-) groups is attributed to water absorption on the surface of the samples[14].

In the case of PBAT composites (Figure 4.6b–e), notable alterations are observed. The most notable variation is the formation of a broad band at 3000–3700 cm^{-1}, which is characteristic of the hydroxyl (OH^{-}) bond. Additionally, there is a marked decrease in the intensity of the carbonyl (C=O) and ester (O=C–O) bonds at 1710 cm^{-1} and 1260 cm^{-1}, respectively[14,15]. This is further corroborated by the formation of a shoulder at 1645 cm^{-1}, which is indicative of the (C=O) bond in carboxylic acids engaged in intermolecular hydrogen bonding[[16]]. These findings indicate the hydrolysis of ester groups within the polymer's chain, which results in the generation of alcohol and carboxyl groups through the addition of water. The simultaneous action of UV radiation and water absorption results in the disintegration of the polymer chain, leading to the formation of free acid groups. These groups have the potential to interact with other molecules, leading to the formation of hydrogen bonds and a shift towards lower wavenumbers in the carbonyl absorption peaks[16].

Additionally, the intensification of the hydroxyl band may be attributed to the formation of hydroxyl groups in the CPG, which is caused by its hydrophilic nature. This behavior is more pronounced in composites with higher concentrations of CPG. Moreover, a peak at 2352 cm^{-1}, corresponding to the stretching of the (P-OH) bond, appears and intensifies as the phosphate glass content and test duration increase[16]. A comparable trend is observed with the band at 520 cm^{-1}, which is associated with the bending vibration of the same bond. The formation of the peak at 2352 cm^{-1} is likely attributable to the solubilization of the glass into the surface-absorbed water during the second phase of the test cycle, resulting in the formation of a thin, homogeneous layer on the specimen surface. This phenomenon has been previously observed in SEM images.

In the case of the LDPE spectra (Figure 4.6f), the primary peaks represent symmetric and asymmetric CH_2 stretching at 2915 and 2848 cm^{-1}, bending deformation at 1471 and 1462 cm^{-1}, and the rocking deformation of the carbon chain at 730–719 cm^{-1} remains unaffected by the aging process[17]. The most significant change is the formation and intensification of a peak between 1700 and 1800 cm^{-1}, which indicates the formation of carbonyl groups and suggests the photooxidative degradation of the polyethylene chain[7,18,19]. Additionally, there is a slight increase in the intensity of the hydroxyl group region. In summary, the aging effects on LDPE samples are negligible in comparison to the degradation of PBAT-CPG composites.

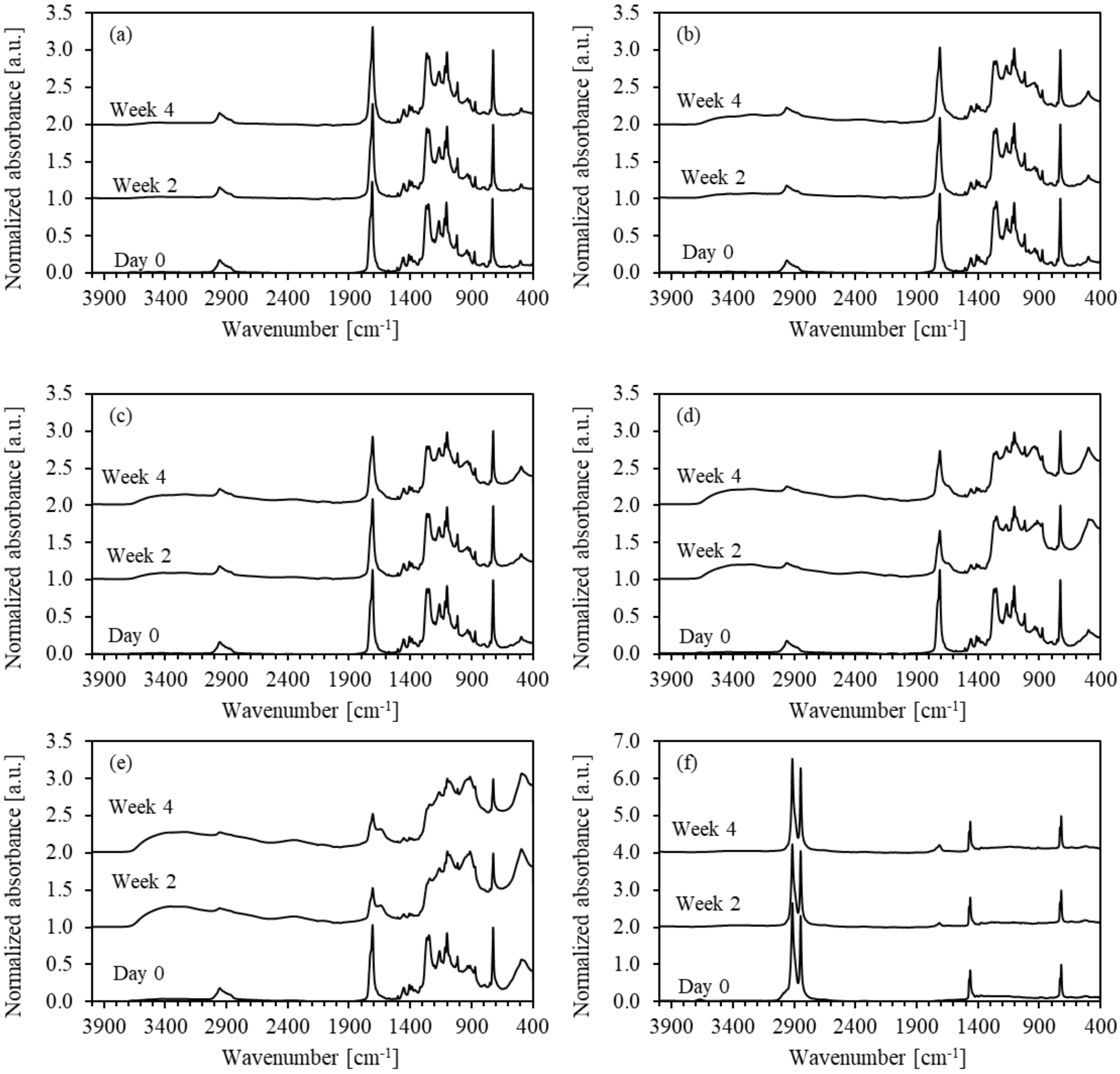

Figure 4.6 *(a) PBAT, (b) PBAT+4%CPG, (c) PBAT+10%CPG, (d) PBAT+20%CPG, (e) PBAT+40%CPG, and (f) LDPE FT-IR spectra over time during weathering test*

4.6 Results and Discussion - Disintegration Test

An initial approach to the evaluation of the degradation potential of polymeric materials is the measurement of disintegration under conditions of composting. The ISO 20200 standard provides a clear and reproducible methodology for conducting these tests in a laboratory setting. However, this method provides insight only into the process of disintegration, and it does not provide any information on the biodegradability of the material in composting environments. Further testing is required to confirm the material's compostability.

4.6.1 Physical Appearance

Optical microscopy represents an appropriate methodology for the examination and documentation of the samples. Figure 4.7 presents a comparison of the overall specimen morphology for the samples at the beginning of the test and after 28, 60, and 88 days. As observed in accelerated weathering tests, the LDPE samples demonstrated no discernible indications of deterioration at the conclusion of the test. In contrast, PBAT and PBAT-based composites exhibited a notable alteration in their visual appearance. The color change exhibited by the samples displayed variability between the PBAT and the composites. While PBAT exhibited a brown coloring and retained some transparency, the composites displayed a similar brown hue but became opaque by the second week of the test. The fragmentation of the specimens increased in correlation with the filler content and over time, rendering the materials increasingly fragile with each removal from the compost. Furthermore, the films exhibited an increasing degree of brittleness and difficulty in handling with the progression of the test, following the recovery period, rinsing, and overnight drying at 40°C.

4.6.2 Compost aspect

Throughout the course of the test, the physical characteristics of the compost were closely monitored, with particular attention paid to its color and odor, in accordance with the established standard. At the initial stage of observation, the compost exhibited a mild earthy odor, predominantly characterized by the scent of sawdust and organic material. By the second week, an ammonia-like odor had developed, suggesting the initiating phase of microbial decomposition. The odor persisted for approximately ten days before gradually reducing in intensity and becoming more neutral, characteristic of compost. Concurrently, the color of the compost transitioned from pale brown to deep, rich brown, indicative of the organic matter undergoing decomposition. Signs of active microbial activity, such as mold growth and the formation of small gas bubbles, became visible on the compost's surface during this phase. These observations align with the expected composting process outlined in the standard protocol.

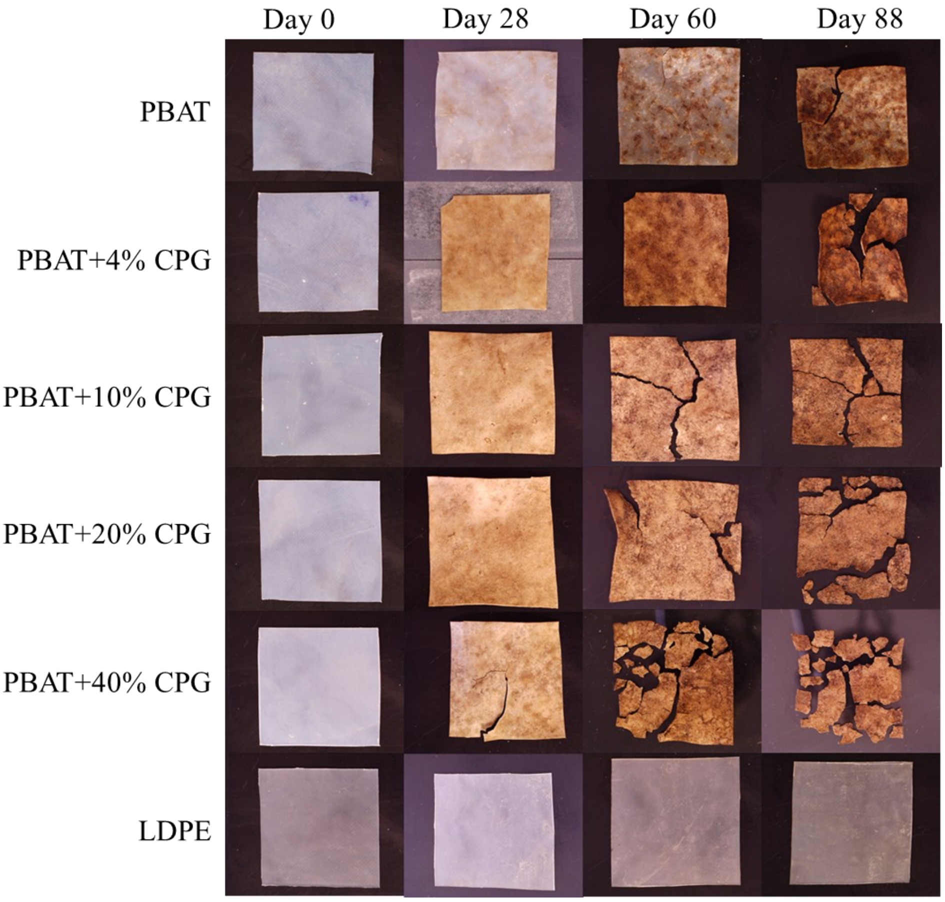

Figure 4.7 *Degradation of PBAT, PBAT-CPG composites, and LDPE over time*

4.6.3 FT-IR characterization

The FT-IR spectra of the samples before and after the fragmentation test are shown in Figure 4.8. All spectra are normalized to the 725 cm^{-1} peak, which is associated with out-of-plane bending of aromatic rings. This normalization is consistent with the approach used in the FT-IR analysis of the samples that were subjected to accelerated weathering.

Significant structural degradation, particularly in the fingerprint region (1200-700 cm^{-1}), is evident when comparing the spectra of the untested and fragmented samples after 88 days. In this region, the peaks become less distinct and their absorbance levels converge to an intermediate-intensity level, making the identification of specific signals more difficult. This suggests a chemical degradation of the polymer matrix. Furthermore, the appearance of a broad band between 3000-3700 cm^{-1}, corresponding to (OH-) bonds, indicates water absorption by the polymer. Superimposed on this band is a peak at 3278 cm^{-1}, which can be attributed to the amide bond from residual urea in the compost[16]. An important difference from the spectra of the aged samples

(Figure 4.6) is the marked decrease in the ester carbonyl (C=O) stretching peak at 1710 cm^{-1}, indicating that microbial activity is breaking down the polymer chain into simpler molecules, not just monomers.

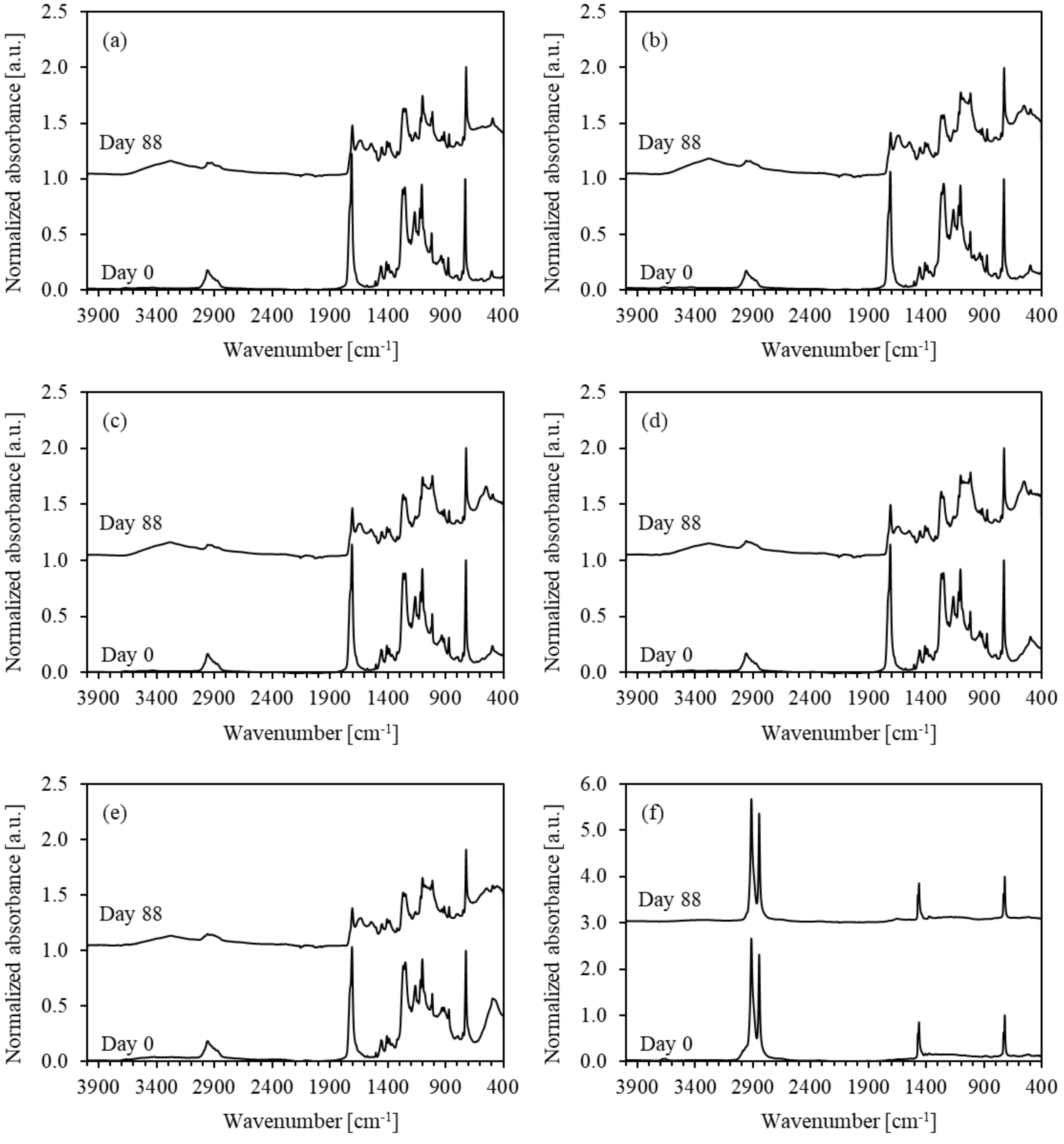

Figure 4.8 *(a) PBAT, (b) PBAT+4%CPG, (c) PBAT+10%CPG, (d) PBAT+20%CPG, (e) PBAT+40%CPG, and (f) LDPE FT-IR spectra at the beginning and at the end of the fragmentation test*

The degradation of PBAT in soil under controlled conditions follows two primary pathways: enzymatic and non-enzymatic. The enzymatic process is carried out by aerobic microorganisms such as bacteria, fungi and algae, while the non-enzymatic process occurs through hydrolysis[20,21]. Often, abiotic hydrolysis initiates the degradation process, breaking the polymer into smaller, lower molecular weight fragments that can be more easily metabolized by microorganisms[22]. In contrast, the LDPE spectra before and after the test show no changes, confirming the absence of degradation as evidenced by the absence of new peaks or changes in existing peaks.

4.6.4 Calculation of the Degree of Disintegration

Visual inspection clearly showed that all PBAT-CPG composite samples exhibited significant weight loss during the test. To calculate and track the *D*, expressed as a percentage of mass loss, Equation 4.1 was applied each time the samples were removed from the reactors. The average *D* values over time, are shown in Figure 4.9.

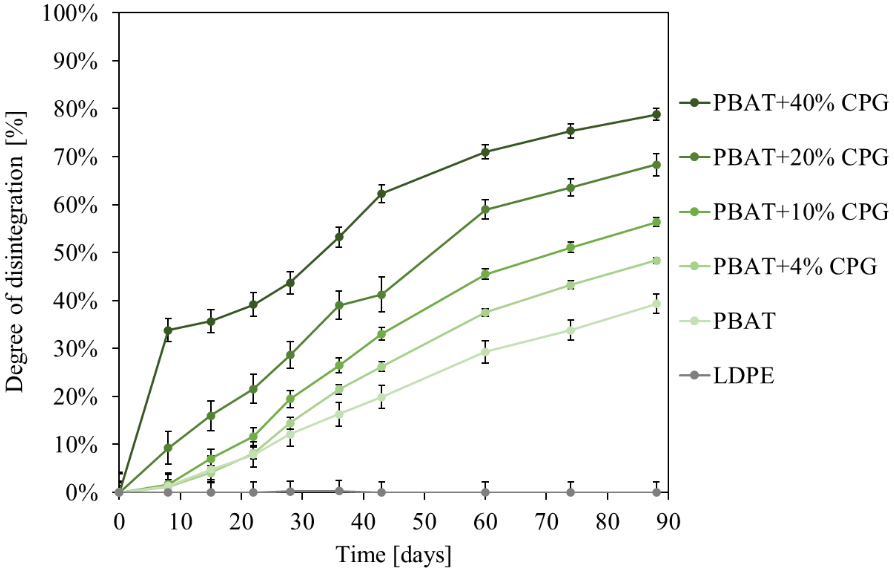

Figure 4.9 *Degree of disintegration D of PBAT, PBAT-CPG composites and LDPE over time*

As expected, LDPE showed no signs of degradation, while pure PBAT and PBAT-CPG composites showed progressive degradation with both time and increasing CPG content. During the first week, the mass of pure PBAT and composites containing 4% and 10% CPG remained relatively stable, while PBAT+20% CPG experienced an initial mass loss. PBAT+40% CPG exhibited a unique behavior, losing over 35% of its mass, likely due to the dissolution of the CPG content in the water within the compost. After 14 days, all biocomposites showed a consistent degradation trend. At the end of the 88-day test, the biocomposites showed degradation rates ranging from 38% for PBAT to 79% for PBAT+40% CPG. In analogy to accelerated weathering, LDPE, an oil-based and non-biodegradable polymer, served as a reference for non-degradability. Incorporating water-soluble CPG further accelerated degradation, with the degradation rate increasing with increasing filler content. The hydrophilic nature of CPG particles led to increased water absorption, especially at higher concentrations, which in turn promoted hydrolysis and polymer chain degradation, a behavior also observed in modified thermoplastic starch/PBAT blends[23]. Since CPGs dissolve completely in aqueous solutions and their solubility can be modified by adjusting the glass composition[24,25], it is assumed that all the CPG content is dissolved in the water present in the compost. After accounting for CPG dissolution, the degradation of the PBAT matrix was between 38% and 46% for all composites. This result is consistent with other studies on PBAT degradation; for example, Kijchavengkul et al. reported biodegradation rates between 33% and 67% within 45 days, depending on the type of compost used[1]. In addition, PBAT composites previously aged by UV irradiation have been observed to have higher degradation rates[26].

The mass reduction ratio, $MR = \frac{m_r}{m_i}$, which represents the reduction in mass relative to the initial mass of the sample, was calculated and analyzed over time for the composites tested. A decreasing exponential function (Equation 4.5) was used to fit the *MR* values plotted as a function of test duration for each composite (Figure 4.10):

$$MR = M_0 e^{-K_R \cdot t} \qquad \text{(Equation 4.5)}$$

where *t* is the time, M_0 represents the mass reduction at the initial time ($t = 0$) and it is imposed equal to 1, and the coefficient K_R represents the mass reduction rate or degradation rate.

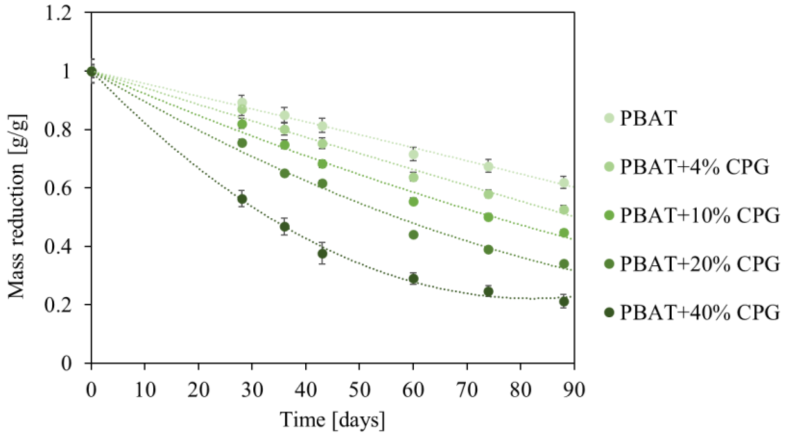

Figure 4.10 *Mass reduction MR of PBAT and PBAT-CPG composites over time. The dotted lines represent the fitting curves to the experimental data*

The data from the first 3 weeks were excluded from the analysis, as this period corresponds to the maturation phase of the compost, during which only small molecules are degraded, and the decomposition process is still developing[27]. As the CPG content increases, the decay trend of the fitted curves becomes more pronounced, indicating faster degradation. This is reflected in the K_R values derived from the fitting, which increase with increasing CPG content as shown in Table 4.5, providing a useful tool for predicting the degradation behavior of composites under aerobic composting conditions over time.

Statistical analysis was performed by calculating the covariance, σ_{xy}, (Equation 4.6) and the correlation coefficient (Equation 4.7) to assess the relationship between the K_R values and the CPG concentrations in the composites.

$$\sigma_{xy} = \frac{\sum_{i=1}^{n}(x_i-\bar{x})(y_i-\bar{y})}{n} \qquad \text{(Equation 4.6)}$$

$$C_C = \frac{\sigma_{xy}}{\sigma_x \cdot \sigma_y} \qquad \text{(Equation 4.7)}$$

Here x_i and x are respectively the i-th value and the average of the examined CPG concentrations, y_i and y are respectively the i-th value and the average of the K_R rates. The terms σ_x and σ_y denote the standard deviations of the two variables, calculated as in Equation 4.8 and Equation 4.9, respectively

$$\sigma_x = \sqrt{\frac{\sum_{i=1}^{n}(x_i-\bar{x})^2}{n}} \qquad \text{(Equation 4.8)}$$

$$\sigma_y = \sqrt{\frac{\sum_{i=1}^{n}(y_i-y)^2}{n}} \qquad \text{(Equation 4.9)}$$

The results obtained are shown in Table 4.5.

The value of σ_{xy} is 0.076, indicating a positive relationship between the two variables. Furthermore, the correlation is strong, as evidenced by the (C_C) of 0.999, which is very close to 1. These findings corroborate the hypothesis that elevating the CPG concentration within the polymer matrix is associated with an augmentation in the values of K_R. Upon plotting K_R as a function of CPG concentration (Figure 4.11), a clear linear relationship with filler content was observed, providing further evidence to support the hypothesis that the composites exhibit a higher disintegration rate compared to pristine PBAT.

To establish a quantitative relationship between CPG concentration and K_R, a simple linear regression was performed, with CPG concentration set as the independent variable and K_R as the dependent variable. The analysis was conducted with a 95% confidence level using Microsoft Excel (Microsoft, USA). The statistical parameters (intercept α, slope β, and coefficient of determination R^2) along with their associated errors are provided in Table 4.5. The equation for the regression line is shown in Figure 4.11. The high R^2 value indicates an excellent fit of the data to the model, enabling reliable predictions of composite disintegration behavior during aerobic composting over time.

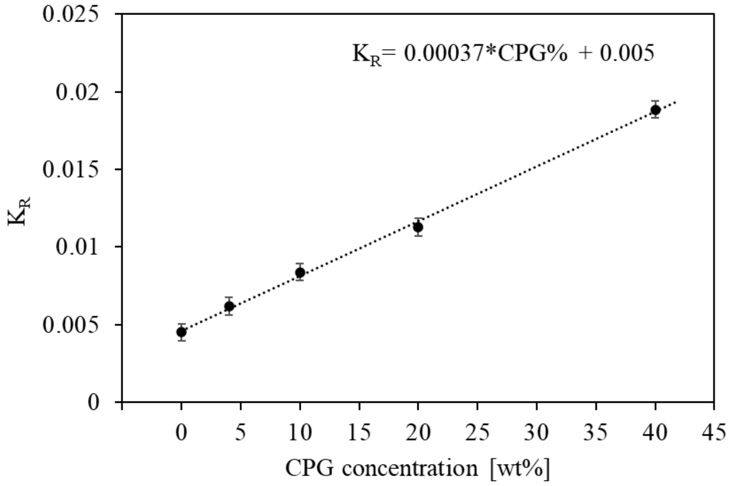

Figure 4.11 *Mass reduction rate K_R as a function of the CPG concentration for PBAT and PBAT-CPG composites. The dotted line represents the linear fitting to the experimental data*

Table 4.5 *K_R values, obtained by the exponential fitting function, and statistical parameters, extracted by statistical analysis*

	K_R value
PBAT	0.0052 ± 0.0002
PBAT+4%CPG	0.0070 ± 0.0003
PBAT+10%CPG	0.0090 ± 0.0004
PBAT+20%CPG	0.0122 ± 0.0004
PBAT+40%CPG	0.0204 ± 0.0007
	Statistical parameters
σ_{xy}	0.076
C_C	0.999
α	0.0052 ± 0.0002
β	0.00037 ± 0.00001
R^2	0.997

4.6.5 Validity of the Test

To ensure the validity of the experiment, the standard requirement is that the *D* measurements for each sample vary by no more than 10%. Table 4.6 presents the final *D* values calculated for each individual sample, along with the respective variations. To confirm the accuracy of the experiment, the reduction in volatile solids within the compost was determined using Equation 4.3. Furthermore, Table 4.7 presents the results of the analysis of two compost samples taken from each reactor. The *R* value exceeded 30% in each reactor, and the *D* variation criteria were satisfied. Therefore, the experiment can be considered valid for all reactors.

Table 4.6 *D values and maximum relative variation*

	D1	**D2**	**D3**	***ΔD*** **(%)**
PBAT	0.37	0.36	0.37	6.88 ± 0.07
PBAT+4%CPG	0.48	0.47	0.46	2.57 ± 0.03
PBAT+10%CPG	0.55	0.55	0.54	2.75 ± 0.03
PBAT+20%CPG	0.64	0.63	0.68	7.60 ± 0.08
PBAT+40%CPG	0.78	0.79	0.77	2.51 ± 0.03
LDPE	0.00	0.00	0.00	0.00 ± 0.00

Table 4.7 *Calculation of the decrease in volatile-solids R*

	M_i	M_f	$(DM)_i$	$(DM)_f$	$(VS)_i$	$(VS)_f$	***R (%)***
PBAT	188.09	105.28	0.41	0.35	0.95	0.90	55 ± 2
PBAT+4%CPG	226.79	129.39	0.40	0.34	0.95	0.90	54 ± 1
PBAT+10%CPG	251.24	144.58	0.40	0.34	0.95	0.89	55 ± 1
PBAT+20%CPG	251.28	143.80	0.41	0.34	0.95	0.90	55 ± 1
PBAT+40%CPG	298.26	179.15	0.42	0.33	0.95	0.85	58 ± 1
LDPE	234.62	131.78	0.40	0.34	0.95	0.90	55 ± 1

4.7 Conclusions

This research represents the continuation of the work carried out in Chapter 2 for the development and characterization of biocomposite materials made of PBAT reinforced with bioabsorbable CPG particles. These materials are proposed as a viable and sustainable alternative to traditional thermoplastic polymers, such as LDPE, currently used in agri-food packaging. The composites were evaluated for degradability under accelerated weathering and laboratory-scale composting conditions, and their performance was compared to that of LDPE.

In addition, oxygen and water vapor permeability tests were performed on films produced from each composite and on LDPE film for comparison. As a result of the permeability test, the composites showed a significant barrier effect against oxygen, even at low filler concentrations, although the resistance to water vapor was significantly lower compared to LDPE. This result was confirmed by the increased degradability under weathering conditions.

Accelerated weathering tests showed that PBAT-CPG composites were sensitive to environmental degradation, with increasing CPG concentration leading to discoloration, embrittlement and degradation. While biodegradability is improved, mechanical stability may be compromised. The disintegration test showed an increasing deterioration trend with filler content, reaching up to 80% disintegration at the highest concentration. The D obtained was a satisfactory value according to the standard followed, and the resulting fragmentation rate can be modulated by adjusting the material composition. On the other hand, LDPE, taken as a reference, confirms its non-biodegradability in both tests.

Overall, the addition of CPG microparticles to the PBAT matrix allowed to improve the mechanical and viscoelastic properties, as shown in Chapter 2, while preserving and modulating the degradation properties of the composite according to specific needs. The results obtained highlight the versatility of PBAT-CPG composites and allow them to be proposed as a promising and environmentally friendly alternative to thermoplastic polymers commonly used in many fields, such as packaging and agriculture, and for applications where end-of-life compostability is critical.

References

1. Kijchavengkul, T. et al. Biodegradation and hydrolysis rate of aliphatic aromatic polyester. Polym Degrad Stab 95, 2641–2647 (2010).

2. Weng, Y. X., Wang, Y., Wang, X. L. & Wang, Y. Z. Biodegradation behavior of PHBV films in a pilot-scale composting condition. Polym Test 29, 579–587 (2010).

3. Bo, L., Guan, T., Wu, G., Ye, F. & Weng, Y. Biodegradation Behavior of Degradable Mulch with Poly (Butylene Adipate-co-Terephthalate) (PBAT) and Poly (Butylene Succinate) (PBS) in Simulation Marine Environment. Polymers 2022, Vol. 14, Page 1515 14, 1515 (2022).

4. McKeen, L. W. Polyolefins, Polyvinyls, and Acrylics. Permeability Properties of Plastics and Elastomers 145–193 (2012) doi:10.1016/B978-1-4377-3469-0.10009-8.

5. Lapa, A., Cresswell, M., Jackson, P. & Boccaccini, A. R. Phosphate glass fibres with therapeutic ions release capability–a review. Advances in Applied Ceramics 119, 1–14 (2020).

6. Wang, L. F., Rhim, J. W. & Hong, S. I. Preparation of poly(lactide)/poly(butylene adipate-co-terephthalate) blend films using a solvent casting method and their food packaging application. LWT - Food Science and Technology 68, 454–461 (2016).

7. Feldman, D. Polymer Weathering: Photo-Oxidation. Journal of Polymers and the Environment 2002 10:4 10, 163–173 (2002).

8. Kockott, D. Natural and artificial weathering of polymers. Polym Degrad Stab 25, 181–208 (1989).

9. Cai, Y., Lv, J. & Feng, J. Spectral Characterization of Four Kinds of Biodegradable Plastics: Poly (Lactic Acid), Poly (Butylenes Adipate-Co-Terephthalate), Poly (Hydroxybutyrate-Co-Hydroxyvalerate) and Poly (Butylenes Succinate) with FTIR and Raman Spectroscopy. J Polym Environ 21, 108–114 (2013).

10. Baia, L., Muresan, D., Baia, M., Popp, J. & Simon, S. Structural properties of silver nanoclusters-phosphate glass composites. Vib Spectrosc 43, 313–318 (2007).

11. Baia, L., Baia, M., Kiefer, W., Popp, J. & Simon, S. Structural and morphological properties of silver nanoparticles-phosphate glass composites. Chem Phys 327, 63–69 (2006).

12. Shankar, S. & Rhim, J. W. Tocopherol-mediated synthesis of silver nanoparticles and preparation of antimicrobial PBAT/silver nanoparticles composite films. LWT - Food Science and Technology 72, 149–156 (2016).

13. Bumbudsanpharoke, N., Wongphan, P., Promhuad, K., Leelaphiwat, P. & Harnkarnsujarit, N. Morphology and permeability of bio-based poly(butylene adipate-co-terephthalate) (PBAT), poly(butylene succinate) (PBS) and

linear low-density polyethylene (LLDPE) blend films control shelf-life of packaged bread. Food Control 132, 108541 (2022).

14. Kijchavengkul, T., Auras, R., Rubino, M., Ngouajio, M. & Fernandez, R. T. Assessment of aliphatic–aromatic copolyester biodegradable mulch films. Part I: Field study. Chemosphere 71, 942–953 (2008).

15. Scarfato, P., Acierno, D. & Russo, P. Photooxidative weathering of biodegradable nanocomposite films containing halloysite. Polym Compos 36, 1169–1175 (2015).

16. Silverstein, R. M., Webster, F. X. & Kiemle, D. J. Infrared spectrometry. in Spectrometric identification of organic compounds (eds. Brennan, D., Yee, J., Wolfman-Robichaud, S. & Rigby, S.) 83–138 (John Wiley and Sons, Inc., 2005).

17. Doğan, F., Şirin, K., Kolcu, F. & Kaya, İ. Conducting polymer composites based on LDPE doped with poly(aminonaphthol sulfonic acid). J Electrostat 94, 85–93 (2018).

18. Gardette, M. et al. Photo- and thermal-oxidation of polyethylene: Comparison of mechanisms and influence of unsaturation content. Polym Degrad Stab 98, 2383–2390 (2013).

19. Gulmine, J. V., Janissek, P. R., Heise, H. M. & Akcelrud, L. Polyethylene characterization by FTIR. Polym Test 21, 557–563 (2002).

20. Ferreira, F. V, Cividanes, L. S., Gouveia, R. F. & Lona, L. M. F. An overview on properties and applications of poly(butylene adipate-co-terephthalate)–PBAT based composites. Polymer Engineering and Science vol. 59 E7–E15 Preprint at https://doi.org/10.1002/pen.24770 (2019).

21. Pinheiro, I. F., Morales, A. R. & Mei, L. H. Polymeric biocomposites of poly (butylene adipate-co-terephthalate) reinforced with natural Munguba fibers. Cellulose 21, 4381–4391 (2014).

22. Shah, A. A., Hasan, F., Hameed, A. & Ahmed, S. Biological degradation of plastics: A comprehensive review. Biotechnology Advances vol. 26 246–265 Preprint at https://doi.org/10.1016/j.biotechadv.2007.12.005 (2008).

23. Wongphan, P., Panrong, T. & Harnkarnsujarit, N. Effect of different modified starches on physical, morphological, thermomechanical, barrier and biodegradation properties of cassava starch and polybutylene adipate terephthalate blend film. Food Packag Shelf Life 32, 100844 (2022).

24. Döhler, F., Mandlule, A., Van Wüllen, L., Friedrich, M. & Brauer, D. S. 31 P NMR characterisation of phosphate fragments during dissolution of calcium sodium phosphate glasses. J Mater Chem B 3, 1125–1134 (2015).

25. Mikhailenko, N. Y., Stroganova, E. E. & Buchilin, N. V. Solubility of Calcium Phosphate Glasses and Glass Ceramic Materials in Water and Physiological Media. Glass and Ceramics (English translation of Steklo i Keramika) 70, 158–163 (2013).

26. Falcão, G. A. M., Almeida, T. G., Bardi, M. A. G., Carvalho, L. H. & Canedo, E. L. PBAT/organoclay composite films—part 2: effect of UV aging on permeability, mechanical properties and biodegradation. Polymer Bulletin 76, 291–301 (2019).

27. Iggui, K. et al. A biodegradation study of poly(3-hydroxybutyrate-co-3-hydroxyvalerate)/organoclay nanocomposites in various environmental conditions. Polym Degrad Stab 119, 77–86 (2015).

Chapter 5

Anaerobic fermentation of GT-plasticized PHB

5.1 Introduction

As previously discussed, an understanding of the degradation behavior of biopolymers is of critical importance for ensuring sustainability, particularly in the context of developing circularity.

Poly(3-hydroxybutyrate) (PHB) is of significant interest due to its microbial origin and inherent biodegradability. These properties render PHB a promising candidate for the exploration of novel pathways towards circularity, as its biodegradation is well aligned with the principles of sustainable practice in material production and disposal.

This chapter presents an examination of the biological degradation of PHB composites with varying concentrations of glycerol trilevulinate (GT), as developed and characterized in Chapter 3. The research was conducted at the Environmental Technology Department (ETE) at Wageningen University and Research (WUR) in the Netherlands.

The principal objective of the study was to examine the impact of the plasticizer GT on the biodegradation behavior of PHB composites under anaerobic conditions, with a particular focus on their suitability for sustainable applications.

The degradation of PHB composites was examined using mixed-culture microbial fermentation under anaerobic conditions. Two experimental setups were utilized to investigate various aspects of the biodegradation process.

In the first experiment, solid particles of PHB and plasticized PHB were subjected to anaerobic fermentation to ascertain the impact of varying concentrations of GT on the degradation rate and mechanism of the biopolymer. The objective of this phase was to identify the optimal plasticizer concentration that balances mechanical properties with biodegradation efficiency. If the concentration of plasticizer is excessive, it can alter the structural integrity of the material and slow down its breakdown or influence the bacterial metabolism.

In the second experiment, PHB with a high GT content was subjected to hydrolysis prior to undergoing anaerobic fermentation. The objective of this pretreatment was to facilitate the biodegradation process by enhancing the breakdown of polymer chains, thereby enabling a comparative assessment of degradation rates and conversion products between untreated and pretreated samples.

Throughout the course of the study, gas chromatographic measurements were employed to monitor the production of volatile fatty acids (VFA), which serve as key indicators of the fermentation process. VFA are essential intermediates in anaerobic digestion, providing a qualitative measure of microbial activity and material breakdown. By monitoring VFA production over time, the study evaluated the efficacy of the degradation process and identified differences in the fermentation profiles between the two experimental setups.

This research contributes to a more thorough comprehension of the biodegradation processes occurring in PHB composites, particularly in relation to the quantity of GT present, and underscores their prospective utility in sustainable, circular production systems.

5.2 Materials

The PHB plasticized with GT produced in Chapter 3 (PHB, PHB2.5GT, PHB5GT, PHB10GT) were used for anaerobic fermentation. The pellets obtained after twin-screw extruder (conditions are described in Chapter 3), were ground (IKA A11 basic) and sifted (stainless steel sieve from Retsch, Germany) to obtain a powder with a particle dimension below 200 μm, to ensure a higher surface for the microbial fermentation.

The nutrient medium was prepared with the following composition: 0.1 g/l of yeast extract, 20 ml/l of stock solution I and 20 ml/l of stock solution II, 1 ml/l of vitamins, and 0.5 ml/l of trace metals. Table 5.1 reports the compositions of the stock solutions. In addition, 5 g/l of 2-bromoethanesulfanoate (BES) (CAS 4263-52-9) was added to the medium to inhibit methane (CH_4) production in favor of carboxylates.

The inoculum used for the fermentation process, in the concentration of 5% v/v, consisted of an undefined mixed culture, including cow rumen (pH 7.22) and different chain elongation strands, named R3 (pH 7.50), R4 (pH 6.84), R5 (pH 5.91), from previous experiments[1] stored at 4 °C. The inoculum was prepared with a composition of 57% cow rumen and 14% each of R3, R4, and R4, flushed with nitrogen (N_2), and stored at 4 °C upon use. The final pH of the inoculum was 7.62.

Table 5.1 *Composition of the stock solutions used to prepare the nutrient medium for the mixed culture fermentation*

	Compound	**Concentration (g/L)**	**Dilution factor**
Stock solution I – Minerals	$NH_4H_2PO_4$	180	50
	$MgCl_2 \cdot 6H_2O$	16.5	
	$MgSO_4 \cdot 7H_2O$	10	
Stock solution II – Minerals	$CaCl_2 \cdot 2H_2O$	10	50
	KCl	7.5	
Trace metals	$FeCl_2 \cdot 4H_2O$	30	2000
	$MnCl_2 \cdot 4H_2O$	0.6	
	H_3BO_4	6.0	
	$CoCl_2 \cdot 6H_2O$	4.0	
	$CuCl_2 \cdot H_2O$	0.2	
	NiCl2 ·6H2O	0.4	
	$ZnSO_4 \cdot 7H_2O$	2.0	
	$Na_2MoO_4 \cdot 4H_2O$	0.6	
	Na_2SeO_3	0.2	
	EDTA	12.4	
Vitamins	Biotin	0.106	1000
	Folic acid	0.005	
	Pyridoxal-HCl	0.0025	
	Lipoic acid	0.015	
	Riboflavin	0.0125	
	Thiamin-HCl	0.413	
	Ca-D-panthotene	0.0125	
	Cyanocobalamin	0.0125	
	P-aminobenzoic acid	0.0125	
	Nicotinic acid	0.0125	
Supplements	Yeast extract	0.1	
	KOH	4M	

5.3 Methodology

5.3.1 Experimental Design

Two series of comparative experiments were designed in this study: I) mixed-culture fermentation of PHB hydrolysates, where PHB with10% GT was first hydrolyzed via hydrothermal process and subsequenty diluted to three different concentrations of Chemical Oxigen Demand (COD), named Hydrolyzed Fermentation (*HF*); II) mixed-culture fermentation of PHB and plasticized PHB solid particles, using the material milled into powder, named Solids Fermentation (*SF*).

Table 5.2 *Overview of experimental design of mixed-culture fermentation*

Experiment	Substrate	Concentration	Duration of experiment	Initial pH
Group I	PHB10GT Hydrolysate	4 g_{COD}/l	15 d	6.77
	PHB10GT Hydrolysate	10 g_{COD}/l	15 d	6.25
HF	PHB10GT Hydrolysate	20 g_{COD}/l	15 d	6.23
Group II	PHB powder	50 $g_{plastic}$/l	120 d	6.75
	PHB2.5GT powder	50 $g_{plastic}$/l	120 d	6.75
SF	PHB5GT powder	50 $g_{plastic}$/l	120 d	6.79
	PHB10GT powder	50 $g_{plastic}$/l	120 d	6.73

5.3.2 Morphological analysis

Granulometry characterization

Particle size distribution curves and dimensions, including the mean diameter as well as the D_{10}, D_{50}, and D_{90} percentiles, were determined using a Mastersizer 3000 laser granulometer (Malvern Instruments Ltd., Malvern, UK) in dry mode, applying the Fraunhofer approximation. This method is applicable in instances where the optical properties of the material are unknown, as is the case here, given that the particles are larger than 20 µm and opaque, producing minimal light scattering at small angles. The D_{10} [µm], D_{50} [µm], and D_{90} [µm] values indicate the diameters of particles present in the sample below which 10%, 50%, and 90% of the sample volume, respectively, can be found.

Scanning Electron Microscopy (SEM) characterization

Scanning Electron Microscopy (SEM) was utilized to examine the microscopic surface characteristics of plastic particles. SEM images were captured using a field emission gun scanning electron microscope (FEG-SEM, Nova NanoSEM 450, FEI Company, USA) with a backscatter detector. All images were obtained with an accelerating voltage of 15 kV, an arbitrary spot size of 4, and a working distance of approximately 6 mm, at different magnifications.

Additionally, an optical microscope (Nikon, SMZ800) was utilized to analyze the morphology of the polymer particles both prior to and following the particle fermentation process, thereby allowing for a comparison of any potential morphological changes caused by fermentation.

5.3.3 Hydrothermal Process

The hydrolysis of PHB pellets was conducted in an 800 mL bench-top stirred reactor (Parr 4857, Parr Instruments Moline, Illinois, USA). 15g of PHB10GT and 0.25M NaOH were dispersed in 700 mL demineralized water. The hydrothermal process was conducted for a total of 24 hours, with the temperature increasing to 160°C within the first hour and remaining at this temperature for the subsequent 22 hours. Subsequently, the system was cooled down to room temperature by the cooling solvent. Throughout the process, the stirring rate was maintained at 85 rpm without any pressure control. Figure 5.1 illustrates the temperature and pressure profiles recorded during the procedure. After hydrolysis, the hydrolysate was collected via centrifugation at 6920 rpm for 18 minutes (Hermle, Z36HK) and filtration through a 0.45 µm membrane (CHROMAFIL Xtra, Machinerey-Nagel, Düren, Germany), with the final pH recorded at 11.37.

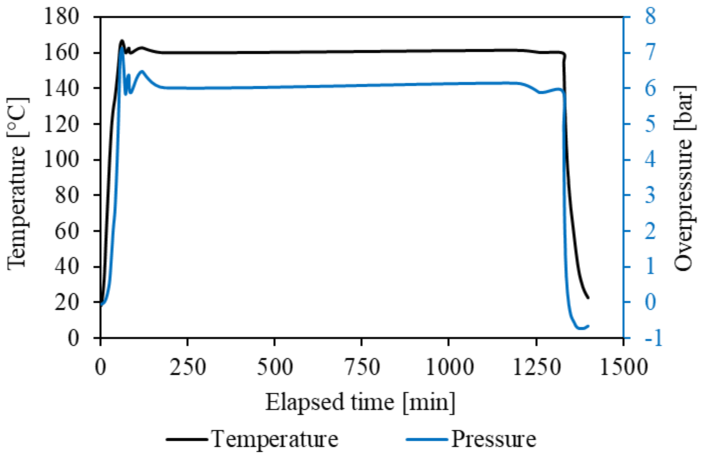

Figure 5.1 *Temperature and pressure profiles during the hydrothermal treatment*

5.3.4 Mixed-culture fermentation setup

For Hydrolysate Fermentation (*HF*), reactors were assembled for each hydrolysate concentration by combining the specified nutrients, as detailed in the Materials section, and adding the appropriate hydrolysate solution to achieve a final working volume of 47.5 ml. Control reactors, which served as references, were prepared in a similar manner but with demineralized water replacing the hydrolysates. The pH of the liquid medium was adjusted to 7.0 ± 0.1 using 4M KOH. The bottles were sealed with rubber stoppers, flushed with nitrogen for 10 minutes to create anaerobic conditions, and inoculated with 2.5 ml of mixed culture, resulting in a total volume of 50 ml. Subsequently, the headspace was filled with an N_2/CO_2 (80%/20%) mixture at 1.5 bar using a gas exchanger (SC920G, KNF Neuberger, Freiburg, Germany). Samples were collected at the beginning (t_0) and at 72-hour intervals for a total of 15 days. Each sample was obtained by collecting 2 ml of the solution and storing it at -18°C for subsequent analysis.

In the case of *SF*, ground PHB and PHB+GT particles, with GT concentrations of 2.5%, 5%, and 10%, were employed as substrates without undergoing any additional processing. Similarly, the batch reactors were filled with nutrients and demineralized water (to a volume of 45 ml) and 2.5 g of plastic particles (with an estimated density of 1 g/ml). The suspension was subjected to mechanical stirring to achieve homogeneity. Additionally, control reactors were prepared with 47.5 ml of demineralized water and nutrients. Gas exchange and inoculation were conducted in accordance with the methodology previously described for *HF*. *SF* sampling was performed at t_0 and at 30-day intervals over a 120-day period, with 2 ml samples stored at -18 °C until analysis.

All experiments were conducted in triplicate, with fermentation carried out in a temperature-controlled shaker (Innova 44) at 35°C and 120 rpm for both *HF* and *SF*.

5.3.5 Analytical measurements

Prior to each sampling, the headspace pressure in each batch bottle was measured with a pressure meter (GMH 3151, GHM Group, Greisinger, Regenstauf, Germany) to verify that overpressure in the headspace atmosphere was maintained. Additionally, the pH was determined with a pH meter (PHM210, RADIOMETER ANALYTICAL SAS, France).

Subsequent to the preparation of the bottles, a gas chromatography (GC) system (Shimadzu GC-2010, Kyoto, Japan) equipped with a dual-column configuration—Porabond Q (50 m × 0.53 mm × 10 µm; Varian, Agilent, The Netherlands) and Molsieve 5A (25 m × 0.53 mm × 50 µm; Varian, Agilent, The Netherlands)—was employed to evaluate headspace gases (N_2 and CO_2). A 50 µL sample was injected at 120 °C, while the oven and detector temperatures were set at 45 °C and 150 °C, respectively. The carrier gas was hydrogen, maintained at a pressure of 0.6 bar.

To monitor the composition of the gases produced during fermentation, an additional GC system (HP-5890, Hewlett Packard, Agilent, USA) equipped with an HP Molsieve 5A (30 m × 0.53 mm × 25 µm) column was employed to analyze the production of hydrogen and verify the absence of methane. Argon was employed as the carrier gas, with an injection volume of 100 µL, and the oven was set to 40 °C [2].

The production of VFA was quantified using liquid gas chromatography (Agilent 7890B, Agilent, USA), employing an HP-FFAP column (25 m × 0.32 mm × 0.50 µm). The flame-ionized detector (FID) and injection were set to 240 °C and 250 °C, respectively. Prior to injection, the samples were subjected to centrifugation at 15,000 rpm for 10 minutes (Eppendorf, 5425), filtered through a 0.45 µm membrane (CHROMAFIL Xtra, Machinerey-Nagel, Germany), diluted, and acidified with formic acid to a concentration of 1.5 wt%. A 1 µL sample was injected with N_2 serving as the carrier gas, flowing at 1.25 mL/min for the initial three minutes and then at 2 mL/min for the remainder of the run. The oven temperature program commenced at 60 °C for three minutes, increased at a rate of 21 °C/min to 140 °C, then rose at a rate of 8 °C/min to 150 °C, held for 1.5 minutes, and finally increased to 240 °C at a rate of 120 °C/min, holding for three minutes.

While the GC method permitted the qualitative identification of 3-hydroxybutyrate (3-HB) and crotonate, quantitative analysis was not feasible due to methodology constraints. This mixture is designated as CR-3HB. The Chromeleon software (version 7, Thermo Fisher Scientific, USA) was employed for data analysis.

5.4 Results and discussion

5.4.1 Morphology characterization

The plastic particles were analyzed by SEM (Figure 5.2a). Observation of the particle morphology shows that mechanical grinding of PHB granules produces irregularly shaped particles, and that the materials exhibit homogeneity at different plasticizer concentrations. The absence of phase separation or regions where the plasticizer exudes indicates a thorough mixing of the additive within the polymer matrix, implying a good compatibility between the two components at the concentrations studied [3].

The size distribution curves (Figure 5.2b) show a consistent trend for all the formulations except PHB10GT, which shows a main peak of lower intensity with a marked shoulder at a smaller size class values. Particle size analysis (data shown in Table 5.3) confirmed the particle size after sieving, with D_{90} ranging from 203 to 232 µm and a volumetric mean diameter (D[4:3]) of about 110 µm. In contrast, the average diameter calculated based on the number of particles (D[1:0]) is approximately ten times smaller. This indicates that many of the particles have a small diameter, which allows them to have a higher specific surface area. The distribution of particle dimensions, and particularly the high specific surface area combined with the rough surface texture of the particles, can be considered as a favorable factor for biodegradation. In fact, it is well known that biodegradation depends on the amount of surface area exposed to enzymatic hydrolysis [4].

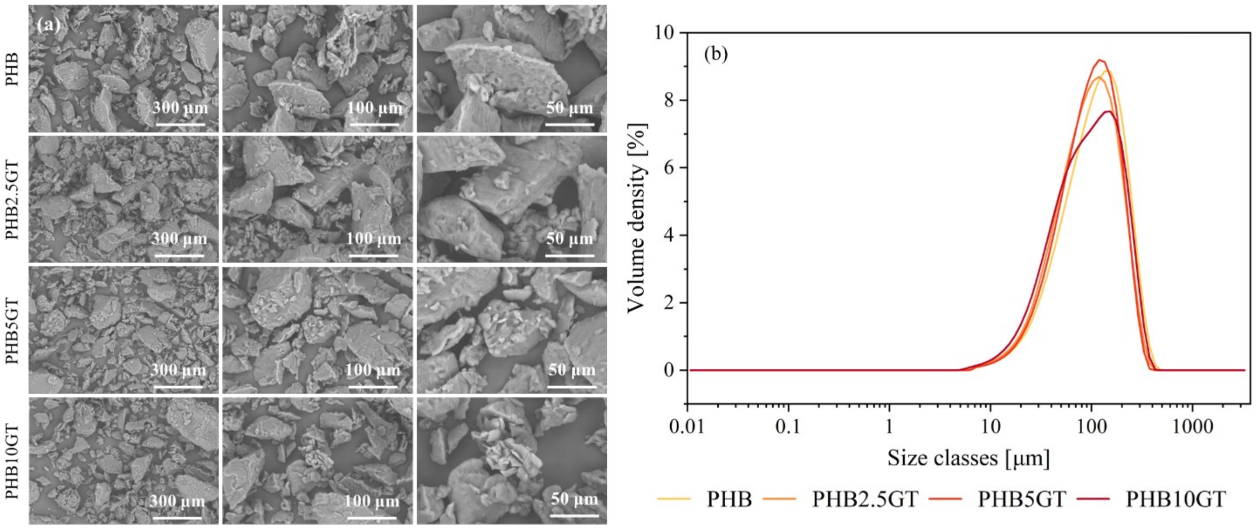

***Figure 5.2** a) SEM images and b) size distribution curves of the milled materials*

***Table 5.3** Particle size analysis of the milled materials*

	D_{10} (µm)	**D_{50} (µm)**	**D_{90} (µm)**	**D[4:3] (µm)**	**Specific Surface Area (m^2/kg)**	**D[1:0] (µm)**
PHB	38.2 ± 0.1	110.0 ± 1.1	232 ± 0.9	124 ± 0.1	79.6 ± 0.2	19.7 ± 0.3
PHB2.5GT	34.3 ± 0.1	95.1 ± 0.9	205.0 ± 2.1	109 ± 1.1	89.9 ± 0.6	17.9 ± 0.2
PHB5GT	36.3 ± 0.1	98.6 ± 0.6	203 ± 1.7	110 ± 1.7	85.7 ± 0.1	20.1 ± 0.1
PHB10GT	31.2 ± 0.3	95.3 ± 0.5	221.0 ± 0.2	113 ± 0.2	94.36 ± 0.5	16.3 ± 0.9

5.4.2 Anaerobic fermentation

At 160 °C hydrothermally treated PHB was anaerobically fermented into VFA

The production of VFA from hydrolyzed plastics was evaluated at initial concentrations of 4 g_{COD}/L and 10 g_{COD}/L (Figure 5.3a, 5.3b). At the beginning of the fermentation, the medium consisted mainly of CR-3HB, confirming that the PHB10GT underwent hydrolysis during the hydrothermal treatment (HTT). Trace amounts of n-butyrate (n-C_4) and n-caproate (n-C_6) were also initially present, likely introduced by the inoculum, as seen in control samples (Figure 5.3D). The average total soluble COD (sCOD) of the identified compounds varied but remained within acceptable standard deviation limits. Discrepancies between the total sCOD and the initial supplied COD indicate the presence of unidentified molecules and oligomers that could not be detected by GC. This is confirmed by the presence of unidentified peaks in the chromatograms obtained (Figure 5.4).

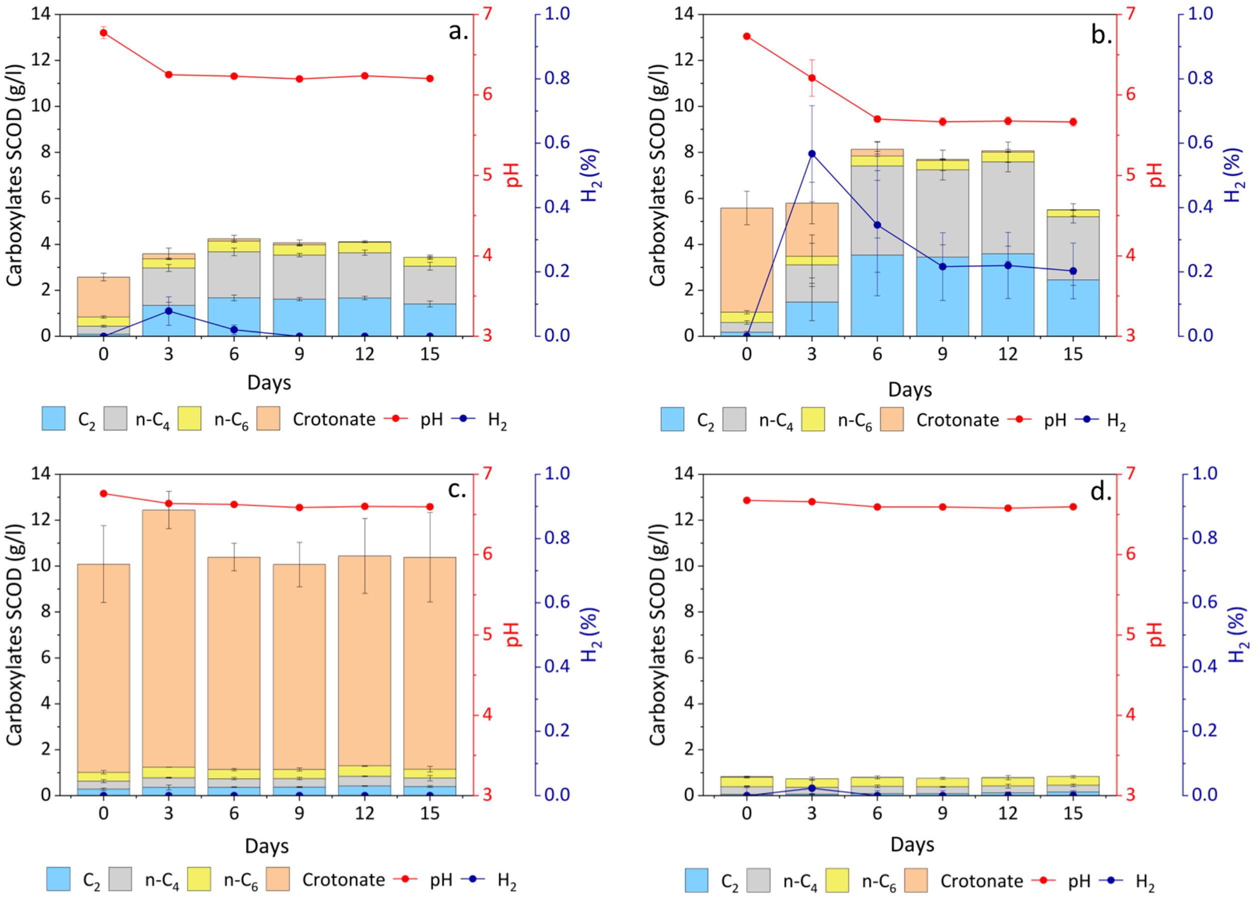

__Figure 5.3__ Carboxylates production, pH and H_2 for HF experiment. a) Hydrolysate 4 g_{COD}/L; b) Hydrolysate 10 g_{COD}/L; c) Hydrolysate 20 g_{COD}/L; d) Control

During anaerobic fermentation, the concentration of CR-3HB was fully depleted in both the 4 gCOD/L and 10 g_{COD}/L samples, with increasing concentrations of acetate (C_2) and n-C_4 observed. It is possible to hypothesize that different species of *Clostridium* present in the mixed inoculum are responsible for using the crotonate as substrate[5]. It is noteworthy that the production of VFA exhibited a correlation with the pH trends (red line). For both concentrations, a decline in pH was accompanied by a reduction in CR-3HB and an increase in C_2 and n-C_4 levels. This VFA profile is consistent with previous findings on alkaline-pretreated PHA plastic fermentation[6].

Concurrently, the headspace analysis indicated the generation of minor quantities of hydrogen (H_2) (blue line) in the 4 g_{COD}/L and 10 g_{COD}/L samples during the same interval. This phenomenon is likely a consequence of microbial metabolism of CR-3HB or butyrate conversion to acetate[7]. No hydrogen was detected in the control or 20 g_{COD}/L samples (Figure 5.3c). The amount of hydrogen produced decreased after an initial peak, suggesting that it could have been utilized, in conjunction with CO_2 for ethanol or C_2 production[8,9]. As anticipated, the addition of BES to the culture medium resulted in the absence of methane detection.

Regarding pH, the reference sample and the sample containing 20 g_{COD}/L demonstrated consistent levels throughout the experimental period. In contrast, the samples containing 4 g_{COD}/L and 10 gCOD/L exhibited a decline in pH from 6.7 to 6.3 and 5.7, respectively, over the initial three to six days. This pH decrement reached a plateau with the complete conversion of CR-3HB[10]. It is noteworthy that in the 20 g_{COD}/L experiment, CR-3HB was not converted to C_2 and n-C_4. This indicates the potential for toxicity from the high concentration of hydrolysate, which is consistent with the literature that VFA inhibition can be concentration-dependent[11]. In conclusion, the findings suggest that hydrolysate concentrations of 4 g_{COD}/L and 10 g_{COD}/L allow for complete microbial conversion to VFA, particularly acetate and n-butyrate.

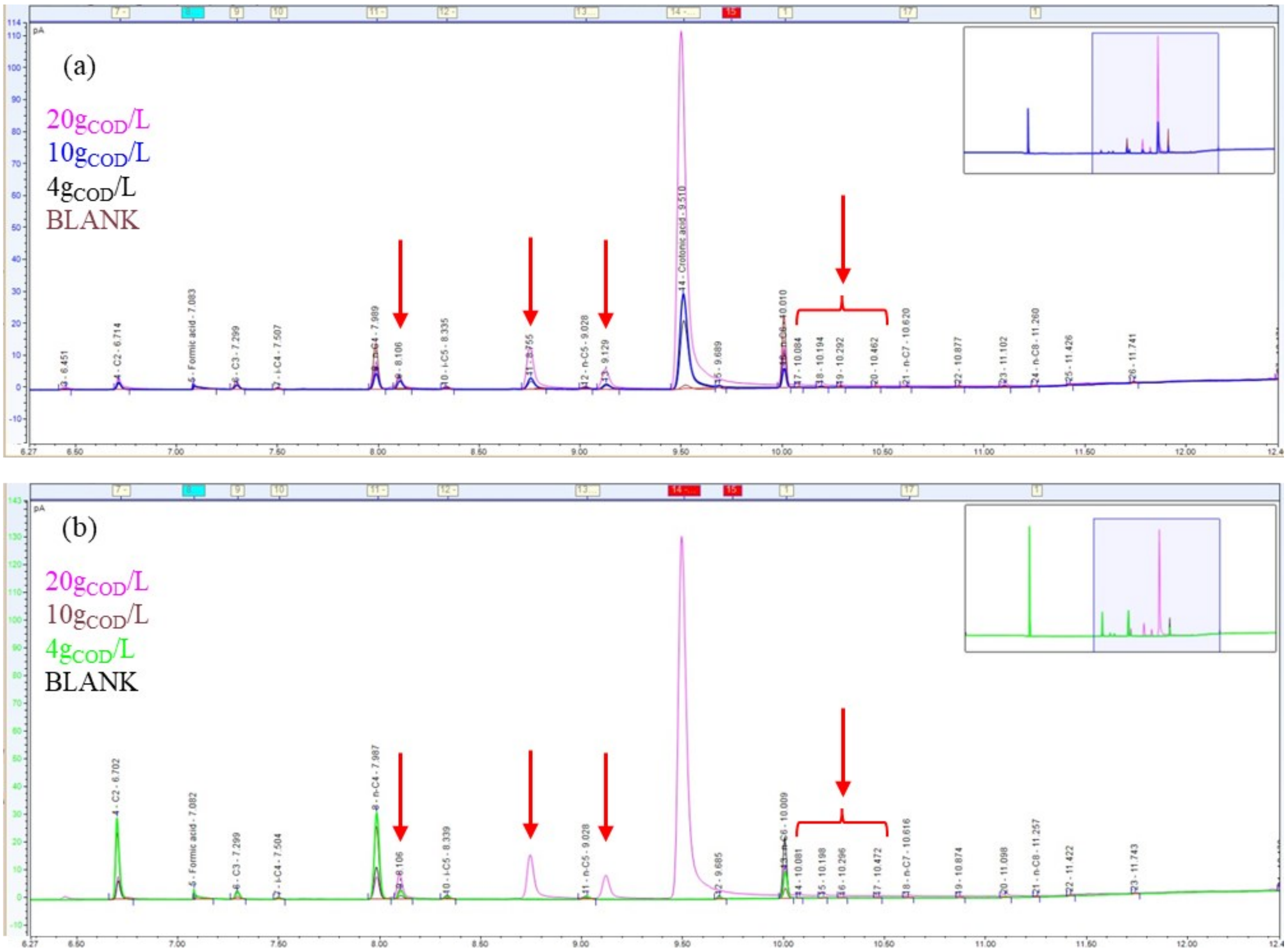

***Figure 5.4** Chromatograms of the HF samples (a) before and (b) after the fermentation, highlighting unidentified peaks*

PHB anaerobically fermented into VFA while crotonate accumulation occurred at long term

The production of VFA in long-term PHB+GT fermentation primarily resulted in the formation of C_2 and n-C_4. At the beginning of the experiment, only trace levels of VFA, specifically n-C_4 and C_6, were detected, which is likely to have originated from the inoculum, as was observed in the control samples (Figure 5.5e). Over time, the concentrations of VFA, particularly C_2 and n-C_4, increased across all PHB formulations and reached a stable level by day 90 (Figure 5.5a-d). Throughout the majority of the experiment, CR-3HB remained at minimal levels, with a notable increase observed only near the conclusion of the process, potentially attributable to delayed microbial activity.

GC analysis (Figure 5.6) revealed the presence of several unidentified peaks alongside the expected VFA, which may indicate the formation of intermediate compounds during the decomposition of plastics. This observation is consistent with the findings of Janssen and Harfoot, who reported the fermentation of 3HB into C_2, n-C_4, and H_2 during PHB biodegradation[12]. These findings indicate the existence of a two-phase degradation process, in which the initial phase involves the hydrolysis of PHB+GT plastic particles into CR-3HB, followed by the microbial conversion of CR-3HB into carboxylates. By day 90, nearly all CR-3HB had been converted to VFA, indicating that under favorable conditions, hydrolysis continues until a critical VFA concentration is reached.

However, low pH values, caused by the accumulation of short-chain VFA[13], may in turn impede further VFA conversion while allowing hydrolysis to persist, which could impact microbial activity. The initial pH value decreased from approximately 6.8 to a range of 4.6–5.7, stabilizing after day 60 in the majority of formulations. An exception was observed in the case of PHB2.5GT, where a continued decrease in pH was noted until day 90. The prolonged decrease in pH observed in certain formulations indicates that fluctuations in pH may be a crucial factor influencing microbial activity and carboxylate yields.

It has been demonstrated in studies that VFA have the potential to inhibit acetogenic bacteria if they accumulate in the system[14]. Furthermore, evidence indicates that VFA toxicity is pH-dependent[13,15], with increased toxicity observed as pH declines. This highlights the necessity for effective pH control to ensure an optimal environment for sustained microbial conversion processes.

Notably, the composition of the gas phase demonstrated considerable variability in hydrogen production in response to alterations in GT content. For the PHB, PHB2.5GT, and PHB5GT formulations, hydrogen levels reached a maximum around day 30 before exhibiting a partial decline, indicating the potential for hydrogen consumption or the initiation of additional metabolic processes. In contrast, hydrogen concentrations in the PHB10GT formulation remained relatively stable throughout, with levels comparable to those observed on day 30. This suggests that increasing GT content may modulate hydrogen dynamics, though not sufficiently to inhibit bacterial degradation. Overall, the addition of the plasticizer GT did not significantly impact the biodegradation of PHB, as indicated by consistent bacterial metabolism and conversion to VFA, regardless of GT concentration.

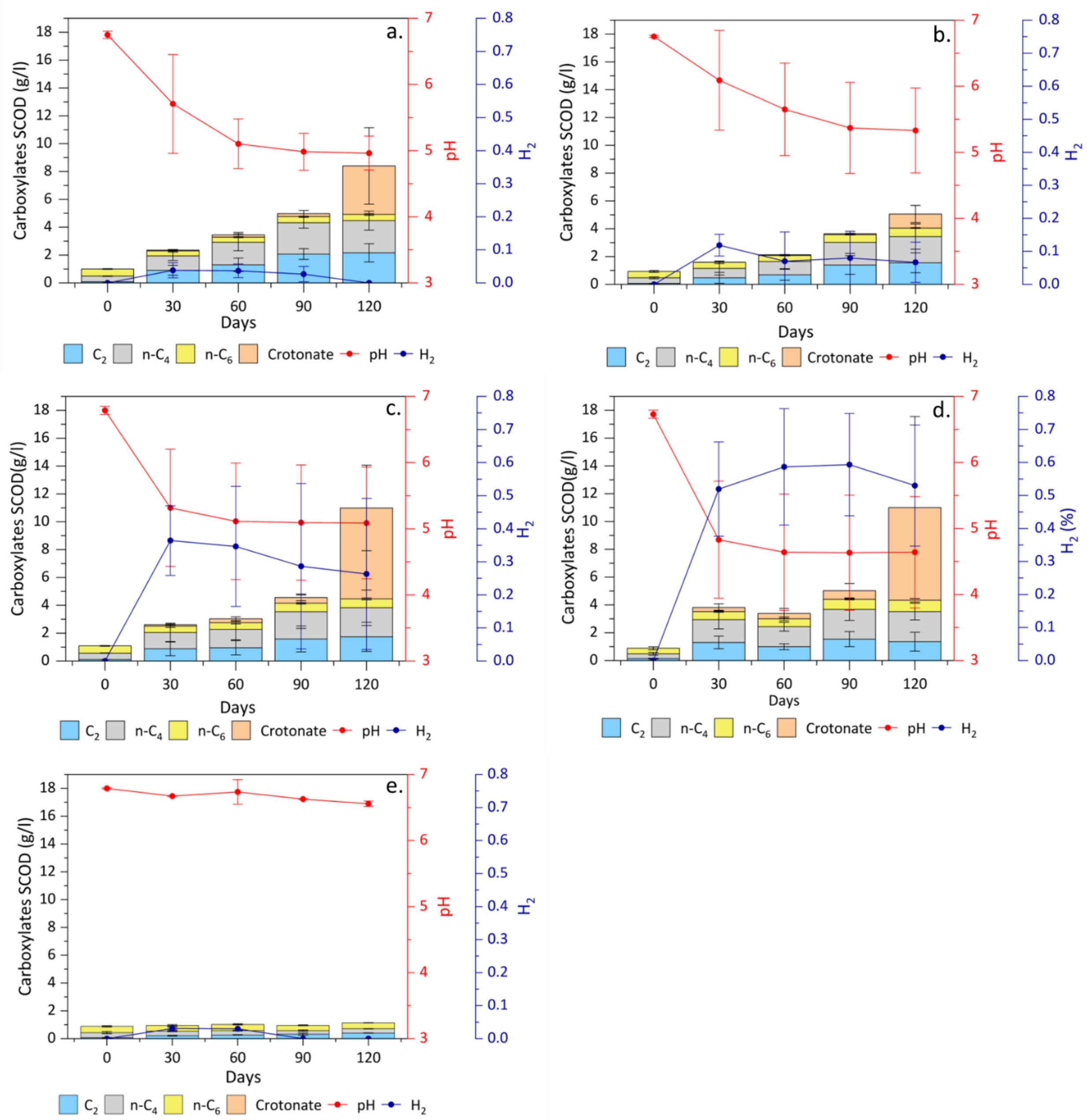

Figure 5.5 *Carboxylates production, pH and H_2 for SF experiment. a) PHB; b) PHB2.5GT; c) PHB5GT; d) PHB10GT; e) Control*

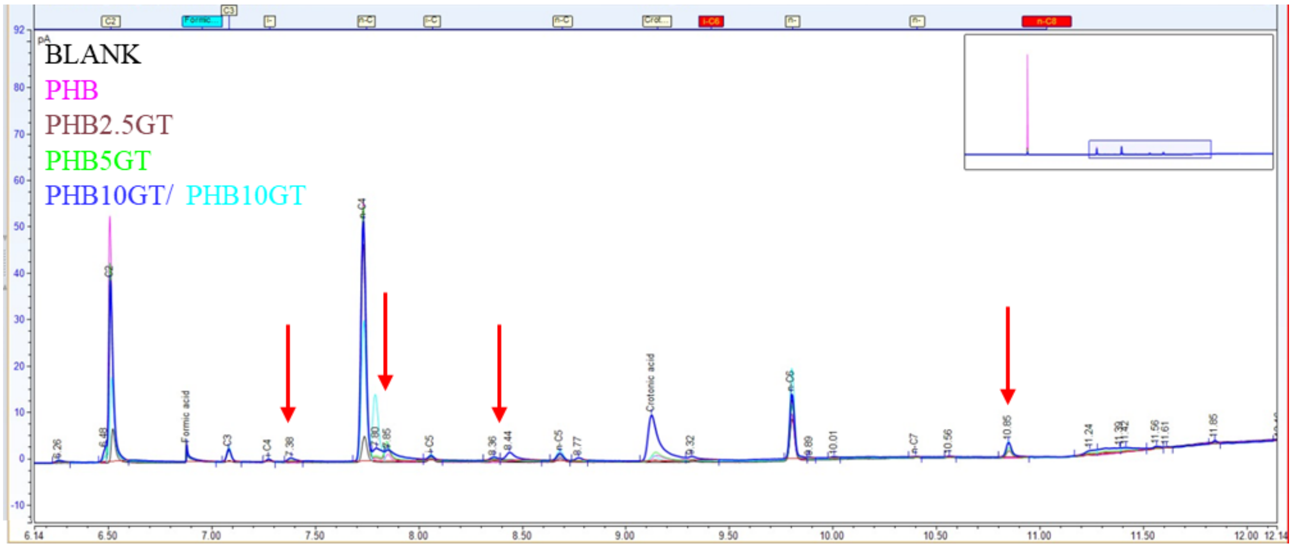

***Figure 5.6** Chromatograms of the SF samples highlighting unidentified peaks*

Figure 5.7 illustrates the optical images of plastic particles both before and after the process of SF. The images displayed in the top row illustrate the dry, milled materials in their original state prior to their introduction into the reactors. In contrast, the bottom row depicts particles immersed in the reaction liquid, sampled with a syringe at the conclusion of the experiment. No substantial reduction in particle size is evident post-fermentation, although a discernible decline in opacity is observed. This alteration in opacity may be attributed to the variation in imaging conditions, with the top row images captured in the absence of a liquid medium, while the bottom row images depict particles within the reaction liquid.

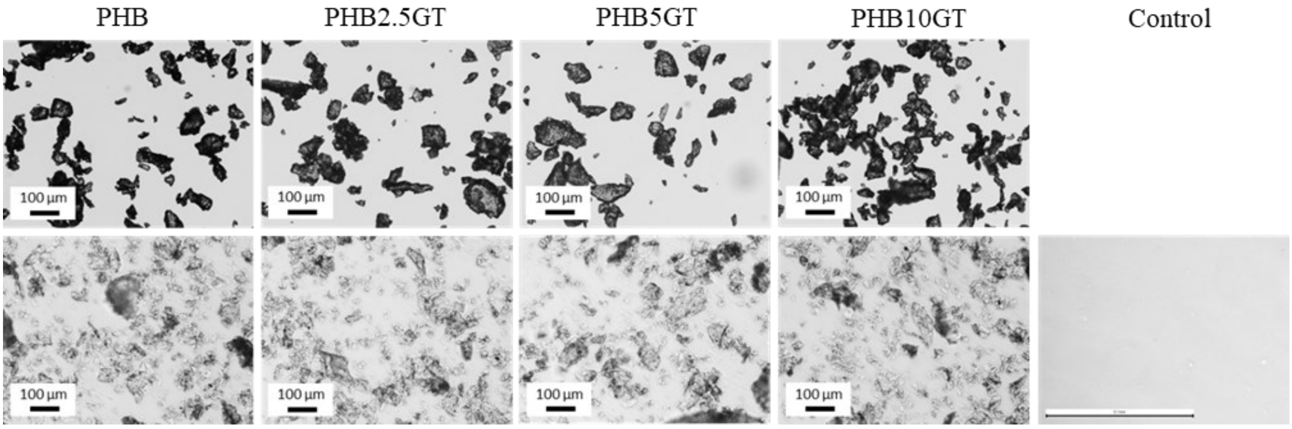

***Figure 5.7** Optical microscopy of the powder materials before (top line) and after (bottom line) the anaerobic fermentation (SF experiment)*

5.5 Conclusions

In conclusion, this study provides, for the first time, valuable insights into the biodegradation of plasticized PHB with GT, a novel green bioplasticizer, under anaerobic conditions. The findings underscore the effectiveness of mixed-culture fermentation, both with and without hydrolysis pretreatment, in generating valuable by-products such as VFA, including acetate and butyrate, which serve as indicators of microbial activity and substrate breakdown.

A low concentration of hydrolysate (4–10 g_{COD}/L) facilitated a complete conversion of the hydrolysate into VFA without inhibitory effects, while a high concentration (20 g_{COD}/L) hindered microbial activity, suggesting the concentration may be toxic to the microbes involved.

It is noteworthy that the study demonstrates that GT concentration within PHB blends did not significantly influence the rate or extent of degradation. However, the control of pH, especially for long-term processes, is essential to ensure optimal conversion. Therefore, GT, in addition to being produced through a green synthesis process and biodegradable, does not negatively impact the metabolic activity of fermenting microorganisms.

The importance of particle size and surface area in facilitating microbial access and enzymatic hydrolysis was demonstrated by the morphological analysis of PHB-GT composites. The degradation process was facilitated using smaller particles with a rough texture.

The utilization of inhibitors, such as BES, permitted the fermentation processes to be concentrated on the generation of VFA, as opposed to biogas, such as methane. Consequently, the fermentation products could be potentially employed in other processes, such as chain elongation, to obtain substrates to produce new PHA.

The findings of the study indicate that PHB-GT blends have the potential to be utilized as sustainable bioplastics within circular production systems. Further research could investigate the use of broader microbial consortia and, through microbial community analysis, identify the most suitable microbial strains to enhance degradation rates and diversify VFA production. Additionally, pH control is essential for optimizing fermentation processes. Overall, this research contributes to the advancement of microbial recycling and provides a foundation for developing efficient, circular materials with minimal environmental impact.

References

1. Contreras-Dávila, C. A., Carrión, V. J., Vonk, V. R., Buisman, C. N. J. & Strik, D. P. B. T. B. Consecutive lactate formation and chain elongation to reduce exogenous chemicals input in repeated-batch food waste fermentation. Water Res 169, 115215 (2020).

2. De Leeuw, K. D., Buisman, C. J. N. & Strik, D. P. B. T. B. Branched Medium Chain Fatty Acids: Iso-Caproate Formation from Iso-Butyrate Broadens the Product Spectrum for Microbial Chain Elongation. Environ Sci Technol 53, 7704–7713 (2019).

3. Vieira, M. G. A., Da Silva, M. A., Dos Santos, L. O. & Beppu, M. M. Natural-based plasticizers and biopolymer films: A review. Eur Polym J 47, 254–263 (2011).

4. García-Depraect, O. et al. Biodegradation of bioplastics under aerobic and anaerobic aqueous conditions: Kinetics, carbon fate and particle size effect. Bioresour Technol 344, 126265 (2022).

5. Bader, J. et al. Utilization of (E)-2-butenoate (Crotonate) by Clostridium kluyveri and some other Clostridium species. Arch Microbiol 125, 159–165 (1980).

6. Jin, Y., de Leeuw, K. D. & Strik, D. P. B. T. B. Microbial Recycling of Bioplastics via Mixed-Culture Fermentation of Hydrolyzed Polyhydroxyalkanoates into Carboxylates. Materials 16, (2023).

7. Nikitina, A. A. et al. Syntrophic Butyrate-Oxidizing Consortium Mitigates Acetate Inhibition through a Shift from Acetoclastic to Hydrogenotrophic Methanogenesis and Alleviates VFA Stress in Thermophilic Anaerobic Digestion. Applied Sciences (Switzerland) 13, 173 (2023).

8. de Leeuw, K. D., Ahrens, T., Buisman, C. J. N. & Strik, D. P. B. T. B. Open Culture Ethanol-Based Chain Elongation to Form Medium Chain Branched Carboxylates and Alcohols. Front Bioeng Biotechnol 9, 697439 (2021).

9. Breznak, J. A. & Kane, M. D. Microbial H2/CO2 acetogenesis in animal guts: nature and nutritional significance. FEMS Microbiol Rev 7, 309–313 (1990).

10. Buckel, W. & Thauer, R. K. Flavin-based electron bifurcation, ferredoxin, flavodoxin, and anaerobic respiration with protons (Ech) or NAD+ (Rnf) as electron acceptors: A historical review. Front Microbiol 9, 346698 (2018).

11. Roghair, M. et al. Effect of n-Caproate Concentration on Chain Elongation and Competing Processes. ACS Sustain Chem Eng 6, 7499–7506 (2018).

12. Janssen, P. H. & Harfoot, C. G. Ilyobacter delafieldii sp. nov., a metabolically restricted anaerobic bacterium fermenting PHB. Arch Microbiol 154, 253–259 (1990).

13. Jankowska, E., Chwialkowska, J., Stodolny, M. & Oleskowicz-Popiel, P. Volatile fatty acids production during mixed culture fermentation – The impact of substrate complexity and pH. Chemical Engineering Journal 326, 901–910 (2017).

14. Reischwitz, A., Stoppok, E. & Buchholz, K. Anaerobic degradation of poly-3-hydroxybutyrate and poly-3-hydroxybutyrate-co-3-hydroxyvalerate. Biodegradation 8, 313–319 (1997).

15. Tenuta, M., Conn, K. L. & Lazarovits, G. Volatile Fatty Acids in Liquid Swine Manure Can Kill Microsclerotia of Verticillium dahliae. https://doi.org/10.1094/PHYTO.2002.92.5.548 92, 548–552 (2007).

Chapter 6

Conclusions

By investigating innovative biocomposite formulations, this project aims to address environmental concerns related to plastic waste and promote the utilization of environmental-friendly solutions across a range of applications. The findings highlight the potential of these materials to be utilized as replacements for conventional plastics, thereby contributing to the development of a circular economy and the promotion of sustainable practices in industries such as packaging and biomedicine.

The initial objective of this research project was to develop and characterize biocomposite materials based on poly(butylene adipate-co-terephthalate) (PBAT) as a sustainable alternative to conventional agrifood packaging materials. The incorporation of calcium-phosphate glass (CPG) and a hybrid zein-titanium dioxide complex (ZTC) into the PBAT matrix resulted in a notable improvement in its mechanical properties, particularly in terms of stiffness. However, some limitations were observed, including reductions in yield strength, elongation at break, and toughness. These findings were corroborated by theoretical models, such as those proposed by Kerner and Pukánszky, which underscored the significance of comprehending the influence of reinforcing phases on polymer properties. The use of scanning electron microscopy (SEM) enabled the confirmation of uniform filler dispersion, with no evidence of agglomeration. Fourier-transform infrared spectroscopy (FT-IR) indicated that the chemical structure of the PBAT-CPG composites remained intact, while energy-dispersive X-ray spectroscopy (EDS) demonstrated successful integration of the fillers. Thermal analysis revealed that the incorporation of fillers did not affect the thermal stability of the material, and in fact, led to significant improvements in viscoelastic and thermo-mechanical properties. These included an increase in the storage modulus and a reduction in creep compliance. These enhanced mechanical and thermal performances render the biocomposite materials suitable for long-term durability applications, particularly in packaging. Moreover, a methodology for the fabrication of PBAT-based biocomposite filaments for Fused Deposition Modeling (FDM) 3D printing was successfully developed.

Preliminary cytocompatibility tests indicated that PBAT-ZTC composites did not harm human dermal fibroblasts (HDFs), showcasing promising biocompatibility for biomedical applications. These results demonstrate that the developed PBAT-based biocomposites represent a viable biodegradable alternative to traditional thermoplastics like polyethylene and a potential solution for sustainable packaging applications. They highlight the potential of these materials to significantly reduce the environmental impact while fulfilling necessary performance criteria in both packaging and biomedical sectors.

Furthermore, the research investigated the potential of polyhydroxybutyrate (PHB) as an alternative to fossil-based plastics. The mechanical properties and processability of PHB were enhanced through the use of glycerol trilevulinate (GT), a green plasticizer. The addition of GT effectively reduced the glass transition and melting temperatures of PHB while simultaneously enhancing flexibility and toughness, which are essential for overcoming the traditional limitations of PHB in melt processability. Moreover, the incorporation of bioactive phosphate glass into the plasticized PHB resulted in the production of composite materials that are well-suited for 3D-printed porous scaffolds, which are essential for biomedical applications such as tissue engineering and regenerative medicine. Rheological studies demonstrated that GT significantly reduced the melt viscosity of PHB, thereby enhancing its processability across a range of manufacturing techniques, including 3D printing. The successful production of scaffolds with an improved surface quality compared to those made with commercial plasticizers validates the effectiveness of GT in this context. Overall, these findings establish PHB as a promising candidate for sustainable materials in biomedical applications, with significant implications for future research and development in biodegradable plastics.

Furthermore, the research included investigations into the degradability of PBAT-CPG composites under accelerated weathering and laboratory-scale composting conditions. The results indicated that the biodegradability of these composites can be enhanced by varying the composition. The barrier properties of the composites were assessed through permeability tests, which demonstrated significant oxygen barrier capabilities, though resistance to water vapor was lower than that of LDPE. These findings emphasize the potential of PBAT-CPG composites to serve as sustainable materials in packaging and agricultural applications, in opposition to conventional materials such as LDPE, while ensuring compliance with end-of-life compostability standards.

The biodegradation behavior of plasticized polyhydroxybutyrate-co-valerate (PHB) enhanced with glycerol trilevulinate (GT) was subjected to systematic analysis under anaerobic conditions, demonstrating effective substrate breakdown and the generation of by-products. The study highlighted the importance of mixed-culture fermentation and underscored the necessity for precise control of hydrolysate concentrations to optimize microbial activity and maximize volatile fatty acid production. These findings indicate that PHB-GT blends can be incorporated into sustainable circular production systems, thereby significantly advancing the development of environmentally friendly bioplastics. Such innovations are crucial for reducing plastic waste and promoting sustainable practices in material production and waste management.

In conclusion, this research demonstrates the successful development of sustainable biocomposite materials with enhanced mechanical, thermal, and degradation properties, rendering them suitable for a range of applications in packaging and biomedicine. The favorable outcomes highlight the potential of these bio-based materials to serve as replacements for conventional plastics, thereby advancing sustainable waste management practices and circular production principles. Future studies should concentrate on further optimizing these materials for specific applications while investigating their long-term environmental impacts and interactions with microbial communities in composting and waste management systems. This research establishes a robust foundation for future advancements in the field of biodegradable materials, encouraging the continued exploration of innovative solutions to address the urgent challenges posed by plastic waste and environmental degradation.

Acknowledgements

The PhD has been a journey, and as with all journeys there have been ups and downs. Moments of joy and excitement for good results and new equipment, and moments of frustration and disappointment for methodologies not working or experiments that did not yield the expected results. In fact, I always say that if there is one thing I learnt during PhD besides research, that thing is patience.

When I started my internship and then my PhD, the pandemic was still going on, the second wave of lockdown was in place, and the lab was still empty, either of instruments or of people. During the PhD, the lab quickly filled up and I met a lot of people who each made their own contribution to the survival of the past years.

First of all, I have to thank **Professor Milanese**. Daniel, thank you for believing in me and offering me the position at the end of my internship. You have always been supportive and available for discussion and suggestions, even though you have the busiest schedule I have ever seen. You have a kind word in every situation, and you are an inspiration to always try and see the positive side of things.

Second thanks go to **Professor Corrado Sciancalepore**, who has been my lead and reference in all the lab activities. You taught me everything I know about the lab work, you involved me in many activities and instrument training, so that I could do my research in the best possible way. You trusted me by delegating measurements and being a reference myself for students and other users of the lab. You also managed to make things work even after I spent hours or days trying only to get poor results. Sometimes there were minor misunderstandings, but that's all part of the journey and helped me to know better.

Thanks to **Stefano**, my first lab buddy. Even if we are not best friends outside work, we can always count on each other. We have gone through all those ups and downs of the PhD together, learning how to use all the new instruments that arrived to populate the lab, overcoming difficulties and providing support in solving doubts and paperwork.

Duccio, you joined the team quietly but soon became a very important figure in the lab. You are a person that I have always been able to count on for help and support with work activities, but also for emotional support when the days were not the brightest. You once told me: “I see how you work, you put part of yourself into it”, and that was inspiring, because it meant that my passion for my research was coming through. Also, your encyclopedic (“wikipedic”) anecdotes added interest and fun to all the lunch and coffee breaks!

Thanks to all the students that over the years populated the lab, to those I had the opportunity of supervising in their activities and to those that are doing their thesis now: it went from being me alone in the lab with my computer and tensile testing to a group of more than 10 people sharing their research days. Even bigger thanks to all of those students that became research fellows colleagues but most importantly friends: **Pierluigi**, **Marzia**, **Elena**, **Francesco** (Franco), **Federico**, **Alice**, **Matteo** (Parn) and **Simone**. We share knowledge, lunch breaks, jokes, and newspaper horoscope readings during coffee. Our diverse academic backgrounds and geographical origins make both work time and time off interesting, funny and worth experiencing. I am happy to have colleagues like you.

Thanks to **Daiana** for bringing together people, you really contributed in creating a unite group in the lab, our "**MEGAlab**", your "Tecnopollicini", instead of just a bunch of people working in the same place. Thanks also for involving the extended lab family from Chemistry Department, "**Lab011**", in our moments of togetherness, like birthdays and festivity lunches.

Thanks to the PhD colleagues, particularly, Natalya, Michele and Claudio, research fellows and Professors from Engineering Department of "Palazzina 7". I was happy to join all-you-can-eat sushi lunches and Secret Santas. A very special thanks goes to **Natalya**: we have been companions since M.Sc. group projects, and even if we did our PhD in different research groups, we have always supported each other and shared even more all-you-can-eat sushi.

During my PhD I had the opportunity to take an exchange period at Wageningen University and Research. There, I met even more people that added value to my journey: I've been involved in curricular and extra-curricular activities since day 1 and became part of a group of very special people. I was surprised by the engaging environment I found, where people of all roles share their working experience and break-time.

Again, I want to start by thanking **Professor David Strik**, my supervisor during my months at WUR, for trusting and supporting me. Working at ETE was not always easy for me as I had no previous background in biotechnology and fermentation processes. You were always available for help and clarification, and you saw the positive in my results when I couldn't see it. **John**, I'm not exaggerating when I say that you were fundamental to my work at ETE. You coached me in the lab, helped me with methodologies and analytical measurements, and became a friend. Thanks also to **Weishen**, for your support with the hydrolysis procedure and for always being present and friendly when I was back in Wageningen. I would like to mention that I certainly won't forget our team-building trip with Prof. Strik to Utrecht Tower with the collection of organic matter from Utrecht canals.

Thanks to all the **Lab team**: **Livio**, **Betty**, **Lucian**, **Pieter**, **Katjia**, **Vinnie**, **Ilse**, and **Julian**. As I said, I did not have a biotechnology background, therefore I am very grateful for all the support you all gave me during my activities. I also would like to thank **Liesbeth** from the Secretariat for organizing all the bureaucracy for my stay at ETE. Thank you **Annemerel** for letting me share the office space and trusting me to water her plants while you were on holiday! I have to admit that I collected a few fallen seedlings of your "Mother of thousands" plant because it is a very cool plant.

A very special thanks to the "special people" that I became more closely friend with, during borrels ad dinners. **Alessia**, you made me find a bit of Italian-ness even far from home, the moving of your stuff will always be memorable, for all a series of motivations. Thanks to **Jorn** and **Selin** for the crazy Pokémon fiever. **Claudia**, you absolutely brought Latina energy to our parties. **Yme**, your "reverse smile" is …, thanks for hosting our barbecues. A lot more of together-ness moments were shared with **Mark, Jos**, **Nick**, **Elizabeth**, **Mika**, **Aladdin**, **Hooman, Kaiyue**, **Tea**. Weekly borrels with drinks and board games were a looking-forward

moment with you all. It was also amazing to meet many Chinese friends: **Sha**, **Zhaolu**, **Xiaofang**, **Bochi**, guy with bandana (sorry I don't remember your name). I will cherish the memory of your kindness and friendliness, and most importantly of the amazing food.
Marko, where to start. You are the most special of the special people I met at ETE, an unexpected bonus that fell into my life thanks to my exchange, and I can't say how lucky I feel to have met you. I am a happier person since I met you, you are a danger for my wallet and constant support for my work activity, but also for my free time passions and interests. Without you, this thesis literally wouldn't have been finished in time.

Thank you to my friends in the dance group. You are the people I share my free time with and take my mind off things at the end of the day. Special mention to **Camilla** and **Debby** for the Tuesday's dinner club: the gossip, venting, and spelt galettes we shared were some of the special moments of the week. Thank you for your support and participation in my thesis writing adventure.

I left the last thanks to my **family**. You know that I am a rather private person, who does not confide everything easily. With you I have shared a lot of good times and a little less of the bad ones, even though it probably would have made me feel better. I know I don't say this often, or more accurately, almost never, but I want you to know how much I love you and how grateful I am for the constant and unconditional support you have always given me, both emotionally and financially, throughout my journey. I hope you are as proud of me as I am of myself.

Appendix A

List of publications

Sciancalepore, C., Togliatti, E., Giubilini, A., Pugliese, D., Moroni, F., Messori, M., & Milanese, D. Preparation and characterization of innovative poly(butylene adipate terephthalate)-based biocomposites for agri-food packaging application. J Appl Polym Sci 52370 (2022) doi:10.1002/app.52370.

Togliatti, E., Milanese, D., Pugliese, D. & Sciancalepore, C. Viscoelastic Characterization and Degradation Stability Investigation of Poly(butylene-adipate-co-terephthalate) – Calcium-Phosphate Glass Composites. J Polym Environ 30, 3914–3933 (2022).

Togliatti, E., Grimaldi, M., Pitirollo, O., Cavazza, A., Pugliese, D., Milanese, D. & Sciancalepore, C. Design of Mechanical Properties of Poly(butylene-adipate-terephthalate) Reinforced with Zein-TiO2Complex. Material Design and Processing Communications 2022, (2022).

Sciancalepore, C., Togliatti, E., Marozzi, M., Rizzi, F., Pugliese, D., Cavazza, A., Pitirollo, O., Grimaldi, M. & Milanese, D. Flexible PBAT-Based Composite Filaments for Tunable FDM 3D Printing. ACS Appl Bio Mater 5, 3219–3229 (2022).

Togliatti, E., Lenzi, L., Degli Esposti, M., Castellano, M., Milanese, D., Sciancalepore, C., Morselli, D. & Fabbri, P. Enhancing melt-processing and 3D printing suitability of polyhydroxybutyrate through compounding with a bioplasticizer derived from the valorization of levulinic acid and glycerol. Addit Manuf 89, (2024).

Appendix B

List of seminars and conferences attended

Oral Presentations

Anaerobic fermentation of PHBV with bioplasticizer for potential application in biological recycling

Togliatti E., Jin Y., Milanese D., Strik D. P. B. T. B., Lenzi L., Degli Esposti M., Morselli D., Fabbri P., Sciancalepore C.*

XXV Convegno Nazionale dell'Associazione Italiana di Scienza e Tecnologia delle Macromolecole (AIM), 08/09/2024 – 11/09/2024 Napoli, Italy

Preparation and characterisation of FDM 3d-printed biocomposite scaffolds for biomedical applications

Santolini c., Togliatti E., Lenzi L., Gallichi-Nottiani D., Morselli D., Degli Esposti M., Sciancalepore C., Fabbri P., Lousteau J., Milanese D.*

XIV Convegno INSTM sulla Scienza e Tecnologia dei Materiali, 09/06/2024 – 12/06/2024 Cagliari, Italy

Characterization of plasticized poly(hydroxybutyrate-co-valerate) (PHBV) for 3D printing applications

E. Togliatti, L. Lenzi, M. Degli Esposti, P. Fabbri, D. Gallichi Nottiani, D. Milanese, D. Morselli e C. Sciancalepore*

ICPMAT 2023 - 17TH International Conference on the Physical Properties and Application of Advanced Materials, 24/10/2023 – 27/10/2023 Torino, Italy

Design of mechanical properties of poly(butylene-adipate-terephthalate) reinforced with zein-TiO complex

E. Togliatti, M. Grimaldi, O. Pitirollo, A. Cavazza, D. Pugliese, D. Milanese, C. Sciancalepore*

XXIV Convegno Nazionale dell'Associazione Italiana di Scienza e Tecnologia delle Macromolecole (AIM), 04/09/2022 – 07/09/2022 Trento, Italy

Viscoelastic properties and degradation of poly (butylene-adipate-terephtalate) – calcium-phosphate glass composites

Elena Togliatti, Daniel Milanese, Diego Pugliese, Corrado Sciancalepore*

Macrogiovani 2022, 16/06/2022 – 17/06/2022 Florence, Italy

Poster Presentations

Study of potential biological recycling through anaerobic fermentation of PHBV blended with bioplasticizer

Togliatti E., Jin Y., Strik D. P. B. T. B., Lenzi L., Morselli D., Degli Esposti M., Fabbri P., Milanese D., and Sciancalepore C.*

XIV Convegno INSTM sulla Scienza e Tecnologia dei Materiali, 09/06/2024 – 12/06/2024 Cagliari, Italy

Characterization of Biodegradable PBAT-based Composites: Dynamic-Mechanical Analysis and Degradation Behaviour

Elena Togliatti, Daniel Milanese, Diego Pugliese, Corrado Sciancalepore*

Polymers 2022 - New Trends in Polymer Science: Health of the Planet, Health of the People, 25/05/2022 – 27/05/2022 Turin

Schools

Lezioni di chimica macromolecolare: la sintesi dei polimeri

XL Convegno-Scuola "Mario Farina", 01/05/2022 – 06/05/2022 Bertinoro (FC), Italy